From Molecular Interactions to Whole Muscle Strength:
connecting small-scale interactions to muscle fiber function through mathematics

By

KATELYN J. JARVIS
DISSERTATION

Submitted in partial satisfaction of the requirements for the degree of

DOCTOR OF PHILOSOPHY

in

APPLIED MATHEMATICS

in the

OFFICE OF GRADUATE STUDIES

of the

UNIVERSITY OF CALIFORNIA
DAVIS

Approved:

Sam Walcott

Tim Lewis

Edward Debold

Committee in Charge

2021

To my mom, my dad, and Conner - for supporting me through every step of this journey.

Acknowledgments

First and foremost, I extend my biggest gratitude to my advisor, Sam Walcott. Thank you for igniting my passion for science and math, and for mentoring me through every challenge and success of graduate school. Thank you for your patience as I discovered new knowledge, and for picking me up when I struggled (once, quite literally!). Thank you for making years of discussing muscle mechanics, debugging code, and solving PDEs both enjoyable and gratifying. Your guidance has shaped me into the scholar I have become, and I'm grateful for your mentorship every day.

Thank you to my experimental collaborators - Ned Debold, Doug Swank, Amy Loya, Kaylyn Bell and Bernie Glasheen - I am grateful for your expertise in biology, and your guidance as I learned the nuances of a new field. A special thank you to Doug, all of the Swank Lab, and especially Bernie, for graciously opening your laboratory to me and for teaching me the challenging and rewarding art of experimental research.

Thank you to the entire mathematical biology family at UC Davis, for creating such a welcoming and supportive cohort of scholars. Being a part of the math-bio community has been the highlight of my time at Davis. Thank you to Tim Lewis, for being a kind mentor and for encouraging me to pursue new opportunities, to Bob Guy for advancing my applied math expertise in many math courses, and especially to Becca Thomases, for being a thoughtful mentor, a champion of all women in math, and especially a dear friend.

Thank you to my math mentors - Mr. Jim Salvi, Dr. Janko Gravner, Dr. Jennifer Schultens, Dr. Habib Najm, Dr. Paloma Gutiérrez Castillo - through each stage of my academic career, you have taught me, in your own unique ways, the beauty of mathematics. To my mentors in biology, Dr. Aenor Sawyer and Mrs. Patti Carothers, thank you for introducing me to the captivating sciences of physiology, medicine, and space.

Thank you to my fellow math graduate students, who lifted me up with late night homework sessions and weekend study groups. To Sam Fleischer, Nicholas Roberts, Carter Johnson, Albert Kim, and many more, I'm grateful for your friendship and your academic support.

Thank you to my Davis friends, who have come and gone over a decade of wonderful years at UC Davis. You have all supported me in different and significant ways. To Calina, thank you for being my partner in crime during graduate school, for helping me find a home in the math department, and for being the most inspiring role model and friend. To Sam Fleischer, thank you for being just as willing to have a late-night study session as you were to watch a baseball game. Mostly, thank you for always fighting for equality in our department, and for encouraging me to do the same. Thank you to Megan Watson, for weeknight dinners and lifelong friendship. Thank you to Andy Jones, Kelly Reynolds, Ari Ghavami, Divya Kernik, Kayla Harff, Danny Eliahu, Brandon Rebotarro, Jess and Oakley Gordon, and many, many more. You all bring joy to my life, and I'm grateful for each of you.

To my parents - Pam and Jeff Jarvis - my role models, my support system, my biggest fans. Thank you for showing up for me, every time. Thank you for instilling confidence in me, and for teaching me that anything is possible with enough grit and hard work. To my mom, thank you for filling my soul with love, and always finding meaningful ways to remind me of your unwavering support. To my dad, thank you for teaching me to be resilient, for inspiring me to chase dreams I never thought were possible, and for being a fellow "space-geek".

For Conner - Thank you for being my anchor during both joyful and challenging times. Thank you for creating adventures, both big and small, and for always keeping me laughing. Thank you for believing in me, for sharing in my victories, and for always encouraging me to pursue my passions. I am a better person because I share my life with you.

Abstract

Muscle contraction is an essential biological process than spans physiological size scales, ranging from molecular interactions between the proteins actin and myosin, to larger cellular behavior, and ultimately whole-muscle function. The mechanisms of contraction are intriguing to study because unique behavior occurs at each physiological size scale. Developing a detailed understanding of the connections across scales is particularly important, because whole-muscle dysfunction and disease are often attributed to small-scale mutations. Thus, a multi-scale model of contraction is necessary to form a comprehensive understanding of muscle function.

In the following dissertation, I develop a multi-scale model of muscle contraction based in well-measured molecular mechanisms that spans physiological size scales to connect to the larger fiber level. In each chapter, I focus on an unexplained attribute of muscle contraction, and using biophysical modeling and quantitative techniques, I extend the theory to describe experimental measurements across scales.

In Chapter 1, I begin by providing an overview of the literature of muscle contraction to contextualize my research within the broader field. In Chapter 2, I explore muscle fatigue, and through development of a model to describe molecular measurements under the fatiguing conditions of acidosis and increased phosphate, provide novel insight into a molecular basis for contractile fatigue. In Chapter 3, I scale molecular interactions to the cellular level to explore the mechanisms behind the force transient response of a muscle fiber after a small, rapid stretch. By adjusting the model to replicate force transient measurements, I suggest a mechanism for unexplained fiber phenomenon, and highlight the complex connection between molecular kinetics and fiber-level behavior. In Chapter 4, I investigate the regime of large-amplitude, rapid lengthening of muscle fibers. To develop the model to describe these measurements, I extend my modeling framework to explicitly model multiple-sarcomere systems, and illustrate the need for such a model in capturing the effects of sarcomere instabilities that arise during rapid large-amplitude lengthening.

Taken together, the work presented in the following chapters seeks to deepen our knowledge of muscle contraction. By developing mathematical models to describe unknown muscle behaviors, we make connections across physiological size scales and provide insight into molecular mechanisms that cause whole-muscle function, ultimately working towards a comprehensive theory of muscle.

Contents

Introduction

Motivation

Muscle contraction is a fundamental biological process that is necessary for a range of physiological functions. Cardiac muscle contraction, for example, results in proper heart function, while skeletal muscle contraction is crucial for actions including human locomotion and insect flight. Additionally, involuntary muscle contraction, such as that which results in blood flow and digestion, is a result of the contraction of smooth muscles. When these processes fail, muscle dysfunction or disease can result in devastating physiological consequences, ranging from muscular dystrophy to cardiac disease. Thus, having a clear understanding of the mechanisms of muscle function and disease are imperative for human-health related fields.

The biological system of muscle contraction spans physiological size scales, beginning with protein interactions at the molecular level and scaling upward approximately eight orders of magnitude to result in whole-muscle contraction. This system is both compelling and challenging to study, because unique behavior occurs at each size scale. Today, there is an extensive amount of experimental work exploring the spectrum of physiological scales from the molecular [e.g. Finer et al., 1994, Guilford et al., 1997, Veigel et al., 2003, Kad et al., 2007, Debold et al., 2008] to whole-fiber [e.g. Huxley and Simmons, 1971, Glasheen et al., 2017, Piazzesi et al., 1997] and whole-muscle [e.g. Hill, 1938, Fenn, 1923] levels. However, given that emergent behavior occurs across physiological size scales, it is challenging to make connections between single molecule mechanisms and larger fiber behavior [Duke, 1999, Baker et al., 2002, Campbell, 2009, Stoecker et al., 2009, Walcott and Sun, 2009]. The ability to associate mechanisms across scales is particularly important, because many muscle diseases have been connected experimentally to molecular-level defects [e.g. Landstrom et al., 2008, Tardiff, 2005, Campbell et al., 2010, Regnier, 2018, Seidman and Seidman, 2001]. For example, it has been shown experimentally that familial hypertrophic cardiomyopathy,

a form of cardiovascular disease, is linked to point mutations in the proteins involved in contraction [Colegrave and Peckham, 2014, Sivaramakrishnan et al., 2009, Seidman and Seidman, 2001, Geisterfer-Lowrance et al., 1990]. Thus, a multi-scale perspective of muscle contraction is essential for a comprehensive understanding of muscle function and disease.

One approach to developing this multi-scale understanding is through mathematical modeling. Throughout the study of muscle, a vast collection of theoretical work has been developed to quantitatively describe experimental results [e.g. Lacker and Peskin, 1986, Piazzesi and Lombardi, 1995, Duke, 1999, Månsson, 2010, Walcott et al., 2012, Campbell, 2014, Tanner et al., 2007]. These models vary in the size scales they describe, the physiological details they include, and the mathematical techniques they employ. In general, each model fits some subset of experimental data, often leading to a few specific implications for understanding muscle mechanisms. However, to the best of my knowledge, there is no single mathematical model that is able to fully describe muscle measurements across physiological size scales.

With the work presented in this dissertation, I aim to develop a mathematical model of muscle contraction, based in well-defined molecular mechanisms, that captures the unique behavior across physiological scales. To do so, I formulate a simple mechanochemical model of contraction at the molecular scale, and through collaboration with experimentalists, expand it to describe various muscle measurements at the molecular and fiber levels. In particular, I focus on three key areas of muscle contraction in which the molecular mechanism behind a cellular phenomenon is unknown. These are (1) the effect of muscle fatigue at the molecular scale, (2) the mechanisms that result in a muscle's force response to rapid, small amplitude stretch, and (3) the behavior resulting from large amplitude muscle lengthening and the effect of sarcomere non-uniformity.

In the following sections, I begin by introducing the biological background and mathematical framework that form the foundation of my research (Introduction), and additionally provide an overview of mathematical modeling in the literature to provide context for my modeling work (Chapter 1). Next, in Chapter 2, I detail my work on muscle fatigue. In this work, I develop a minimal cross-bridge model to describe the effects of acidosis and increased phosphate on molecular kinetics. These factors are characteristic of muscle fatigue at the fiber level, and thus our successful model provides insight into the molecular mechanisms of large-scale contractile fatigue (Chapter

2, [Jarvis et al., 2018]). In Chapter 3, I explore the transient force response of a muscle fiber to a rapid, small amplitude stretch. Through development of a model to describe this behavior, I illustrate the complex connection between fiber level measurements and molecular kinetics, and in particular, suggest a mechanism for the unexplained cellular-scale phenomenon of stretch-activation (Chapter 3, [Jarvis et al., 2021]). Finally, in Chapter 4, I extend this modeling work to additionally consider large amplitude muscle lengthening. With this work, I show that sarcomere instabilities arise when muscle fibers are stretched to sizable lengths, resulting in the necessity of using explicit multi-sarcomere models to appropriately model the response (Chapter 4). Taken together, my findings provide insight into the connections across physiological scales of muscle and work towards a multi-scale model of muscle contraction.

Biological Background

Muscle contraction is a biological system that spans about eight orders of magnitude from the smallest molecular scale to the larger whole-muscle level (Fig. 0.1). At the largest scale, a whole muscle is made up of many muscle fibers, which are individual muscle cells. These fibers are composed of specialized organelles responsible for contraction, or myofibrils. Each myofibril is sectioned into sarcomeres, which are the fundamental unit of muscle contraction. Sarcomeres contain two sets of protein filaments: thick filaments, which include the protein myosin, and thin filaments, which include the protein actin. At this scale, it is the cyclical interaction between actin and myosin that powers relative sliding of the two protein filaments, which ultimately scales up to result in macro-level contraction. In this section, I provide a brief introduction to muscle activation, outline the complex dynamics of the interaction between actin and myosin, and discuss some of the unexplained phenomena of contraction that motivate this work.

Muscle Activation and Cross-Bridge Dynamics: When a muscle fiber is in a pre-activation state, the actin filament interacts with two regulatory proteins, troponin and tropomyosin. Tropomyosin wraps around the actin filament, sterically blocking the myosin binding sites and preventing the formation of cross-bridges (Fig. 0.2). When a muscle cell receives a neural input to

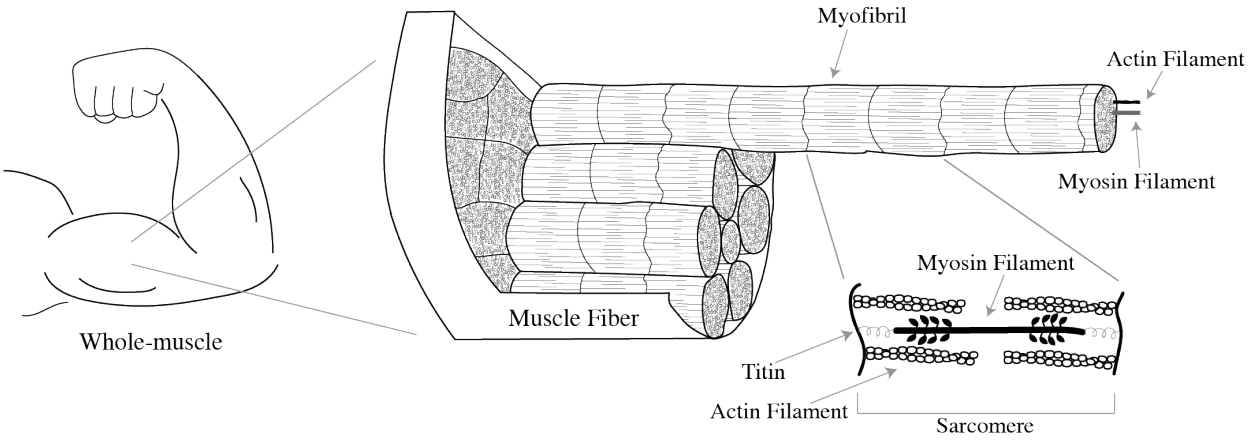

Figure 0.1. Sketch of muscle physiology across scales. Unique behavior occurs at each scale, spanning from whole-muscle contraction down to the smallest molecular scale. *Adapted from Art and Science Graphics*, Ruona

signal for contraction, calcium is released from the sarcoplasmic reticulum and binds to troponin. This causes a conformational change in tropomyosin, shifting the protein to expose some of the binding sites on the actin filament. Myosin can then bind to actin in a cooperative process whereby a bound myosin molecule locally displaces tropomyosin further, enhancing myosin binding in a local region.

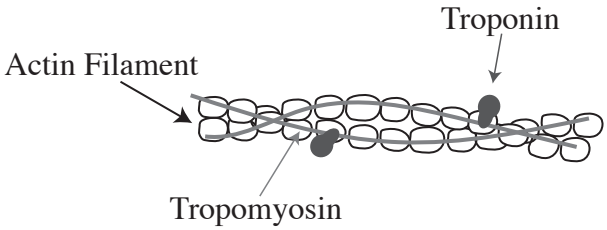

Figure 0.2. Sketch of actin filament in a pre-activation state. In the absence of calcium, proteins troponin and tropomyosin interact with the actin filament, blocking myosin binding sites and inhibiting contraction.

Once full activation has occurred, the proteins myosin and actin interact in a cyclical process in which ATP-hydrolysis drives myosin molecules to transiently interact with actin filaments, forming cross-bridges. Once bound, the myosin molecule undergoes a conformational change, called the power-stroke, which applies a force on the actin filament and results in the two filaments sliding past one another. ATP binding to the myosin molecule causes dissociation of actin and myosin, and finally the hydrolysis of ATP primes the cycle to begin again.

This interaction can be represented with a simple kinetic scheme in which myosin and actin cycle through discrete states (Fig. 0.3). Beginning in an unbound configuration, myosin is unattached

from actin with ADP and inorganic phosphate (P_i) in its active site (state 4, Fig. 0.3). In some order, P_i is released, myosin binds to actin, and the power-stroke conformational change occurs (transition 4 to 1, Fig. 0.3). In this configuration, myosin is strongly-bound to actin and producing force, with ADP in its active site. ADP can then be released in a force-dependent manner, and myosin stays bound to actin in a rigor state (state 2, Fig. 0.3). ATP can then bind to the now empty active site of myosin, which causes myosin to detach from actin (state 3, Fig. 0.3). Finally, with myosin unbound from actin, ATP can be hydrolyzed into products ADP and P_i (transition from 3 to 4, Fig. 0.3), and the cycle can repeat.

The mechanical and chemical details included in this scheme are well-studied, and this minimal model is generally accepted to describe the most basic actomyosin interaction. Additionally, many simple kinetic schemes similar to that presented here are able to describe molecular muscle measurements [e.g. Walcott et al., 2012, Pate and Cooke, 1989, Baker et al., 2002, Kad et al., 2007] and even have predictive power at larger scales [e.g. Piazzesi and Lombardi, 1995, Månsson, 2010, Newhard et al., 2019]. However, these simplistic models all lack some details, and many only describe some subset of muscle measurements or provide only qualitative predictions. A truly comprehensive theory would replicate the entire spectrum of muscle measurements and have predictive power at all physiological scales. The modeling work presented in this dissertation aims to further our comprehensive knowledge of contraction by using this four-state kinetic scheme as foundation and extending it to describe a wider range of muscle measurements, as detailed in the following chapters.

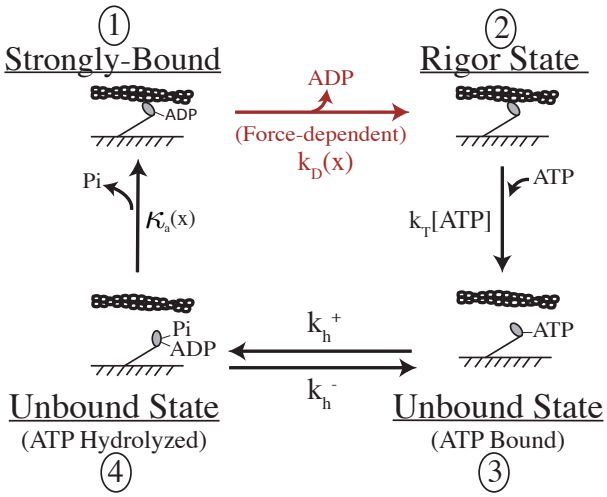

Figure 0.3. *Adapted from Jarvis et al. [2021].* A simple four-state kinetic scheme describes the interaction between actin and myosin, including two bound states (states 1 and 2) and two unbound states (states 3 and 4).

Muscle Fatigue: Under normal skeletal muscle conditions, the above actomyosin dynamics drive muscle contraction, resulting in force and motion at larger scales. However, when muscles are stimulated repeatedly or at a high frequency, their ability to generate force and motion quickly diminishes, resulting in muscle fatigue. While there are likely many factors that contribute to overall muscle fatigue, including neural mechanisms, decreased calcium, increased metabolic by-products, and more, the effect of fatigue on the molecular mechanisms of contraction are not well understood [Debold, 2012].

It has been shown experimentally that fatigued muscle fibers exhibit acidosis, due to increased levels of hydrogen ions from the dissociation of lactic acid to lactate [Fitts, 1994] and a by-product of ATP-hydrolysis [Robergs et al., 2004], as well as increased levels of inorganic phosphate (P_i), due to the breakdown of ATP to creatine phosphate. During severe fatigue, the pH in a muscle fiber can fall from a neutral 7.0 to as low as 6.2 [Wilson et al., 1988, Cady et al., 1989, Nelson et al., 2014], and the P_i levels can rise from just a few mM to as high as 30 mM [Nelson et al., 2014]. Many experimental studies have illustrated a link between these agents and loss of contractile function [e.g. Cooke and Pate, 1985, Debold et al., 2004, Nelson et al., 2014, Debold, 2012, Knuth et al., 2006]. It has been shown, for example, that acidosis alone can significantly reduce unloaded shortening velocity and power produced by a muscle fiber [Pate et al., 1995, Knuth et al., 2006], and that increased P_i and decreased pH in muscle fibers decrease both force and velocity [Cooke and Pate, 1985, Debold et al., 2004]. However, while it is clear that acidosis and increased P_i concentrations contribute to contractile fatigue, it is unclear how these factors affect the interaction between actin and myosin.

Additionally, the individual effects of pH and P_i at the molecular level of muscle are complex. The effect of increased P_i has been studied extensively due to its connection to the conformational change of myosin that results in force production. Experimental work has established that P_i can rebind to myosin in a strongly-bound configuration prior to ADP release, causing early dissociation of myosin from actin, and resulting in decreased force [Debold et al., 2013]. However, the details of this transformation, and exactly how P_i rebinding affects the actomyosin interaction, are still controversial.

The molecular effect of pH is much less studied, but it has been shown experimentally that low pH decreases myosin's average step size in a laser trap [Debold et al., 2008] and reduces actin velocity in a motility assay [Debold et al., 2011]. It has hypothesized that low pH affects myosin's ADP release rate, resulting in slower detachment from actin, and thus depressing actin velocity [Debold et al., 2008, Debold, 2012]. However, given that acidosis does not result in an increase in force, as would be expected from slower detachment rates and thus longer force-generating lifetimes, pH must be affecting additional steps in the cross-bridge cycle.

Ultimately, a decrease in pH and an increase in P_i occur concurrently during muscle fatigue, and thus in order to have a comprehensive understanding of fatigue, we must understand their combined effects. The complex dynamics and unknown mechanisms of these agents motivate the work presented in Chapter 2. By investigating molecular level measurements and developing a mathematical model, we provide a possible mechanism for the combined effects of pH and P_i at the molecular level, and contribute to a deeper understanding of muscle fatigue across scales.

Stretch-Activation: Stretch-activation (SA) is a cellular phenomenon of muscle defined as a delayed increase in force following a rapid lengthening of a muscle fiber [Glasheen et al., 2017, Zhao and Swank, 2016]. Nearly all muscle types exhibit some magnitude of stretch-activation, and this phenomenon is thought to be biologically advantageous because it can enhance the amount of force produced beyond that possible from only calcium activation [Glasheen et al., 2017, Zhao and Swank, 2016, Josephson et al., 2000]. Cardiac muscle, for example, is moderately stretch-activatable, and it is hypothesized that stretch-activation contributes to the intrinsic ability of cardiac muscle to adapt to differential volumes of blood flow, an effect known as the Frank-Starling mechanism [Zhao and Swank, 2016, Campbell and Chandra, 2006]. Additionally, insect flight muscles are a form of skeletal muscle that elicit a significant stretch-activation response. To maintain flight, insect flight muscles contract at a very high frequency [Josephson et al., 2000]. It is hypothesized that this is, at least in part, due to stretch-activation, which moderates force levels without the need for constant calcium cycling, leading to more economical force and power production, and resulting in flight [Josephson et al., 2000, Glasheen et al., 2017].

Experimentally, stretch-activation is observed in the force transient response of a muscle after a rapid stretch is applied to the fiber. In this protocol, the muscle fiber is calcium-activated and held at an isometric length. At a particular point in time, the fiber is rapidly (e.g. < 0.5 ms) stretched a small percentage of its length, and then held isometrically again. The transient response of the muscle fiber occurs in four phases (Fig. 0.4). At the time of stretch, the force quickly increases (phase I). After this initial peak, the force rapidly decays (phase II), followed by a delayed increase in force known as stretch-activation (phase III), and finally a slow recovery phase (phase IV).

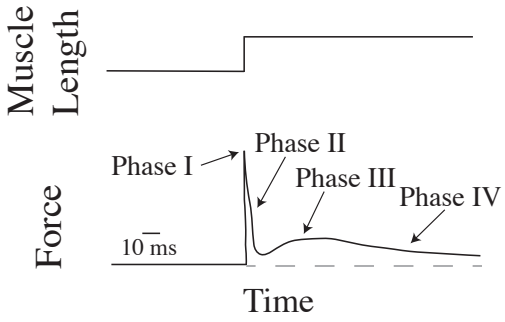

Figure 0.4. *Adapted from [Jarvis et al., 2021].* Sketch of a typical skeletal muscle force response to a rapid, small-amplitude stretch.

While stretch-activation is physiologically relevant and studied experimentally, the molecular mechanisms that cause it are unknown [Ford et al., 1977, Glasheen et al., 2017, Kawai and Halvorson, 2007, Galler et al., 1997, Linari et al., 2004]. In Chapter 3, we develop a cross-bridge model to reproduce two complementary fiber-level measurements including force transients after stretch and the force-velocity relationship. By determining the model components necessary to simultaneously fit these measurements, we develop a hypothesis for the mechanism of stretch-activation, provide insight into the connection across scales, and take steps towards a comprehensive theory of contraction.

Muscle Lengthening: Human locomotion is dependent on eccentric contraction, during which active muscles are forcibly lengthened to produce negative mechanical work. A variety of muscular movements involved in motion and exercise, such as walking downhill, descending stairs, or running, rely on the proper lengthening of muscle [Balnave and Thompson, 1993, Clarkson and Hubal, 2002, Hody et al., 2019, Lindstedt et al., 2001]. Eccentric contraction is a particularly interesting contractile regime because it can result in stretch-induced muscle damage, followed by a recovery period that fortifies the muscle against further eccentric-related injury [Proske and Morgan, 2001, Clarkson and Hubal, 2002, Morgan and Allen, 1999, McHugh et al., 1999]. This phenomenon,

known as the "repeated bout effect" is a compelling area of study, because fortification against muscle damage could have implications for restoring or preserving muscle function in aged or injured muscle [Hody et al., 2019, Brown et al., 1997, Schwane and Armstrong, 1983].

At the cellular scale, experimental studies demonstrate that muscle lengthening causes structural changes at the myofibril and sarcomere levels. Studies show disruption in Z-lines [Clarkson and Hubal, 2002, Friden et al., 1981], disorganization of sarcomere structure [Proske and Morgan, 2001, Brown and Hill, 1991, Wood et al., 1993], and evidence of non-uniform lengthening among sarcomeres [Wood et al., 1993, Proske and Morgan, 2001]. The exact mechanisms of these changes, and how they scale to larger physiological levels, is not well understood.

In addition to unexplained experimental results, the majority of theoretical muscle models have been developed to describe isometric and shortening muscle, without consideration of lengthening. Further still, many models approximate muscle fiber dynamics with the behavior of a single half-sarcomere, and such models would not be able to capture multi-sarcomere effects, such as non-uniformity in sarcomere lengthening, which are observed in muscle measurements. As a result, there is no detailed theory to describe eccentric contraction, and the connections between molecular interactions, cellular behaviors, and whole-muscle lengthening phenomenon are unclear.

The work presented in Chapter 4 is motivated by eccentric contraction, and the advantageous and yet unexplained features of this regime. By extending our modeling framework to describe a multiple-sarcomere system, we investigate rapid, large-amplitude lengthening, and provide new perspective on the model components necessary to accurately capture lengthening muscle dynamics.

Mathematical Framework

At a broad level, the objective of this dissertation research is to develop a comprehensive mathematical model of muscle contraction that spans physiological size scales. To do so, we develop mechanochemical models of the interaction between actin and myosin based in well-defined molecular mechanisms and use mathematical tools to connect this molecular behavior to larger scales. In this section, I briefly introduce some of the mathematical framework used in the following work,

illustrate how we use mathematics to make connections across scales, and discuss how mathematical results are connected to experimental measurements.

Actin and myosin interact in a cyclical process that is fueled by ATP-hydrolysis. To model this process, we express the interactions with simple kinetic schemes that describe the physical, mechanical, and chemical details (e.g. Fig. 0.3 or 3.1B). We then implement a variety of quantitative techniques to simulate these dynamics, choosing specific mathematical tools depending on the experimental protocols and measurements we consider. When comparing the model to single molecule or small ensemble measurements, for example, the kinetic scheme can be simulated using Monte Carlo (MC) methods. For larger-scale measurements, we use a system of partial differential equations (PDEs) to make connections across scales.

First, when considering molecular measurements, we implement a modified Gillespie algorithm (a version of a Monte Carlo method) to simulate the time evolution of small ensembles. Throughout time, we keep track of the state of each myosin molecule, the extension of the molecule when bound to actin, and the reaction time for each molecule to transition to the next state. These reaction times are determined by sampling from the appropriate distributions, given the rate constants for the available transitions between states. To determine these, we consider a cross-bridge transition between two states as a simple forward chemical reaction. This is modeled with a standard ordinary differential equation of the form $dn/dt = -kn$ where n is the fraction of molecules in the current state and k is the forward rate constant to the next state. Thus, the fraction of molecules in the current state exponentially decreases throughout time with the form, $n = n_0 e^{-kt}$. The Gillespie algorithm works by randomly picking a reaction time from this distribution. To implement this, we define the transition time for each molecule with the following, where $\mathbb{X}$ is a uniformly distributed random number between 0 and 1, and k_{ij} is the rate constant to transition from state i to state j:

$$T = -\frac{1}{k_{ij}} \ln(\mathbb{X})$$

At each iteration in our simulation, we determine the smallest reaction time for all molecules, and step forward in time by this value. The corresponding molecule transitions to the next state, and the system is updated appropriately. The use of this variable time step is characteristic of the

Gillespie algorithm, and is advantageous over a standard Monte Carlo method because time steps only occur when reactions occur. Additionally, our method is a "modified" Gillespie algorithm because some of the reaction rates in our system are force-dependent, and we must adjust these calculated reaction times each time a molecule binds or unbinds. Employing Monte Carlo methods is a straightforward way to simulate the interaction between actin and myosin on a small scale. (For more information on Monte Carlo methods, see section 1.4).

When we scale the actomyosin interaction upwards and compare to fiber level measurements, Monte Carlo simulations become computationally costly and inefficient. Therefore, we also employ a system of integro-PDEs to make connections across scales. Here, I describe this process for a simple four-state kinetic scheme (Fig. 0.3), and in the following chapters, the same general methods are used for similar cross-bridge models.

To transform our four-state model into a system of differential equations, we use chemical kinetics. However, the dynamics of the system are dependent on the force molecules experience, and so we must take care to appropriately model this force-dependence. Let x be the extension of a myosin molecule. When a molecule is in an unbound state (states 3, 4 in Fig. 0.3), the molecule is unbound from actin and therefore experiences no force. Thus, the probability of being in an unbound state, $N_i(t)$, is simply a function of time. When a molecule binds to the actin filament (states 1, 2 in Fig. 0.3), it does so with a particular extension, x. Thus, as with continuous random variables, we must define the probability density that myosin is in a bound state i with extension x as $\eta_i(x,t)$. The integral $N_i(t) = \int_{-\infty}^{\infty} \eta_i(x,t)dx$ then defines the probability that myosin is bound in state i at time t. Transitions between most states are defined by constants, however the attachment rate of myosin to actin (transition from state 4 to 1 in Fig. 0.3) must also be defined as a probability density function, since myosin binds with a particular extension. Finally, ADP release rate has been measured experimentally to be dependent on the force a molecule experiences, and given that we model myosin as a linear spring and thus extension is proportional to force, ADP release rate is also dependent on x.

Assuming that myosin can bind anywhere along the actin filament (i.e. the dense binding limit, see section 1.2) and that there is a sufficiently large number of cross-bridges, the four-state kinetic scheme can be expressed as follows, with the final equation preserving conservation of mass:

$$
\begin{aligned}
\frac{\partial \eta_1}{\partial t} + v\frac{\partial \eta_1}{\partial x} &= \kappa_a(x)N_4 - k_D(x)\eta_1 \\
\frac{\partial \eta_2}{\partial t} + v\frac{\partial \eta_2}{\partial x} &= k_D(x)\eta_1 - k_T[\text{ATP}]\eta_2 \\
\frac{dN_3}{dt} &= k_T[\text{ATP}]\int_{-\infty}^{\infty}\eta_2 dx + k_h^- N_4 - k_h^+ N_3 \\
\frac{dN_4}{dt} &= k_h^+ N_3 - \left(k_h^- + \int_{-\infty}^{\infty}\kappa_a(x)dx\right)N_4 \\
1 &= \int_{-\infty}^{\infty}\eta_1 dx + \int_{-\infty}^{\infty}\eta_2 dx + N_3 + N_4
\end{aligned}
\tag{0.1}
$$

We solve this system under a variety of different conditions, such as steady-state and isometric ($v = 0$), depending on the experimental measurements we are interested in describing. To solve, we use a collection of both numerical and analytical tools including standard ODE solvers, the method of characteristics, and asymptotic approximations, as described in detail in the following chapters. The results of these differential equations are then directly relatable to experimentally measured quantities. In particular, we define force as the product of the probability a myosin molecule is bound times the force it produces when it is. Letting κ represent the stiffness of myosin and given that a molecule undergoes a power-stroke of size d nm once bound (and thus the extension when bound is $(x + d)$), force produced is then:

$$
F = \int_{-\infty}^{\infty}\kappa \cdot \eta_1 \cdot (x + d)dx + \int_{-\infty}^{\infty}\kappa \cdot \eta_2 \cdot (x + d)dx \tag{0.2}
$$

With this mathematical representation of the mechanochemical cycle of actin and myosin, we are able to relate molecular interactions to fiber-level behavior. This mathematical framework forms the general principles and techniques of the work presented in the following chapters, with adjustments and advancements made to the modeling work as necessary.

CHAPTER 1

Literature Review

1.1. First Muscle Physiology Studies: The Sliding Filament Theory

Given the physiological importance of muscle contraction, it has been a subject of study for centuries. In the early 1900s, scientists began proposing questions regarding the structure of muscle and the mechanisms of contraction across physiological scales. Even with the limited experimental techniques available at the time, researchers were able to develop a preliminary description of contraction, and much of this work is still the foundation of the muscle field today.

Throughout the extensive history of studying muscle, two classic experiments on whole muscles give motivation for the work presented in this dissertation, and provide foundation for our review of the sliding filament theory. First, in 1923, W.O. Fenn performed experiments on frog sartorius muscle that enabled him to study the relationship between the energy liberated by a muscle and the work performed during contraction [Fenn, 1923]. In this work, he measured the heat a muscle produced when it was maximally stimulated and allowed to shorten a fixed distance under an imposed load. Fenn's measurements showed that the heat a muscle generated increased linearly with load. As the load increased, the muscle eventually became unable to shorten the full distance in the time allotted, after which the heat decreased linearly (Fig. 3.1C). Additionally, Fenn determined that the excess heat produced during a contraction in which the muscle was allowed to shorten under a fixed load (i.e. an isotonic contraction), in comparison with a contraction in which the muscle was held at a fixed length (i.e. an isometric contraction), was proportional to the amount of work done by the muscle. Today, this is known as the Fenn effect [Fenn, 1923].

Subsequently, in 1938, A.V. Hill extended the experimental work on the energetics of muscle and derived a relationship between force and velocity of contraction [Hill, 1938]. Hill's measurements resulted in a hyperbolic relationship between force and velocity, in which increasing force results in a decrease in shortening velocity (Fig. 3.1D). While more recent experiments suggest deviations

from this relationship under some conditions [e.g. Edman et al., 1976, Duke, 1999], Hill's force-velocity relationship remains an excellent phenomenological description and is still used in many current muscle studies [e.g. Knuth et al., 2006, Jarvis et al., 2018, Eldred et al., 2010, Widrick et al., 1996, Piazzesi and Lombardi, 1995].

As biologists became increasingly curious about the molecular scale in the 1950s, there was increased interest in understanding how smaller-scale mechanisms produced whole-muscle behaviors. Many experimentalists turned to novel imaging techniques that illuminated the structure of muscle at different physiological size scales. By the early 1950s, a general picture of the structure of muscle had emerged. This work illustrated that whole muscles were comprised of many muscle fibers. Fibers were made of bundles of myofibrils, which were long, cylindrical objects that were sectioned into repeating units in series. These units, now known as sarcomeres, were originally defined based on their isotropic regions (i.e. I-bands) and anisotropic regions (i.e. A-bands). It was later determined that these light and dark regions constitute thin and thick filaments, and contain the proteins responsible for contraction. We now know that the thick filaments contain the protein myosin and the thin filaments contain the protein actin.

In 1954, A.F. Huxley and R. Niedergerke used imaging techniques to study the structure of a muscle fiber during the contraction process [Huxley and Niedergerke, 1954]. In particular, they looked at how the size of the light and dark regions changed under different contraction protocols. They found that, during contraction, the length of the A-band region stayed constant, but the length of the I-band region decreased as a muscle shortened [Huxley and Niedergerke, 1954]. These results provided some of the first evidence of the thick and thin filaments sliding past one another during contraction [Huxley and Niedergerke, 1954]. Further evidence for sliding filaments was proposed by H.E. Huxley and J. Hanson in their work on myofibrils [Huxley and Hanson, 1954], where they additionally experimented with varying concentrations of ATP in their experimental systems. Their findings were some of the first to suggest that when filaments slide, connections are formed between actin and myosin in an ATP-dependent manner [Huxley and Hanson, 1954]. Together, these studies presented a compelling view of the sliding filaments and cross-bridge dynamics within muscle.

With these preliminary muscle experiments, a theory of the basic mechanisms of muscle contraction began to emerge. This theory, known as the sliding filament theory, detailed a process

in which the thick and thin filaments transiently interact in an ATP-dependent manner to form connections (known as cross-bridges), resulting in the production of force and the sliding of the filaments. To further explore contraction, researchers soon began to quantitatively describe muscle. In his pioneering work in 1957, A.F. Huxley mathematically formalized many of these preliminary findings into the first quantitative cross-bridge theory (see section 1.2). Today, improved experimental techniques and enhanced mathematical modeling have led to a more detailed and accurate picture of muscle physiology across scales. However, these first muscle experiments and the sliding filament theory were vital to the development of this knowledge, and still form the foundation of the field of muscle contraction today.

1.2. Introduction to Cross-Bridge Theory: Huxley PDE Model

Huxley's PDE Model. Soon after the sliding filament theory was first proposed, A.F. Huxley developed one of the first mathematical explanations for this process [Huxley, 1957]. In his formulation, Huxley depicts thick filaments as containing cross-bridges, which he describes as spring-like extensions of the myosin filament that can connect with discrete sites on the actin filament. Cross-bridges form and detach in a cyclical process, leading to a two-state model where myosin is either bound or unbound to actin. In the detached state, myosin fluctuates due to thermal agitation. When the myosin cross-bridge is within range of an actin binding site, it has the potential to bind to the filament. When this binding occurs, the cross-bridge exerts a force on the actin filament, resulting in the sliding of the filaments, and thus muscle shortening [Huxley, 1957].

To express this mathematically, Huxley had to make a few simplifying assumptions, motivated both by mathematical feasibility and by the lack of physiological details available at the time. Huxley assumed that binding sites on actin were sparsely distributed, that cross-bridges were able to bind to only one site, and that cross-bridges could not interact (an assumption noted here as the independent force generator hypothesis, discussed below). Likely motivated by mathematical convenience, Huxley employed piecewise linear functions, $f(x)$ and $g(x)$, to describe the rates at which attachment and detachment occurred, respectively. Notably, these rates were dependent on x, the distance of the closest actin binding site relative to an unstrained cross-bridge.

With these assumptions, Huxley used chemical kinetics to express the probability that a cross-bridge was bound at position x at time t. Denoting this probability as $n(x,t)$, and letting v be the velocity of the thin filament relative to the thick filament, Huxley described cross-bridge dynamics with the following partial differential equation:

$$\frac{\partial n}{\partial t} + v\frac{\partial n}{\partial x} = f(x)(1-n) - g(x)n$$

Given that an attached cross-bridge acted as a linear spring, and thus a cross-bridge with position x generated a force κx, Huxley was able to calculate force using the probability that a cross-bridge was attached and the force produced when bound. Assuming that the distance between binding sites on the actin filament was L, this force calculation was,

$$F = \frac{1}{L}\int_{-\infty}^{\infty} \kappa x n(x,t) dx$$

With this mathematical formulation, Huxley developed a quantitative explanation of the sliding filament theory. He then used this model to reproduce steady-state experimental measurements at the whole muscle level, including the force-velocity measurements of Hill [1938] [Huxley, 1957]. Notably, Huxley's model was a crucial first link across physiological size scales of muscle, and provided a quantitative way to connect the behavior of single myosin cross-bridge with larger fiber behavior.

Extensions and Development of Huxley's Model. Huxley's mathematical formulation of cross-bridge dynamics provided a new perspective on muscle contraction, and his remarkable modeling work is still used today [e.g. Jarvis et al., 2021, Walcott et al., 2012, Campbell, 2014, Eisenberg et al., 1980, Lacker and Peskin, 1986, Månsson, 2010, Piazzesi and Lombardi, 1995]. However, due to the limitations on experimental work at the time, the Huxley model includes some simplifying assumptions regarding the details of the interaction between actin and myosin. Additionally, in the original formulation, Huxley only applied his theory to a small selection of steady-state muscle measurements [Huxley, 1957].

In the years following Huxley's theory, improved experimental techniques resulted in measurements that allowed for Huxley's theory to be expanded to capture a wider range of muscle dynamics.

In 1971, Huxley and Simmons extended the framework to describe transient muscle dynamics [Huxley and Simmons, 1971]. Experimentally, they imposed a stepwise length change to muscle fibers to measure the force transient response, and theoretically, they updated the model to reflect the findings [Huxley and Simmons, 1971]. As experimental techniques advanced further, new insight was gained regarding the ATP-dependence and general biochemistry of the interaction between actin and myosin. In 1971, Lymn and Taylor explored the mechanisms of ATP hydrolysis and its connection to the cross-bridge cycle [Lymn and Taylor, 1971]. With their results, they were able to draw connections between enzymatic reactions of actin and myosin and the mechanisms proposed in the sliding filament theory. In 1980, Eisenberg and Hill incorporated these results into a mathematical model that accounted for both the mechanics and biochemistry of the actomyosin interaction [Eisenberg et al., 1980]. Additionally, in 1974, Terrell Hill developed a detailed discussion on using statistical mechanics to connect the biochemical and mechanical properties of muscle, and extended Huxley's model to be consistent with the laws of thermodynamics [Hill, 1974].

In these preliminary extensions of Huxley's work, the models employ similar foundational assumptions to that of Huxley, and therefore the overall model structure is equivalent to that presented in Huxley's original formulation. However, there is another collection of models during this time that further develop the original model by modifying some of the assumptions. These changes ultimately alter the structure of the mathematical formulation.

One key assumption of Huxley [1957] was that each cross-bridge could attach to at most one binding site on the actin filament. This assumption, known as the sparse binding limit, is crucial for the mathematical formulation presented in Huxley [1957]. In particular, this lends to the definition of x as the distance between a cross-bridge and the nearest binding site, as well as the choice of $n(x,t)$ to represent the dimensionless probability that myosin is bound at position x, and the resulting PDE that governs the dynamics of the cross-bridge.

In the years that followed Huxley's work, various models relaxed this sparse binding site assumption to different degrees. In Terrell Hill's work on the thermodynamics of muscle, he extended Huxley's original model, with a sparse binding limit, to be thermodynamically accurate [Hill, 1974], but also explored two additional binding site configurations [Hill, 1976]. Hill considered the cases when 1) cross-bridges can interact with a small, localized group of actin sites, and 2) cross-bridges

have access to an unlimited array of equivalent groups of binding sites. In the first case, the modeling of a small group of actin binding sites is fundamentally the same as the single binding site case, except that the kinetic scheme is adjusted to include the increased binding possibilities. For example, a cross-bridge can now be in a strongly-bound configuration at any of $i = 1, 2, ..., m$ binding sites, resulting in m strongly-bound states in the kinetic scheme, instead of the original one. With this adjusted kinetic scheme, the original mathematical methods of Huxley can be applied [Hill, 1976]. In the latter case, each cross-bridge can interact with an infinite set of equivalent groups of binding sites, each comprised of a subset of non-equivalent binding sites. While Hill argues that this configuration is likely the most physiologically relevant, it is also complex and challenging to model [Hill, 1976].

In 1986, Lacker and Peskin extended this binding site limit even further with a model that approximates the thin filament as a continuum. This dense binding limit is used today [e.g. Walcott et al., 2012, Debold et al., 2013, Jarvis et al., 2018, 2021, Srinivasan and Walcott, 2009, Walcott and Sun, 2009, Walcott, 2014], and ultimately changes the structure of the model from a system of PDEs to a system of integro-PDEs. In this case, x represents the displacement or extension of a bound cross-bridge with reference to some initial bound configuration. This is distinct from Huxley's original formulation, in which x represented the distance between a cross-bridge and the nearest binding site, since this distance has no meaning if the thin filament is a continuum of binding sites. In Lacker and Peskin, the population of cross-bridges is then described by $u(x, t)$, the probability density function (with units of length^{-1}) that a cross-bridge is bound with a particular extension x at time t (note that in this dissertation, we will use $\eta(x, t)$ to denote this quantity). The integral of this function over a particular interval is then the fraction of attached cross-bridges on that interval. Using chemical kinetics in the same manner as Huxley, this lends to a system of integro-PDEs, since the partial differential equations in terms of u now depend on the integral of u [Lacker and Peskin, 1986].

In 2001, Steffen and colleagues made significant advances in determining the physiological distance between binding sites by mapping the thin filament structure using optical trapping [Steffen et al., 2001]. This work showed that the thin filament, which is composed of a double helix of actin monomers, had binding sites on each monomer, about every ~ 5.5 nm [Steffen et al., 2001]. This

distance is much smaller than that assumed with the sparse binding implementation of Huxley and larger than assumed in a dense binding formulation, and thus neither assumption explicitly models the true binding site spacing. However, in 2009, Walcott and Sun presented a cross-bridge model that included a mathematical justification that a dense binding limit accurately captures the physiological binding site spacing, but an equivalent model with sparse binding would not [Walcott and Sun, 2009]. Thus, in the work presented in the following chapters, I assume a dense binding site configuration [Jarvis et al., 2018, 2021].

Another key assumption of Huxley [1957] and many cross-bridge models [e.g. Walcott et al., 2012, Lacker and Peskin, 1986] is that there are no local effects between cross-bridges, an assumption notated here as the independent force generator hypothesis (note that this phrase has alternate meanings in some muscle literature). This independence allows for the overall behavior of an ensemble of cross-bridges to be described by the average state distributions, leading to a system of PDEs that connect molecular scale dynamics to ensemble behavior. This assumption is valid at saturating calcium concentrations when a muscle fiber is fully activated, and while this is reasonable for experimental protocols in which calcium concentration is controlled and maximal (such as in the steady-state measurements considered in Huxley [1957]), physiological muscle rarely performs at full activation. At sub-saturating levels of calcium, there is cooperativity in the binding of cross-bridges and the regulatory proteins in a muscle fiber, resulting in local coupling between cross-bridges [Longyear et al., 2017, Walcott, 2014]. In this case, the behavior of a single cross-bridge is dependent on the state of the neighboring cross-bridges, and thus the independent force generator assumption is violated.

The physiological details of activation are detailed in the biological background of the introduction. Briefly, prior to activation, the regulatory protein tropomyosin is positioned to sterically block the myosin binding sites on the thin filament (Fig. 0.2). When calcium enters into the system, tropomyosin undergoes a conformational change, shifting to expose some of the binding sites on the thin filament. Myosin molecules then bind to the actin filament in a cooperative manner in which a molecule binding locally displaces tropomyosin, exposing more binding sites and encouraging further cross-bridge binding. Throughout the years, several models have been developed to

describe this process, with varying degrees of physiological detail. Due to the complexity of modeling the cooperativity, many models lack molecular detail and include modifications that allow for easy simulation and qualitative results [Hill et al., 1980, 1981, Sich et al., 2010, McKillop and Geeves, 1993]. Other models incorporate an accurate molecular picture, but this level of detail results in systems that are computationally complex, generally requiring Monte Carlo methods to simulate each individual cross-bridge [Kad et al., 2005, Tanner et al., 2007, 2012]. And while this implementation is useful to describe the detailed kinetics and cooperativity, the simulations are inefficient compared to differential equation models, making it hard to optimize model parameters and scale to larger physiological levels.

In recent years progress has been made in using differential equations to express accurate cross-bridge models that include activation dynamics in a computationally efficient way [Walcott, 2013, 2014, Campbell et al., 2018]. For example, in the work of Walcott [2014], a model is developed in which Huxley-like PDEs and a set of coupled ODEs are implemented to describe cross-bridge and activation dynamics, respectively. In this model, myosin ensembles are separated into two distinct groups, 1) an active phase in which the thin filament is fully active so local cross-bridge coupling does not occur, resulting in a regime in which the independent force generator assumption holds and cross-bridge dynamics can be expressed as a system of PDEs, and 2) an inactive phase in which tropomyosin blocks the binding sites on the thin filament and myosin molecules cannot bind [Walcott, 2014]. Throughout time, clusters of myosin molecules cycle between these extremes, with active and inactive clusters growing and shrinking. To model the time evolution mathematically, Walcott uses a system of coupled ODEs to describe the dynamics of the clusters of myosin, and once activated, cross-bridge dynamics are described by a set of Huxley-like PDEs. With this mathematical formulation, Walcott [2014] resolves the independent force generator issue and describes both activation and cross-bridge dynamics with a numerically efficient model.

Taken together, the first Huxley-like models laid the groundwork of muscle theory, and provided new ideas for future experimental techniques and modeling methods that would be developed in the years to come.

1.3. Advances in Experimental Techniques

The sliding filament theory and the modeling work of Huxley and colleagues created a solid foundation for the field of modeling muscle contraction. In the years since this preliminary research, new experimental methods have been developed to study a range of muscle mechanisms, from the smallest scale of a myosin power-stroke to the larger scale of whole muscle behavior. These new techniques have led to the development of new mathematical models with more accurate molecular details. In this section, I introduce some fundamental experimental advances in studying muscle, and highlight a few experimental protocols that motivate the research presented in this dissertation.

Single Molecule Measurements. In 1994, Finer and colleagues performed novel experiments to study the mechanisms of single myosin molecules [Finer et al., 1994]. At the time, recent experimental work on the crystal structure of the myosin molecule had illustrated a conformational change in the myosin head that was proposed to be related to the force produced by a bound cross-bridge [Rayment et al., 1993]. However, the details of this conformational change were still unknown. Finer et al. [1994]employed an innovative single molecule optical trapping technique to measure the force and displacement of a single myosin molecule interacting with an actin filament. The three-bead optical trap used by Finer was unprecedented at the time for its ability to capture such small-scale details, and is still widely used today [e.g. Baker et al., 2002, Debold et al., 2005, Takagi et al., 2006, Debold et al., 2008, Spudich et al., 2011, Woody et al., 2018, Nag et al., 2015, Liu et al., 2018, Woody et al., 2019].

In a classic three-bead optical trap, two beads are attached to the ends of an actin filament and are trapped in place by lasers (see Fig. 2.5B). This "dumbbell" structure is held above another bead, coated with a low density of myosin molecules. The dumbbell is then lowered close enough to the myosin molecule (if one is present) that interactions can occur. The displacement of the actin filament, measured by the displacement of the attached beads, provides data on the interaction between actin and myosin. In particular, when the myosin molecule is unbound from the actin filament, the position of the bead fluctuates due to Brownian motion. When a molecule binds to the filament, it undergoes its power-stroke and reduces the fluctuations of the bead position, resulting in a shifted mean and reduced variance in the displacement trace, respectively. This

general experimental set-up can be modified in various ways to measure different quantities [e.g. Veigel et al., 2003, Debold et al., 2008, 2005, Baker et al., 2002, Capitanio et al., 2012, Greenberg et al., 2017, Arbore et al., 2019].

With this technique, Finer and colleagues were able to make some of the first measurements of the size of the step a single molecule undergoes when it binds to actin, i.e. myosin's power-stroke size [Finer et al., 1994]. Given that force is proportional to the displacement of the molecule, this also gave measurements of the force produced by single myosin molecules. Finer et al. [1994] measured a power-stroke size of around 11 nm, corresponding to about 3-4 pN of force per molecule under isometric conditions [Finer et al., 1994]. In the years that followed, an array of similar measurements were performed, leading to a collection of values for myosin's power-stroke size ranging from 4 nm to 17 nm [Molloy et al., 1995, Ishijima et al., 1994, Guilford et al., 1997].

In addition to measuring myosin's power-stroke size and force production capabilities, single molecule experimental work has also been focused on studying the force-dependence of the acto-myosin interaction. Since as early as the modeling work of Huxley, it has been proposed that the transition rates in the interaction between actin and myosin are dependent on the load a myosin molecule experiences [Huxley, 1957, Huxley and Simmons, 1971, Smith and Geeves, 1995, Cremo and Geeves, 1998]. In the pioneering work of Veigel et al. [2003], an optical trap was used to explore the effect of force on the kinetics of smooth muscle by applying a force at the onset of myosin binding. Analysis of the displacement traces suggested that myosin movement occurs in two phases: the first of which is dependent on load and the second of which is dependent on ATP concentration [Veigel et al., 2003]. The force-dependent detachment rate of myosin was determined to be exponential, with higher forces resulting in slower ADP release rates, and thus longer binding times [Veigel et al., 2003]. These findings were validated with laser trap experiments of smooth muscle by Kad et al. [2007], with optical trapping techniques with β-cardiac myosin by Greenberg et al. [2014], and with harmonic force spectroscopy with β-cardiac myosin by Sung et al. [2015]. This exponential force-dependent detachment rate is used in many models today [e.g. Månsson, 2010, Mijailovich et al., 2016, Campbell, 2009, Walcott et al., 2012, Jarvis et al., 2018, 2021], and is consistent with theoretical predictions [e.g. Bell, 1978].

Ensemble Measurements. Single molecule measurements are crucial in the study of muscle, as they provide explicit measurements of molecular interactions. However, to understand larger whole-muscle function and to make connections across scales, we must also understand how molecules work together. To provide this insight, experimentalists have developed a variety of methods to study myosin ensembles of different sizes and their corresponding interactions with actin filaments. These ensemble measurements are useful because the larger number of molecules results in longer binding lifetimes, increasing temporal resolution of binding and providing insight into possible cooperative effects.

For example, in addition to using optical trapping with single myosin molecules, a similar experimental protocol can be implemented to explore myosin ensembles by using a higher density of myosin molecules on the bead below the dumbbell (see Fig. 2.5C). In this case, multiple myosin molecules can bind to the actin filament together, resulting in traces of actin position as a function of time with runs of motility, where multiple myosin molecules bind in succession before all detaching (see example in Fig. 2.2A). These optical trap experiments allow for measurements of the lifetime and force produced from multiple-molecule binding events, providing information on how myosin molecules work together when attached to a common actin filament [e.g. Debold et al., 2013, Longyear et al., 2017, Woodward and Debold, 2018, Walcott et al., 2012, Jarvis et al., 2018]. Further, the laser trap protocol is versatile, and can be extended to study other muscle mechanisms. For example, the actin filament can be replaced with a regulated filament to study the interactions of myosin molecules with troponin and tropomyosin during muscle activation [Longyear et al., 2017, Kad et al., 2005].

Additionally, an *in vitro* motility assay is a technique developed for studying larger ensembles of myosin molecules [Kron and Spudich, 1986]. In this method, a higher density of molecules are attached to a surface. Fluorescently labeled actin filaments are added, and as myosin molecules bind and unbind to actin, the filaments glide across the surface of myosin (see Fig. 2.5D). The speed of the actin filaments is measured, providing information on how an ensemble of myosin molecules operate together to move actin [Debold et al., 2011, Haldeman et al., 2014, Harris and Warshaw, 1993]. Again, this experimental protocol is adaptable, and it is used in a variety of ways, including to study the dependence of filament length on actin speed (as in [Walcott et al., 2012, Harris and

Warshaw, 1993, Hilbert et al., 2013]), to produce curves of actin velocity as a function of ATP-concentration (as in [Debold et al., 2011]), and in an inverted configuration to more accurately mimic muscle lattice geometry (as in [Brizendine et al., 2015, 2017, Brenner et al., 2012, Previs et al., 2012]).

Taken together, these single molecule and small-ensemble experimental protocols provide important insight into the molecular mechanisms of muscle contraction, leading to the development of modeling work that is based in well-studied molecular dynamics and experimentally-defined measurements.

Fiber Scale Measurements. In addition to molecular scale measurements, there is a vast collection of experimental work at larger scales. This work ranges from measurements done on single myofibrils to whole-muscle studies, and explores a variety of muscle mechanisms such as steady-state contraction [e.g. Knuth et al., 2006, Nelson et al., 2014, Widrick et al., 1996, Eldred et al., 2010, Newhard et al., 2019], and transient lengthening and shortening [e.g. Glasheen et al., 2017, Zhao and Swank, 2016, Huxley and Simmons, 1971, Vanzi et al., 1995, Galler et al., 1994, 1996, Straight et al., 2019, Piazzesi et al., 1997, Lombardi and Piazzesi, 1990]. The specific details of these experimental protocols are beyond the scope of the research presented here. However, to establish a fully comprehensive model of muscle, we must employ a spectrum of experimental measurements across scales, and thus these larger-scale cellular and fiber measurements are critical in the development of a theory of contraction.

1.4. Current Muscle Models

Stemming from the first experimental muscle measurements and the sliding filament theory, the field of muscle contraction now includes an extensive collection of mathematical models that describe contraction in a quantitative way. The framework and methods of these models fall on a spectrum, varying in the physiological size scales they model, the molecular details they include, and the mathematical techniques they employ. Here, we focus on models that explicitly model molecular interactions, however there is also a vast literature of more phenomenological models that describe

the contraction of whole muscles or muscle groups. Additionally, while there are many ways to classify these molecular models, here we focus specifically on mathematical implementation, and categorize models as differential equation models or models simulated by Monte Carlo methods. These two techniques have advantages and disadvantages, detailed below, that ultimately determine the rigor and value of the resulting model in describing specific muscle measurements.

Muscle Models with Monte Carlo Simulations. Monte Carlo (MC) methods are a common and useful way to simulate cross-bridge dynamics [e.g. Duke, 1999, Kad et al., 2005, Tanner et al., 2007, Geeves et al., 2011, Walcott et al., 2012, Jarvis et al., 2018]. To model the stochastic interaction between actin and myosin, MC methods simulate the dynamics of each individual myosin molecule within an ensemble, and use random numbers to simulate the stochasticity of the chemical reactions that occur when molecules transition between states. In general, standard Monte Carlo simulations are performed as follows. Throughout time, the state of each myosin molecule, along with other relevant information such as molecule extension or force, is saved. The simulation iterates through time at a defined time step (often a constant time step, though see the Mathematical Framework section for the Gillespie algorithm which implements a variable time step), and at each point in time, scans through myosin molecules to determine if each undergoes transition to the next state. Which transitions occur are determined by comparing random numbers to the probability that a forward chemical reaction occurs, with these distributions dependent on the rate constants of the state transitions. Once the appropriate molecules have transitioned to the next state, the system is updated accordingly, including re-defining any force-dependent rate constants. At the end of the simulation, information such as force produced, velocity achieved, and lifetime of myosin attachment can be determined from the extensions of the myosin molecules and position of the actin filament throughout time. This general process can be applied to models with different kinetic schemes, and can be adjusted to simulate various experimental protocols. Monte Carlo simulations can directly produce molecular level dynamics [e.g. Walcott et al., 2012, Debold et al., 2013, Jarvis et al., 2018], as well as be related to larger-scale fiber measurements [e.g. Duke, 1999, Geeves et al., 2011, Walcott et al., 2012, Tanner et al., 2007].

Monte Carlo Advantage: Experimental Detail

Monte Carlo simulations of the interaction between actin and myosin are advantageous in that they provide ample opportunity for including experimental details. For example, in Walcott et al. [2012], a model is developed to study the differences in force production across scales. Using Monte Carlo simulations, a four-state kinetic scheme of the interaction between actin and myosin is compared to measurements of both single molecules and mini-ensembles of myosin interacting with an actin filament in an optical trap (see section 1.3, [Walcott et al., 2012]). The use of Monte Carlo allows Walcott and colleagues to model the details of the optical trap, such as the Brownian motion of the system, the compliance and stiffness of the trap, and the adjustment that occurs when myosin binds to the actin filament [Walcott et al., 2012]. The result of the MC simulation is the position of the actin filament as a function of time, which is the same as the output of the optical trap measurements. Model and measurement can then be analyzed and compared directly [Walcott et al., 2012]. Thus, simulating the actomyosin dynamics using a Monte Carlo method allows for an accurate depiction of the physical experimental system and the protein interactions that result.

Monte Carlo Advantage: Physiological Detail

In addition to specifying experimental elements, simulating the interaction between actin and myosin with Monte Carlo methods allows for the inclusion of accurate and complex physiological details. At the smallest scale, it is straightforward to include force-dependent rate constants based in experimental measurements [e.g. Daniel et al., 1998, Walcott et al., 2012, Jarvis et al., 2018]. For example, it has been shown experimentally that ADP release rate varies exponentially with myosin molecule strain [Veigel et al., 2003, Kad et al., 2007, Greenberg et al., 2014, Sung et al., 2015]. Many cross-bridge models include this specific force-dependence [e.g. Walcott et al., 2012, Debold et al., 2013, Mijailovich et al., 2016, Jarvis et al., 2018], and Monte Carlo simulations make it simple to include this detail. Walcott and colleagues, for example, achieve this with a modified version of a Monte Carlo method known as the Gillespie algorithm. As in a standard Gillespie algorithm, they keep track of the extension and state of each myosin molecule, and iterate by taking steps forward in time when reactions occur and molecules transition between states (see Mathematical Framework section for more detail). Since ADP release rate is dependent on the

force a molecule experiences and force is proportional to myosin extension, any bound molecule will have a slightly variable ADP release rate, dependent on the current extension of the molecule. In their modified Gillespie algorithm, Walcott and colleagues keep track of the individual ADP release rate for each molecule throughout time, given the current extensions. When a molecule binds or unbinds, the force on any other bound molecule changes, and thus the ADP release rates of these molecules must be re-calculated. This technique, employed by Walcott and colleagues in Walcott et al. [2012], Debold et al. [2013], and Jarvis et al. [2018], allows for explicit simulation of a well-defined molecular mechanism.

Additionally, since MC simulations keep track of each individual molecule, it is possible to include complex details at larger scales beyond the direct actomyosin interactions [e.g. Tanner et al., 2007, 2012, Powers et al., 2018]. These details are significant when considering fiber level measurements, as muscle fibers are composed of a lattice of thin and thick filaments including regulatory proteins like tropomyosin and troponin. The ultimate interaction of actin and myosin is dependent on the interaction between calcium, the regulatory proteins, and the cross-bridges (see Biological Background section). Thus, it is important to consider these physiological details, and Monte Carlo simulations are one way to achieve this.

In the context of muscle activation, a collection of models have explored the regulatory proteins tropomyosin and troponin, and their role in regulating cross-bridge dynamics and force production in a calcium-dependent manner [e.g. Kad et al., 2005, Tanner et al., 2012]. In 2005, Kad and colleagues explored the mechanism of thin filament regulation at the molecular level by performing laser trap experiments with both unregulated and reconstituted actin filaments interacting with small ensembles of myosin molecules [Kad et al., 2005]. They developed a simple mechanistic model, based on the dynamics observed in the laser trap data, and simulated it using a Monte Carlo algorithm. To incorporate regulation, the cross-bridge attachment rate included inhibitory and cooperativity constants that were tuned appropriately [Kad et al., 2005]. The success of their minimal model in describing their measurements provided preliminary insight into the details of thin filament regulation through MC simulations.

In the context of filament geometry within the sarcomere, Tanner et al. [2007] developed a spatially explicit molecular model that includes features of sarcomere lattice geometry. At the

largest scale, the model includes a physiologically accurate sarcomere lattice including thick and thin filaments properly spaced in a hexagonal shape. In addition to this geometry, the model includes two three-state kinetic schemes to describe thin-filament activation and cross-bridge dynamics. Mathematically, the model is implemented with a system of linear springs, with various spring constants for myosin, actin, and attached cross-bridges, and simulated using Monte Carlo. With this modeling work, Tanner and colleagues showed that a model incorporating a physiologically accurate 2:1 ratio of thin to thick filaments made predictions that were more consistent with experimental measurements than an equivalent two-filament model, leading to the conclusion that there is an inseparable relationship between the geometry, kinetics, and mechanical behavior of the sarcomere [Tanner et al., 2007].

While the model of Tanner et al. [2007] included some preliminary dynamics of activation, it did not appropriately model the kinetics of thin-filament activation, and failed to account for the cooperative effect of myosin binding and local coupling on activation. In subsequent work, Tanner and colleagues further developed their preliminary model to incorporate these details, and again implemented Monte Carlo methods to do so [Tanner et al., 2012]. This improved model additionally includes activation rates that are dependent on the local state of the thin-filament and the neighboring cross-bridges [Tanner et al., 2012]. These details are complex, since reaction rates are now uniquely defined based on the spatial and biochemical state of the local region, and simulating these dynamics is dependent on Monte Carlo methods and the straightforward manner in which they simulate each individual molecule.

Beyond activation and sarcomere geometry, an extensive collection of models have implemented Monte Carlo methods to explore other muscle properties. Williams et al. [2010], for example, developed a complex cross-bridge model to explore radial forces within the sarcomere lattice. Most cross-bridge models describe myosin as a linear spring that only produces force in a direction parallel to the actin filament, and Williams et al. [2010] extension to additionally include forces orthogonal to the actin filaments provided a more detailed understanding of the relationship between sarcomere geometry and force production. In other work, Powers et al. [2018] extended a previous spatially-explicit model to include the protein titin. Many minimal cross-bridge models do not explicitly model titin, so this work provided preliminary insight into the effects of the protein

on muscle mechanics and energetics [Powers et al., 2018]. Further, Chase et al. [2004] developed a half-sarcomere model including calcium-dependent activation and myofilament compliance to understand the effect of compliance on the regulation of contraction. Notably, all of these models implement Monte Carlo methods, which allow for accurate and detailed simulation of cross-bridge dynamics and physiological elements, and result in new knowledge of the mechanisms of contraction.

Challenges of Monte Carlo Methods

While the advantage of using Monte Carlo simulations to directly describe the interaction between actin and myosin is clear from these successful models, MC simulations also present a variety of challenges. First, while these detailed simulations are useful for describing single molecule or small ensemble behavior, they are often computationally expensive for large ensembles ([e.g. Walcott et al., 2012, Walcott, 2014], also see section 4.6). Simulating large ensembles of molecules (e.g.$\sim$ 350 in a half-sarcomere) or multi-sarcomere systems can be inefficient or infeasible, making it challenging to achieve rigorous multi-scale associations. Many models that do explicitly simulate multiple half-sarcomeres, for example, require differential equations to do so ([e.g. Campbell, 2009, Stoecker et al., 2009, Denoth et al., 2002], also see section 4.6).

The computational cost of MC simulations also means that it is challenging, if not impossible, to optimize model results to fit experimental data. For example, in the modeling work of Tanner et al. [2007] discussed above, the model includes numerous parameters such as cross-bridge stiffness and reaction rates that are not fully defined from the literature. One method for obtaining unknown parameters is by fitting model results to experimental data. However, because MC simulations are employed in Tanner et al. [2007], it is too computationally costly to do so. Instead, these unknown parameters must be estimated or assumed from previous work, leading to model results that may not be quantitatively rigorous. If a model with these assumptions fails to describe data, it is unclear if the failure is a result of an incorrect model or improperly defined parameters, and Monte Carlo methods are limiting in this way.

In addition, while MC simulations do allow for the incorporation of larger-scale features like activation and sarcomere geometry, due to the complexity of these elements, models that incorporate them often sacrifice on some smaller scale molecular details. For example, in Tanner et al. [2007],

while the lattice geometry and spatially explicit details are unprecedented, the model implements a detachment rate function that is not based in experimental measurements of the detachment process [Kad et al., 2007, Veigel et al., 2003]. Again, when models without these well-defined molecular mechanisms fail to reproduce data, it is unclear why this occurs, resulting in molecular mechanisms that do not describe experimental measurements but cannot be ruled out due to imprecise modeling. Thus, while Monte Carlo simulations of muscle models are advantageous for incorporating complex physiological details as well as exploring small scale protein interactions, they are often computationally limiting and present challenges when connecting molecular mechanisms to cellular behavior.

Differential Equation Muscle Models. In addition to Monte Carlo methods, another collection of models implement systems of differential equations (DE) to describe cross-bridge dynamics. Models of this form are particularly useful in making explicit and numerically efficient connections across scales. In general, differential equation models assume that myosin molecules act independently (though see section 1.2). This independence between molecules allows for use of a mean-field approximation to represent ensemble behavior with the dynamics of an average molecule. Though they differ in their details, DE models generally implement either a set of partial differential equations (PDEs) to describe the probability that myosin is bound to discrete binding sites (as in a sparse binding site approximation), or a set of integro-PDEs to describe the probability density that myosin is bound with a particular extension (as in a dense binding site approximation). The solutions to these equations describe the time-evolution of the average state distributions of myosin molecules, which then describe the behavior of larger ensembles. Though they present some challenges (see below), these models are mathematically rigorous and provide unprecedented knowledge regarding the connections across physiological size scales.

Differential Equations Advantage: Efficiency of Numerical Solutions

One of the key differences between Monte Carlo simulations and differential equation models is computational cost. While MC simulations of large ensembles can be inefficient due to the explicit

simulation of each molecule, differential equation models provide a more efficient way to simulate cross-bridge dynamics.

In general, differential equation models can be solved under a variety of conditions, such as steady-state or isometric, depending on the objective of the modeling results. Depending on these details, different numerical methods can be implemented to solve the system. For example, for steady-state conditions or for fixed time, techniques such as Forward Euler [e.g. Piazzesi and Lombardi, 1995], Runge-Kutta methods [e.g. Albet-Torres et al., 2009, Debold et al., 2013], or standard ODE solvers in programs such as Matlab [e.g. Stoecker et al., 2009, Jarvis et al., 2021] can be implemented. For non-steady-state conditions, numerical methods for PDEs, such as the method of characteristics ([e.g. Jarvis et al., 2021], section 4.6), can be used. These numerical solutions provide accurate depictions of muscle dynamics and are more computationally efficient than corresponding Monte Carlo simulations.

In some cases, the efficiency of solving differential equations numerically makes it possible to optimize model parameters through fits to experimental measurements [e.g. Campbell et al., 2018]. For example, Campbell and colleagues have developed a differential equation model to understand the mechanisms of length-dependent activation in cardiac muscle [Campbell et al., 2018]. This model couples together the cooperative and calcium-dependent dynamics of the thin-filament with regulated cross-bridge dynamics. The kinetic scheme includes three thin-filament states and three cross-bridge states, and the flux between the states are determined by functions that account for factors including calcium concentration, cooperative activation, phosphorylation, and force, where applicable. This formulation leads to a system of 45 differential equations, 4 of which describe the flux between states and 41 of which describe the cross-bridges when in a force-generating state (with extensions of -10 nm $\leq x \leq 10$ nm and 0.5 nm spacing). Campbell and colleagues solve this system numerically using an adaptive step size with an embedded Runge-Kutta 2,3 method. The numerical efficiency of their simulations allows them to fit the model results to experimental data using simplex minimization algorithms for multidimensional parameter optimization. Based on their model fits, Campbell et al. [2018] argue for the necessity of thick-filament mechanosensitivity, and conclude that the force-dependent recruitment of myosin heads contributes to the length-dependent activation seen in cardiac muscle. It is the efficiency of their numerical solutions,

in particular, that allows for the rigorous fitting of model to data, and ultimately leads to new insight regarding an unknown mechanism of muscle [Campbell et al., 2018].

Differential Equations Advantage: Analytical Solutions

In addition to the advantage of numerical solutions, differential equation models are also beneficial because they can often be solved analytically. Under some assumptions, like steady-state, it is possible to calculate an explicit analytical solution [e.g. Lacker and Peskin, 1986], and in other contexts, mathematical techniques such as asymptotic expansions can be implemented to develop analytical approximations to DE systems [e.g. Walcott et al., 2012, Jarvis et al., 2018]. These analytical solutions to cross-bridge models are valuable because they provide explicit associations between the molecular and cellular levels, further improving computational efficiency and allowing for global parameter optimization.

One of the key benefits of using analytical solutions to differential equations is the efficiency with which cross-bridge dynamics can be simulated. While numerical solutions provide a reasonably efficient way to solve differential equation models (see previous section), in some situations, numerically solving complex ODEs and PDEs can still be too expensive to fit model to data [e.g. Jarvis et al., 2021]. For example, solving a system of integro-PDEs under non-steady-state conditions requires use of the method of characteristics, a numerical method for solving ODEs along the characteristics, and a root find to satisfy the integral constraint (as in [Debold et al., 2013, Jarvis et al., 2021]), resulting in a costly computation and making parameter optimization a challenge. In cases like this, developing analytical solutions results in much faster computation, making it feasible to fit a complex model to experimental measurements. And while analytical approximations can be less accurate than numerical results, a combination of these methods can lead to rigorous global parameter optimization [e.g. Jarvis et al., 2021].

In addition, analytical solutions to differential equations are beneficial in that they allow for direct calculation of, and therefore estimation of, specific model parameters. Often, differential equation models can be formulated in a way that individual molecular properties, such as myosin's force-dependence or a specific time scale, can be described by a single model parameter (as in [Walcott et al., 2012, Jarvis et al., 2021, Newhard et al., 2019, Lacker and Peskin, 1986]). Fitting

model to measurements, or further mathematical analysis, can then be done to estimate values for such parameters. The work of Newhard et al. [2019] provides an example of such parameter estimation. The objective of this work was to explore the effect of myosin's converter domain on the curvature of the force-velocity relationship, which is at least in part due to the force-dependent chemistry of myosin (see section 3.5.3). To fit model to data, Newhard and colleagues express their cross-bridge model with a system of differential equations, including a single parameter to describe myosin's force-dependence. The system can be solved explicitly for force as a function of velocity, resulting in an analytical expression that can easily be fit to experimental measurements for estimation of the force-dependent parameter [Newhard et al., 2019]. Ultimately, it is the analytical solution to the differential equations, and the simple representation of model parameters, that make this optimization and analysis possible.

Finally, analytical solutions provide an opportunity for making a unique connection between scales through an inverse problem, whereby cellular level measurements are used to infer molecular level properties. In this case, differential equation models are formulated based in molecular dynamics, the systems are solved analytically, and the resulting quantities, which include explicit formulation of molecular details, are related to experimental measurements. The work of Lacker and Peskin [1986] is an example of such an inverse problem in muscle. In this work, Lacker and Peskin assume a dense binding site approximation and formulate a system of integro-PDEs which can be solved explicitly in steady-state. Through implementation of a Laplace transform and other mathematical manipulation, they are able to determine myosin's attachment and detachment functions from steady-state force-velocity and energetics measurements [Lacker and Peskin, 1986]. Notably, this modeling work set the stage for future work in which molecular level dynamics are characterized based on cellular level measurements and the PDE systems that connect them.

Differential Equations Advantage: Mathematically Rigorous Connections Across Scales

Differential equation models of muscle are most advantageous because they allow for mathematically rigorous associations to be made between the interaction of actin and myosin and the larger cellular level. Through implementation of both numerical and analytical methods, differential equation models are computationally efficient and enable comprehensive optimization to experimental

measurements, ultimately providing precise insight into how molecular mechanisms scale up to result in fiber-level phenomenon.

One of the first mathematical formulations to make this connection was the original cross-bridge theory proposed by A.F. Huxley, in which he used a system of differential equations to relate cross-bridge kinetics to the evolution of an ensemble of cross-bridges throughout time (see section 1.2 for more detail). Since this original theory, many differential equation models have been developed from this foundation, and have been used to connect cross-bridge dynamics to a variety of muscle functions in computationally efficient and mathematically rigorous ways [e.g. Lacker and Peskin, 1986, Piazzesi and Lombardi, 1995, Walcott et al., 2012, Duke, 1999, Campbell, 2014, 2009, Månsson, 2010]. In the work of Piazzesi and Lombardi [1995], for example, Huxley-PDEs are utilized to describe a five-state cross-bridge model and the results are used to understand the behavior of shortening muscle. In this work, Piazzesi and Lombardi assume a sparse binding limit, leading to a set of PDEs that describe the state of the cross-bridges throughout time, and numerically integrate the system using Euler's method. The model is implemented to reproduce mechanical and energetic measurements of muscle after steady and stepwise shortening protocols, providing insight into the mechanisms that result in shortening, and making direct connections between molecular properties and larger-scale shortening behavior [Piazzesi and Lombardi, 1995].

Another example of a differential equation model that associates muscle dynamics across scales is found in the work of Månsson [Månsson, 2010]. Here, Månsson uses a detailed kinetic scheme of the actomyosin interaction, and develops a system of nonlinear ordinary differential equations to describe the state probabilities of steady-state contraction. The system is numerically solved using fourth-order Runge-Kutta-Fehlberg method, and the model is fit to a range of experimental measurements. In his fitting procedure, Månsson finds that a velocity-dependent attachment rate is necessary to successfully describe all of the shortening measurements. This PDE model and the corresponding results suggest a possible connection between myosin binding rate and fiber-level measurements [Månsson, 2010].

While the details of the kinetic schemes and mathematical methods used in these models are unique, they all share a common theme - the use of differential equations to describe muscle measurements across scales in a way that enhances computational efficiency and rigor in comparison

to standard Monte Carlo methods. The distinction between DE and MC models in connecting physiological scales, and in particular the benefit of differential equation models, is well illustrated in the work of Walcott et al. [2012]. At the time of this work, it had been shown experimentally that actin speed while interacting with a small ensemble of myosin molecules *in vitro* was faster than that predicted from interactions with single molecules [Baker et al., 2002, 2003]. However the reason for this disparity was unknown, and Walcott and colleagues were interested in quantitatively understanding this complex connection [Walcott et al., 2012]. To do so, they compared a four-state kinetic scheme to measurements at different scales, including single molecule step size and binding lifetime, *in vitro* actin motility speed, filament length-dependence of actin motility, and force-velocity of small ensembles in a laser trap. They implemented both Monte Carlo simulations and a system of integro-PDEs to compare the model to their measurements. Notably, their results led to the conclusion that mechanical coupling occurs between myosin molecules bound to a common actin filament, which causes decreased binding lifetime and increased attachment distance, and ultimately results in an acceleration of actin speed [Walcott et al., 2012].

This multi-scale finding of Walcott et al. [2012] is dependent on both Monte Carlo simulations and solutions to integro-PDEs, but it is the differential equation modeling in particular that lends to the rigor of the final conclusions. With Monte Carlo simulations of the kinetic scheme, Walcott and colleagues are able to adjust parameters to reproduce the experimental measurements, resulting in general conclusions regarding the mechanism of ensemble-increased actin velocity. However, by additionally expressing the system with integro-PDEs, they are able to solve for semianalytic expressions of specific values of interest, like average actin speed, which are only dependent on a single model parameter that describes myosin coupling. In doing so, they are able to make mathematically justified conclusions regarding the mechanochemical coupling of myosin molecules and rigorous connections between size scales. Notably, these associations are made possible by the differential equation model, providing rigor beyond that possible solely with Monte Carlo simulations.

Challenges of Differential Equation Models

While differential equation models provide a variety of assets in describing muscle, they also have a few disadvantages. First, while DE models are advantageous for making connections across scales,

it is often challenging to explicitly incorporate larger-scale physiological details. For example, the dynamics of muscle activation include cooperativity between myosin molecules. This cooperativity violates the independent force generator hypothesis, making classic PDE models invalid to describe ensemble behavior, and requiring significant changes to standard Huxley-like PDE models (see section 1.2, [Walcott, 2014, Campbell, 2014]). Additionally, including physiologically accurate sarcomere geometry is challenging with PDE models. Since ensemble behavior is described by average state distributions instead of individual molecule dynamics, it is difficult, if not impossible, to include intricate details of the sarcomere lattice in a system of PDEs. To the best of my knowledge, there is no PDE model that includes the hexagonal structure of thin and thick filaments in the myofibril.

One critical flaw of many differential equation models is the accuracy with which they describe the molecular scale. Many differential equation models are based in the preliminary work of Huxley [1957], and while this work provides a solid foundation for describing muscle, it lacks many molecular details due to the information that was available at the time (see section 1.2). Throughout the years, novel experimental techniques have improved our knowledge on the molecular dynamics of the interaction between actin and myosin, but many differential equation models have not been updated to include these findings [e.g. Campbell et al., 2018, Schappacher-Tilp et al., 2015, Piazzesi and Lombardi, 1995]. DE models that do not include well-measured molecular mechanisms, like myosin's force-dependent chemistry for example, do not accurately describe the dynamics of muscle, and if these models fail to fit experimental measurements, it is unclear why the disparity occurs. Notably, models that do not include accurate molecular details cannot be ruled out if they do not capture data, since the discrepancy could be due to a lack of a key known molecular detail. Thus, while differential equation models are crucial for comprehensively modeling muscle, they must be developed with accurate molecular measurements.

Connection to the Mathematical Modeling of Jarvis and Colleagues. Today, the field of muscle contraction includes an extensive collection of experimental measurements and theoretical models. However, there is still much to be learned about the mechanisms of contraction, and in particular, about the connections across physiological size scales. The work presented in this

dissertation aims at furthering our comprehensive knowledge of contraction. In this section, I contextualize the work presented in the following chapters in connection to the literature discussed above, and highlight the benefits and uniqueness of the modeling techniques we employ.

Combination of Monte Carlo Simulations and Differential Equation Models

In the work presented in the following chapters, we use both Monte Carlo simulations and differential equation models to describe cross-bridge dynamics and model muscle across scales. This is a favorable approach because these methods are distinct in their benefits and shortcomings (described above), and by implementing both we are able to exploit the advantages unique to each method.

In particular, we use Monte Carlo simulations to accurately describe single molecule and small-ensemble dynamics. In Jarvis et al. [2018], we study the effects of muscle fatigue at the molecular level through laser trap measurements under fatiguing conditions. Monte Carlo simulations allow us to accurately model the experimental system and result in a model output that is directly comparable to the results from our experimental protocol.

Additionally, we implement a system of integro-PDEs to describe our model when we scale cross-bridge dynamics to larger levels. In Jarvis et al. [2018], we use our model that is successful at describing molecular measurements to predict fiber level behavior, and to do so, we express it as a system of integro-PDEs. In Jarvis et al. [2021] and in Chapter 4, we use a similar system of integro-PDEs to relate cross-bridge dynamics to fiber-level lengthening measurements, and in doing so, provide insight into molecular mechanisms that cause cellular phenomenon.

Using both Monte Carlo simulations and differential equation models provides flexibility in our modeling, allowing us to capture unique experimental and physiological details, and accurately describe muscle at various scales.

Accurate Molecular Details

One of the key aspects of the modeling work detailed in this dissertation is the accuracy with which we model the molecular scale of muscle contraction. In all of our modeling work, we aim to

develop a minimal model of muscle that is based in well-defined molecular mechanisms. Our cross-bridge kinetics are informed by single molecule measurements, and we only include details that have been validated through experimental findings. By only including the minimal cross-bridge features necessary to describe muscle measurements, we elucidate the most essential molecular mechanisms that result in fiber phenomenon.

For example, in our kinetic schemes, we employ an exponential ADP release rate guided by experimental measurements [Veigel et al., 2003, Kad et al., 2007, Greenberg et al., 2014, Sung et al., 2015]. This formulation, $k_D(x) = k_D^0 e^{-Ex}$, only has two unknown parameters k_D^0 and E, and we can perform fits to experimental measurements to determine the values of the parameters. Additionally, we only include well-studied cross-bridge features (such as the power-stroke), and do not include behavior that has not been thoroughly measured (such as the reversal of the power-stroke). Thus, if our models are unable to capture muscle measurements, we can conclude that our models are lacking some necessary attribute of muscle, and we can further develop the model to explore this.

Global Parameter Optimization

Perhaps the most beneficial component of our modeling work is the combination of the above: implementing integro-PDE modeling of minimal cross-bridge models. Together, these techniques allow us to rigorously fit our models to experimental measurements.

To solve our system of integro-PDEs, we employ both numerical methods, which provide accurate solutions, and analytical approximations, which are less accurate but more computationally efficient. This combination of techniques allows us to perform global parameter optimization. In general, we first fit our model results to measurements using our analytical approximations, where we can efficiently sweep through all of parameter space and determine a region around the best-fit parameters. We can then use this as an initial condition to our numerical solutions, and optimize these less efficient solutions to fit our data with higher accuracy.

Additionally, our use of molecular models based in well-defined measurements makes this global parameter optimization powerful. Because our models only include well-measured molecular details, if we perform global parameter optimization to fit model to measurement and the model is unable to reproduce the measurement for any parameter set, we can reject the model as stated. The ability

to reject models in this way is significant, because we can conclude that a minimal model is lacking some molecular feature that contributes to the muscle measurement under consideration.

In the following chapters, we employ our adaptable and advantageous modeling techniques to explore a variety of muscle phenomena, providing a quantitative perspective on muscle function.

CHAPTER 2

Acidosis affects muscle contraction by slowing the rates myosin attaches to and detaches from actin

Published on October 31, 2018 in the *Journal of Muscle Research and Cell Motility*

Joint work with:

Mike Woodward

Department of Kinesiology, University of Massachusetts, Amherst, Amherst, MA

Edward P. Debold

Department of Kinesiology, University of Massachusetts, Amherst, Amherst, MA

Sam Walcott

Department of Mathematics, University of California, Davis, Davis, CA

2.1. Abstract

The loss of muscle force and power during fatigue from intense contractile activity is associated with, and likely caused by, elevated levels of phosphate (P_i) and hydrogen ions (decreased pH). To understand how these deficits in muscle performance occur at the molecular level, we used direct measurements of mini-ensembles of myosin generating force in the laser trap assay at pH 7.4 and 6.5. The data are consistent with a mechanochemical model in which a decrease in pH reduces myosin's detachment from actin (by slowing ADP release), increases non-productive myosin binding (by detached myosin rebinding without a powerstroke), and reduces myosin's attachment to actin (by slowing the weak-to-strong binding transition). Additional support of this mechanism is found by incorporating it into a branched pathway model for the effects of P_i on myosin's interaction with actin. Including pH-dependence in one additional parameter (acceleration of P_i-induced detachment), the model reproduces experimental measurements at high and low pH, and variable P_i, from the single molecule to large ensemble levels. Furthermore, when scaled up, the model predicts force-velocity relationships that are consistent with muscle fiber measurements. The model suggests that reducing pH has two opposing effects, a decrease in attachment favoring a decrease in muscle force and a decrease in detachment favoring an increase in muscle force. Depending on experimental details, the addition of P_i can strengthen one or the other effect, resulting in either synergistic or antagonistic effects. This detailed molecular description suggests a molecular basis for contractile failure during muscle fatigue.

2.2. Introduction

Muscle fatigue from intense contractility activity is likely the result of numerous factors, including the accumulation of metabolic byproducts, generation of reactive oxygen and nitrogen species, and compromised calcium release from the sarcoplasmic reticulum [Fitts, 1994, Allen et al., 2008]. At least part of the decrease of muscle performance during fatigue is a result of the accumulation of inorganic phosphate (P_i) and of hydrogen ions (H^+), which inhibit the function of muscle's molecular motor, myosin. P_i accumulates from the breakdown of ATP (T) and creatine phosphate, while H^+ accumulates from ATP hydrolysis [Robergs et al., 2004] and dissociation of lactic acid to lactate [Fitts, 1994]. During moderate to severe fatigue, the P_i concentration can increase from a few mM to over 15mM, and the pH (the negative $\log_{10}$ of the H^+ concentration) can decrease from 7.2 to 6.2 [Wilson et al., 1988, Cady et al., 1989]. Elevating P_i and decreasing pH in a rested single skinned muscle fiber directly depresses force and velocity, providing evidence of a causal link between these agents and fatigue [Cooke and Pate, 1985, Debold et al., 2004]. Notably, decreasing pH from 7.1 to 6.2 causes only a small decrease in isometric force, but pronounced reductions in unloaded shortening velocity and peak power [Pate et al., 1995, Knuth et al., 2006]. Thus, it is clear that increased P_i and decreased pH inhibit the function of the contractile proteins and likely contribute significantly to the loss of contractile function during fatigue; however, it is still unclear precisely how increased P_i and decreased pH alter the cross bridge cycle (i.e., myosin's ATP-dependent interaction with actin).

The molecular mechanisms underlying the effects of acidosis (i.e., low pH) are unclear, in part because its effects on contractile function remain highly debated [Allen and Westerblad, 2004, Lamb et al., 2006, Westerblad, 2016, Fitts, 2016]. Some researchers have even suggested that acidosis may play a protective role in fatigue [Pedersen et al., 2004]. Initial observations in single muscle fibers suggested pH values similar to those in fatigued muscle strongly depress both force by $\sim 50\%$ and unloaded shortening velocity by $\sim 30\%$. However these observations were made well below mammalian physiological temperatures (10-15°C), and subsequent observations at 30°C revealed that acidosis induces a minor depression in force ($\sim$ 10-20%) [Pate et al., 1995, Westerblad et al., 1997, Knuth et al., 2006], leading some to conclude that acidosis plays little or no role in fatigue. However, the effect of reduced pH on shortening velocity is much less temperature-sensitive, causing

nearly identical reductions (20-30%) at both 15 and 30°C [Knuth et al., 2006]. Indeed, this decrease in velocity explains much of the observed acidosis-induced reduction in peak fiber power [Knuth et al., 2006]. Thus, while its effects on force are now thought to be less severe than originally proposed [Nosek et al., 1987, Cooke et al., 1988, Chase and Kushmerick, 1988], because of the magnitude of its effects on shortening velocity and power, acidosis remains a putative agent of fatigue [Debold et al., 2016].

Experiments at the molecular level support the observation that acidosis reduces unloaded shortening velocity by directly affecting myosin's ability to translocate actin [Debold et al., 2008, 2011]. In a motility assay, acidosis (decreasing pH from 7.4 to 6.5) decreases actin filament velocity over 50% [Debold et al., 2008] and experiments using a single myosin molecule indicated that this velocity decrease likely results from acidosis slowing the rate of ADP release from myosin strongly bound to actin (AM.ADP, Debold et al. [2008, 2004]). However, this cannot be the only step in myosin's cross-bridge cycle affected by acidosis. In particular, if the only effect of acidosis were an increase in the AM.ADP lifetime, an ensemble of myosin would generate more force under acidic conditions because more cross-bridges would be bound at any moment. This prediction is contradicted by fiber experiments where acidosis either has little effect or causes a slight decrease in maximal isometric force [Pate et al., 1995, Knuth et al., 2006]. Therefore, ADP release and some other step(s) in myosin's cross-bridge cycle must be affected by acidosis.

To identify the effect of acidosis on myosin's interaction with actin, we recently measured the impact of a drop in pH from 7.4 to 6.5 on the ability of a mini myosin ensemble to generate force in a laser trap assay [Woodward and Debold, 2018]. Analysis of these data with a mathematical model, and subsequent solution experiments that support the model predictions, allow us to propose a mechanism for how reduced pH affects myosin's interaction with actin. We then discuss how this mechanism is consistent with a previous model of the effects of P_i [Debold et al., 2013], describing experimental measurements from single molecules to muscle fibers. The success of this mechanism in describing a wide range of measurements across size scales, which to our knowledge other mechanisms cannot, suggests that it provides a molecular basis for the depressive effects of these two key fatigue agents.

2.3. Methods

The mini-ensemble and solution experiments are described in more detail in a separate publication [Woodward and Debold, 2018]; however, as these measurements played a critical role in model development and validation, relevant details of the experimental methods and results are provided in brief.

2.3.1. Proteins. The experimental data were from measurements on fast skeletal muscle myosin isolated from chicken pectoralis muscle as previously described [Margossian and Lowey, 1982].

2.3.2. Mini-ensemble laser trap assay. The effect of a drop in pH from 7.4 to 6.5 on myosin's force generating capacity was determined using a mini-ensemble laser trap assay (at 25°C, 100μM MgATP, and a total ionic strength of 125mM) using methods and instrumentation previously described [Debold et al., 2013]. Two beads were trapped in time-shared optical traps and subsequently attached to a single actin filament. A pretension of 3-4pN was applied to the actin filament. At the laser power used (2 Watts), this resulted in a two-trap stiffness of $\sim$ 0.02pN/nm. Combining this stiffness with measurements of bead displacement gives the amount of force generated with each actomyosin interaction. These data were analyzed using a custom Matlab program described previously [Longyear et al., 2017], which uses a thresholding algorithm to identify displacements that remain greater than 10nm from a defined baseline for a duration $\geq$ 10ms.

2.3.3. MgATPase assay. The effect of acidosis on myosin's steady-state MgATP hydrolysis rate was determined using an NADH-linked assay solution with the heavy meromyosin (HMM) fragment of myosin at 30°C, using established methods [De La Cruz et al., 2000] in a low salt buffer, including 20mM KCl, 25 mM imidazole, 1 mM EGTA, 4 mM $MgCl_2$, and 1 mM dithiothreitol at pH 7.4 and 6.5.

2.3.4. Modeling and simulations. We modeled the interaction between actin and myosin with the kinetic scheme shown in Fig. 2.1 [Walcott et al., 2012]. In the model, myosin can exist in four states (Fig. 2.1). The states are, using the numbering convention in Fig. 2.1: 1. a weakly-bound state, where myosin is in the pre-powerstroke configuration, it is not bound to actin, and it has

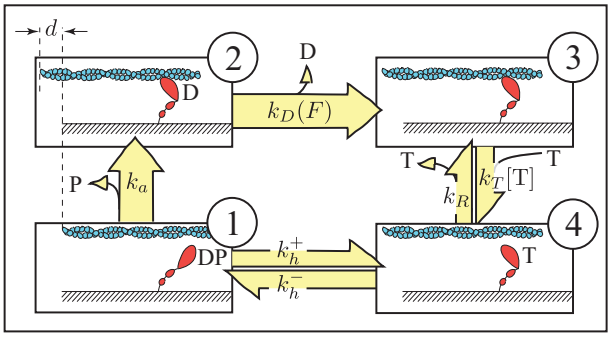

Figure 2.1. Kinetic model for myosin's interaction with actin. Myosin is shown in red and actin in blue. For clarity, only one of myosin's two heads is drawn. The occupancy of myosin's active site is indicated as T (ATP), D (ADP) and DP (ADP+P_i).

ADP and P_i in its active site; 2. a strongly-bound state, where myosin is in the post-powerstroke configuration, it is strongly bound to actin, and it has ADP in its active site; 3. a rigor state, where myosin is in the post-powerstroke configuration, it is strongly bound to actin, and its active site is empty; and 4. an unbound state where myosin is in the post-powerstroke configuration, it is unbound from actin, and it has ATP in its active site. The release of ADP (the transition from state 2 to 3) is force-dependent, according to Bell's approximation [Bell, 1978, Veigel et al., 2003, Kad et al., 2007]

$$k_D(F) = k_D^0 \exp\left(\frac{\delta F}{k_B T}\right) \tag{2.1}$$

where δ is a distance parameter (interpreted as the distance to the transition state), $k_B T$ is Boltzmann's constant times temperature, and k_D^0 is the reaction rate in the absence of force. All other biochemical steps are independent of force.

This model simplifies many of the molecular details of myosin's ATP-dependent interaction with actin. For example, the transition from state 1 to state 2 (see Fig. 2.1) must minimally include the weak-to-strong binding transition, the powerstroke, and release of P_i, though not necessarily in that order. In the model, all of these steps (and potentially more) are modeled by a single rate constant, k_a. Another simplification is the omission of the small sub-step that occurs on ADP release, between states 2 and 3, [Veigel et al., 2003, Capitanio et al., 2006]. Despite these simplifications, the model fits a wide range of experimental measurements, from the level of a single molecule to large myosin ensembles [Walcott et al., 2012], including mini myosin ensemble measurements at pH 7.4 [Debold

et al., 2013]. Since the aim of this work is to understand the effect of pH on mini myosin ensemble measurements, adding further detail to the model would be necessary only if the current model is unsuccessful in describing the data; however, since many of the kinetic steps in the model represent combinations of sub-steps, we cannot clearly identify which of these sub-steps is affected by pH.

We used Monte Carlo simulations to compare this model to experimental results. Specifically, we implemented a modified Gillespie algorithm to iterate through time and keep track of the state of the system, making adjustments to this simulation to appropriately model single molecule, mini-ensemble, and large ensemble measurements as in Walcott et al. [2012], Debold et al. [2013].

The basic steps of this algorithm are as follows. First, the times of all possible reaction rates are determined, given the current states of each myosin molecule and the rate constants for the available state transitions, by picking random numbers from the appropriate distribution. Second, the system undergoes the chemical reaction associated with the shortest time, t_s. Finally, the system is updated appropriately (time is incremented forward by t_s and mechanical equilibrium is restored), and the process repeats again.

To model myosin's force dependence, we kept track of the extension of all myosin molecules and the position of the actin filament. We assumed that mechanical equilibrium occurs immediately in the system, and when binding or unbinding occurs, we adjusted the position of the bound myosin molecules and the actin filament to achieve this equilibrium. Additionally, since the force on the system changes with binding or unbinding, the force-dependent ADP release rate must be re-calculated. In general, the forces applied to the myosin molecules are different, so each bound myosin molecule has a unique ADP release rate associated with it.

The result of these simulations is actin position as a function of time. A few adjustments were necessary to make the simulated data comparable to the experimental results. First, we interpolated the simulated data to match the laser trap sampling rate of 4 kHz. Additionally, we added noise to model both the Brownian motion of the system and external noise observed in the raw data traces. To achieve this, we added random noise from Gaussian distributions with standard deviations of $\sigma = \sqrt{k_B T/\kappa_{tot}}$ and $\sigma = 6.6$nm, respectively, where κ_{tot} is the overall stiffness of the system at a given point in time. The resulting simulated data were then analyzed using the same methods used to analyze the experimental data (additional simulation details are provided in Appendix A).

2.4. Results

We have previously performed a series of experiments measuring force generation and attachment time of mini myosin ensembles [Woodward and Debold, 2018]. In these experiments, a laser trap was used to manipulate a single actin filament over a pedestal (a 3μm diameter bead attached to the flow cell surface) coated with myosin. With these experimental conditions, at pH 7.4 and a MgATP concentration of $[T] = 100\mu$M (the Control condition), short runs of motility are observed, as the motors take several concerted steps before they all detach and the actin filament returns to the center of the trap (see Fig. 2.2). Using customized software, maximum force (laser trap stiffness times maximum displacement) and duration of each of these binding events were determined.

These mini-ensemble experiments were also performed in an Acidic condition (same as the Control condition, but at pH 6.5). Median maximum event forces and event durations are given in Table 2.1, and histograms are shown in Fig. 2.2. The Acidic condition is significantly different from the Control condition. In particular, in the Acidic condition, events were significantly shorter in duration and had a significantly smaller maximum force than in the Control condition. To determine the molecular basis for these pH-dependent differences in the measurements, we used a mathematical model.

Table 2.1. Results of mini ensemble measurements [Woodward and Debold, 2018]. Median plus/minus half the difference between upper and lower quartiles. †Absolute value of max forces. ***Significance ($p < 0.001$ Kruskal Wallis ANOVA; Dunn's method), data significantly different ($p < 0.05$ Shapiro-Wilk) from normal.

Condition	Control	Acidic
Median Event Force† (pN)	0.78 ± 0.27	$0.63 \pm 0.13^{***}$
Median Event Lifetime (s)	0.0175 ± 0.0084	$0.0150 \pm 0.0061^{***}$

2.4.1. The model at pH 7.4. Although all model parameters have previously been characterized (see Table 2.2), we used our current data at pH 7.4 to determine two parameters, N and k_a^2 (see Debold et al. [2013], Longyear et al. [2017] for more about these parameters). The first of these parameters, N, is the ensemble size, i.e. the number of independent myosin heads available to interact with the actin filament. Previously, this value was estimated to be $N = 21$, but maximum forces in our current data are smaller than observed previously [Debold et al., 2013]. We attribute

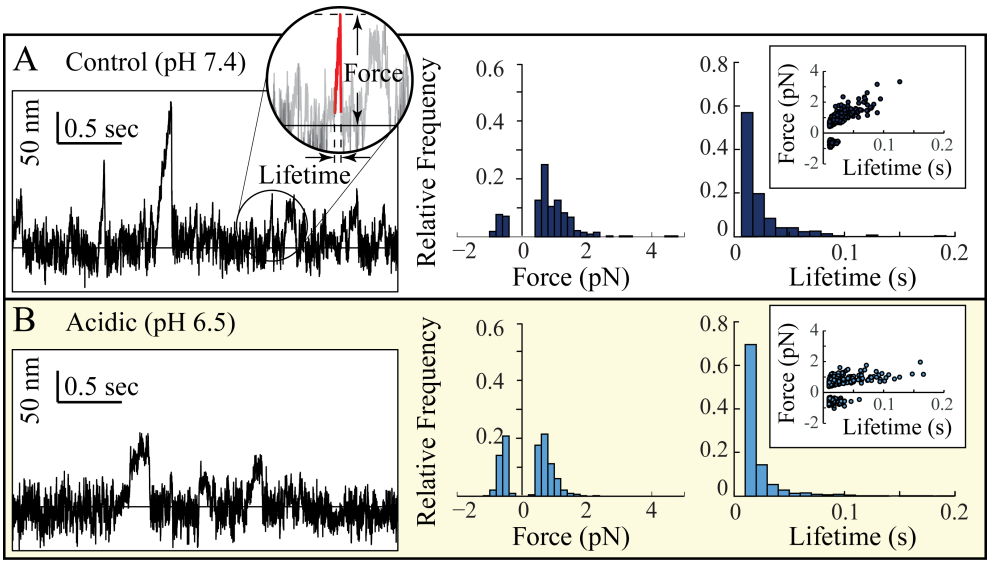

Figure 2.2. Changes in pH affect the interaction between a mini myosin ensemble and a single actin filament. In each panel, a section of raw data (bead position as a function of time) is shown (left). Binding events were determined automatically, and maximum force and lifetime were determined (illustrated in an inset in the top raw trace). Histograms of maximum event force (middle) and event lifetime (right) were determined from multiple raw data traces. Insets show scatter plots of event force and lifetime, demonstrating correlations between these two variables. The panels show the two different experimental conditions. Data from Woodward and Debold [2018].

this difference to variability between myosin preparations, resulting in a lower concentration of active myosin in the current measurements. We therefore expect a smaller ensemble size.

The second of these parameters, k_a^2, models physical details of the mini-ensemble laser trap assay. In particular, in the laser trap, a single myosin molecule binds to actin at $k_a^1 = 2.2\text{s}^{-1}$ [Longyear et al., 2017]. However, in solution at saturating actin concentrations, this binding rate is $k_a = 40\text{s}^{-1}$ [Pastra-Landis et al., 1983, Kovács et al., 2004]. This discrepancy has been attributed to a lower effective actin concentration in the laser trap due to fluctuations in the height of the actin filament above the myosin [Longyear et al., 2017]. In the mini-ensemble assay, when one myosin molecule binds, it restricts these height fluctuations, increasing the effective actin concentration. This is a form of cooperativity, since the binding of one myosin increases the attachment rate of subsequent myosin, but it is specific to the mini-ensemble assay. We model it by assuming that the first myosin molecule binds at $k_a^1 = 2.2\text{s}^{-1}$, the second myosin binds at k_a^2, which we determined from fitting the data, and subsequent myosin bind at $k_a = 40\text{s}^{-1}$, the attachment rate at saturating actin. Previously, single molecule attachment frequency had not been determined,

Table 2.2. Parameter values used in the model. [a]Parameter values from fits to the present data (see Appendix A for justification). [b]Parameter value from measurements in Longyear et al. [2017]. [c]Parameters not fit individually; rather, the relative relationship between k_a^1, k_a^2 and k_a was assumed fixed, and the three parameters were scaled uniformly. The best-fit value for this scaling parameter at pH 6.5 was 0.25 (see Appendix A).

[Debold et al., 2013]		pH 7.4	pH 6.5
Param.	Value	Value	Value
N	21	12[a]	12[a]
k_a^1	1s^{-1}	2.2s^{-1}[b]	0.55s^{-1}[a,c]
k_a^2	1s^{-1}	2.2s^{-1}[a]	0.55s^{-1}[a,c]
k_a	40s^{-1}	40s^{-1}	10s^{-1}[a,c]
k_T	$2\mu\text{M}^{-1}\text{s}^{-1}$	$2\mu\text{M}^{-1}\text{s}^{-1}$	$2\mu\text{M}^{-1}\text{s}^{-1}$
k_h^+	100s^{-1}	100s^{-1}	100s^{-1}
k_h^-	10s^{-1}	10s^{-1}	10s^{-1}
k_D^0	350s^{-1}	350s^{-1}	100s^{-1}[a]
k_R^1	0	0	8.8s^{-1}[a]
k_R^2	0	0	8.8s^{-1}[a]
k_R	0	0	10s^{-1}[a]
δ	1.86nm	1.86nm	1.86nm
d	10nm	10nm	10nm
κ	0.3 pN/nm	0.3 pN/nm	0.3 pN/nm

so a value of $k_a^1 = 1\text{s}^{-1}$ was used [Debold et al., 2013], which gave a best fit value of $k_a^2 = 1\text{s}^{-1}$; here, we determined k_a^2 from our fits, given the recent measurement of $k_a^1 = 2.2\text{s}^{-1}$. We predict an ensemble size of $N = 12$ and second myosin attachment $k_a^2 = 2.2\text{s}^{-1}$ (Fig. 2.3A, and Appendix A). This prediction is in reasonable agreement with an independent estimate, based on the myosin concentration used (25μg/mL) and the geometry of the assay [Debold et al., 2005], which suggests that roughly 10 myosin molecules were available to interact with the single actin filament.

2.4.2. A minimal model for the effect of reduced pH. Varying pH affects intramolecular interactions throughout the myosin molecule. Thus, at pH 6.5, the rate constants and other parameters that depend on those intramolecular interactions (i.e. myosin's stiffness, κ, the force dependent distance δ, etc.) could all differ from the values determined at pH 7.4. It is unfeasible to determine all model parameters from a single data set, so we instead determined which parameters, minimally, we had to change in order to fit our measurements.

Previously, pH has been shown to decrease the average step size and extend the lifetime of single myosin molecules in the laser trap [Debold et al., 2008]. The decrease in step size was attributed to

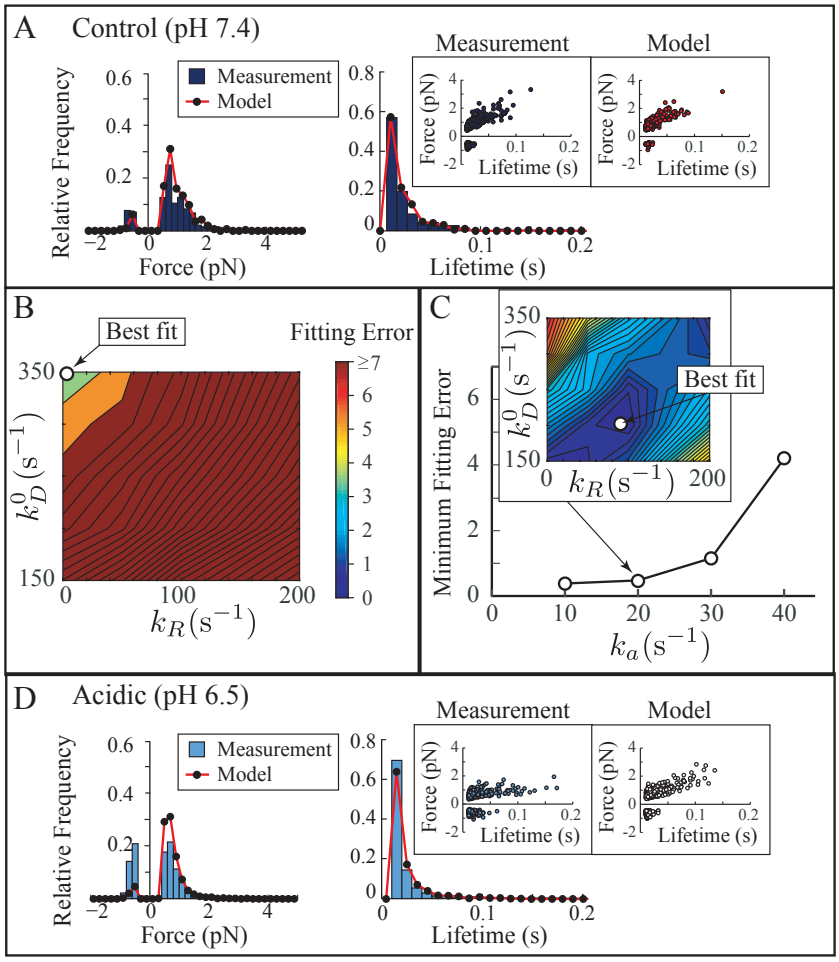

Figure 2.3. A pH-dependent reduction in attachment is required to fit mini-ensemble measurements. **A)** The model fits mini-ensemble measurements at pH 7.4. Histograms of maximum event force (left) and event lifetime (right) produced by a mini-ensemble of myosin in the laser trap and by a computer simulation of 12 independent myosin heads are comparable. Inset shows scatter plots of maximum event force and lifetime, demonstrating that the model reproduces the correlations between the two. **B)** Decreases in ADP release rate (k_D^0) and/or increases in rebinding rate (k_R) cannot explain our mini-ensemble measurements at pH 6.5. The plot shows fitting error (sum of the squared difference in cumulative probability distributions of binding event lifetime and force) between simulation and measurement as a function of k_D^0 and k_R (red colors indicate a poor fit, blue colors a good fit). The model not only generates a poor fit to the data, but the best fit values ($k_D^0 = 350\mathrm{s}^{-1}$ and $k_R = 0$) are the parameter values at pH 7.4, indicating that the model cannot reproduce the observed reduction in event force and lifetime that occurs under acidic conditions. **C)** The model fits the measurements with a decrease in attachment (k_a, the weak to strong binding transition). The plot shows minimum fitting error, defined as the minimum error between simulation and measurement upon varying k_D^0 and k_R, as a function of k_a. Inset shows an example heatmap at $k_a = 20\mathrm{s}^{-1}$, which shows a much better fit than at $k_a = 40\mathrm{s}^{-1}$ (as shown in panel B) and the best-fit parameters show the expected reduction in k_D^0 and increase in k_R (color scale the same as in panel B). **D)** With a decrease in attachment, and best-fit values of k_D^0 and k_R, the model fits mini-ensemble measurements at pH 6.5. Plots are the same as in panel A. Data from Woodward and Debold [2018]

acidosis-dependent rebinding to the rigor state (k_R in Fig. 2.1), resulting in a population of events with 0 average displacement. The increase in lifetime was attributed to an acidosis-dependent decrease in ADP release rate (k_D^0, in Eq. 2.1). Consistent with the latter observation, actin speed in the motility assay at saturating ATP (which, if detachment limited, is determined by ADP release rate [Siemankowski et al., 1985]) decreases with decreasing pH [Debold et al., 2011]. Thus, as a first hypothesis, we assumed that ADP release (k_D^0) and rebinding to the rigor state (k_R) are the only pH-dependent parameters.

Fitting the model to the data, the best fit parameters at pH 6.5 were $k_D^0 = 350\text{s}^{-1}$ and $k_R = 0$ (see Fig. 2.3B). These are the same values as pH 7.4 (see Table 2.2). However, the data at pH 6.5 are significantly different from the data at pH 7.4 (Table 2.1). Thus, we conclude that, by only varying k_R and k_D^0, the model cannot capture the observed acidosis-dependent differences in mini-ensemble force generation and lifetime (see Appendix A for more details). So, minimally, another parameter must change. As a likely candidate, we picked the weak-to-strong binding transition rate, k_a.

Varying k_a, k_D^0 and k_R gave better fits to our mini-ensemble measurements, and allowed us to capture the acidosis-dependent differences we observed in force generation and lifetime (Fig. 2.3C, D). The best fit values point to an acidosis-dependent decrease in both ADP release rate (k_D^0) and weak-to-strong binding transition rate (k_a), along with an acidosis-dependent increase in rebinding rate (k_R).

Note that, for any binding or rebinding reaction (i.e., the reactions governed by k_R and k_a), we must additionally define the cooperativity that occurs in the laser trap due to restrictions in height fluctuations of the actin filament caused by myosin binding. As a first approximation, we assume that the relative scaling of k_R^1, k_R^2 and k_R is the same as the relative scaling for k_a^1, k_a^2 and k_a we obtained by fitting the mini ensemble measurements at pH 7.4. This is equivalent to assuming an identical affinity for actin in the two states (see Appendix A for more information on this assumption, and for alternate assumptions).

2.4.3. Steady-state MgATPase measurements confirm an acidosis-dependent decrease in attachment. At high actin concentrations, the hydrolysis of ATP is rate-limited by the weak-to-strong binding transition rate, k_a (Fig. 2.1, and Lymn and Taylor [1971]). Therefore,

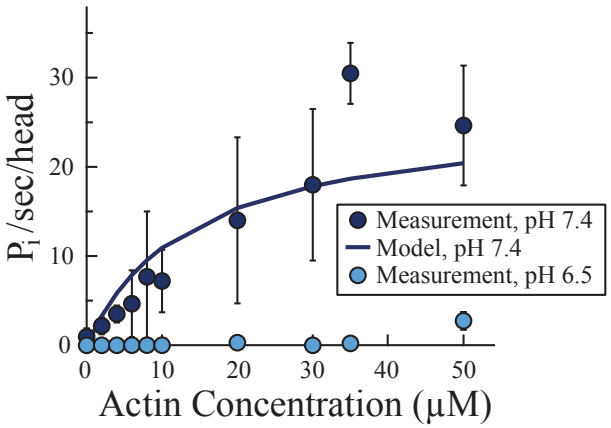

Figure 2.4. Steady state ATP hydrolysis rate is inhibited by a decrease in pH. Under control conditions, we measured significant ATP hydrolysis at variable actin concentration (dark blue dots). With a single free parameter, myosin's weak-binding affinity for actin, the model fits the data (blue line). Under acidic conditions, ATP hydrolysis is strongly decreased at all actin concentrations (light blue dots). Data from Woodward and Debold [2018].

to test the model's prediction of a decrease in k_a with decreasing pH, we measured steady-state MgATP hydrolysis rate in solution at pH 7.4 and 6.5 [Woodward and Debold, 2018]. If the model's prediction is correct, MgATP hydrolysis at saturating actin at pH 6.5 should be strongly decreased compared to pH 7.4; indeed, the data clearly show this acidosis-dependent decrease (Fig. 2.4).

Taken together, the mini-ensemble and the steady-state MgATPase measurements suggest that decreasing pH has three separate effects on myosin's interaction with actin. First, it reduces myosin's ADP release rate (k_D^0). Second, it reduces myosin's weak to strong binding rate (k_a). Third, it enhances myosin's rebinding to the rigor state (k_R). This latter effect is only important at low ATP concentrations; otherwise, the rigor state is not sufficiently occupied for rebinding to have much of an effect [e.g., Debold et al., 2008].

2.5. Discussion

To gain a deeper understanding of the molecular basis of muscle fatigue, we considered measurements of the force generation of mini-myosin ensembles interacting with an isolated actin filament in the laser trap at pH 7.4 and 6.5 [Woodward and Debold, 2018]. These measurements show a significant decrease in binding event force and lifetime at decreased pH. To interpret these measurements, we modified a previously published model [Walcott et al., 2012], demonstrating that

decreasing ADP release rate (k_D^0) and increasing rebinding to the rigor state (k_R) could not reproduce the measurements at low pH. Additionally decreasing the weak-to-strong binding rate, k_a, was necessary to allow the model to fit the data. We find support for this prediction of an acidosis-induced decrease in k_a in steady-state solution ATPase measurements [Woodward and Debold, 2018], which are strongly inhibited at low pH. We therefore propose that, at physiological ATP, decreasing pH decreases both myosin's weak-to-strong binding transition rate and myosin's ADP release rate. However, since decreased pH occurs concomitantly with increased P_i in fatigued muscle *in vivo* [Cady et al., 1989], an additional understanding of the effects of P_i on myosin is necessary to fully understand the molecular basis of fatigue.

2.5.1. Modeling the effects of P_i on myosin's interaction with actin. The effect of P_i on the cross bridge cycle is controversial. While there is general agreement that P_i reduces muscular force by rebinding to myosin molecules that are strongly bound to actin in a post-powerstroke configuration with ADP in the active site (e.g. state 2 in Fig. 2.1), the details of this mechanism remain equivocal [Llinas et al., 2015, Muretta et al., 2015]. The drop in force upon P_i binding can be explained by a reversal of myosin's powerstroke and dissociation from actin (e.g. a transition from state 2 to state 1 in Fig. 2.1) [Hibberd et al., 1985, Webb et al., 1986, Pate and Cooke, 1989, Smith, 2014]. This mechanism, however, does not explain the observation that P_i accelerates actin filament velocity at low pH in a motility assay [Debold et al., 2011] or the observation that P_i has only a small effect on myosin's MgATP hydrolysis rate [Linari et al., 2010]. Rather, these data suggest an alternative "branched pathway" hypothesis, where the rebinding of P_i to myosin causes myosin to detach directly from a post-powerstroke state without reversing the powerstroke [Debold et al., 2011]. Indeed, a mathematical model of this branched pathway hypothesis quantitatively reproduces the observed effects on force and velocity from the single molecule to muscle fiber level [Debold et al., 2013] and predicts the differential effects of P_i on muscle force and MgATP hydrolysis rate [Bowater and Sleep, 1988, Potma et al., 1995, Linari et al., 2010]. Note that, by including effects not considered here (e.g. non-linear cross-bridge elasticity), other models are able to reproduce both the effect of P_i on force and ATPase [Smith, 2014]; however, these models do not reproduce the P_i-induced acceleration of actin filament velocity at low pH [Debold et al., 2011].

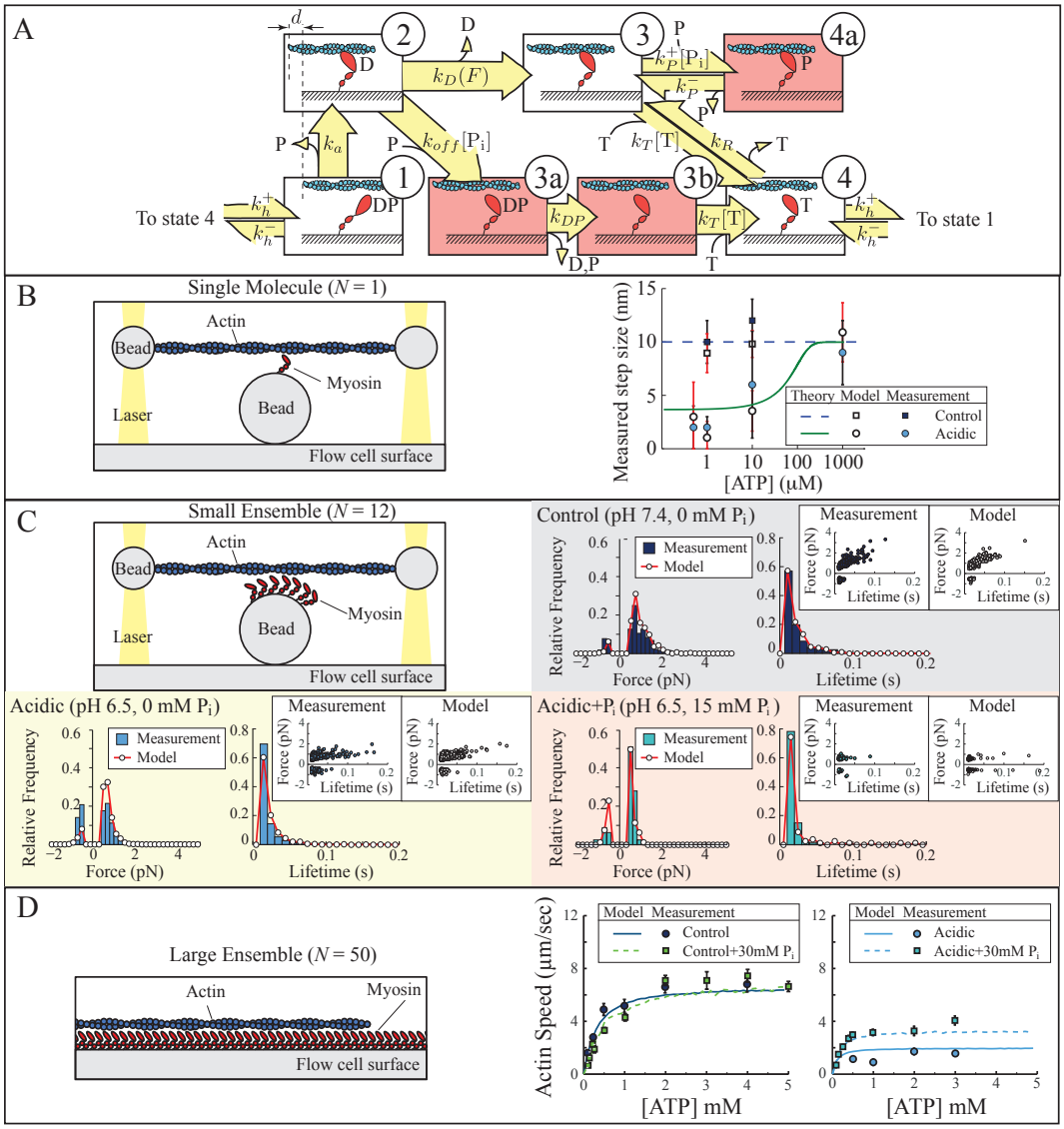

Figure 2.5. With a single parameter set, the model describes myosin's interaction with actin from the single molecule to ensemble level at variable P_i, both at pH 7.4 and 6.5. In each of the bottom three panels, a cartoon of the experimental system is shown at left. **A)** The branched pathway model for myosin's interaction with actin in the presence of P_i. Symbols as in Fig. 2.1; three additional states (3a, 3b and 4a) indicated in red. This model reduces to the one in Fig. 2.1 when $P_i = 0$. **B)** Model describes the ATP-dependent drop in myosin step size at low pH in the single molecule laser trap. Measurements from Debold et al. [2008]; theoretical curves derived in Appendix A. **C)** Model describes mini ensemble measurements. In each shaded box, histograms of maximum event force (left) and event lifetime (right) produced by a mini-ensemble of myosin in the laser trap and by a computer simulation of 12 independent myosin heads are shown. Inset shows scatter plots of maximum event force and lifetime, demonstrating that the model reproduces the correlations between the two. Model parameters were tuned to fit the Control and Acidic conditions, but were not tuned to fit the Acidic+P_i condition. Data from Woodward and Debold [2018]. **D)** Model describes actin speed as a function of ATP in the motility assay in the presence and absence of 30mM P_i, both at pH 7.4 (left) and pH 6.5 (right). Data from Debold et al. [2011]. Importantly, the model reproduces the P_i-dependent increase in motility speed seen at pH 6.5.

There are published measurements at pH 7.4 and 6.5, and at variable P_i, that span size scales from single molecules to large ensembles [Debold et al., 2008, 2011, Woodward and Debold, 2018]. To our knowledge, only one model quantitatively fits these experimental measurements at pH 7.4 [Debold et al., 2013]. If our mechanism for the effects of acidosis is correct, then by modifying k_a, k_D^0 and k_R in that model, we should be able to reproduce the combined effects of reduced pH and variable P_i. Finally, the same model should be able to qualitatively reproduce measurements of these effects at the muscle fiber level. We therefore tested the model against a wide range of previously published experimental data.

2.5.2. Model describes single molecule, mini-ensemble and large ensemble measurements. With two modifications, described below, the model successfully fits experimental measurements that span size scales from single molecules to large ensembles [Debold et al., 2008, 2011, Woodward and Debold, 2018] (Fig. 2.5A for kinetic scheme of model, Fig. 2.5B-D for fits, Table 2.3 for parameter values). First, fitting motility measurements in the presence of P_i at pH 6.5 required increasing P_i-dependent detachment from the strongly bound state (the transition from state 2 to state 3a in Fig. 2.5A) from $k_{off} = 30\text{mM}^{-1} \cdot \text{s}^{-1}$ at pH 7.4 to $k_{off} = 100\text{mM}^{-1} \cdot \text{s}^{-1}$ at pH 6.5 (see Appendix A). Second, fitting the ATP-dependence of single molecule step size measured in the laser trap required us to specify cooperativity in rebinding to the rigor state (see Appendix A). When fitting the mini ensemble data alone (section 2.4.2), we assumed that the cooperativity in rebinding occurs via the same mechanism as attachment, so that the relative scaling of k_R^1, k_R^2 and k_R is the same as for k_a^1, k_a^2 and k_a. This is equivalent to assuming an identical affinity for actin in the two states; however, our model is more consistent with the single molecule data if we assume a greater affinity for rebinding (see Appendix A).

With these modifications, the model reproduces the following experimental results. At the single molecule level, the model reproduces the ATP dependent decrease in step size measured in the laser trap at pH 6.5 (Fig. 2.5B, Debold et al. [2008]). This reduction in step size is thought to occur because, in acidic conditions, binding events occur through two pathways: first, the usual transition from an unbound/weakly bound state to a strongly bound state, including a powerstroke and 10nm step (state 1 to state 2 in Fig. 2.1), and second, rebinding from an unbound state to the

Table 2.3. Additional parameter values (in addition to those in Table 2.2) used in the branched pathway model that only apply in the presence of P_i. [a]Parameter values from fits to the present data (see Appendix A for justification).

[Debold et al., 2013]		pH 7.4	pH 6.5
Param.	Value	Value	Value
k_{off}	$30\text{mM}^{-1}\text{s}^{-1}$	$30\text{mM}^{-1}\text{s}^{-1}$	$100\text{mM}^{-1}\text{s}^{-1}$[a]
k_P^+	$0.7\text{mM}^{-1}\text{s}^{-1}$	$0.7\text{mM}^{-1}\text{s}^{-1}$	$0.7\text{mM}^{-1}\text{s}^{-1}$
k_P^-	10s^{-1}	10s^{-1}	10s^{-1}
k_{DP}	40s^{-1}	40s^{-1}	40s^{-1}

rigor state, that includes no rotation in myosin's lever arm, and thus no step (state 4 to state 3 in Fig. 2.1). This apparent ATP-dependence is thought to arise because at high ATP, the rebinding events with a step size of 0 become short-lived and undetectable. The model reproduces these findings (modeled step size at 1μM ATP and pH 6.5 not significantly different from measured value (t-test, $p > 0.05$) but significantly lower than modeled step size at pH 7.4 (t-test, $p < 0.001$); modeled step size at pH 7.4 not significantly different from measured value (t-test, $p > 0.05$); modeled step size at 1000μM ATP and pH 6.5 not significantly different from measured value (t-test, $p > 0.05$), but significantly greater than modeled or measured step size at 1μM ATP (t-test, $p < 0.001$)).

With the same parameters, the model reproduces the acidosis- and acidosis+P_i-dependent changes observed in mini-ensemble experiments [Woodward and Debold, 2018] (Fig. 2.5C). Importantly, model parameters were tuned to fit the Control (pH 7.4, 0mM P_i) and Acidic (pH 6.5, 0mM P_i) conditions, but were not tuned to fit the Acidic+P_i (pH 6.5, 15mM P_i) condition (see Appendix A). Instead, these results are a prediction of the model, based on the effect of P_i (given in Fig. 2.5A), and the change in k_{off} necessary to fit motility measurements at pH 6.5. Although the differences between the mini-ensemble measurements at pH 6.5 in the presence and absence of P_i are not significant (see Table 2.4), the model nevertheless reproduces the trends in the measurements, with a decrease in both median force and attachment time (Table 2.4).

Again, without changing parameters, the model reproduces the acidosis- and acidosis+P_i-dependent changes in actin filament speed as a function of ATP, as measured in the motility assay [Debold et al., 2011]. Notably, the model reproduces the P_i-dependent increase in motility speed that occurs at high ATP and at low pH (Fig. 2.5D). This result is non-trivial, since the model

Table 2.4. Results of mini ensemble simulations. Median plus/minus half the difference between upper and lower quartiles. †Absolute value of max forces. [a] values repeated from Table 2.1

Condition	Control	Acidic	Acidic+P_i
Median Event Force† (pN)	0.79 ± 0.21	0.66 ± 0.14	0.56 ± 0.06
[Woodward and Debold, 2018]	(0.78 ± 0.27^a)	(0.63 ± 0.13^a)	(0.59 ± 0.06)
Median Event Lifetime (s)	0.0188 ± 0.0079	0.0173 ± 0.0073	0.0160 ± 0.0099
[Woodward and Debold, 2018]	(0.0175 ± 0.0084^a)	(0.0150 ± 0.0061^a)	(0.0148 ± 0.0036)

predicts that lowering pH decreases myosin's attachment rate to actin, a prediction supported by our ATPase measurements. It is therefore possible that the observed acidosis-dependent decrease in motility speed could arise only from a decreased attachment rate, where actin filaments move slowly because there are periods of time when no myosin molecules are bound, i.e. motility becomes attachment limited (as in the decrease in motility speed observed when myosin concentration is decreased sufficiently, Uyeda et al. [1990], Harris and Warshaw [1993]). However, given the kinetic scheme in Fig. 2.5A, a P_i-dependent increase in motility speed can occur only if motility remains detachment limited. Thus, there must be simultaneous decreases in both attachment and detachment (limited by ADP release at high ATP), in order to explain these motility data. Indeed, the model predicts a relatively narrow range of parameters capable of describing all of these data, from the single molecule to ensemble scale (see Appendix A).

Thus, the same model, with the same parameters, fits experimental measurements of the effects of decreased pH and the combined effects of decreased pH and variable P_i, from the scale of a single myosin molecule to an ensemble of around 50 myosin molecules. In all of the measurements, a decrease in pH causes changes associated with a decrease in power output (a decreased step size, a reduction in force production, and a decrease in motility speed). However, in the mini ensembles, the addition of P_i introduces a synergistic effect, further dropping force; while in the motility assay, the addition of P_i introduces an antagonistic effect, partially reversing the drop in speed seen at decreased pH without P_i. The ability of the model to describe these measurements across scales, and to capture context-dependent synergistic/antagonistic effects of acidosis and P_i gives us confidence that it captures the essential molecular interactions between actin and myosin.

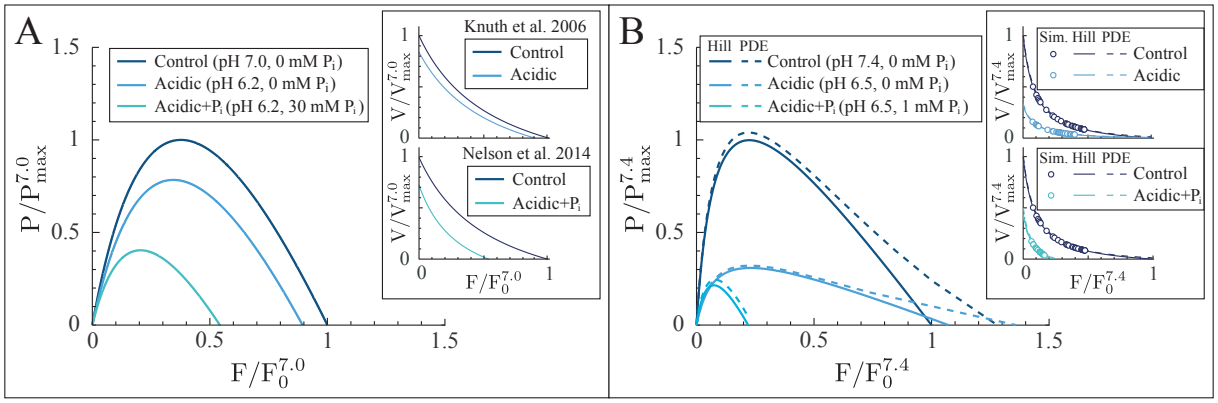

Figure 2.6. Model qualitatively reproduces the pH- and pH+P_i-dependence of steady-state muscle fiber experiments. **A)** Force-power curves measured in single muscle fibers at 30°C. Reduction of pH from 7.0 to 6.2 decreases peak power without greatly changing the force at which peak power occurs or isometric force (curves are Hill fits reported in Knuth et al. [2006]); further addition of 30 mM P_i causes decreases in peak power, force of peak power and isometric force (curves are Hill fits reported in Nelson et al. [2014]). Insets show force-velocity curves from which the force-power curves are calculated. **B)** Force power curves predicted by the model. In each plot, solid curves are Hill fits to simulated experiments (inset shows individual simulation results as hollow dots), and dashed lines are numerical solutions to the partial differential equations (PDEs) that describe the model in the large ensemble limit. Regardless of simulation technique, the qualitative predictions of the model agree with the measurements: reducing pH decreases peak power without greatly changing the force at which peak power occurs or isometric force; addition of P_i causes decreases in peak power, force of peak power and isometric force.

2.5.3. Model is consistent with recent solution measurements. A recent study examined the effect of acidosis, temperature, P_i and ADP on the unbinding of pyrene-labeled myosin from actin in solution upon the addition of a small amount of ATP [Karatzaferi et al., 2017]. For our model, the relevant findings of that work are that ATP-induced dissociation (k_T in our model) shows only a small increase (20-25%) upon decreasing pH from 7.0 to 6.2, and that P_i acts as a competitive inhibitor for this dissociation, with a K_I of 20-30mM, independent of pH [Karatzaferi et al., 2017]. Here, we assume k_T is unaffected by a drop pH, which is consistent with the small change observed in this study. The branched pathway model predicts that P_i will act as a competitive inhibitor for ATP-induced detachment, via the transition from state 3 to state 4a (Fig. 2.5A), with $K_I = k_P^-/k_P^+ = 14$mM (see Table 2.4) and these rates are assumed unaffected by a drop in pH. The value of K_I and its independence of pH are consistent the measurements in Karatzaferi et al. [2017].

One apparent discrepancy between this study and our model is that Karatzaferi et al. [2017] measured no effect of acidosis on the ADP affinity of myosin, whereas the model, consistent with

previous single molecule measurements [Debold et al., 2008], predicts an acidosis-induced decrease in ADP release rate. One explanation for this discrepancy is that the model combines two sub-steps (a force-dependent isomerization, followed by release of ADP) into a single transition (from state 2 to state 3 in Fig. 2.1). Thus, acidosis may decrease the isomerization, but not the release rate of ADP, which would be consistent with both measurements [Debold et al., 2008, Karatzaferi et al., 2017].

2.5.4. Model qualitatively predicts fiber measurements. If our model reasonably describes the effects of acidosis and P_i at the molecular level, then the model should also reasonably describe muscle fiber experiments, with a few caveats. Specifically, unlike fiber experiments, the molecular experiments in Fig. 2.5 do not preserve fiber geometry or allow fiber compliance [Tanner et al., 2007, 2012, Campbell, 2016, Mijailovich et al., 2016], the experiments lack regulatory and accessory proteins (e.g. troponin, tropomyosin, titin and myosin binding protein-C), and do not include interactions between sarcomeres [Campbell, 2009, Stoecker et al., 2009, Walcott and Sun, 2009]. Additionally, the experiments were performed on chicken pectoralis muscle at 25-30°C [Woodward and Debold, 2018], while most fiber experiments are performed on other muscle types at different temperatures. Because of these differences, we do not expect quantitative agreement with experiments. However, inasmuch as vertebrate fast skeletal muscle is similar, and that the primary force generation comes from myosin's interaction with actin, if our model is correct we should expect to see qualitative agreement with experimental results.

In muscle fiber experiments, a decrease in pH generally has a small effect on force production at physiological temperature [Pate et al., 1995, Westerblad et al., 1997, Knuth et al., 2006], with only small changes in isometric force and the force of peak power (Fig. 2.6A). When pH is decreased simultaneously with an increase in P_i, there is a significant decrease in both isometric force and the force of peak power (Nelson et al. [2014] Fig. 2.6A). The model reproduces these qualitative results, both when we simulate an experimental protocol (i.e., performing Monte-Carlo simulations, measuring contraction velocity at a series of fixed forces and fitting the results with a Hill curve), and when we numerically solve the integro-PDEs that govern the mathematical model (see Fig. 2.6B, and Appendix A for methodology). Therefore, the model, which quantitatively describes experimental results from single molecule to large ensembles (Fig. 2.5), also qualitatively

reproduces cellular measurements (note that attachment and detachment rates can be scaled to provide quantitative agreement with fiber experiments at high temperature and, if attachment is more temperature sensitive than detachment, at low temperature as well, see Appendix A).

Though the qualitative agreement between simulated fiber experiments and measurements is good, they do differ in one respect: in the simulated force-velocity curves at low pH, the addition of P_i leads to an increase in the V_{max} of the Hill fit (Fig. 2.6B, inset); while measured curves show a decrease [Nelson et al., 2014, Karatzaferi et al., 2008]. This result is not surprising, since the model parameters are based on in vitro motility measurements, which show an increase in velocity upon the addition of P_i at low pH (Fig. 2.5D, data from Debold et al. [2011], also see Debold et al. [2012]). It is unclear why these measurements disagree. There are obvious differences between the experimental conditions, e.g. in the motility experiments, myosin molecules are isolated and adhered to a glass coverslip and isolated actin is observed sliding freely over it. This treatment might introduce artifacts that are not present in a working muscle [Homsher et al., 1992]. Similarly, the muscle fiber experiments contain structural, regulatory, and accessory proteins as well as inter-sarcomere interactions that might mask or even counter pH- and/or P_i-induced changes in myosin's interaction with actin.

A more specific explanation for the differences is that the fiber experiments generally report changes in V_{max} from a Hill fit. With this measurement, a drop in pH alone induces a $\sim 20\%$ drop in velocity [Knuth et al., 2006], while addition of 30mM P_i induces a further $\sim 20\%$ drop from the low pH V_{max} [Nelson et al., 2014]. However, unloaded shortening from a slack test, which is generally 1.5-2 times V_{max} [Bottinelli et al., 1996, Knuth et al., 2006, Nelson et al., 2014], shows a larger, $\sim 30\%$ drop in velocity when pH is reduced [Knuth et al., 2006], and the addition of P_i results in no further reduction [Nelson et al., 2014]. It is therefore possible that inaccuracies extrapolating to 0 force with a Hill fit (see Appendix A) or some aspect of the force-velocity measurement (e.g. sarcomere non-uniformity, [Widrick et al., 1996]) obscure the effects of P_i at low pH. Additionally, thin filaments in a sarcomere likely experience a larger resistive load than free actin filaments in the motility assay (e.g. myosin binding protein-C is might act as a viscous drag, [Previs et al., 2012]), and even a small resistive load can mask or reverse the P_i-dependent acceleration observed at low pH in our model (see Appendix A). Thus, this difference between

the model-predicted and measured force-velocity curves might be explained by differences in the measured parameter or the presence of a viscous drag.

Given the agreement between model and data, we look to the model to resolve an apparent contradiction between molecular and cellular measurements. In particular, given that acidosis has only minor effects on muscle force generation at the cellular level, one might expect that acidosis has little effect on muscle at the molecular level [e.g. Westerblad, 2016]. However, single molecule experiments [Debold et al., 2008], motility experiments [Debold et al., 2011] and mini-ensemble experiments (Woodward and Debold [2018], Table 2.1) all show significant effects from acidosis. In the model, this discrepancy is explained by acidosis introducing two effects: (1) a decrease in attachment rate, which decreases the force produced by a myosin ensemble; and (2) an increase in attachment duration, which increases the force produced by a myosin ensemble. At the cellular level, these effects nearly balance, resulting in only a small change in isometric force; however, at the molecular level, each of the two effects result in measurable changes. Thus, our model for the combined effects of acidosis and P_i resolves apparent contradictions in the literature, and provides a possible molecular basis for muscle fatigue.

2.6. Acknowledgements

This work was supported, in part, by the grant: NSF DMS-1413185, awarded to Sam Walcott.

CHAPTER 3

Force-velocity and tension transient measurements from *Drosophila* jump muscle reveal the necessity of both weakly-bound cross-bridges and series elasticity in models of muscle contraction

Published on February 18, 2021 in the *Archives of Biochemistry and Biophysics*

Joint work with:

Kaylyn M. Bell

Department of Biological Sciences, Center for Biotechnology and Interdisciplinary Studies, Rensselaer Polytechnic Institute, Troy, NY

Amy K. Loya

Department of Biomedical Engineering, Rensselaer Polytechnic Institute, Troy, NY

Douglas M. Swank

Department of Biological Sciences, Center for Biotechnology and Interdisciplinary Studies and Department of Biomedical Engineering, Rensselaer Polytechnic Institute, Troy, NY

Sam Walcott

Department of Mathematical Sciences, Worcester Polytechnic Institute, Worcester, MA

3.1. Abstract

Muscle contraction is a fundamental biological process where molecular interactions between the myosin molecular motor and actin filaments result in contraction of a whole muscle, a process spanning size scales differing in eight orders of magnitude. Since unique behavior is observed at every scale in between these two extremes, to fully understand muscle function it is vital to develop multi-scale models. Based on simulations of classic measurements of muscle heat generation as a function of work, and shortening rate as a function of applied force, we hypothesize that a model based on molecular measurements must be modified to include a weakly-bound interaction between myosin and actin in order to fit measurements at the muscle fiber or whole muscle scales. This hypothesis is further supported by the model's need for a weakly-bound state in order to qualitatively reproduce the force response that occurs when a muscle fiber is rapidly stretched a small distance. We tested this hypothesis by measuring steady-state force as a function of shortening velocity, and the force transient caused by a rapid length step in *Drosophila* jump muscle fibers. Then, by performing global parameter optimization, we quantitatively compared the predictions of two mathematical models, one lacking a weakly-bound state and one with a weakly-bound state, to these measurements. Both models could reproduce our force-velocity measurements, but only the model with a weakly-bound state could reproduce our force transient measurements. However, neither model could concurrently fit both measurements. We find that only a model that includes weakly-bound cross-bridges with force-dependent detachment and an elastic element in series with the cross-bridges is able to fit both of our measurements. This result suggests that the force response after stretch is not a reflection of distinct steps in the cross-bridge cycle, but rather arises from the interaction of cross-bridges with a series elastic element. Additionally, the model suggests that the curvature of the force-velocity relationship arises from a combination of the force-dependence of weakly- and strongly-bound cross-bridges. Overall, this work presents a minimal cross-bridge model that has predictive power at the fiber level.

3.2. Introduction

Muscle contraction is a multi-scale biological process that drives essential physiological functions. At the smallest scale, contraction is a result of interactions between two proteins, actin and myosin, contained in thin and thick filaments, respectively. Coupled to the hydrolysis of ATP, transient interactions occur between these proteins, whereby a myosin molecule binds to an actin filament and forms a cross-bridge. Once bound, myosin undergoes a conformational change (the power-stroke), which results in one filament sliding past the other. The binding of ATP to the myosin active site causes the myosin molecule to detach from actin. ATP is then hydrolyzed while myosin is detached from actin, and the process repeats. Direct and indirect measurements of these molecular interactions *in vitro* provide insight into this process.

Optical trapping experiments with isolated actin filaments and a single myosin molecule provide direct measurements of the lifetime of myosin binding and the size of the power-stroke [Finer et al., 1994, Saito et al., 1994, Molloy et al., 1995, Guilford et al., 1997]. Similar experiments provide measurements of the force-dependence of myosin's detachment from actin [Veigel et al., 2003, Kad et al., 2007, Greenberg et al., 2014, Sung et al., 2015]. Additionally, small ensembles of (~ 10) myosin molecules can be used in optical trapping protocols, resulting in measurements of actin sliding rate as a function of force [Debold et al., 2005, Walcott et al., 2009] or the duration and maximum force of multiple molecule binding events [Debold et al., 2013, Longyear et al., 2017, Woodward and Debold, 2018]. Though these small ensemble results are not direct measurements of single molecule properties, the presence of multiple myosin both increases the temporal resolution of the measurement by increasing the lifetime of binding events, and also provides information about how myosin molecules interact with each other through a common actin filament. Additionally, the *in vitro* motility assay, which measures the velocity of actin filaments displaced by an ensemble of ~ 100 myosin molecules [e.g. Kron and Spudich, 1986, Harris and Warshaw, 1993], provides complementary information about how groups of myosin function while moving a common actin filament.

At a larger scale, experiments with whole muscle or isolated muscle fibers can provide steady-state measurements of the force a muscle produces as a function of shortening velocity [e.g. Hill,

1938], as well as transient measurements of force produced throughout time [e.g. Huxley and Simmons, 1971]. In addition, energetics measurements inform on how the energy liberated by a muscle is related to the work produced [e.g. Fenn, 1923]. While all of these techniques lead to an extensive amount of experimental data across ∼eight orders of magnitude, it is challenging to make direct comparisons between measurements at different scales, because unique behavior emerges at each level [Duke, 1999, Baker et al., 2002, Campbell, 2009, Stoecker et al., 2009, Walcott and Sun, 2009, Walcott et al., 2012, Hilbert et al., 2013]. Thus, it is unclear how to directly associate molecular *in vitro* measurements to larger fiber and whole muscle measurements [e.g. Månsson et al., 2018].

One way to make connections across scales is through development of mathematical models. In 1957, shortly after the sliding filament theory was proposed [Huxley and Niedergerke, 1954, Huxley and Hanson, 1954], A.F. Huxley developed a molecular-scale cross-bridge model which replicates steady-state, whole muscle measurements [Hill, 1938]. This model was later adjusted in various ways to replicate transient muscle measurements [Huxley and Simmons, 1971], to be thermodynamically consistent [Hill, 1974], and to fit biochemical measurements [Eisenberg et al., 1980]. Subsequently, as experimental techniques at the muscle fiber scale advanced, these mathematical models have evolved to be consistent with some subset of muscle measurements, typically at the fiber or whole muscle scale [e.g. Pate and Cooke, 1989, Piazzesi and Lombardi, 1995, Smith and Geeves, 1995, Albet-Torres et al., 2009, Månsson, 2010].

Though they differ in their details, these models are all formulated in a similar manner. In particular, myosin molecules transition between some number of discrete chemical states. Each state is associated with a particular conformation, and in some, myosin is bound to actin. The rate constants that govern the transitions between these states are force-dependent and, since myosin is assumed to act as a linear spring, are proportional to myosin's molecular extension, x. However, until molecular measurements became possible, the x-dependence of these rates was unknown, so modelers had to rely on either intuition or mathematical convenience.

Molecular measurements of the x-dependence of myosin's reaction rates significantly constrain these models. ADP release ($k_D(x)$), for example, depends exponentially on molecular extension in smooth [Veigel et al., 2003, Kad et al., 2007] and cardiac [Greenberg et al., 2014, Sung et al., 2015] myosin, consistent with theoretical predictions [e.g. Bell, 1978]. Thus, recent models no

longer must define an entire function ($k_D(x)$), but rather two parameters (k_D^0 and E) that define it ($k_D(X) = k_D^0 e^{EX}$). Of the current models that are informed by these molecular measurements [e.g. Campbell, 2009, Månsson, 2010, Mijailovich et al., 2016], we focus on the model of Walcott et al. [2012] (Fig. 3.1A), due to its relative simplicity and its ability to describe *in vitro* measurements from the scale of single molecules to ∼100 molecules, all with a single set of parameters [Walcott et al., 2012]. In addition, the model is able to fit force-velocity measurements from muscle fibers, and infer molecular properties from these cellular measurements [Newhard et al., 2019].

While the success of such modeling approaches in bridging the molecular to cellular scale is exciting, all models neglect some details. For example,Walcott et al. [2012] neglect a rapid, transient interaction between myosin and actin (the weakly-bound state) that occurs prior to myosin's strong binding to actin and power-stroke [Eisenberg and Hill, 1985, Brenner, 1987, Cooke and Holmes, 1986]. Although this interaction is too fast to be observed with standard single molecule techniques (though see [Capitanio et al., 2012]), its presence has been inferred from solution [Lymn and Taylor, 1971, Stein et al., 1979, Chalovich et al., 1981, Chalovich and Eisenberg, 1982] and muscle fiber measurements [Brenner et al., 1982, 1984, Yu and Brenner, 1989]. Given that this model without weakly-bound cross-bridges is validated across size scales, it is of interest to understand the effect and necessity of a weakly-bound interaction.

With this in mind, we aim to develop a minimal cross-bridge model based on well-defined molecular mechanisms that is able to scale up and have predictive power at the fiber and cellular levels. The organization of the paper is as follows: In the **Motivation** section (section 3.3), we hypothesize that such a model must include both weakly- and strongly-bound cross-bridges, based on fits to steady-state force-velocity and force-energetics experiments performed on frog muscle fibers under similar, but not identical, conditions. We propose a five-state model that can fit both experiments. Adding support to this hypothesis, this model qualitatively reproduces the delayed increase in force following a rapid lengthening of a muscle fiber (stretch-activation). However, in the **Results** section (section 3.4), we show that this model is not consistent with our measurements of steady-state force-velocity and tension transients performed with *Drosophila* muscle fibers under identical experimental conditions. To reproduce our measurements, both force-dependent detachment of weakly-bound cross-bridges and an elastic element in series with the cross-bridges

are necessary. In the **Discussion** section (section 3.5), we describe the implications of these results on inferring molecular mechanisms from muscle fiber measurements.

3.3. Motivation

How does myosin's weakly-bound state contribute to force production? Under what circumstances, if at all, can it be neglected? These are the central questions we wish to address. To do so, we consider two alternative models: the first (Fig. 3.1A) is a four-state model of myosin's interaction with actin that is based solely on molecular measurements [Walcott et al., 2012]. This model reproduces measurements at the single molecule to large ensemble scale *in vitro* [Walcott et al., 2012] and is consistent with some fiber measurements [Newhard et al., 2019]. The second (Fig. 3.1B) is a five-state model, identical to the first, but including a fifth state in which myosin has bound to actin but has not undergone a power-stroke, and is therefore not producing force. We have organized our results into two separate sections. In the first (this section), we motivate our hypothesis that this fifth, weakly-bound state is necessary to consistently model muscle measurements at the fiber scale. In the next section (the Results section), we describe experiments and modeling that test our hypothesis.

3.3.1. Weak binding is necessary for consistent force-dependence. As a first test of the effect of myosin's weakly-bound state on muscle measurements, we fit the model to two classic experiments, both of which are influenced by myosin's force-dependent reaction rates: 1) the Fenn effect and the energetics of muscle contraction, and 2) the Hill relationship between steady-state muscle force and shortening velocity.

In the first set of measurements we consider, W. O. Fenn measured the relationship between energy liberation and work performed during muscle contraction [Fenn, 1923]. With this work, Fenn determined that the excess heat, i.e. the heat produced by a muscle during an isotonic experiment minus the heat produced during an isometric experiment, was proportional to the work done by the muscle. This phenomenon, known as the Fenn Effect, is attributed to myosin's force-dependent reaction rates [Veigel et al., 2003]. In the second set of data we model, A.V. Hill measured the relationship between force and velocity during isotonic contractions [Hill, 1938]. Hill's

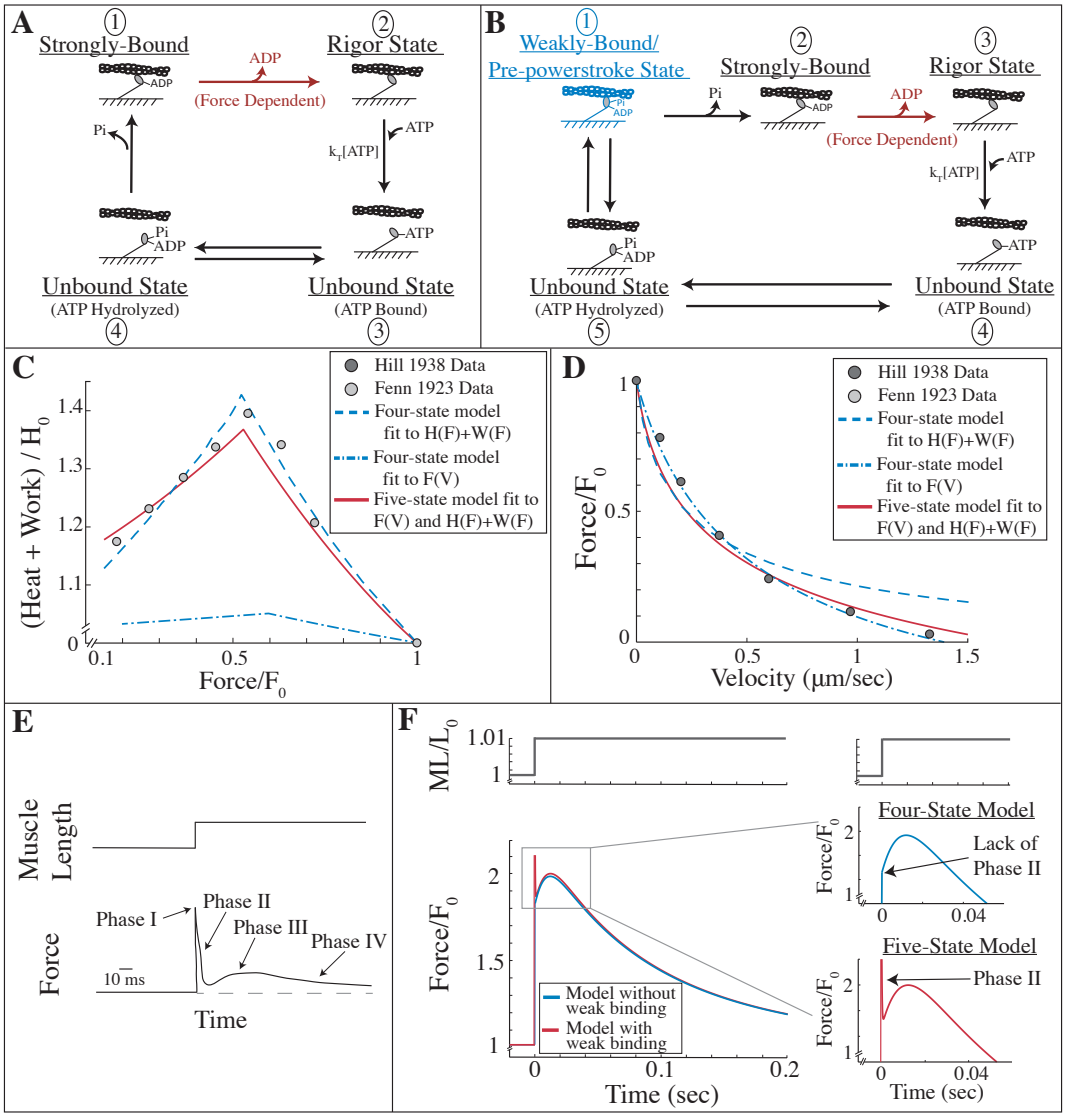

Figure 3.1. Motivation for weakly-bound cross-bridges in a model of muscle contraction based on molecular measurements. **A)** Four-state kinetic scheme of myosin's interaction with actin including two bound states (states 1 and 2) and two unbound states (states 3 and 4). **B)** Five-state kinetic scheme that is the same as that in A, except with the addition of a weakly-bound state labeled in blue (state 1), where myosin is bound to actin but has not undergone its power-stroke. **C, D)** Measurements of the heat produced and work done by a muscle as a function of load (C, [Fenn, 1923]) and force produced as a function of shortening velocity (D, [Hill, 1938]). The four-state model was fit to the energetics data (dashed blue line in C), and the corresponding force-velocity relationship is plotted in D. The four-state model was also fit to the force-velocity measurements (dash-dotted blue line in D), and the corresponding energetics relationship is plotted in C. The five-state model is able to simultaneously fit both measurements (red lines, C and D). **E)** Illustration of a typical skeletal muscle force transient response to a quick stretch. **F)** Four- and five-state model response to quick stretch (blue and red lines, respectively). Insets illustrate the lack of phase II in the four-state model response, and the clear phase II in the five-state model response.

measurements suggest an approximately hyperbolic relationship between force and velocity, with shortening rate decreasing as load on the muscle increases (Fig. 3.1D). The non-linearity of this relationship is also attributed to myosin's force-dependent reaction rates [Newhard et al., 2019, Huxley, 1957].

Given that the Hill and Fenn data were collected under similar experimental conditions and are both influenced by myosin's force-dependent reaction rates, we compared our two models, without (Fig. 3.1A) and with (Fig. 3.1B) weak binding, to the measurements. To do so, we expressed each model mathematically, solving for force as a function of velocity and ATP consumption as a function of shortening velocity to compare to Hill and Fenn's data, respectively (see section 3.7 and Appendix B). In all of our calculations, myosin's force-dependence is defined by a single non-dimensional parameter, $E = \kappa\delta d/k_BT$, where κ is the stiffness of myosin, δ is a parameter (with units of distance) that describes myosin's force-dependent chemistry, d is myosin's power-stroke size, and k_BT is Boltzmann's constant times temperature.

By varying the parameters of the four-state model (without weak binding) we optimized the fit to each of the two measurements individually (see Appendix B). The agreement between model and data is good (dashed blue line in Fig. 3.1C and dash-dotted blue line in Fig. 3.1D). However, the parameters that optimize the model fit to Fenn's energetics measurements are not consistent with Hill's shortening velocity measurements as a function of load, predicting a relationship that is too curved (dashed blue line in Fig. 3.1D). Similarly, the parameters that optimize the model fit to Hill's shortening velocity measurements are not consistent with Fenn's heat plus work measurements as a function of load, predicting a linear relationship that is not sufficiently steep (dash-dotted blue line in Fig. 3.1C). The inconsistency between the fits is due to a difference in force-dependence, with the force-velocity measurements predicting a smaller force-dependence ($E = 0.57$) and the force-energetics measurements predicting a larger one ($E = 1.88$).

The five-state model (with weak binding), however, is able to simultaneously fit both data sets with a single force-dependence ($E = 1.42$, red curves in Figs. 3.1C, D) and generates a significantly better fit than the four-state model (F-test, $p < 0.05$). This improved fit is made possible by the weakly-bound cross-bridges, which act as a viscous drag on the system (see Appendix B), providing a resistive force that varies linearly with shortening velocity. Thus, in the simulations

of the force-velocity measurements, force comes from both the weakly-bound cross-bridges, with a linear force-velocity relationship, and the strongly-bound cross-bridges, with a curved force-velocity relationship whose curvature depends on E. Fitting Hill's data with the five-state model therefore requires a greater curvature for the force from the strongly-bound cross-bridges (i.e. a larger E) to balance the absence of curvature from the force of the weakly-bound cross-bridges. For Fenn's energetic measurements, however, weak binding has a minimal effect. In particular, although the muscle must do more work to overcome the resistive force of the weakly-bound cross-bridges, the magnitude of this work is small compared to the work done by the muscle raising the weight (see Appendix B). Thus, weakly-bound cross-bridges effectively mask the force-dependence predicted from force-velocity measurements, allowing both fiber level data sets to be fit together.

3.3.2. Weak binding is necessary to reproduce force transient response. While the Fenn and Hill measurements provide preliminary motivation for weak-binding, these experiments are nearly 100 years old and are done under similar, but not identical conditions. Additionally, heat measurements are challenging to interpret, because other ATP-consuming reactions besides cross-bridge cycling occur in a muscle [Woledge et al., 1985]. Thus, to further understand the contribution of weakly-bound cross-bridges to muscle force, we consider the transient behavior produced by a muscle (or muscle fiber) after a quick stretch [e.g. Huxley and Simmons, 1971]. In this experiment, the muscle (or fiber) is activated isometrically. It is then rapidly stretched a small percentage of its length, and held isometric again. The response after stretch is often called the tension transient [Huxley and Simmons, 1971, Ford et al., 1977, Lombardi and Piazzesi, 1990, Vanzi et al., 1995, Huxley and Tideswell, 1996, Piazzesi et al., 1997], presumably because the measured quantity is the tension in the muscle or muscle fiber. Here, we will refer to the response after stretch as the force transient, because our model makes predictions of the force generated from the interaction of myosin with actin. The force response of a muscle, or muscle fiber, post-stretch is a peak in force at the time of stretch (phase I), followed by a rapid decay (phase II), a delayed increase in force (phase III/stretch-activation) and finally a slower recovery period (phase IV) (Fig. 3.1E) [Huxley and Simmons, 1971, Ford et al., 1977, Vanzi et al., 1995, Galler et al., 1996, Glasheen et al., 2017]. The molecular mechanism behind this force response is unknown [Ford et al., 1977, Glasheen et al., 2017, Kawai and Halvorson, 2007, Galler et al., 1997, Linari et al., 2004].

Simulating this quick stretch (see section 3.7), we find that the four-state model is unable to reproduce all of the qualitative behavior of the force response, and in particular, is lacking the quick decay of phase II. This model predicts a large increase in force at the time of stretch (i.e. phase I), followed by a transient increase in force (i.e. phase III), and finally a subsequent decay (i.e. phase IV) (Fig. 3.1F, upper inset). This response is due to the fact that strongly-bound cross-bridges are extended with stretch and, since they act as linear springs in the model, therefore experience a proportional increase in force. This force decreases the ADP release rate (transition from state 1 to 2 in Fig. 3.1A, see Eq. 3.2), which therefore slows the rate at which the cross-bridge detaches. The attachment rate of cross-bridges is unaffected, so new cross-bridges continue to attach. This results in a net increase in the amount of bound cross-bridges, and thus the transient increase in force post-stretch. This result suggests that phase III is attributable to strong binding, and in particular the force-dependent decrease in ADP release rate post-stretch.

The five-state model, however, is able to reproduce each of the four phases of the force response (Fig. 3.1F, lower inset). In this model, both strongly-bound and weakly-bound cross-bridges are extended with stretch. The strongly-bound cross-bridges have the same effect as in the four-state model, with a decreased detachment rate resulting in a net increase of bound cross-bridges and thus phase III. The weakly-bound cross-bridges, however, act on much faster time scale. Post-stretch, these cross-bridges rapidly re-equilibrate, resulting in the quick decay of phase II.

Taken together, our simulation results show that the four-state model, without weak binding, cannot simultaneously fit Hill's force-velocity and Fenn's energetics measurements, nor does it reproduce the qualitative behavior of force transients following a rapid stretch. In contrast, the five-state model, with weak binding, simultaneously fits Hill's and Fenn's measurements and reproduces the four phases of the force transient post-stretch. Given these results, we hypothesize that a weakly-bound interaction between actin and myosin is necessary to consistently model muscle across scales. To test this hypothesis, we performed force-velocity and force transient measurements on the same muscle fiber type under the same experimental conditions. We then fit our measurements with the four- and five-state models.

3.4. Results

We performed two different muscle mechanical experiments (force-clamps to obtain force-velocity curves and force transients in response to length steps) on permeabilized (skinned) *Drosophila* jump muscle fibers to test our hypothesis that a weakly-bound interaction between actin and myosin is necessary to consistently model muscle across scales. Note that the jump muscle is mechanically equivalent to a fast skeletal muscle type with maximum shortening velocity and tension generation similar to mouse fast-twitch muscle type 2B [Eldred et al., 2010]. In the first experiment, we performed force transient measurements on fibers at a sarcomere length of 3.6 μm with length increase amplitudes ranging from 0.25% to 2% of the muscle fiber length (e.g. Fig. 3.2A). We varied the stretch amplitudes to ensure that the muscle fiber gave a linear force response to the stretch. A non-linear response would indicate some yielding behavior (i.e. the forcible detachment of myosin from actin, see Chapter 4), which is not included in our model. We observe a linear relationship for stretches less than 1% of muscle fiber length (Fig. 3.2B), and only fit the model to measurements with stretch amplitudes in this linear range, to ensure that cross-bridges are not being forcibly detached.

In the second experiment, we performed force-velocity measurements on fibers under the same conditions as the force transient measurements (Fig. 3.2C, see section 3.7). These measurements produced force-velocity curves that are comparable to our previous measurements with jump muscle fibers from the same fly line, *pwMhc2* [e.g. Newhard et al., 2019, Eldred et al., 2010, Swank, 2012], and can be well-fit with the four-state model with an $E = 0.62$, or with the five-state model with a range of E values above $E = 0.62$ (Fig. 3.2C, D, see Appendix B).

Given that either the four- or five-state model reproduces these force-velocity measurements, we further test our hypothesis by fitting the force transient measurements with both of our models. If the four-state model fits our force transient measurements and our force-velocity measurements with a consistent set of parameters, then we reject the hypothesis that weakly-bound cross-bridges are necessary to model muscle. If the five-state model fits the force transient measurements and the force-velocity measurements with a consistent set of parameters, but the four-state model does not, then we cannot reject the hypothesis. If neither model fits both measurements, we cannot

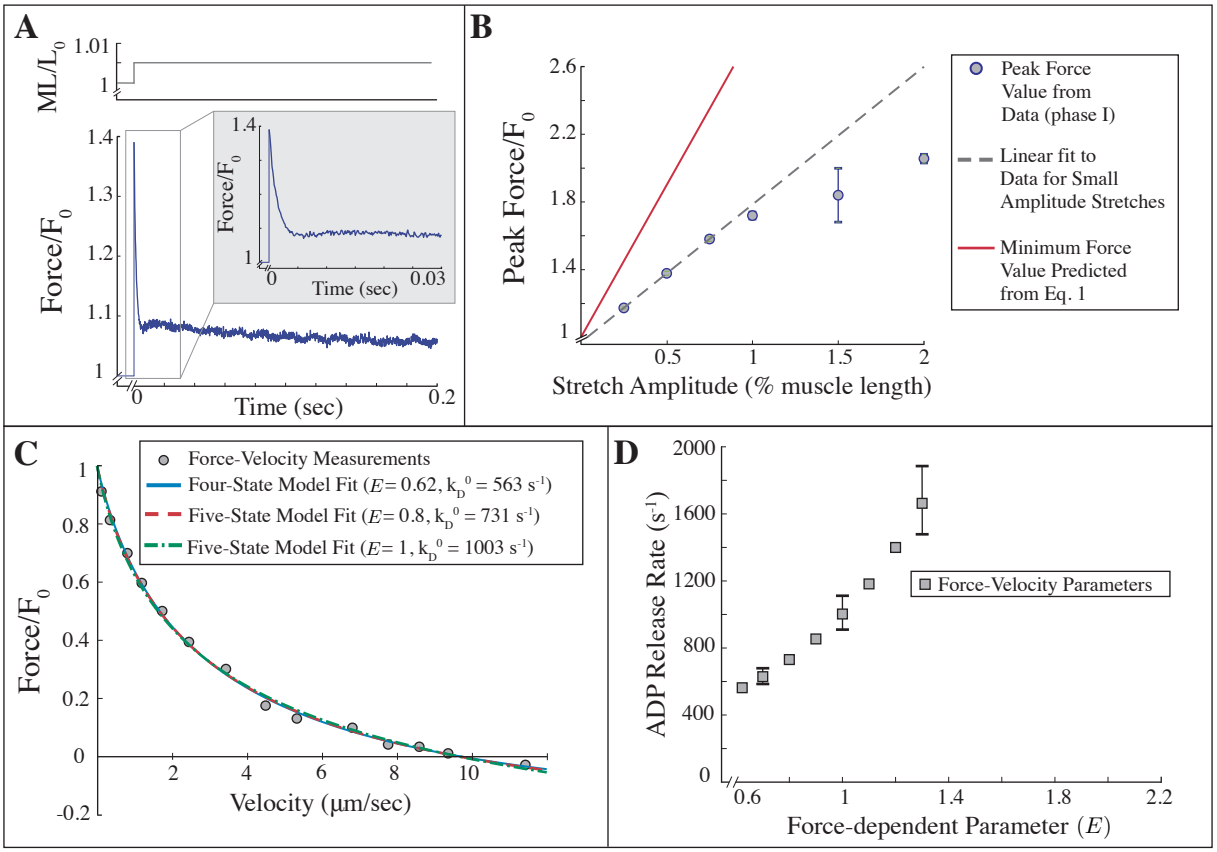

Figure 3.2. Comparison between our measurements and model simulations show that the model can fit force-velocity measurements but is inconsistent with force transient measurements. **A)** Force transient measurement from a jump muscle fiber that was stretched 0.5% of its fiber length over 0.5 ms. Inset is the same force transient on a smaller time scale. **B)** Relationship between peak force post-stretch (phase I) and stretch amplitude. Each data point (blue circles) is the mean ± SD of transients from three different fiber preparations. The dashed line is a linear fit to measurements of stretch amplitudes less than 1%. The red line is the model prediction (Eq. 3.1). **C)** Force-velocity measurements from an equivalent jump muscle fiber preparation are well-fit by the four- and five-state models. **D)** Lower bound on combinations of unloaded ADP release rate and the force-dependent parameter that fit force-velocity measurements with the five-state model (see Appendix B).

reject the hypothesis as stated, but we can reject both models and conclude that the models do not capture some effect contributing to muscle force.

3.4.1. Mismatch between force transient data and model. We fit the four- and five-state models to both the force transient and force-velocity measurements. While both models could reproduce our force-velocity measurements, neither model was able to reproduce our force transient measurements. One obvious difference between the modeled and measured force transients was a

discrepancy in the peak force obtained post-stretch (phase I). This discrepancy is surprising, since this peak in force occurs over such a rapid time scale (Stretch duration: 0.5 ms, Measurement resolution: 0.125 ms) that myosin molecules would likely not undergo chemical state transitions, and therefore the force response should represent the elastic stretching of myosin molecules bound to actin. Given this simple interpretation, we investigated this difference between the peak force predicted by model and measurement in more detail; however, as we will show, even if this discrepancy is explained, neither the four- nor the five-state model can simultaneously fit our measurements.

A simple calculation allows us to understand the mismatch between the peak force we measured, and that which was predicted by the model. In the experiments, the half-sarcomere of the muscle fiber is set at a length of 1.8 μm. The muscle fiber is then stretched a particular fraction, s, of its length (e.g. a 0.5% stretch corresponds to $s = 0.005$). Assuming each sarcomere stretches equally, a stretch of s muscle lengths is equivalent to stretching each sarcomere s sarcomere lengths, and therefore s of each half-sarcomere length. The length of stretch in nanometers at the half-sarcomere level is therefore $\mathcal{S} = 1800 \text{ nm} \cdot s$. We can calculate a lower bound on the peak force post-stretch for a given stretch amplitude by considering the force from cross-bridges that are strongly-bound before stretch. Pre-stretch, these cross-bridges have undergone a power-stroke and therefore have an average extension of $d = 10$ nm. Post-stretch, these cross-bridges have now been stretched an additional $\mathcal{S}$ nm, giving an average extension of $\mathcal{S} + d$ nm. Assuming linear cross-bridge elasticity and myosin stiffness of κ, the force produced by a cross-bridge post-stretch is $F_p = (\mathcal{S} + d)\kappa$. Normalizing this to the pre-stretch value, we get,

$$\frac{F_p}{F_0} = \frac{(\mathcal{S} + d)\kappa}{d\kappa} = \frac{\mathcal{S}}{d} + 1 = \frac{1800 \cdot s}{d} + 1 \tag{3.1}$$

We emphasize that this estimate is a lower bound because we neglect the contribution of weakly-bound cross-bridges, which (if present) would also be stretched and would add to this force.

The measured values of peak force following stretch are much less than this estimated lower bound (Fig. 3.2B). Importantly, only a few model assumptions lead to this model prediction, namely linear cross-bridge elasticity, a power-stroke size of $d = 10$ nm, and the assumption that a particular length change at the fiber level corresponds to the same relative change at the sarcomere level. While it might be argued that estimates of power-stroke size vary [e.g. Finer et al., 1994,

Molloy et al., 1995, Guilford et al., 1997, Pate and Cooke, 1989, Kaya and Higuchi, 2010], we would need a power-stroke size of $d > 25$ nm in order to reproduce the experimental measurement, since Eq. 3.1 is a lower bound. Thus, with the assumptions of linear elasticity, a power-stroke size of 10 nm (or less), and the same relative stretch amplitude across scales, the model and data are inconsistent.

While a discrepancy between model and data means that we reject both models and neither reject nor support our hypothesis, this conclusion depends on all of the assumptions that led to Eq. 3.1. We therefore consider two explanations for the discrepancy that would adjust the result from Eq. 3.1: (1) the relative change in sarcomere length is smaller than the relative change in fiber length, resulting in an overestimation of stretch amplitude of the half-sarcomere, and (2) the force transient data includes an "unexplained" force due to factors other than actin and myosin. We discuss these two possibilities below, keeping in mind that they are not mutually exclusive.

3.4.2. Explanation 1: Overestimated stretch amplitude. Our calculation of peak force (phase I) following stretch (Eq. 3.1) relies on the assumption that a relative change in fiber length results in an equivalent relative change in sarcomere length. However, it is possible that the change in sarcomere length is smaller than that measured at the fiber level, due to the elasticity of structures in series with the cross-bridges. There are a variety of elastic elements that are in series with cross-bridges (e.g. titin, Z-disks), in series with the muscle fiber (e.g. the thin-filament), in the experimental equipment, and at the fiber ends from sarcomeres that are damaged when the fiber is clamped. When a muscle fiber is stretched, these elastic structures (which we refer to as the series elastic element) are also stretched, and therefore the change in sarcomere length is smaller than the corresponding change in fiber length.

To account for this overestimation of stretch amplitude, we let stretch amplitude be a parameter of fit, along with the other unknown model parameters (see Appendix B). In doing so, we account for the effect of the series elastic element on the stretch amplitude, but neglect any dynamic interaction between the cross-bridges and the series elastic element (also see section 3.4.4). Additionally, in the force transient measurements, the isometric force post-stretch is slightly higher than the pre-stretch isometric force (residual force enhancement). Since the model does not include a mechanism for

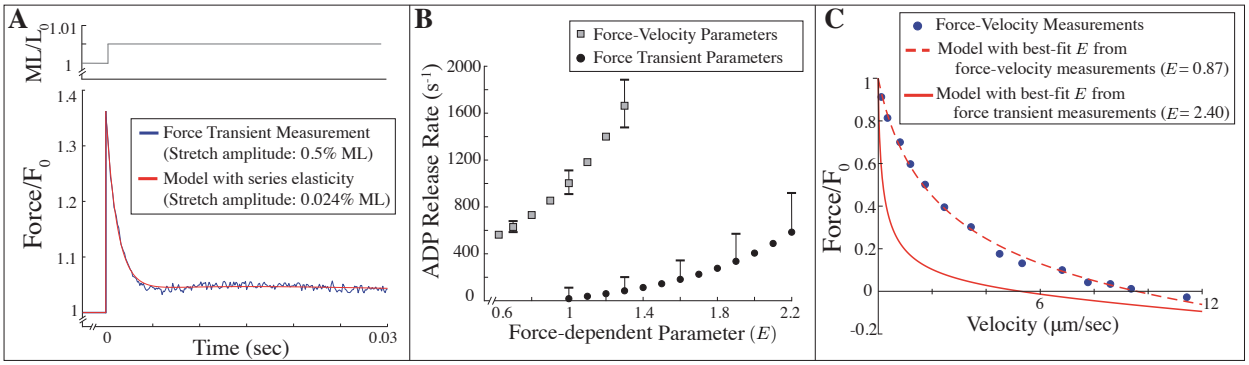

Figure 3.3. With a decreased stretch amplitude, the model reproduces force transient measurements, but the results are inconsistent with force-velocity measurements. **A)** The five-state model fits our force transient measurements for a 0.5% muscle length stretch with a best-fit half-sarcomere stretch amplitude of 0.437 nm (compared to a 9 nm stretch without series elasticity). **B)** Combinations of unloaded ADP release rate and the force-dependent parameter that fit force-velocity (gray squares) and force transient (black circles) measurements with the stretch amplitude fixed at $\Delta s = 0.437$ nm. Error bars denote parameter values that give results within one standard deviation of the best-fit error. **C)** Model fits to force-velocity measurements with k_D^0 fixed from the best-fit to the force transient measurement, and E from the best-fit to the force transient measurement (sold line) and best-fit to the force-velocity measurements (dashed line).

residual force enhancement, we account for this by adding a small force to the model post-stretch, so that the modeled force returns to the measured post-stretch isometric force for long time (see Appendix B). With these specifications, we fit the model to our measurements. The optimization converges to a good fit to the entire force transient measurement, reproducing all parts of the force response (i.e., phases I-IV, Fig. 3.3A).

Though the model reproduces the force transient measurements, there are two reasons that we reject this explanation. The first is that the best-fit predicts that the stretch amplitude at the sarcomere level is an order of magnitude smaller than that imposed experimentally at the fiber level (experimental stretch amplitude: 9 nm for a 0.5%ML stretch, predicted stretch amplitude: 0.437 ± 0.08 nm, see Appendix B). While series elastic elements can result in an overestimation of the stretch amplitude at the sarcomere level, it is unlikely that the effect is of this magnitude.

The second reason that an overestimation of stretch amplitude is unlikely to explain the discrepancy between simulation and measurement is that, with this small stretch amplitude, the model requires a large force-dependence to fit the force transient measurements. This is because in the model, phase III of the force transient response arises from stretching strongly-bound cross-bridges.

Since the cross-bridges act as linear springs, this stretch results in a proportionate force on the cross-bridge, which then decreases that cross-bridge's ADP release rate (via the parameter E). Thus, if the stretch amplitude is decreased by an order of magnitude, the force-dependent parameter E must be increased by an order of magnitude in order to obtain the same decrease in ADP release rate. This large force-dependence required to fit force transient measurements is inconsistent with the force-dependence predicted from force-velocity measurements (Fig. 3.3B), resulting in a force-velocity relationship that is too curved (Fig. 3.3C). Thus, we reject the explanation that series elasticity results in an overestimation of stretch amplitude, and instead consider the effect of an "unexplained" force on our calculation.

3.4.3. Explanation 2: Unexplained force. In our calculation of peak force following stretch (Eq. 3.1), we also assume that all of the measured muscle force arises from the interaction of myosin cross-bridges with actin. While we account for the force contribution of passive elements by measuring the force production in experiments at low calcium concentrations (see Appendix B), it is possible that other calcium-dependent, non-cross-bridge elements contribute to force. Indeed, such a mechanism has been proposed to account for the increase in isometric force following a stretch (i.e. residual force enhancement, [Leonard and Herzog, 2010, Nishikawa et al., 2012, Schappacher-Tilp et al., 2015, Koppes et al., 2015, Labeit et al., 2003, Campbell and Campbell, 2011, Herzog et al., 2016]).

To account for this potential non-cross-bridge force, we let it be a parameter in the model. With this addition, we find that the optimization converges to a good fit to the entire force transient measurement (Appendix B, Fig. B.13). However, we find that these results mirror the inconsistencies we found with stretch amplitude as a model parameter (Sec. 3.4.2 and Fig. 3.3), and thus we must reject this hypothesis. In particular, the best-fit predicts an implausibly large post-stretch unexplained force of over 28 times the isometric force from cross-bridges. Additionally, this large magnitude of unexplained force then requires a large force-dependence to fit our force transient measurements, which is then inconsistent with our force-velocity measurements (see Appendix B for details).

The net result of the comparison of our model to our measurements is that neither the four-state nor the five-state model can reproduce both our force-velocity and force transient measurements, allowing us to reject both models as stated. We can therefore infer that neither model captures all of the effects contributing to muscle force in these experiments, and conclude that at least one of our model assumptions is wrong.

However, the success of the five-state model in fitting Fenn's and Hill's measurements and reproducing both our force transient and force-velocity measurements (albeit with different parameters), suggests that some modification of the five-state model might successfully fit both of our measurements. We therefore considered various alternative model assumptions. We found that none of these alternative assumptions, individually, allows the model to fit our measurements. Neither non-linear elasticity of myosin, force-dependent detachment of weakly-bound cross-bridges, nor thin-filament activation could explain the discrepancy (see Appendix B for details). However, when we allow the series elastic element to interact dynamically with the cross-bridges and include force-dependent detachment of weakly-bound cross-bridges, we can fit our measurements with the five-state model.

3.4.4. Model with force-dependent detachment of weakly-bound cross-bridges and series elasticity is able to consistently model muscle measurements. In section 3.4.2, we invoked a series elastic element to motivate our efforts to fit our measurements with a stretch amplitude at the sarcomere level that is smaller than the imposed stretch. In doing so, we made the assumption that this series elastic element does not change length after the initial stretch. However, this elasticity, possibly due to a variety of factors (e.g. titin, Z-disks, the experimental apparatus; see Sec. 3.4.2), may be more dynamic. If we relax our original assumption, allowing a dynamic interplay between the contractile element and the series elastic element, the model remains unable to fit the data. However, if we additionally include force-dependence in the detachment from the weakly-bound state [Capitanio et al., 2012], the model is consistent with our measurements (Fig. 3.4, see Appendix B for details of the fitting procedure and the model).

To fit our force transient measurements, we must again account for residual force enhancement, the increase in isometric force post-stretch. Adding a small force post-stretch (as discussed in

section 3.4.2), allows the model to fit phase I and II of the force transient. However, adding a slightly larger force allows the model to fit phases I-III of the force transient, and to partially reproduce phase IV (Fig. 3.4A, dashed line shows added force, Fig. 3.4B shows the four phases of the simulated force transient). With the same parameters, the model fits our force-velocity measurements (Fig. 3.4C). To our knowledge, this is the first cross-bridge model that accurately captures both the dynamics of the force transient after stretch and steady-state force-velocity measurements.

3.5. Discussion

Bridging the molecular to cellular (and larger) scales has been a central focus in the study of muscle contraction. Such a multi-scale understanding would have a profound impact on both science and medicine, e.g. improving the understanding of human movement [Alexander, 2005] and the treatment of genetic heart disease [Seidman and Seidman, 2001]. Over fifty years ago, the sliding filament theory [Huxley and Niedergerke, 1954, Huxley and Hanson, 1954] and A. F. Huxley's mathematical model [Huxley, 1957] suggested that this multi-scale understanding was within reach. Subsequent successful predictions of the sliding filament theory [e.g. Gordon et al., 1966], biochemical and structural measurements of myosin interacting with actin [e.g. Lymn and Taylor, 1971, Rayment et al., 1993] and molecular-scale measurements [e.g. Finer et al., 1994, Kron and Spudich, 1986] further contributed to the idea that a multi-scale understanding of muscle contraction was at hand. Nevertheless, to our knowledge, there is still no mathematical muscle model capable of explaining all (or even more than a little) of muscle phenomenology at the cellular scale.

We aim to develop a cross-bridge model that consistently describes muscle measurements across scales. To do so, we start with a molecular-scale model that incorporates many molecular measurements [Walcott et al., 2012], but we make a few critical assumptions motivated by mathematical convenience when we apply our model to the fiber scale (e.g. that sarcomeres are uniform and contain a large number of myosin molecules). This allows us to employ a suite of mathematical tools (see section 3.7 and Appendix B) and perform global parameter optimization when we fit our experimental measurements. Optimization of this form is powerful, because it allows us to rule

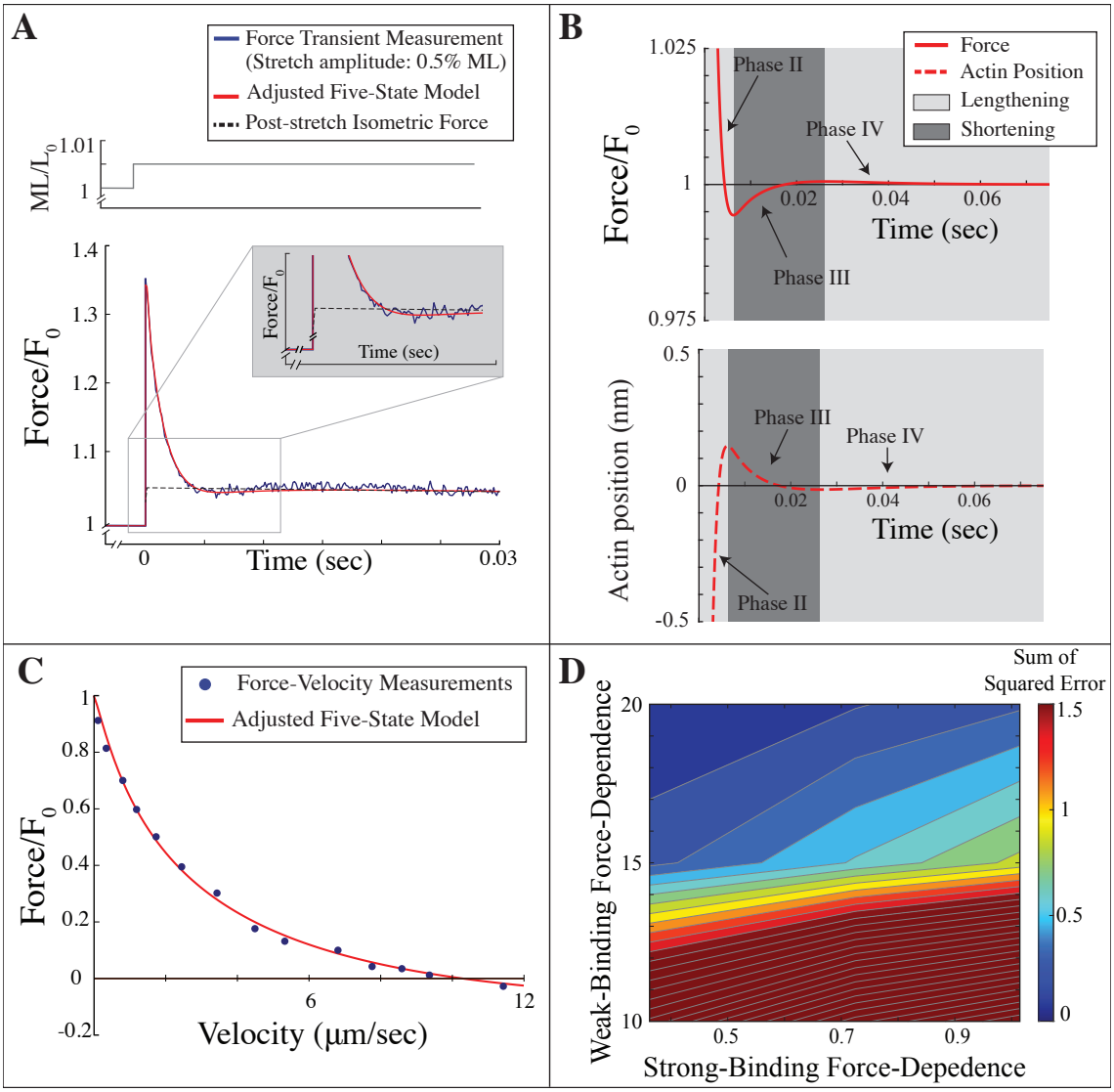

Figure 3.4. The five-state model adjusted to include force-dependent detachment of weakly-bound cross-bridges and an elastic element in series with the cross-bridges is able to reproduce our measurements. **A)** The adjusted model reproduces all four phases of the force transient response. Inset shows that the force in both measurement and model briefly drops below the post-stretch isometric force (dashed line). **B)** Force (relative to isometric, top panel), and actin position (relative to a steady-state position of 0, bottom panel), as a function of time during the force transient response. The light grey regions represent time during which actin is moving in the lengthening direction relative to myosin. The dark grey regions represent time during which actin is moving in the shortening direction relative to myosin. **C)** The adjusted model replicates our force-velocity measurements. **D)** Sum of the squared error in comparing model to measurements for combinations of the magnitude of force-dependence of weakly- and strongly-bound cross-bridge detachment, model parameters E_{wb} and E, respectively. Each axis plots the non-dimensional values of the respective force-dependencies (see Sec. 3.5.3). The model requires a small force-dependence for strong-binding and a large force-dependence for weak-binding to accurately fit our measurements.

out specific models. Here, for example, we can conclude that the model assumptions in our four and five-state models (Fig. 3.1A,B) are wrong, since neither are able to reproduce our data for any parameter choice.

Upon rejection of these proposed models, we tested some of the assumptions we made when we applied the five-state model to our measurements. In particular, we found that including either non-linear elasticity of myosin, force-dependent detachment of weakly-bound cross-bridges, or thin-filament activation did not allow the model to fit our measurements. However, extending the five-state model to include force-dependent detachment of weakly-bound cross-bridges as well as a dynamic interaction with a series elastic element allows the model to simultaneously fit our measurements. As with any successful model fit, this does not guarantee that the model is correct; however, given the difficulty in fitting the model to the data and the large number of alternative models we were able to reject, it is an attractive hypothesis that the force transient response after a small amplitude stretch is due the interaction of a series elastic element and weakly-bound cross-bridges that detach from actin in a force-dependent manner. This result has implications to the connection between cross-bridge dynamics and muscle fiber measurements.

3.5.1. Strongly-bound cross-bridges are unlikely to cause stretch-activation. Our preliminary simulations of force transients using our two proposed models led us to hypothesize that strongly-bound cross-bridges are responsible for the delayed increase in force of phase III (stretch-activation). In the model, this occurs due to the force-dependence of strongly-bound cross-bridges, which, upon stretch, experience forces that decrease their detachment rate, resulting in a net increase in bound cross-bridges and therefore increased force (section 3.3.2). However, we reject this hypothesis as described by the models, because neither model can fit our force transient and force-velocity measurements. Adjusting for the possible effects of series elasticity or an unexplained force allows the five-state model to fit our measurements of the force transient, but then it cannot also fit our force-velocity measurements (section 3.4.2, 3.4.3).

The failure of the five-state model is due to significant differences in the force-dependence required to fit our two experiments. In the force transient fits, large force-dependence is needed to decrease the detachment rate of the strongly-bound cross-bridges enough to get a sufficient increase

in force to fit the stretch-activation response. These large values are then inconsistent with those predicted from force-velocity measurements (Fig. 3.3B). This discrepancy persists even when the model is adjusted to include either non-linear elasticity of myosin, force-dependent detachment of weakly-bound cross-bridges, or thin-filament activation (see Appendix B). Thus, we conclude that strongly-bound cross-bridges cannot be solely responsible for the stretch-activation response.

When we adjust the model to include both a series elastic element interacting dynamically with cross-bridges and force-dependent detachment of weakly-bound myosin, it can simultaneously reproduce both the force transient response and the force-velocity relationship (Fig. 3.4A, C). Interestingly, in the simulated force response, cross-bridge force drops below isometric at the end of phase II (Fig. 3.4A, inset). This drop in force occurs because, even though the fiber length is held constant, both the length of the series elastic element and the length of the contractile element (i.e., the position of actin relative to myosin) are changing. The drop in force coincides with a time when actin moves beyond its steady-state position relative to myosin. Actin moving beyond its steady-state position causes the series elastic element to relax, producing less force. Actin then moves in the shortening direction, extending the series elastic element and causing force to rise in phase III. There is another small overshoot and drop in force which produces phase IV (Fig. 3.4B). In the simulations of the force from the fiber, this drop is masked by the small force we add post-stretch to account for residual force enhancement (dashed line, Fig. 3.4A). However, in some measurements of stretch-activation, particularly at larger stretch amplitudes, a clear drop in force below even the initial isometric force is observed [Galler et al., 1994, Stelzer et al., 2006, 2007]. Such sub-isometric force could not occur if stretch-activation were caused by prolonged attachment of strongly-bound cross-bridges. After stretch, there would be at least as many strongly-bound cross-bridges as pre-stretch, and each cross-bridge would produce more force. Thus, strongly-bound cross-bridges cannot cause sub-isometric forces post-stretch, since together they will result in more, and not less, force. This observation further strengthens our conclusion that stretch-activation is not solely caused by prolonged binding of strongly-bound myosin molecules, and that the major contributor is more likely a dynamic interaction between cross-bridges and a series elastic element.

3.5.2. Series elasticity results in a complex connection between the rates of the force transient response and cross-bridge kinetics. Force transient measurements have been employed to make direct connections between force decay rates and the kinetic steps of the interaction between actin and myosin [Huxley and Simmons, 1971, Piazzesi and Lombardi, 1995, Galler et al., 1996, 1994]. Our results, however, suggest that the connection between force transients and molecular kinetics may not be straightforward. In particular, in our simulations, the extension rate of the series elastic element, and therefore the velocity of actin relative to myosin, varies post-stretch on the same time scale as phase I and II of the force transient response. Thus, the rate at which the phase II decay occurs reflects both the kinetics of cross-bridge unbinding and also this rapidly changing actin velocity. This result provides further insight into why our original five-state model, without a dynamic series elastic element, was unable to fit our force transient measurements (Fig. 3.3). In this model, there is a mismatch in time scales between our force transient and force-velocity measurements, with the former requiring slower ADP release than the latter (Fig. 3.3B). The addition of a dynamic series elastic element resolves this discrepancy (Fig. 3.4).

This result fits with previous modeling studies that have highlighted the importance of series elasticity in other contexts. For example, myofilament elasticity has been shown to have a significant effect on cross-bridge dynamics and force in computational muscle models [Tanner et al., 2007, Daniel et al., 1998, Campbell, 2006]. Similarly, a computational model used to reproduce the stress relaxation response of muscle illustrates that series elasticity has a large effect on the resulting force transient [Luo et al., 1993]. This previous modeling work highlights the necessity of appropriately modeling filament elasticity in cross-bridge models, and that time scales of force production do not directly relate to kinetic steps in the cross-bridge cycle. Our findings expand these results to the context of stretch-activation. We show that the individual phases of the force transient response cannot be directly linked to specific kinetic steps, and further, that series elasticity must be included in cross-bridge models to accurately capture stretch-activation.

3.5.3. Strongly and weakly-bound cross-bridges contribute to force-velocity curvature. It is generally thought that the curvature of the force-velocity relationship is due to the force-dependent chemistry of myosin molecules [e.g. Newhard et al., 2019]. In particular, it has

been shown experimentally that ADP release rate and myosin detachment are dependent on the load the molecule experiences [Veigel et al., 2003, Kad et al., 2007], and that even small ensembles of myosin molecules can produce force-velocity curves that are similar to those from entire muscle fibers [Debold et al., 2005]. Additionally, muscle models that include force-dependent ADP release produce force-velocity relationships with appropriate curvature both at the molecular scale [Walcott et al., 2012], and at the fiber scale [Newhard et al., 2019]. Quantitatively, this force-dependence can be described by a single non-dimensional parameter, E (see Sec.3.3.1), generally ranging between 0.7-1.9 for skeletal muscle [Veigel et al., 2003, Kad et al., 2007, Walcott et al., 2012, Newhard et al., 2019]. Thus, it is at least a plausible hypothesis that the curvature of the force-velocity relationship is determined by the force-dependence of ADP release. While other steps in myosin's cross-bridge cycle have also been measured to be force-dependent [Capitanio et al., 2012], the contribution of these states to force production is unclear.

Our fits to Fenn's [Fenn, 1923] and Hill's [Hill, 1938] data required, in addition to force-dependent ADP release, force-independent weakly-bound cross-bridges that act as a viscous drag (Figs. 3.1C, D). While the viscous drag has little impact on the Fenn effect, overall force-velocity curvature is a combination of the curved force from the force-dependent strongly-bound cross-bridges, and the linear drag from the force-independent weakly-bound cross-bridges. In effect, the weakly-bound cross-bridges are masking the force-dependence that would be predicted from strong binding alone.

In contrast, fits to our measurements of force transients and force-velocity were possible only with significant force-dependence in unbinding of the weakly-bound state, and minimal force-dependence in unbinding of the strongly-bound state (Fig. 3.4D). Our best fit has a non-dimensional force-dependence of $E = 0.36$ for strongly-bound cross-bridges, a bit smaller than previously reported values [Veigel et al., 2003, Kad et al., 2007, Walcott et al., 2012, Newhard et al., 2019]. The model also includes a single non-dimensional parameter that describes the force-dependence of weakly-bound cross-bridges, E_{wb}. By non-dimensionalizing these two force-dependencies, they are directly comparable (note, however, that while an increase in force slows the rate of detachment for strongly-bound cross-bridges, it increases the detachment rate of weakly-bound cross-bridges, so they have opposite sign). The large best-fit force-dependence for weakly-bound cross-bridges,

$E_{wb} = 20$, indicates that the curvature of the force-velocity relationship in the model is largely due to the force-dependence of the weakly-bound state.

In fitting both of our data sets, we find that the curvature of the force-velocity relationship represents a combination of the force-dependence of the weakly- and strongly-bound states. Therefore, in interpreting force-velocity curvature, it is critical to consider the contributions and force-dependencies of both weakly- and strongly-bound cross-bridges.

3.6. Conclusion

Over the past two decades, the molecular picture of muscle contraction has been brought sharply into focus by single molecule techniques. However, a gap remains between that molecular picture and the behavior of muscle at the cellular and larger scale. Modeling approaches are critical in bridging this gap. We have demonstrated that the addition of a weakly-bound state allows a cross-bridge model, extensively validated with molecular-scale data, to describe several whole muscle experiments. Further, we show that this model, even with a weakly-bound state, cannot explain our own measurements on *Drosophila* jump muscle fibers. However, if both elastic elements in series with the cross-bridges and force-dependent unbinding from a weakly-bound state are included in the model, it is able to simultaneously fit our measurements. Taken together, the successes and failures of our cross-bridge models in describing fiber level measurements provide insight into the molecular mechanism of stretch-activation, demonstrate a lack of a direct connection between the force transient response and kinetic steps in the cross-bridge cycle, and suggest that the curvature of the classic force-velocity relationship results from a combination of the force-dependencies (or lack thereof) of weakly- and strongly-bound cross-bridges. This work represents a step toward a minimal cross-bridge model that has predictive power at the fiber level.

3.7. Materials and Methods

3.7.1. Experiments. We used jump muscles from the *Drosophila* line *pwMhc2* [Swank et al., 2000], which we have used as a control line in all of our previous jump muscles experiments. This provided us with a large data pool with which to compare our current results and enabled

accurate determination of the quality of our current experimental results. Skinned jump muscle fiber bundles were prepared as previously described [Newhard et al., 2019, Eldred et al., 2010, Swank, 2012]. Briefly, jump muscles were removed from three-day-old female flies and chemically demembranated (skinned) for one hour. Muscles were pared down to 6 - 8 fibers and aluminum T-clips were attached to either end resulting in a fiber bundle of approximately 150 μm in length, 100 μm width, and 50 μm depth. The bundle was mounted on a muscle mechanics apparatus and attached to a force transducer and a piezo motor while bathed in relaxing solution (pCa 8.0, 12 mM MgATP, 30 mM creatine phosphate, 600 U/ml creatine phosphokinase, 1 mM free Mg^{2+}, 5 mM EGTA, 20 mM BES (pH 7.0), 200 mM ionic strength, adjusted with Na methane sulfonate, 1 mM DTT) at 15°C. Starting sarcomere length was set to 3.6 μm by lengthening the fiber bundle. The fiber bundle was transferred to pre-activating solution (same as relaxing solution, but no EGTA) for two minutes and then into activating solution (same as relaxing solution, but pCa 5.0). Isometric tension was measured once force reached a steady-state maximum level.

To obtain force transients in response to rapid length increases, fiber bundles were first activated as described above and then rapidly lengthened over 0.5 ms and held at the increased length for 500 ms before returning to the starting fiber length. The length increases tested ranged from 0.25% to 2% fiber length. The same length increases were performed at pCa 8.0 to determine if passive properties contributed significantly to force amplitudes (see Appendix B).

Separate jump muscle fiber bundles were used to obtain force-velocity curves. Force-velocity curves were performed using the force-clamp technique as previously described [Newhard et al., 2019, Eldred et al., 2010, Swank, 2012]. Briefly, after the fiber reached its maximum activated tension level the fiber bundle was initially rapidly shortened for 0.5 ms and then the velocity of shortening adjusted until the velocity of shortening produced the desired tension level based on feedback from the force transducer. 14 different tension levels were chosen starting with low tension loads, and increased load in each subsequent force clamp. To produce a force-velocity data point from each force-clamp, the average velocity and tension between 5 ms and 13 ms was calculated, the earliest time following the initiation of shortening that tension was consistently clamped.

3.7.2. Modeling Details. We model the interaction between actin and myosin with the kinetic schemes detailed in Fig. 3.1A and B. In the five-state model, myosin and actin interact in the

following consecutive steps: (1) myosin binds to actin in a pre-power-stroke state with inorganic phosphate (P_i) and ADP in its active site, (2) in some order, P_i is released and myosin undergoes a conformational change, transitioning into a strongly-bound, post-power-stroke state, (3) ADP is released and myosin stays strongly-bound to actin in a rigor state, (4) ATP binds to the empty active site of myosin, causing dissociation of myosin from actin, (5) ATP is hydrolyzed into P_i and ADP, and the cycle repeats. The four-state model is identical to the five-state, with the exception that it does not include a weakly-bound state.

To quantitatively compare the models to cellular level data, we express each kinetic scheme as a system of integro-PDEs. Each equation corresponds to a particular state in the model, and describes the dynamics of myosin in that state. For unbound states, myosin and actin do not interact, and thus the probability of being in one of these states is simply a function of time. However, when myosin is bound to actin, it is bound with a particular extension, which determines the force on the molecule. Thus, the equations corresponding to bound states describe the probability density that myosin is in a bound state with a particular extension. Transitions between states are defined by constant rates except for: (1) the transition between a bound and unbound state is defined as a rate density, since this is dependent on the extension with which myosin binds, and (2) ADP release rate is force-dependent with the following form based on Bell's approximation [Veigel et al., 2003, Kad et al., 2007, Bell, 1978]:

$$k_D(F) = k_D^0 \exp\left(- \frac{\delta F}{k_B T} \right) \tag{3.2}$$

where δ is a parameter that describes myosin's force-dependent chemistry, $k_B T$ is Boltzmann's constant times temperature and k_D^0 is the reaction rate in the absence of force. All other transition rates in the model are independent of force.

To compare the model to experimental measurements, we solve the system using a variety of numerical and analytical techniques. Numerically, we implement a standard ODE solver, together with a root find for the integral constraint, to solve the system under steady-state conditions (as in force-velocity and heat measurements). To solve the system without a steady-state assumption (as in force transients), we use a method of characteristics to transform the system of PDEs into one of ODEs. These ODEs are then solved along the characteristics using another standard ODE

solver, e.g. fourth-order Runge-Kutta. To simulate the quick stretch of the force transient protocol, we solve the ODEs using an initial condition of steady-state shifted by the half-sarcomere stretch amplitude.

While these numerical techniques provide accurate solutions, they are too inefficient to perform global parameter optimization. Thus, in order to fit the model to experimental data, we additionally need analytical solutions. We implement a matched asymptotic expansion to solve the system analytically under steady-state conditions. Without the steady-state assumption, we use a separation of time scales and a moment approximation to reduce the system to a set of ODEs [Zahalak, 1981]. While this does not allow for an explicit analytical solution, it does result in a system that is efficient enough to optimize with standard techniques.

Once the system is solved, we have expressions for the probability that myosin is in each state. This lends to a calculation for force, given that the force produced per myosin molecule is the probability that myosin is bound times the force produced when it is. With this, the model results can be related back to measurements from a variety of experimental protocols. Thus, with this mathematical formulation of the kinetic schemes in Fig. 3.1A and B, we have connected the molecular interactions to cellular behavior in a way that is robust enough to optimize parameters and fit the model to experimental measurements. (See Appendix B for a detailed discussion of the modeling techniques used.)

3.8. Acknowledgements

This work was supported by the grants: NIH-R01GM135923-1, awarded to Sam Walcott, and NIH-R01AR064274, awarded to Douglas Swank.

CHAPTER 4

Muscle models require forcible detachment of myosin and multiple-sarcomere systems to accurately describe muscle lengthening phenomena

Joint work with:

Sam Walcott

Department of Mathematics, Worcester Polytechnic Institute, Worcester, MA

4.1. Introduction

Muscle contraction results in a diverse array of physiological functions, each of which is a consequence of a combination of muscle shortening (i.e. concentric contraction), isometric contraction (i.e. fixed length contraction), or muscle lengthening (i.e. eccentric contraction). While each type of contraction is essential, eccentric contraction is particularly important for human movement and exercise. Eccentric contraction occurs when the magnitude of force that is applied to the muscle is greater than the force produced by the muscle, and thus lengthening of the muscle results [Katz, 1939, Lindstedt et al., 2001, Hody et al., 2019]. In this process, a muscle performs negative work as it absorbs energy and dissipates it as heat [Hody et al., 2019, Katz, 1939].

Skeletal muscle lengthening is crucial for locomotion. Walking downhill, for example, relies on the eccentric contraction of extensor muscles in the knee [Hody et al., 2019, Proske and Morgan, 2001], and running is a result of muscle undergoing a stretch-shortening cycle, in which both eccentric and concentric contraction are necessary [Lindstedt et al., 2001]. Additionally, eccentric contraction has been shown to result in greater muscle force and power, while requiring less metabolic cost than other contraction types [Hody et al., 2019].

A notable feature unique to eccentric contraction is that it results in stretch-induced muscle damage, followed by a recovery and fortification period [Proske and Morgan, 2001, Clarkson and Hubal, 2002, Morgan and Allen, 1999, McHugh et al., 1999]. After an intense or new eccentric movement, muscle pain and soreness are experienced, and this is thought to be due to muscle damage [Morgan and Allen, 1999, Friden et al., 1981]. However, it has been shown experimentally that muscle can recover from such an injury in a way in which it is strengthened against further muscle damage from similar eccentric contractions [Schwane and Armstrong, 1983, Brown et al., 1997, McHugh et al., 1999]. This phenomenon, known as the "repeated bout effect", suggests that muscle can be fortified against injury with proper tuning of eccentric contraction, and has implications for sports medicine training and for restoring or maintaining function to aged or injured muscle [Hody et al., 2019, Brown et al., 1997, Schwane and Armstrong, 1983].

While the physiological importance of eccentric contraction and general details of the repeated bout effect are established, the exact mechanisms behind stretch-induced damage and subsequent muscle strengthening are unknown [McHugh et al., 1999, Schwane and Armstrong, 1983, Brown

et al., 1997]. Experimental results and corresponding theories have proposed a variety of explanations for what occurs at the cellular and molecular levels during eccentric-induced damage. One common hypothesis is that eccentric contraction causes disruption in excitation-contraction coupling that ultimately results in muscle weakness and injury [Morgan and Allen, 1999, Proske and Morgan, 2001, Clarkson and Hubal, 2002]. This can be attributed to various steps in the excitation-contraction process, including modifications to the neuromuscular junction, changes in motor neuron recruitment, or decreases in the concentration of calcium released [Morgan and Allen, 1999, Proske and Morgan, 2001, Clarkson and Hubal, 2002]. Other possible explanations for the mechanisms causing eccentric muscle damage focus on structural changes at the sarcomere and myofibril levels. Experimental work shows that this occurs in various ways, including disruption in the Z-lines of the myofibril, called Z-line streaming [Clarkson and Hubal, 2002, Friden et al., 1981], overextension and disorganization of sarcomeres [Proske and Morgan, 2001, Brown and Hill, 1991, Wood et al., 1993], and non-uniform lengthening of sarcomeres [Wood et al., 1993, Proske and Morgan, 2001]. Mostly likely, the stretch-induced muscle injury following eccentric contraction is due to a combination of the above factors [McHugh et al., 1999].

While there is interest in experimentally studying eccentric contraction, the majority of muscle theories (including our own) focus on describing isometric or shortening regimes, where lengthening does not occur. Additionally, for computational feasibility, many existing theories assume sarcomere uniformity, and scale the behavior of a single half-sarcomere to the fiber level [e.g. Walcott et al., 2012, Jarvis et al., 2021, Campbell, 2014, Duke, 1999, Månsson, 2010]. Models of this form are unable to capture multi-sarcomere behavior observed during eccentric contraction, like Z-line streaming and non-uniform sarcomere lengthening, which may result from instabilities and (small) inherent non-uniformities among sarcomeres. In fact, to the best of our knowledge, there is no molecular-based model that describes the details of muscle mechanisms during all regimes of lengthening.

However, given that eccentric contraction is both essential and advantageous to human movement, it is vital to understand how molecular mechanisms scale up to result in muscle lengthening. Developing a theory of eccentric contraction would provide insight into how muscles function under physiological conditions, and also how muscle is damaged after stretch. With this work, we are

motivated by these unknown features of eccentric contraction, and are interested in exploring muscle lengthening in a quantitative way. To do so, we develop a cross-bridge theory to successfully replicate two complementary lengthening muscle measurements: force transients after rapid stretch and force at constant lengthening velocities. Analysis of our cross-bridge model suggests that both forcible detachment of myosin from actin as well as multiple-sarcomere systems are necessary to describe lengthening muscle measurements.

4.2. Motivation

The first question we must address in modeling eccentric muscle contraction with a cross-bridge model is what modifications, if any, are necessary to replicate experiments. In this section, we show that the exponential slowing of ADP release from the strongly-bound state [Veigel et al., 2003, Kad et al., 2007, Sung et al., 2015, Greenberg et al., 2014] results in non-physical behavior during muscle lengthening, where myosin cross-bridges become stuck to actin and lengthen indefinitely. To resolve this issue, some mechanism must be incorporated to allow for forcible detachment of myosin from actin.

4.2.1. Muscle measurements result in yielding behavior for lengthened muscle. To explore the essential molecular details to include in a cross-bridge model, we focus on two experimental measurements of muscle lengthening that display unexplained behavior. First, we consider measurements of the force response of a muscle fiber after a rapid lengthening. Experimentally, a muscle fiber is activated and then held at an isometric length. At a particular time, the fiber is quickly ($\sim$ 0.5 ms) stretched a percentage of its length ($\sim$ 0.2 - 2.5 % muscle length), and then held isometrically again. The response of the fiber to stretch is a peak in force at the time of lengthening, followed by a rapid decay in force, a delayed increase in force, and finally a recovery period (see Fig. 3.1E). We are particularly interested in the relationship between the peak force obtained with rapid lengthening and the amplitude of the imposed stretch. This relationship is linear for small amplitude stretches, but becomes non-linear with decreasing force for larger amplitude stretches (see Fig. 3.2B, Jarvis et al. [2021]).

In addition to force transient measurements, we consider the behavior of the lengthening side of the force-velocity relationship. Experiments of this relationship show that slow lengthening results in an increase in force above isometric. However, for faster velocities, a yielding behavior is observed, and the force produced plateaus so that further increasing velocity does not additionally increase force [Morgan and Allen, 1999, Harry et al., 1990, Joyce et al., 1969, Katz, 1939].

In both measurements, muscle lengthening results in yielding behavior. The exact mechanism(s) underlying this phenomenon are unknown. Understanding this change in regime is crucial to developing a comprehensive theory of eccentric contraction, and thus force transient and force-velocity measurements provide a basis for our model development.

4.2.2. Minimal model requires forcible detachment of myosin from actin to reproduce yielding behavior. To understand the implication of the experimentally observed yielding behavior during muscle lengthening, we used a simple cross-bridge model to simulate these experiments (Fig. 4.1). In brief, myosin begins unbound from the actin filament, with ADP and inorganic phosphate (P_i) in its active site (state 1, Fig. 4.1). In some order, P_i is released, myosin binds to actin, and myosin undergoes a conformational change called the power-stroke. In this state (state 2, Fig. 4.1), the myosin molecule is strongly-bound to actin and therefore producing force. ADP is then released in a force-dependent manner, and myosin and actin stay bound in a rigor conformation (state 3, Fig. 4.1). ATP can then bind to myosin, resulting in the dissociation of myosin from actin (state 4, Fig. 4.1). Finally, ATP is hydrolyzed into products ADP and P_i (state 1, Fig. 4.1), which re-primes the cycle to begin again. With this mechanochemical description of the interaction between actin and myosin, we then use a collection of mathematical tools to connect this molecular behavior to larger scales (see section 4.6

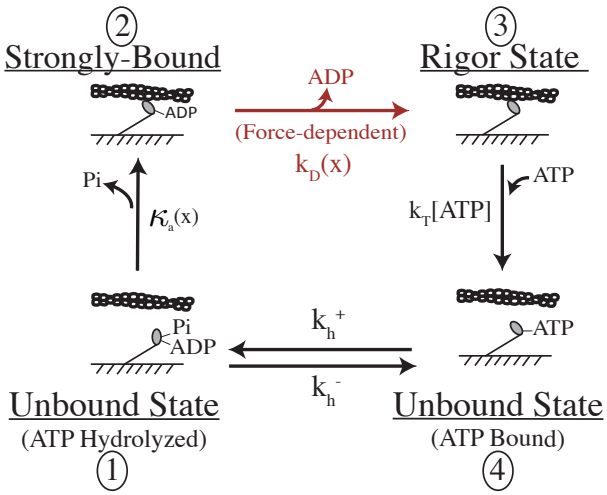

Figure 4.1. *Adapted from Jarvis et al. [2021]* A simple four-state kinetic scheme describes the interaction between actin and myosin, including two bound states (states 2 and 3) and two unbound states (states 1 and 4).

for details), and simulating force transient and force-velocity protocols, the final model results are directly comparable to experimental measurements.

Single-molecule measurements of the actomyosin interaction provide information on the details of the kinetic scheme. For example, the bond that myosin forms with actin is dependent on the force a molecule experiences, with assistive loads decreasing, and resistive loads increasing, the lifetime of the bond. In smooth and cardiac muscle, bond lifetime depends exponentially on the force a molecule experiences [Veigel et al., 2003, Kad et al., 2007, Greenberg et al., 2014, Sung et al., 2015]. Thus, given that myosin acts as a linear spring (and so force is proportional to extension, x), we model ADP release rate as:

$$k_D(x) = k_D^0 \exp\left(- \frac{\kappa\delta(x+d)}{k_B T} \right) \tag{4.1}$$

where κ is the stiffness of myosin, $k_B T$ is Boltzmann's constant times temperature, k_D^0 is ADP release rate in the absence of force, and δ is a parameter that describes myosin's force-dependence. In previous work (i.e. Chapter 2 and 3), we have used this functional form for ADP release rate to successfully model isometric, shortening, and small-amplitude lengthening protocols [Jarvis et al., 2018, 2021].

Comparing the model results to equivalent experimental measurements (see section 4.6 for more details), we find that our cross-bridge model is unable to capture the qualitative behavior of lengthening. In particular, it is lacking the yielding behavior observed in lengthening measurements. In experimentally measured force transients, the relationship between peak force after rapid stretch and stretch amplitude is linear for small stretch amplitudes ($< 1\%$ muscle length), but becomes nonlinear and decreases for larger amplitudes ($> 1\%$ muscle length). The four-state model is unable to replicate this, resulting in a strictly linear relationship between peak force post-stretch and stretch amplitude (Fig. 4.2A, gray circles). Similarly, experimental measurements of force-velocity in lengthening show an increase in force for small velocities that quickly plateaus as lengthening velocity increases. The model, however, results in molecules with huge extensions for even small lengthening velocities (Fig. 4.2B inset, dashed gray line), resulting in a force-velocity curve that increases rapidly with no yielding behavior (Fig. 4.2B, dashed gray line).

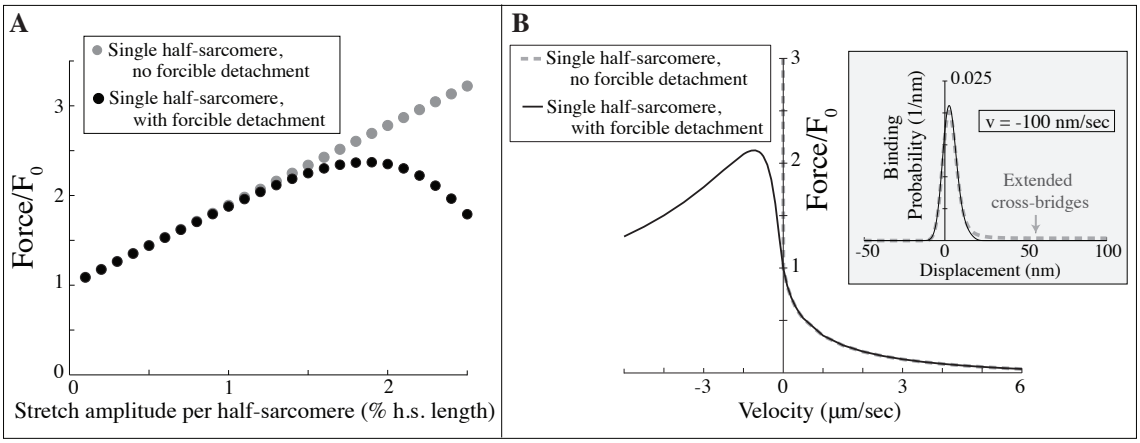

Figure 4.2. Single half-sarcomere model requires forcible detachment of myosin to capture yielding behavior in lengthening muscle. **A)** Model predicted relationship for peak force after rapid stretch as a function of stretch amplitude for a single half-sarcomere model without forcible detachment of myosin (gray circles) and with forcible detachment of myosin (black circles). **B)** Model predicted force-velocity relationship for single half-sarcomere model without forcible detachment (gray dashed line) and with forcible detachment of myosin (solid black line). Inset plots myosin binding probability as a function of molecule extension, illustrating that myosin molecules stay bound for unreasonably large extensions in a model without forcible detachment (gray dashed line), but do not for a model with forcible detachment (black solid line).

The disagreement between the model and measurements arises from the functional form of the force-dependence of myosin's detachment from actin. Intuitively, it is plausible that including forcible detachment of myosin, whereby myosin is ripped off the actin filament at large extensions resulting in a decrease in force production, may result in the yielding behavior of lengthening muscle that is absent in the preliminary simulations from the cross-bridge model. To test this idea, we adjusted the functional form of ADP release rate to include both the experimentally observed force-induced decrease (a catch component) and also a force-induced increase at larger forces (a slip component). ADP release rate is then modeled with the equation,

$$k_D(x) = k_D^0 \exp\left(-\frac{\kappa\delta(x+d)}{k_BT}\right) + k_D^F \exp\left(\frac{\kappa\delta_F(x+d)}{k_BT}\right) \tag{4.2}$$

where k_D^F and δ_F are parameters that describe the slip component of the bond.

Upon inclusion of forcible detachment of myosin, the cross-bridge model captures the yielding behavior observed in both measurements. The adjusted model produces a peak force as a function of stretch amplitude curve that is linear for small amplitudes and turns over as lengthening

amplitude becomes large (Fig. 4.2A, black circles). Additionally, the model now predicts that force-velocity will yield for large lengthening velocities, qualitatively replicating the behavior observed in experimental measurements (Fig. 4.2B, black curve). We therefore conclude that cross-bridge models must include forcible detachment of myosin from actin to accurately capture features of eccentric muscle contraction.

Additionally, forcible detachment of myosin from actin suggests another potential issue with modeling eccentric contraction. In particular, we hypothesize that when we are in a lengthening regime where forcible detachment of myosin is significant, sarcomere instabilities will arise, and it will be necessary to explicitly model multi-sarcomere systems. The intuition is as follows. When myosin can be forcibly detached from actin, cross-bridges begin to fail when they are stretched to large extensions. Failure of a few myosin molecules results in the same amount of force spread over a smaller population of cross-bridges, leading to more failure. Within a larger myofibril, the failure of all cross-bridges in a particular sarcomere would then result in more force on the next sarcomere, causing failure here as well. Thus, we expect forcible detachment of myosin to work as a positive feedback system, where cross-bridge failure propagates throughout a sarcomere, eventually spreading to other sarcomeres, and ultimately causing catastrophic failure.

We therefore propose that muscle models must include forcible detachment of myosin to accurately capture the yielding behavior of lengthening muscle, and when such cross-bridge failure occurs, sarcomere instabilities will arise, resulting in the need for multi-sarcomere models. To investigate this hypothesis, we expand our modeling framework to explicitly model multi-sarcomere systems. By adding sarcomeres in both series and parallel, we explore the distinct model results of single and multi-sarcomere theories, and examine the effect of the elasticity of parallel connections.

4.3. Results

To test the hypothesis that forcible cross-bridge detachment leads to sarcomere instabilities during muscle lengthening, we developed a collection of single and multi-sarcomere models (see section 4.6 for details). With each model, we simulate force transients and force-velocity in lengthening, and compare the results. We find that multi-sarcomere systems produce lengthening behavior

that is different than that produced by a single half-sarcomere. The multi-sarcomere results are dependent on the number of sarcomeres in series and parallel as well as the elasticity of the connections. These findings have implications for developing a theory of lengthening muscle, and justify the need for accurately modeling multi-sarcomere systems.

4.3.1. Multiple sarcomeres in series results in different lengthening behavior than a single half-sarcomere. To provide preliminary insight into the effect of modeling multiple-sarcomere systems, we first connect multiple half-sarcomeres in series. To account for non-uniformity among sarcomeres, we include variation in the number of cross-bridges in each half-sarcomere by selecting the amount of molecules in each from a normal distribution with a mean of 350 and a standard deviation of 30 (see inset, Fig. 4.3A). Then, by accounting for the necessary force and length requirements of sarcomeres in series, we can simulate force transient and force-velocity experimental protocols and analyze the results (see section 4.6 for more detail).

4.3.1.1. *Sarcomeres in series result in catastrophic failure in force transients.* First, we employ our force transient simulations to consider the peak force obtained post-stretch as a function of the stretch amplitude. In the case of a single half-sarcomere with forcible detachment, we observed a linear relationship that gradually yields for large stretch amplitudes (Fig. 4.3A, black circles). Including any number of sarcomeres in series, however, results in different behavior, with catastrophic failure occurring for large amplitude stretches (Fig. 4.3A, colored symbols). The exact extension that causes failure is dependent on the number of sarcomeres in series (Fig. 4.3A).

In our simulations, the total failure we observe in the multi-sarcomere case is dictated by the sarcomere with the smallest number of cross-bridges, i.e. the "weakest" half-sarcomere (Fig. 4.3A, inset). For example, in 500 simulations of 3 half-sarcomeres in series, failure always began in the half-sarcomere with the smallest number of cross-bridges (Fig. 4.3A, inset). In these simulations, each sarcomere experiences the same force because they are arranged in series and are in mechanical equilibrium. The half-sarcomere that has the smallest number of cross-bridges therefore experiences the most force per cross-bridge, and is where cross-bridge failure begins. As cross-bridges fail within this half-sarcomere, force drops (Fig. 4.3C, top). The remaining half-sarcomeres must adjust by shortening, which causes the weakest half-sarcomere to lengthen (Fig. 4.3C, bottom). This

lengthening leads to more cross-bridge failure and ultimately to catastrophic failure of this half-sarcomere (Fig. 4.3A, C).

However, this behavior is distinct from the single half-sarcomere system because, in these simulations, the length of the single half-sarcomere is fixed. That is, as the half-sarcomere is stretched and cross-bridges begin to fail, there is no additional lengthening to initiate the positive feedback resulting in catastrophic failure. We consequently observe a gradual drop in force at large stretch amplitudes for the single half-sarcomere case.

4.3.1.2. *Sarcomeres in series result in fluctuation in the force-velocity relationship.* Next, we consider the effect of adding sarcomeres in series on the force-velocity relationship. To do so, we begin with a set of sarcomeres in series, each with a variable numbers of cross-bridges (see above), and impose a constant velocity stretch. After a period of time, the cross-bridges will have reached steady-state, and we can extract the force value that corresponds to the imposed velocity (i.e. the final force value at $t = 0.08$ sec in the insets of Fig. 4.3B corresponds to points on the force-velocity curve for each velocity value, see section 4.6 for more details). Repeating for various velocity values, we obtain a force-velocity curve for lengthening muscle.

Comparing our multi-sarcomere results to the model with a single half-sarcomere, we see similar results for small lengthening velocities, but very different behavior for larger velocities. In the multi-sarcomere case, force smoothly increases for small lengthening velocities, because the individual force traces smoothly approach steady-state in time (Fig. 4.3B, right inset). However, beyond a critical lengthening velocity there is a significant amount of variability in the force-velocity relationship (Fig. 4.3B, green line). The apparent variation is due to an oscillatory behavior of the cross-bridges in the weakest half-sarcomere, which leads to an oscillatory force trace for a given velocity, and thus significant variation in the force-velocity relationship (Fig. 4.3B, left inset). In more detail, cross-bridges in the weakest half-sarcomere undergo a cyclical pattern which begins when they are lengthened to large extensions and fail due to forcible detachment. After this preliminary detachment, cross-bridges rebind and go through the cross-bridge cycle again, until they are extended beyond a threshold and forcible detachment occurs once more. Thus, cross-bridges

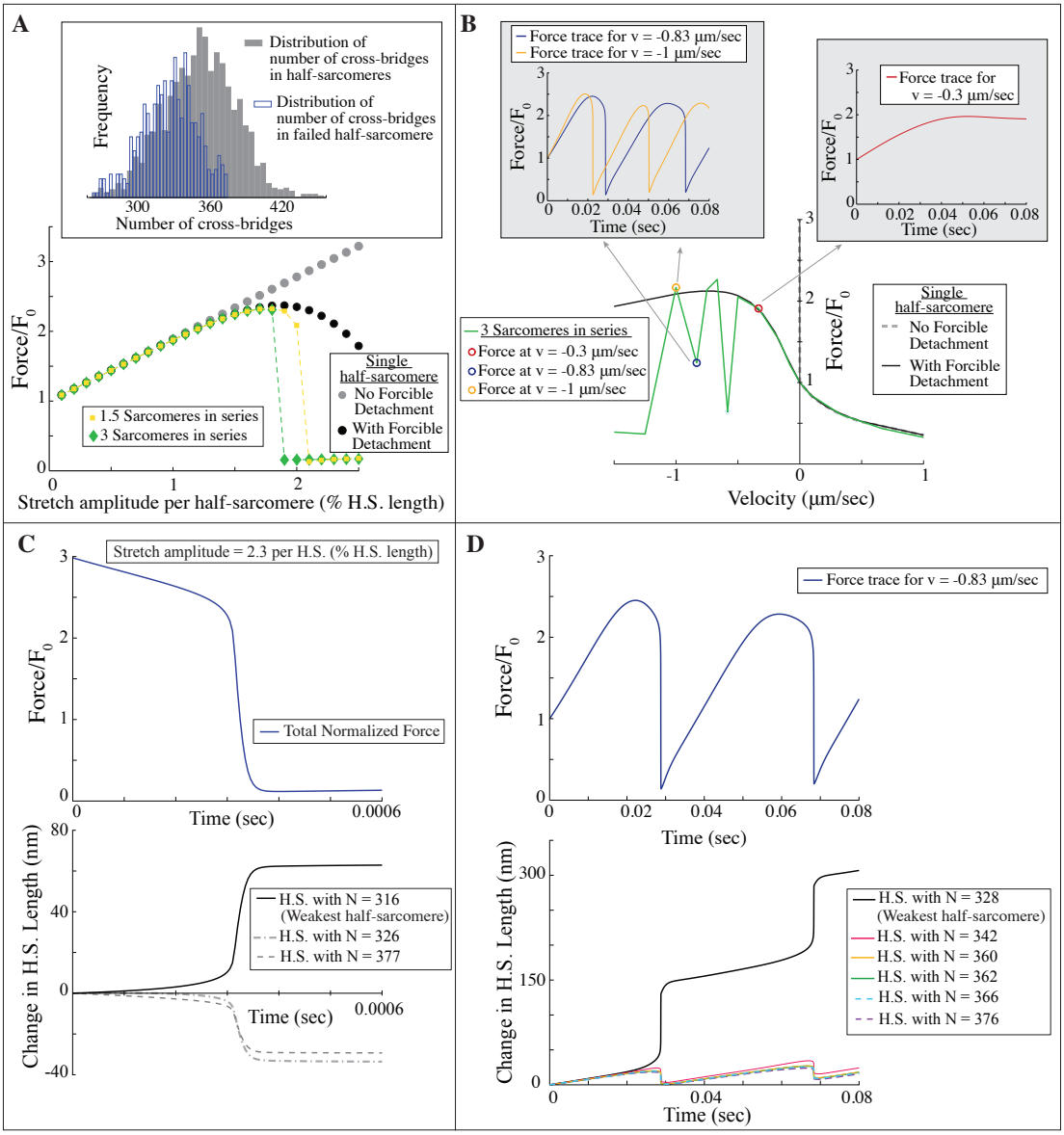

Figure 4.3. A multi-sarcomere model consisting of sarcomeres in series results in catastrophic failure that is distinct from a single half-sarcomere model. **A)** Relationship of peak force after rapid stretch as a function of stretch amplitude for a single half-sarcomere (gray and black circles) compared to a model with 1.5 (yellow squares) or 3 (green diamonds) sarcomeres in series. **B)** Force-velocity in lengthening for a single half-sarcomere (gray dashed and solid black lines) compared to a model with 3 sarcomeres in series (green solid line). Insets shows force as a function of time for fixed lengthening velocities, illustrating the smooth results for small lengthening velocities (red solid line is $v = -0.3\mu$m/sec) and the oscillations in force for large lengthening velocities (blue and yellow solid lines are $v = -0.83\mu$m/sec and $v = -1\mu$m/sec, respectively) that result in the observed variability in the force-velocity curve. **C, D)** Normalized force (top) and change in half-sarcomere length (bottom) throughout time. When force fails, the half-sarcomere with the smallest number of cross-bridges lengthens, while the rest shorten.

fail, rebind, and fail in a repeated pattern, leading to an oscillatory force trace (Fig. 4.3B, left inset), and ultimately resulting in irregularities in the lengthening portion of the force-velocity curve (Fig. 4.3B, green curve).

Together, model simulations of both force transient and force-velocity measurements demonstrate that including sarcomeres in series results in behavior that is unique compared to a single half-sarcomere model, ultimately resulting in catastrophic failure that is dictated by the weakest half-sarcomere.

4.3.2. A system of sarcomeres in series and parallel results in unique behavior dependent on the elasticity of the connections. While exploring sarcomeres solely in series provides insight into the effect of horizontal connections among sarcomeres, in physiological muscle, sarcomeres are connected in both series and parallel. Thus, to extend our study, we additionally include parallel rows of sarcomeres connected in series. These parallel connections are a composition of a variety of interfilamentary links (e.g. Z-disks connecting actin filaments, the protein titin, intermyofibril linkages, inter-fiber connections, etc). For computational feasibility, we combine these potential parallel linkages, and therefore there is some variability in the elasticity of the parallel connections we model. However, given the complexity and computational inefficiencies associated with modeling large systems of sarcomeres in series and parallel (see section 4.6 for details), it is challenging to do an exhaustive study into different elasticities. Thus, we choose to consider two extremes of the elasticity of parallel connections: 1) extremely rigid vertical connections, and 2) weak or no vertical connections (see section 4.6 for modeling details). In doing so, we provide preliminary insight into the effects of lateral coupling and suggest areas for further exploration.

4.3.2.1. *Rigid vertical connections result in catastrophic failure.* First, we consider adding parallel sets of sarcomeres in series with rigid vertical connections, and simulate our two experimental protocols (see section 4.6 for details). Implementing stiff connections in our force transient simulations, we again observe catastrophic failure in the relationship of peak force as a function of stretch amplitude. However as the number in parallel increases, the peak force tends towards that of a single half-sarcomere (Fig. 4.4A). This behavior results because adding rigid parallel connections decreases the relative variability among sarcomeres. As the number of sarcomeres in parallel increases,

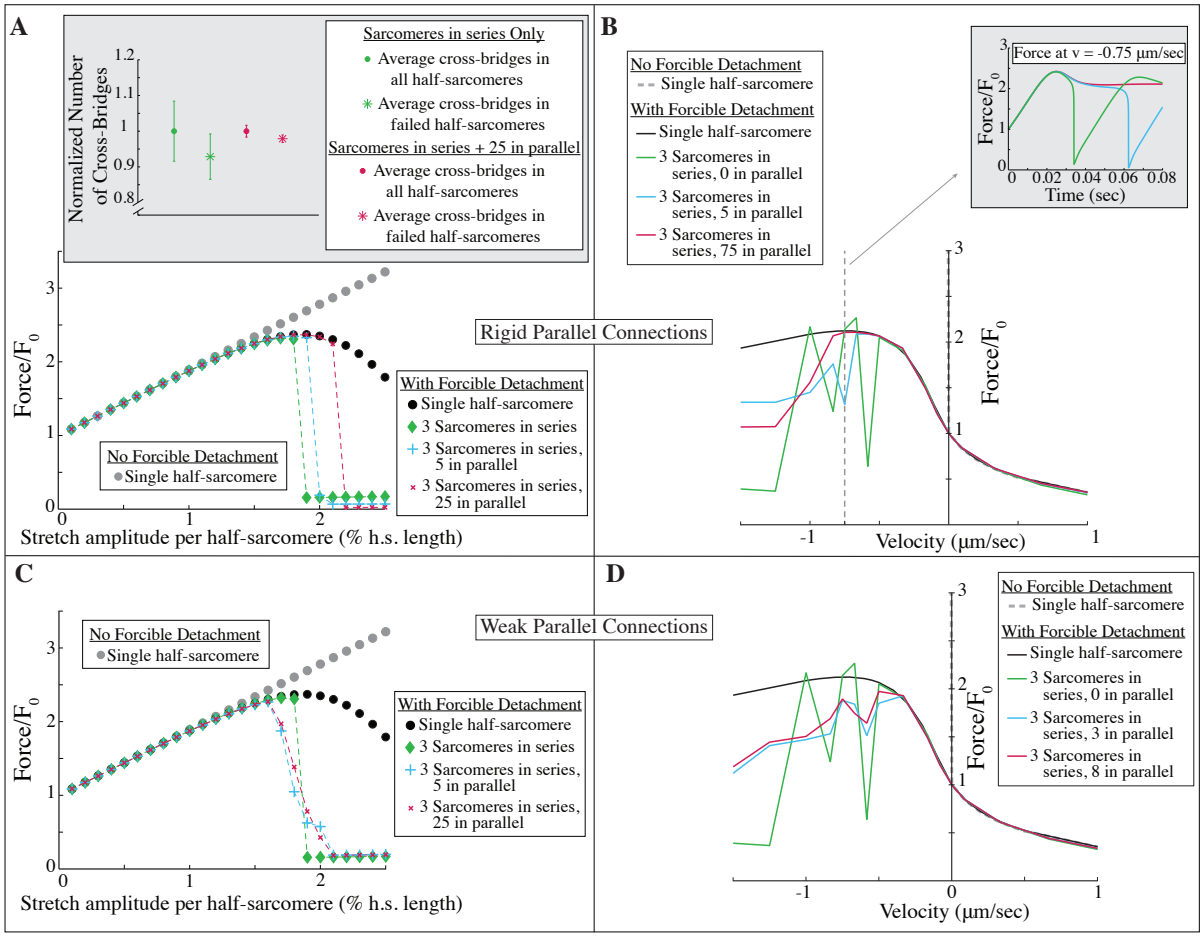

Figure 4.4. A multiple-sarcomere model with sarcomeres in series and parallel exhibits emergent behavior dependent on the elasticity of the parallel connections. **A)** A model with sarcomeres connected in parallel with rigid elasticity results in catastrophic failure in peak force after rapid stretch (green, blue, and red symbols). Inset plots mean ± standard deviation of numbers of cross-bridges in half-sarcomeres from simulations with sarcomeres solely in series (green) and simulations with 25 rigidly connected parallel sets of sarcomeres in series. Circles represent mean number of cross-bridges in all half-sarcomeres, and stars represent mean number of cross-bridges in the half-sarcomeres that resulted in failure, normalized to the appropriate mean number from all half-sarcomeres. **B)** The same model produces oscillations in force throughout time (inset) that result in fluctuations in the force-velocity relationship, but as the number of parallel connections increases, the oscillations begin at increasingly large lengthening velocities. Inset illustrates force traces for a fixed velocity of $v = -0.75\mu$m/sec. The model without connections in parallel results in force oscillations (green curve), while the model with 75 rigid parallel connections does not (red curve). **C)** A model with sarcomeres connected in parallel with weak elasticity results in gradual failure in peak force after rapid stretch (green, blue, and red symbols). **D)** The same model results in a force-velocity curve (red and blue solid lines) with less variation than the model with sarcomeres in series only (green solid line).

the standard deviation of the number of cross-bridges in each half-sarcomere decreases, resulting in the weakest half-sarcomere becoming more similar to the average half-sarcomere (Fig. 4.4A, inset).

Thus, the weakest half-sarcomere effectively becomes stronger, resulting in an overall peak force curve that is more robust, with failure resulting from only large stretches (Fig. 4.4A).

Similarly, simulating the force-velocity relationship with stiff parallel connections results in a more robust curve (Fig. 4.4B). In this case, while we still observe fluctuations in force leading to an irregular force-velocity relationship, as we add sarcomeres in parallel the magnitude of the critical velocity value at which the oscillations begin increases, due to the decrease in sarcomere variability (Fig. 4.4B, inset). This results in a force-velocity curve that is smoother and approaches that of the single half-sarcomere case (Fig. 4.4B, red line).

4.3.2.2. *Weak vertical connections result in gradual failure.* On the other extreme, sarcomeres could be connected in parallel by very weak interfilamentary connections. To explore such a system, we adjusted our simulations to include sets of laterally connected sarcomeres in parallel with no vertical connections (see section 4.6 for more detail). In this case, we observe very different force transient behavior that no longer includes complete failure, but instead results in gradual failure as extension becomes large (Fig. 4.4C). This behavior occurs because, while the weakest half-sarcomeres are still failing as before (see section 4.3.1.1), the weak parallel connections average out the behavior of sets of sarcomeres in series, preventing catastrophic failure and resulting in gradual decline (Fig. 4.4C).

In force-velocity simulations of weak connections, a similar averaging occurs. In this case, while fluctuations in the force-velocity curve begin around the same critical lengthening velocity, the oscillations in the individual force traces are averaged with those from all other sarcomeres in parallel, resulting in a smoother force-velocity curve (Fig. 4.4D).

Taken together, our results illustrate that the behavior of a system of sarcomeres in series and parallel is dependent on the elasticity of the parallel connections, with rigid elasticity resulting in catastrophic failure, and weak elasticity stabilizing this effect and causing gradual decline. These distinct regimes, contingent upon the elastic connections within the network, have implications for modeling lengthening muscle and for our greater understanding of contraction across scales.

4.4. Discussion

Given the necessity of eccentric contraction in human locomotion, and the potential for muscle strengthening with the repeated bout effect, it is crucial to develop theories to describe lengthening muscle in order to connect molecular mechanisms with larger-scale eccentric phenomena. With this work, we aim to take a step towards developing a theory of lengthening muscle. We begin with a minimal cross-bridge model, and build upon it as necessary to replicate behavior observed in experimental measurements. Our results suggest that a cross-bridge model must include the forcible detachment of myosin from actin at large extensions, and when muscle is in a regime where this is occurring, sarcomere instabilities will arise and dictate the overall dynamics. Together, these findings demonstrate the need for the characterization of forcible detachment of myosin, and highlight the opportunity to improve upon muscle models by explicitly modeling multi-sarcomere systems to capture emergent behavior in measurements of eccentric contraction.

4.4.1. Muscle models require accurate characterization of forcible detachment. By theoretically investigating the features of eccentric contraction, we have determined that a mathematical model of muscle must include forcible detachment of myosin to accurately capture the yielding behavior observed in experimental measurements of rapid muscle lengthening. Intuitively, the need for forcible detachment is reasonable, since any bond will eventually break given enough applied force. Additionally, various experimental studies have demonstrated that such a behavior occurs when large forces are applied to bound myosin molecules [e.g. Guo and Guilford, 2006, Nishizaka et al., 1995, Reconditi et al., 2004]. However, the kinetic details of this detachment are unknown.

Experimental studies exploring the bond that myosin forms with actin have established key molecular details that have advanced the way we model shortening muscle. In particular, experiments measuring the force-dependence of this bond, and the finding that resistive force on a molecule increases bond lifetime, allow theorists to accurately depict molecular kinetics of shortening and small amplitude lengthening. However, measuring this force-dependence under physiological conditions is challenging, and there are limited experimental results on this force-dependence for myosin stretched to large extensions. To measure force-dependence, experimentalists must detect

when a single myosin molecule binds to actin, apply a force of known magnitude to the bond that forms, and measure the lifetime of attachment. Under physiological conditions for skeletal muscle, this process is unattainable with a standard optical trap, since myosin is bound for $\sim$ 3ms and the resolution of the trap is $\sim$ 8ms. Thus, most measurements of myosin's force-dependence have been performed with cardiac and smooth muscle because of their slower kinetics [Veigel et al., 2003, Kad et al., 2007, Greenberg et al., 2014, Sung et al., 2015], and the ADP release rate of skeletal muscle has been presumed from these findings.

In addition to the challenge of simply measuring force-dependence, another challenge arises when we want to separate myosin's strongly-bound and rigor states. Experimentally, the lifetime of attachment can be increased by decreasing the ATP concentration, which slows the rate at which ATP binds and myosin detaches from actin. However, in doing so, the rate-limiting step of the cross-bridge cycle becomes the transition from the rigor state to an unbound state, resulting in most cross-bridges populating the rigor state. Decreasing ATP concentration is advantageous in that it can increase myosin's attachment time beyond the resolution of the optical trap, making force-dependent measurements more feasible. In fact, some experimental studies have investigated the forcible detachment of myosin in this way [Nishizaka et al., 1995]. However, these experiments ultimately measure the forcible detachment of myosin from a rigor state, not the forcible detachment of strongly-bound myosin, and therefore do not directly inform upon our unknown model parameters (Eq. 4.2).

Given the necessity of including the forcible detachment of myosin in ADP release rate, we must develop methods to fully characterize the details of myosin detachment. Working with slower cardiac or smooth muscle myosin, or implementing a combination of experimental and theoretical techniques, may make obtaining kinetic information on forcible detachment more feasible. Developing such methods would deepen our understanding of the biochemistry of the interaction between actin and myosin, allow us to more accurately model actomyosin kinetics, and would ultimately lead to models that capture lengthening behavior of muscle.

4.4.2. Non-uniformity observed during rapid lengthening in a multi-sarcomere model is stable. Non-uniformities in sarcomere lengthening and potentially associated instabilities have

led to a variety of hypotheses regarding the effects of sarcomere variation, including the concept of sarcomere popping. "Sarcomere popping" has been proposed to arise during lengthening regimes, during which variation in individual sarcomere lengths causes non-uniform lengthening. Stronger sarcomeres shorten, while weaker sarcomeres lengthen to extensions where there is no myofilament overlap, and thus they have "popped" [Morgan, 1990, 1994, Rassier and Herzog, 2004]. This instability in lengthening has been attributed to the negative slope of the descending limb of the force-length relationship, since any sarcomeres with lengths in this unstable region would continue to lengthen, eventually reaching a point of no filament overlap [Allinger et al., 1996, Morgan, 1990]. Such non-uniformities with stretch have been observed experimentally [e.g. Talbot and Morgan, 1996, Brown and Hill, 1991], and the sarcomere popping hypothesis has been used to explain muscle phenomena such as residual force enhancement [Morgan, 1990, 1994]. However, in contrast to these hypotheses, there is a significant amount of both experimental and theoretical evidence to suggest that muscle is potentially stable on the descending limb of the force-length relationship [Rassier and Herzog, 2004, Allinger et al., 1996]. In one such study, Rassier and Herzog [2004] actively stretched sarcomeres in series, and found that while sarcomeres did lengthen by non-uniform amounts, they remained at constant lengths, and therefore stable, under isometric conditions after stretch.

Our findings strengthen this idea of stable non-uniformities in lengthening. The concept of sarcomere popping hinges on the presence of instabilities in lengthening, and while we also see a form of failure, the instabilities we observe are distinct from a popping mechanism. While a popping hypothesis predicts large, non-uniform changes in length with passive elements eventually producing all force [Rassier and Herzog, 2004], our results show minimal changes in length that are a result of changes in force (Fig. 4.3D). We observe a stick-slip pattern of force production during which force is lost as cross-bridges in the weakest half-sarcomere detach, but can be regained as these cross-bridges rebind (Fig. 4.3D, top). During this cycle, the weakest half-sarcomere experiences small slips in length when failure occurs, and the other half-sarcomeres adjust by shortening (Fig. 4.3D, bottom). Additionally, unlike in a popping regime, in our model, failure is not permanent, and when stretch is stopped, force and length are appropriately recovered. Thus, while our findings do suggest non-uniformities among sarcomeres during lengthening, with the weakest half-sarcomere

dictating overall dynamics, the changes we observe are stable and temporary, providing further evidence of stable non-uniformities during muscle lengthening.

4.4.3. Emergent behavior in multi-sarcomere systems: Implications for modeling lengthening muscle. While theoretical modeling of muscle contraction has been a subject of study for many years, the majority of muscle models focus on shortening muscle or isometric contraction without consideration of eccentric measurements. Thus, the theory behind lengthening muscle is more limited, and because of the unique and unexplained behaviors of lengthening muscle, exactly how to develop such a theory is still unknown. Through investigation of single and multi-sarcomere models, we propose that explicitly modeling multi-sarcomere systems is necessary to capture lengthening muscle regimes, and results in emergent behavior dependent on the details of the connections among sarcomeres.

The suggestion of emergent behavior in multiple-sarcomere models is not new to muscle literature. While the majority of muscle models take a reductionist approach, modeling fiber-level dynamics with the behavior of a single half-sarcomere scaled upward [e.g. Walcott et al., 2012, Jarvis et al., 2018, Campbell, 2014, Duke, 1999, Geeves et al., 2011, Månsson, 2010], a collection of other models do consider multiple-sarcomere networks [e.g. Denoth et al., 2002, Telley and Denoth, 2007, Stoecker et al., 2009, Campbell, 2009]. In these models, simulations of multi-sarcomere systems result in complex dynamics that shed light on phenomena, such as sarcomere non-uniformities, that would not be possible to describe with single-sarcomere models. However, while these models do provide insight into emergent behavior of multi-sarcomere systems, many only consider sarcomeres in series and thus would not see additional emergent behavior from sarcomeres in parallel (as in [Stoecker et al., 2009, Denoth et al., 2002]). Additionally, these models generally lack key molecular details, including a lack of explicit formulation of cross-bridge kinetics (as in [Denoth et al., 2002]), or when such kinetics are incorporated, a lack of molecularly accurate rate constants (as in [Stoecker et al., 2009, Campbell, 2009, Tanner et al., 2007]). Further, the experimental measurements these models consider are limited. To the best of our knowledge, no multi-sarcomere model investigates a rapid-lengthening regime, and in particular, none explore the yielding behavior fundamental to lengthening measurements that we seek to model.

The findings from our modeling work enhance our understanding of emergent behavior in multi-sarcomere models beyond that of the current literature. First, we contribute the finding that the specific emergent behavior observed depends on the size of the matrix of sarcomeres and the elasticity of the connections in the network. When we preliminarily connect sarcomeres in series, we observe catastrophic failure that could not result from the dynamics of a single half-sarcomere alone. Then, extending our model to additionally include sarcomeres in parallel, distinct emergent behavior develops, and the results are dependent on the elasticity of the parallel connections. Rigid connections in parallel result in a system that displays sudden failure, similar to a material that is brittle, while weak parallel connections stabilize this effect, resulting in smoother and more gradual failure that is analogous to a ductile material. Our findings suggest a potential connection between the behavior of a network of sarcomeres during stretch and the properties of deformed materials.

Additionally, by using our models to specifically describe muscle measurements of force transients after rapid stretch and force for large lengthening velocities, we are able to explore emergent behavior that is particular to the regime of rapid-lengthening muscle. We can propose, for example, that the emergent behavior observed for sarcomeres in series only is insufficient to describe such a contractile regime, but that sarcomeres connected weakly in parallel may provide stability that is present in physiological muscle. Together, our findings highlight an opportunity within muscle literature to more precisely develop models of eccentric contraction, and to extend current theories to describe rapid-lengthening muscle.

4.5. Conclusion

Eccentric contraction results in a variety of unique and essential functions, ranging from human locomotion to potential mechanisms for rehabilitating and strengthening damaged muscle. Our findings indicate that in order to accurately model rapid lengthening muscle, theories must explicitly model multi-sarcomere systems and include forcible detachment of myosin, and that tuning the elasticity of the connections between sarcomeres results in unique emergent behavior. These results suggest potential connections between molecular mechanisms and cellular phenomenon of eccentric contraction. For example, lengthening a muscle fiber that is composed of many interfilamentary

links of different elasticities could result in inconsistent structural changes in the myofibril, like non-uniform lengthening of sarcomeres or Z-line streaming. Additionally, the vastly different behavior observed for sarcomeres connected stiffly or weakly, and in particular the potential for catastrophic failure, may have implications for genetic muscle diseases. The suggestion of potential mechanisms for these experimentally observed behaviors can inform upon future studies. Taken together, the results of our modeling work highlight important details in modeling lengthening muscle, and ultimately work towards a more comprehensive theory of contraction across scales.

4.6. Methods

To explore the mechanisms of muscle lengthening, we model the interaction between actin and myosin using a simple kinetic scheme and scale this behavior to the larger fiber level using a variety of mathematical tools. The mathematical methods we employ fall into two categories (described in detail below): 1) We simulate the interaction between actin and myosin using Monte Carlo methods, and by simulating the dynamics of a large ensemble of myosin molecules, the results are comparable to fiber-level measurements. 2) We use a system of integro-PDEs to scale the molecular interactions of actin and myosin to the fiber level. With each method, the final model results are directly comparable to experimental measurements, allowing for exploration into lengthening muscle.

4.6.1. Monte Carlo Simulations.

4.6.1.1. *Single Half-Sarcomere:* One way in which we simulate cross-bridge dynamics to explore muscle lengthening is through Monte Carlo simulations. To model the behavior of a single half-sarcomere, we simulate an ensemble of about ~ 350 myosin molecules using a modified Gillespie algorithm. Throughout time, we keep track of the state of each molecule, the extension of a molecule when bound, and each molecule's reaction time for transition to the next state of the cross-bridge cycle. The reaction time of each molecule is chosen by sampling from an appropriate distribution, dependent on the rate constant that dictates each molecule's rate of transition to the next state. At each iteration, the molecule with the smallest transition time iterates to the next cross-bridge state, time is increased by the appropriate transition time, and the overall force is saved.

Our method is a "modified" Gillespie algorithm because we must adjust for the force-dependence in the system. When myosin molecules are bound, they are bound with a particular extension and, given that they act as linear springs, experience a proportional force. Since ADP release is dependent on force, each molecule experiences a slightly variable ADP release rate given the current extensions. Thus, throughout time, we must save ADP release rate values for each molecule, and update each value whenever the overall force on the system changes. Simulating our modified Gillespie algorithm in this way, the final result is half-sarcomere force as a function of time, where the force produced by a single molecule is its extension times the stiffness of myosin, and total half-sarcomere force is the sum of the forces from all bound myosin, or

$$F_{\mathrm{HS}} = \sum_{i=1}^{N_{cb}} \kappa x_i$$

where κ is the stiffness of myosin, N_{cb} is the number of bound cross-bridges, and x_i is the extension of each bound molecule.

We can use Monte Carlo simulations of this form to replicate force transient measurements. To do so, we begin by simulating the actomyosin interaction from a given initial distribution. Once steady-state has been achieved, we apply the stretch by lengthening all bound cross-bridges at a specific point in time, and then continue to iterate the ensemble throughout time. The final simulated force trace is directly comparable to muscle fiber measurements for force transients after a rapid, small amplitude stretch.

4.6.1.2. *Multiple Half-Sarcomeres:* These Monte Carlo simulations become more complex when we explicitly simulate a multi-sarcomere system. To model this, we simulate the dynamics of multiple half-sarcomere units in series. We account for any slight non-uniformities among half-sarcomeres by including variation in the number of cross-bridges in each half-sarcomere. To do so, for each half-sarcomere we pick the number of cross-bridges from a normal distribution with mean of 350 and standard deviation of 30. Since the half-sarcomeres are in series, they must have equal forces at any point in time. In order to achieve this, the model must include an elastic element in parallel with each half-sarcomere. The necessity of a parallel elastic element comes from the constraint of force equality at steady-state. At steady-state, individual half-sarcomeres all have the

same distributions, however, because each half-sarcomere has a variable number of cross-bridges, the steady-state force produced by each half-sarcomere is slightly variable. In order to obtain equal forces, we must include a parallel elastic element to account for the slight differences between the half-sarcomeres at steady-state.

Thus, the model consists of half-sarcomere units (half-sarcomere plus parallel elastic element) in series. The force from each unit, which must be equal throughout time, is the sum of the force from the half-sarcomere and the force from the parallel spring. The system is additionally constrained by the fact that we are simulating an isometric experimental protocol, so the overall length of the fiber must be constant.

As in the single half-sarcomere case, throughout the simulation we keep track of the extension of any bound myosin and the transition times for all molecules. At each step in time, the molecule with the overall smallest transition time among molecules in all half-sarcomeres transitions to the next state. When any molecule binds or unbinds, the force in the corresponding half-sarcomere changes, and we must impose a force balance to ensure that the force is equal across all half-sarcomere units. This force balance is achieved by calculating the necessary shift to each unit, s_j, such that the total length change is zero, and the force per unit is equal. This gives,

$$\sum_{i=1}^{N_{cb}^1} \kappa(x_{i,1} - s_1) + \hat{\kappa}(L_1 - s_1) = \quad \dots \quad = \sum_{i=1}^{N_{cb}^m} \kappa(x_{i,m} - s_m) + \hat{\kappa}(L_m - s_m)$$

$$\text{with} \quad \sum_{i=1}^{m} s_i = 0$$

where m is the number of units in series, N_{cb}^j is the number of bound cross-bridges in the j-th half-sarcomere, $x_{i,j}$ is the extension of the i-th bound myosin in the j-th half-sarcomere, L_j is the length of the parallel elastic element in the j-th unit, and κ and $\hat{\kappa}$ are the stiffnesses of myosin and the parallel spring, respectively. Simulating the system in this way, the result of the Monte Carlo simulations is total fiber force as a function of time.

As in the single half-sarcomere case, we can adjust this multi-sarcomere simulation to simulate a force transient protocol. To do so, we begin with initial cross-bridge distributions for each half-sarcomere, and iterate the system throughout time. When steady-state is reached, we impose

a stretch to any bound cross-bridges. At the instance of stretch, we first calculate the individual stretch amplitudes that must be imposed to each half-sarcomere so that the force in each unit is equal and the overall length change is equal to the experimental stretch amplitude. Once stretch is imposed, we iterate through time as above, resulting in a final force transient including rapid stretch.

4.6.1.3. *Modeling with Monte Carlo Simulations:* While Monte Carlo simulations are an accurate way of describing the interactions between actin and myosin at a small scale, they are computationally inefficient for large ensembles of myosin. Thus, the usefulness of such simulations is limited when we are interested in simulating multiple half-sarcomeres in series, which requires very large ensembles of myosin molecules coupled together (i.e. ~ 350 molecules per half-sarcomere and $\sim 2-6$ half-sarcomeres in series). Thus, in addition to our MC simulations, we develop a system of partial differential equations (PDEs) to describe cross-bridge dynamics at larger scales (see section 4.6.2). Our Monte Carlo simulations are still useful, however, in that they can verify that our PDE solutions. While the PDE results are an approximation, the two simulation methods are comparable (Fig. 4.5).

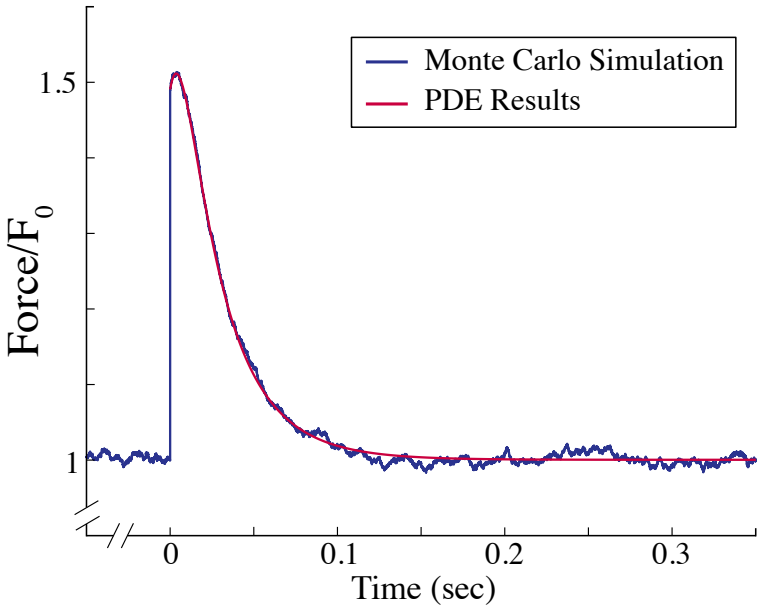

Figure 4.5. Monte Carlo simulations and PDE solutions are comparable. Simulation of three half-sarcomeres in series, stretch amplitude of $\Delta s = 6$ nm per half-sarcomere, and model including forcible detachment.

4.6.2. Differential Equations Model.

4.6.2.1. *Single Half-Sarcomere:* Another way in which we connect cross-bridge dynamics to fiber muscle function is through a system of integro-PDEs. For this method, we express the kinetic scheme using chemical kinetics, taking care to appropriately account for the force-dependence within the system (see Mathematical Framework for details). Note that under physiological conditions, ATP concentration is high enough that the ATP-dependent transition from a rigor state to an unbound state occurs very quickly (i.e. transition from state 3 to 4 in Fig. 4.1), and the rigor state is negligibly populated. Thus, since the experimental measurements we consider are performed for high [ATP], our four-state model can be approximated with a three-state model, in which the strongly-bound configuration transitions directly to an unbound state (i.e. state 2 transitions directly to state 4 with a transition rate of $k_D(x)$ in Fig. 4.1).

With this simplification, we use chemical kinetics to express our kinetic scheme as the following set of integro-PDEs:

$$\frac{dN_1}{dt} = k_h^+ N_4 - \left(k_h^- + \int_{-\infty}^{\infty} \kappa_a(x)dx \right) N_1$$

$$\frac{\partial \eta_2}{\partial t} + v\frac{\partial \eta_2}{\partial x} = \kappa_a(x)N_1 - k_D(x)\eta_2$$

(4.3)

$$\frac{dN_4}{dt} = k_h^- N_1 + \int_{-\infty}^{\infty} k_D(x)\eta_2 dx - k_h^+ N_4$$

$$1 = N_1 + N_2 + N_4$$

where $\eta_i(x,t)$ is the probability density function that myosin is strongly-bound in state i with extension x, N_i is the probability that myosin is in state i, $\kappa_a(x)$ and $k_D(x)$ are myosin's attachment and detachment rates, respectively, and k_h^+, k_h^- are transition rates between states defined in Fig. 4.1.

We can solve this system under various assumptions to compare the model to experimental measurements of force transients after rapid stretch and the force-velocity relationship. First, to

solve this system under conditions that are comparable to force transient measurements, we solve for isometric conditions. This means that $v = 0$, reducing the system to:

$$\frac{dN_1}{dt} = k_h^+(1 - N_2) - (k_h^+ + k_h^- + k_a)N_1$$

$$\frac{\partial \eta_2}{\partial t} = \kappa_a(x)N_1 - k_D(x)\eta_2$$

This simplified system can be solved numerically by implementing 4th-order Runge-Kutta to iterate through time, solving the system for all x at each t. In the force transient measurements, the fiber is activated and allowed to come to isometric steady-state before the stretch is instantaneously imposed. Thus, to accurately model this protocol, we first solve for steady-state distributions and then shift these by the given stretch amplitude, Δs. We use these stretched distributions as the initial condition to our simulation, and iterate through time using RK4.

The result is the distribution of strongly-bound cross-bridges, $\eta_2(x, t)$. Assuming that cross-bridges act as a linear spring with stiffness κ, we can use the distribution of strongly-bound (and thus force-producing) cross-bridges to calculate force per cross-bridge. Multiplying this value by the number of cross-bridges in the half-sarcomere, N, we obtain force as a function of time:

$$F(t) = N \int_{-\infty}^{\infty} \kappa \cdot \eta_2 \cdot (x + d)dx$$

This force as a function of time is then directly comparable to our force transient measurements from the instance of stretch onward.

Additionally, we can solve the system to generate a force-velocity relationship. Force-velocity measurements involve fibers that are not isometric (since $v \neq 0$) but are in steady-state. Thus, the system of equations (Eq. 4.3) simplifies to a single ODE in terms of η_2:

$$\frac{d\eta_2}{dx} = \frac{1}{v}\Big(\mathcal{C}\kappa_a(x)(1 - N_2) - k_D(x)\eta_2\Big) \tag{4.4}$$

where $\mathcal{C} = k_h^+/(k_h^+ + k_h^- + k_a)$. This can be solved using a standard ODE solver in Matlab with a root find to solve the integral constraint. Solving Eq. 4.4 for η_2 for a given velocity value allows us

to solve for force,

$$F(v) = N \int_{-\infty}^{\infty} \kappa \cdot \eta_2 \cdot (x + d) dx$$

Solving for force for a variety of imposed velocity values results in a force-velocity relationship that is comparable to experimental measurements.

4.6.2.2. *Multiple Half-Sarcomeres in Series:* To extend our differential equation model to explicitly model a multi-sarcomere system, we describe each half-sarcomere using the system of integro-PDEs derived from our kinetic scheme (Eq. 4.3), and couple these sets of integro-PDEs together based on force and length constraints (described below). Again, we are interested in simulating a force transient after stretch and the force-velocity relationship.

Beginning with force transients, this experimental protocol is performed under isometric conditions. In the single half-sarcomere case, this means that $v = 0$. In the multi-half-sarcomere case however, while the overall fiber velocity is zero, the individual half-sarcomere velocities are not necessarily zero. Simplifying the system of integro-PDEs (Eq. 4.3) without this assumption, each half-sarcomere is described by a system of the form:

$$\frac{dN_1}{dt} = k_h^+(1 - N_2) - (k_h^+ + k_h^- + k_a)N_1$$

(4.5)

$$\frac{\partial \eta_2}{\partial t} + v\frac{\partial \eta_2}{\partial x} = \kappa_a(x)N_1 - k_D(x)\eta_2$$

To solve each system of this form, we use the method of characteristics to reduce the PDEs to be a system of ODEs. This transformation occurs as follows. Let

$$\xi = x - u(t)$$

$$\frac{du}{dt} = v(t)$$

Then the system of integro-PDEs in Eq. 4.5 becomes,

$$\frac{dN_1}{dt} = k_h^+(1 - N_2) - (k_h^+ + k_h^- + k_a)N_1$$

$$\frac{\partial \eta_2}{\partial t} = \kappa_a(\xi + u(t))N_1 - k_D(\xi + u(t))\eta_2 \tag{4.6}$$

$$\frac{du}{dt} = v(t)$$

Since the half-sarcomeres are in series, they must have equal forces at any point in time. In order to achieve this, the model must include a parallel elastic element in series with each half-sarcomere (see section 4.6.1.2 for justification). Thus, the force produced by the ith unit (half-sarcomere plus parallel elastic element) is given by:

$$F_{tot}^i = F_{HS}^i + \hat{\kappa}\hat{u}^i = N_{cb}^i \int_{-\infty}^{\infty} \kappa \cdot \eta_2^i \cdot (\xi + u^i + d)d\xi + \hat{\kappa}\hat{u}^i \tag{4.7}$$

where N_{cb}^i is the number of cross-bridges in the ith half-sarcomere, κ is myosin's stiffness, $\hat{\kappa}$ is the stiffness of the parallel elastic element, and $\hat{u}^i$ is the current length of the ith spring. At any point in time, the overall length of the ith spring is $\hat{u}^i = L_0^i + u^i$ where L_0^i is the initial length of the ith spring and u^i is the value from the integro-PDEs.

Finally, the isometric conditions require that overall fiber velocity is zero, and thus total fiber length is constant throughout time. Putting all of this together, a system of three half-sarcomeres

in series (labeled a, b, c) are described by the following system of ODEs:

$$\begin{aligned}
\frac{dN_1^a}{dt} &= k_h^+(1-N_2^a) - (k_h^+ + k_h^- + k_a)N_1^a \\
\frac{\partial \eta_2^a}{\partial t} &= \kappa_a(\xi^a + u^a(t))N_1^a - k_D(\xi^a + u^a(t))\eta_2^a \\
\frac{du^a}{dt} &= v^a(t)
\end{aligned}$$

$$\begin{aligned}
\frac{dN_1^b}{dt} &= k_h^+(1-N_2^b) - (k_h^+ + k_h^- + k_a)N_1^b \\
\frac{\partial \eta_2^b}{\partial t} &= \kappa_a(\xi^b + u^b(t))N_1^b - k_D(\xi^b + u^b(t))\eta_2^b \\
\frac{du^b}{dt} &= v^b(t)
\end{aligned}$$

$$\begin{aligned}
\frac{dN_1^c}{dt} &= k_h^+(1-N_2^c) - (k_h^+ + k_h^- + k_a)N_1^c \\
\frac{\partial \eta_2^c}{\partial t} &= \kappa_a(\xi^c + u^c(t))N_1^c - k_D(\xi^c + u^c(t))\eta_2^c \\
\frac{du^c}{dt} &= v^c(t)
\end{aligned}$$

$$\text{Force constraint:} \quad F_{tot}^a = F_{tot}^b = F_{tot}^c$$

$$\text{Length constraint:} \quad 0 = v^a(t) + v^b(t) + v^c(t)$$

To solve this system, we implement a hand-written 4th order Runge-Kutta method. At the start of each time step, a root find must be solved to determine the individual velocity values for each half-sarcomere that satisfy the constraints of equal force and constant fiber length. Once satisfied, an RK4 step is iterated. The initial condition for our simulations is the system at the instance of stretch. To calculate this, we solve the system explicitly in isometric steady-state, and then we calculate the necessary lengths to shift each half-sarcomere unit so that the overall change in fiber length is equal to the stretch amplitude, and the forces between half-sarcomere units are

equal. With this initial condition, we can iterate throughout time to result in a force transient trace that is directly comparable to measurements of fiber force after rapid stretch.

In addition to force transient measurements, we use this basic multi-sarcomere framework to get a model prediction for the force-velocity relationship. In this case, we begin with an initial condition of isometric steady-state for each half-sarcomere. We then impose a constant velocity stretch by defining overall fiber velocity to be a particular value. Again, the individual half-sarcomere velocities vary, but the overall velocity is fixed (now at a non-zero value). We solve the system using the method of characteristics and RK4, with the constraint that half-sarcomere forces are equal and velocity is fixed. The simulation result is fiber force throughout time given an imposed constant velocity. After ≈ 0.08 seconds, the cross-bridges have reached steady-state, and the force at this time is the value that corresponds to the fixed velocity value. Repeating for many velocities, we get a force-velocity relationship for our multi-sarcomere integro-PDE model.

4.6.3. Multiple Half-Sarcomeres in Series and Parallel: In addition to connecting half-sarcomeres in series, we are interested in the dynamics of a system where half-sarcomeres are also connected in parallel. With a network of sarcomeres in series and parallel, we can use the mathematical techniques above to compare the model results to both force transient and force-velocity measurements. To add sarcomeres in parallel, we must define the elasticity of the parallel connections, and to extensively explore this, we consider two extreme regimes for the vertical connections: 1) rigid vertical connections and 2) weak vertical connections.

4.6.3.1. *Parallel Sarcomeres Connected with Rigid Stiffness:* To study a system of sarcomeres that has vertical connections that are very rigid, we simulate our integro-PDE system for multiple half-sarcomeres in series many times, each time increasing the amount of cross-bridges in each half-sarcomere. Specifically, at the start of each simulation, we pick the number of cross-bridges for each half-sarcomere in series from a normal distribution with a mean of 350 and standard deviation of 30. With each subsequent run, we increase the amount of cross-bridge values we pull from this distribution and sum the values. For example, in the first simulation, the number of cross-bridges in each half-sarcomere is defined by picking a value from the distribution. In the second run, the

number of cross-bridges in each half-sarcomere is defined as the sum of two values picked from the distribution, and so on. As we increase the number of values picked from the distribution that defines the cross-bridges in each half-sarcomere, by the central limit theorem, the standard deviation will scale with $\sqrt{N}$, where N is the number in parallel. Thus, the variability gets smaller and the solutions become more robust.

4.6.3.2. *Parallel Sarcomeres Connected with Weak Stiffness:* To simulate a system of sarcomeres that has very weak or no vertical connections, we repeatedly solve our integro-PDE system for a fixed number of half-sarcomeres in series, and average the results of these simulations.

4.7. Acknowledgements

This work was supported, in part, by the Dissertation Year Fellowship awarded to Katelyn Jarvis by the University of California, Davis.

APPENDIX A

Chapter 2 Appendix (Fatigue Paper)

Supplementary Information for

"Acidosis affects muscle contraction by slowing the rates myosin attaches to and detaches from actin"

Published on October 31, 2018 in the *Journal of Muscle Research and Cell Motility*

Joint work with:

Mike Woodward

Department of Kinesiology, University of Massachusetts, Amherst, Amherst, MA

Edward P. Debold

Department of Kinesiology, University of Massachusetts, Amherst, Amherst, MA

Sam Walcott

Department of Mathematics, University of California, Davis, Davis, CA

A.1. Mathematical Implementation of the Model

To model myosin's interaction with actin in the presence and absence of phosphate (P_i), we use the branched pathway model of Debold et al. [2013] (see Fig. 2.5A, and Fig. A.1). Here, we discuss how to write this kinetic scheme as a set of integro-partial differential equations (integro-PDEs), how to solve them under simplifying conditions, and how these results can help us understand experimental measurements at the level of muscle fibers.

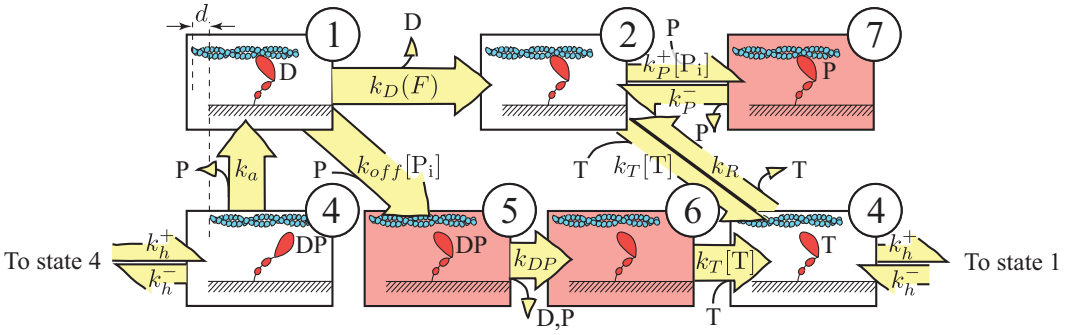

Figure A.1. The branched pathway model. This figure is identical to Fig. 2.5A of the main text, except for the numbering of states. In this supplement, we use this numbering convention.

A.1.1. Derivation of integro-PDEs. To express this model mathematically, we must keep track of the force on myosin since at least one of the rate constants in Fig. A.1 depends on force. Naturally, a myosin molecule in a state unbound from actin (states 3, 4, 5, and 6) experiences no force, and therefore the probability of being in one of these states is simply a function of time, $N_i(t)$ (where $i = 3, 4, 5, 6$). However, when myosin molecules are bound to actin, they are bound with a particular extension, which determines the force on the molecule. Thus, for bound states (states 1, 2, and 7), we must consider the probability of being in that state with a particular extension, x. For continuous random variables, the probability that the random variable takes on any particular value is zero. The realization of the random variable is instead defined in terms of a particular interval in which the random variable might fall, and calculated as the integral of the probability density function of the random variable over the interval. Similarly, the probability that myosin binds with a particular extension x is 0, but the probability that myosin binds somewhere between x and $x + \Delta x$ on the actin filament is given by $\int_x^{x+\Delta x} \eta_i(s,t)ds$ (where $i = 1, 2, 7$). Thus, we define

this probability density of a myosin molecule being bound with an extension x as $\eta_i(x,t)$, and the probability of being in this bound state is then $N_i(t) = \int_{-\infty}^{\infty} \eta_i(x,t)dx$.

We must also consider the force dependence in the transition rates between states. In particular, ADP release, and the transition from state 1 to state 2, is dependent on force, and therefore this rate is a function of molecular extension, $k_D(x)$. Additionally, we must consider the rate of transition from an unbound to bound state as a rate density, because this transition is dependent on the particular extension, x, with which the myosin molecule binds. Thus, $\kappa_a(x)$ is the rate density of this transition, and the overall weak-to-strong binding rate is $k_a = \int_{-\infty}^{\infty} \kappa_a(x)dx$. Similarly, $\kappa_R(x)$ is the rate density of rebinding to the rigor state with a particular extension x, and $k_R = \int_{-\infty}^{\infty} \kappa_R(x)dx$ is the overall rigor rebinding rate.

Thus, given that $N_i(t)$ and $\eta_i(x,t)$ are probabilities and probability densities respectively, and k_i and $\kappa_i(x)$ are rate constants and rate densities respectively, our model is governed by the following system of coupled integro-PDEs:

$$
\begin{aligned}
\frac{\partial \eta_1}{\partial t} + v\frac{\partial \eta_1}{\partial x} &= \kappa_a(x)N_4 - \Big(k_{off}[\mathrm{P_i}] + k_D(x)\Big)\eta_1 \\
\frac{\partial \eta_2}{\partial t} + v\frac{\partial \eta_2}{\partial x} &= k_D(x)\eta_1 + \kappa_R(x)N_3 + k_P^-\eta_7 - \Big(k_P^+[\mathrm{P_i}] + k_T[T]\Big)\eta_2 \\
\frac{dN_3}{dt} &= \int_{-\infty}^{\infty} k_T[T]\eta_2(x)dx + k_T[T]N_6 + k_h^- N_4 - \Big(\int_{-\infty}^{\infty} \kappa_R(x)dx + k_h^+\Big)N_3 \\
\frac{dN_4}{dt} &= k_h^+ N_3 - \Big(\int_{-\infty}^{\infty} \kappa_a(x)dx + k_h^-\Big)N_4 \\
\frac{dN_5}{dt} &= \int_{-\infty}^{\infty} k_{off}[\mathrm{P_i}]\eta_1(x)dx - k_{DP}N_5 \\
\frac{dN_6}{dt} &= k_{DP}N_5 - k_T[T]N_6 \\
\frac{\partial \eta_7}{\partial t} + v\frac{\partial \eta_7}{dx} &= k_P^+[\mathrm{P_i}]\eta_2 - k_P^-\eta_7
\end{aligned}
\tag{A.1}
$$

subject to the constraint that mass is conserved:

$$
\int_{-\infty}^{\infty} \eta_1(x,t)dx + \int_{-\infty}^{\infty} \eta_2(x,t)dx + N_3(t) + N_4(t) + N_5(t) + N_6(t) + \int_{-\infty}^{\infty} \eta_7(x,t)dx = 1 \tag{A.2}
$$

ADP release rate is force dependent, well-fit by Bell's approximation [Bell, 1978, Veigel et al., 2003, Kad et al., 2007], and can be expressed as,

$$k_D(x) = k_D^0 \exp\left(- \frac{\kappa(x+d)\delta}{k_B T} \right) \tag{A.3}$$

where we have assumed a linear force extension relationship ($F = -\kappa(x+d)$) with $\kappa = 0.3$ pN/nm is the stiffness of myosin (not to be confused with a rate density), k_D^0 is the reaction rate in the absence of force, $k_B T$ is Boltzmann's constant times temperature, d is myosin's step size, and $\delta = 1.86$ nm (see Table 2.2).

Additionally we define the rate density of the transition from weak to strong binding as,

$$\kappa_a(x) = k_a \sqrt{\frac{\kappa}{2\pi k_B T}} \exp\left(- \frac{\kappa x^2}{2 k_B T} \right) \tag{A.4}$$

and the rate density of rigor rebinding as,

$$\kappa_R(x) = k_R \sqrt{\frac{\kappa}{2\pi k_B T}} \exp\left(- \frac{\kappa x^2}{2 k_B T} \right) \tag{A.5}$$

which follow from assuming that attachment rate varies exponentially with the energy required to achieve a particular extension (see Walcott et al. [2012] for more details of this assumption).

A.1.2. Steady-State Solution. Solving the system of integro-PDEs in steady-state reduces the system to a set of coupled integro ordinary differential equations (integro-ODEs) plus a probability constraint:

$$\begin{aligned}
v\frac{d\eta_1}{dx} &= \kappa_a(x) N_4 - \big(k_{off}[\mathrm{P_i}] + k_D(x)\big)\eta_1 \\
v\frac{d\eta_2}{dx} &= k_D(x)\eta_1 + k_P^- \eta_7 - \big(k_P^+[\mathrm{P_i}] + k_T[T]\big)\eta_2 + k_T[T] N_2 + k_{off}[\mathrm{P_i}] N_1 - k_a N_4 \\
v\frac{d\eta_7}{dx} &= k_P^+[\mathrm{P_i}]\eta_2 - k_P^- \eta_7 \\
1 &= \left(1 + \frac{k_{off}[\mathrm{P_i}]}{k_{DP}} + \frac{k_{off}[\mathrm{P_i}]}{k_T T}\right) N_1 + N_2 + N_7 + \frac{k_h^+ + k_a + k_h^-}{k_h^+} N_4
\end{aligned} \tag{A.6}$$

where

$$N_i = \int_{-\infty}^{\infty} \eta_i(x) dx, \quad \text{for } i = 1, 2, 7$$

To numerically solve this, for a given velocity value, v, we perform a numerical root find (using Matlab's `fsolve` function) to find the values of N_1, N_2, and N_7. With the best values for these integrals, we then numerically solve the system of ODEs (using Matlab's `ode15s` function), and we can calculate the resulting force, by numerically approximating the following integrals

$$F = \int_{-\infty}^{\infty} \kappa(x+d)\eta_1(x)dx + \int_{-\infty}^{\infty} \kappa(x+d)\eta_2(x)dx + \int_{-\infty}^{\infty} \kappa(x+d)\eta_7(x)dx$$

Repeating this process for various velocity values gives a force-velocity relationship (Fig. 2.6B, dashed lines).

A.1.3. Isometric Force. At high ATP concentrations, we can analytically solve the system of equations for isometric force. When there is a sufficient amount of ATP in solution, the transition from the rigor/AM state (state 2 in Fig. A.1) to the A+MT state (state 3) is so fast that the force resulting from the rigor state is negligible. Therefore we can simplify the system by having the AMD state (state 1) transition directly to the A+MT state (state 3) at a rate of $k_D(x)$. Similarly, the MDP (state 5) transitions directly to the A+MT state (state 3) at a rate of k_{DP}. With this simplification, our system becomes a set of 4 integro-PDEs plus a probability constraint.

$$\begin{aligned}
\frac{\partial \eta_1}{\partial t} + v\frac{\partial \eta_1}{\partial x} &= \kappa_a(x)N_4 - (k_{off}[\mathrm{P_i}] + k_D(x))\eta_1 \\
\frac{dN_3}{dt} &= \int_{-\infty}^{\infty} k_D(x)\eta_1(x)dx + k_{DP}N_5 + k_h^- N_4 - k_h^+ N_3 \\
\frac{dN_4}{dt} &= k_h^+ N_3 - \left(\int_{-\infty}^{\infty} \kappa_a(x)dx + k_h^-\right)N_4 \\
\frac{dN_5}{dt} &= \int_{-\infty}^{\infty} k_{off}[\mathrm{P_i}]\eta_1(x)dx - k_{DP}N_5 \\
1 &= \int_{-\infty}^{\infty} \eta_1(x)dx + N_3 + N_4 + N_5
\end{aligned} \tag{A.7}$$

Solving for steady-state and isometric force ($v = 0$), the system reduces to one integro-algebraic equation, for η_1 in terms of $N_1 = \int_{-\infty}^{\infty} \eta_1(x)dx$. Integrating both sides, we obtain an expression for N_1, which then gives an analytical expression for η_1:

$$\eta_1(x) = \frac{\kappa_a(x)c(1-bN_1)}{k_{off}[\mathrm{P_i}] + k_D(x)} \text{ , and } N_1 = \frac{cI}{1+cbI}$$

where

$$I = \int_{-\infty}^{\infty} \frac{\kappa_a(x)}{k_{off}[\mathrm{P_i}] + k_D(x)} dx \ , \ c = \frac{k_h^+}{k_a + k_h^- + k_h^+} \ , \text{ and } b = 1 + \frac{k_{off}[\mathrm{P_i}]}{k_{DP}}$$

With this, we get the following expression for force,

$$\begin{aligned} F &= \int_{-\infty}^{\infty} \eta_1(x)\kappa(x+d)dx \\ &= \int_{-\infty}^{\infty} \frac{\kappa_a(x)c(1-bN_1)}{k_{off}[\mathrm{P_i}] + k_D(x)} \kappa(x+d)dx \\ &= \kappa c(1-bN_1) \int_{-\infty}^{\infty} \frac{\kappa_a(x)}{k_{off}[\mathrm{P_i}] + k_D(x)} (x+d)dx \end{aligned}$$

In the absence of $\mathrm{P_i}$, this expression is simplified (since $k_{off}[\mathrm{P_i}] = 0$), and becomes,

$$F = \kappa c(1-N_1) \int_{-\infty}^{\infty} \frac{\kappa_a(x)}{k_D(x)} (x+d)dx \tag{A.8}$$

With this expression, we can make a simple comparison between the forces achieved at neutral and low pH values. Using Eq. A.8, at pH 7.4, force is calculated as,

$$F_{7.4} = \kappa c(1-N_1) \int_{-\infty}^{\infty} \frac{\kappa_a(x)}{k_D(x)} (x+d)dx$$

with $N_1 = cI/(1+cI)$, $c = k_h^+/(k_a^{7.4} + k_h^- + k_h^+)$, and I is expressed above.

Our findings suggest (see parameter justification below) that as pH is decreased, both attachment rate, $\kappa_a(x)$, and ADP release rate, $k_D(x)$, are decreased. Assuming that attachment rate is scaled by ψ ($\kappa_a^{6.5}(x) = \psi\kappa_a^{7.4}(x)$), and ADP release rate is scaled by ϕ ($k_D^{6.5}(x) = \phi k_D^{7.4}(x)$), force at pH 6.5 is calculated as,

$$F_{6.5} = \frac{\kappa\psi\tilde{c}}{\phi}(1-\tilde{N_1}) \int_{-\infty}^{\infty} \frac{\kappa_a(x)}{k_D(x)} (x+d)dx \tag{A.9}$$

where $\tilde{N_1} = (\tilde{c}\psi I/\phi)/(1+\tilde{c}\psi I/\phi)$, $\tilde{c} = k_h^+/(k_a^{6.5} + k_h^- + k_h^+)$, and I is expressed above.

Comparing these two results, we find that the ratio of the forces is equal to the ratio of the duty ratios, since

$$\begin{aligned}\frac{F_{6.5}}{F_{7.4}} &= \frac{\frac{\kappa\tilde{c}\psi}{\phi}(1-\tilde{N}_1)}{\kappa c(1-N_1)} \\ &= \frac{\tilde{N}_1}{N_1}\end{aligned}$$

or expressing this ratio in terms of the changing parameters,

$$\frac{F_{6.5}}{F_{7.4}} = \frac{\tilde{c}\psi + c\tilde{c}\psi I}{c\phi + c\tilde{c}\psi I} = \frac{1+cI}{\alpha + cI} \tag{A.10}$$

where, defining $K = (k_h^- + k_h^+)/k_a^{7.4}$, the parameter

$$\alpha = \frac{\phi}{\psi}\frac{c}{\tilde{c}} = \frac{\phi}{\psi}\frac{\psi k_a^{7.4} + k_h^- + k_h^+}{k_a^{7.4} + k_h^- + k_h^+} = \frac{\phi}{\psi}\frac{\psi + K}{1+K}$$

Note that if $\alpha < 1$, then a drop in pH causes an increase in isometric force; if $\alpha > 1$, then a drop in pH causes a decrease in isometric force; and if $\alpha = 1$, then a drop in pH causes no change in isometric force. Any of these results is possible for $0 < \phi, \psi < 1$, depending on their values (see Fig. A.2).

A.1.4. Unloaded Shortening Velocity. We begin this section with an asymptotic approximation for unloaded shortening velocity. This result is similar to the result of Walcott et al. 2012, but is a little more mathematically precise (here we use matched asymptotics instead of a delta function approximation of $\kappa_a(x)$), and we non-dimensionalize with a different length scale (v/k_D^0, as opposed to d). We end the section by showing that unloaded shortening velocity scales linearly with ϕ (which is defined by $k_D^{6.5}(x) = \phi k_D^{7.4}(x)$).

A.1.4.1. *Asymptotic approximation of unloaded shortening.* To find an analytical approximation for unloaded shortening velocity, we begin with the assumption of high ATP, resulting in the simplified system of 4 integro-PDEs in Eq. A.7. Solving in steady-state, this reduces to one integro-ODE,

$$v\frac{d\eta_1}{dx} = \kappa_a(x)c\left[1 - \left(1 + \frac{k_{off}[\mathrm{P_i}]}{k_{DP}}\right)N_1\right] - \big(k_{off}[\mathrm{P_i}] + k_D(x)\big)\eta_1$$

where $N_1 = \int_{-\infty}^{\infty} \eta_1(x)dx$, and $k_D(x)$ and $\kappa_a(x)$ are expressed in Eq. A.3 and A.4 respectively.

It is convenient to introduce the following non-dimensional parameters,

$$\overline{X} = \frac{xk_D^0}{v},\ \epsilon = \frac{k_D^0}{v}\sqrt{\frac{k_BT}{\kappa}},\ \beta = \frac{\delta\kappa v}{k_BTk_D^0},\ \gamma = \frac{dk_D^0}{v},\ \text{and}\ \alpha = \frac{ck_a}{k_D^0\sqrt{2\pi}}$$

where $c = (k_h^+)/(k_a + k_h^- + k_h^+)$. Then a non-dimensionalized version of the system is,

(A.11)
$$\frac{d\tilde{\eta}}{d\overline{X}} = \frac{\alpha}{\epsilon}\exp\left\{\left(-\frac{1}{2}\left(\frac{\overline{X}}{\epsilon}\right)^2\right)\right\}\left[1-\left(1+\frac{k_{off}[\mathrm{P_i}]}{k_{DP}}\right)N\right] - \left[\frac{k_{off}[\mathrm{P_i}]}{k_D^0} + \exp\big\{\big(-\beta(\overline{X}+\gamma)\big)\big\}\right]\tilde{\eta}$$

where $\tilde{\eta} = \eta v/k_D^0$ and $N = \int_{-\infty}^{\infty}\tilde{\eta}d\overline{X}$.

Using a matched asymptotic expansion, we can construct an approximate solution in the following way. Away from 0, the first term in Eq. A.11 will be $\mathcal{O}(\epsilon)$. Therefore, for the solution away from zero, which we denote as the outer solution, we can neglect the first term in the Eq. A.11. Integrating and solving for this outer solution, we get the result

(A.12)
$$\eta_{\text{out}}\big(\overline{X}\big) = \eta_{\text{out}}(0)\exp\left(-\frac{k_{off}[\mathrm{P_i}]}{k_D^0}\overline{X} + \frac{e^{-\beta\gamma}}{\beta}\big(e^{-\beta\overline{X}}-1\big)\right)$$

To solve for the solution of Eq. A.11 near 0, we define a layer coordinate, and re-scale the problem as follows. Note that, for large velocity values (as is the case for unloaded shortening velocity), the non-dimensional parameter ϵ is small (for our parameters, we estimate $\epsilon \approx 0.15$). Letting $\widehat{X} = \overline{X}/\epsilon$, Eq. A.11 becomes,

(A.13)
$$\frac{d\widehat{\eta}}{d\widehat{X}} = \alpha\exp\left(-\frac{1}{2}\widehat{X}^2\right)\left[1-\left(1+\frac{k_{off}[\mathrm{P_i}]}{k_{DP}}\right)N\right] - \epsilon\left[\frac{k_{off}[\mathrm{P_i}]}{k_D^0} + \exp\big(-\beta(\epsilon\widehat{X}+\gamma)\big)\right]\widehat{\eta}$$

For the case of the solution near 0, which we denote as the inner solution, we can neglect higher order terms, and therefore we only need to consider the first term in Eq. A.13, since the second term is now $\mathcal{O}(\epsilon)$. Integrating and solving this, we get,

(A.14)
$$\widehat{\eta}_{\text{in}}\big(\widehat{X}\big) = \widehat{\eta}_{\text{in}}(0) + \alpha\left[1-\left(1+\frac{k_{off}[\mathrm{P_i}]}{k_{DP}}\right)N\right]\sqrt{\frac{\pi}{2}}\mathrm{erf}\left(\frac{\widehat{X}}{\sqrt{2}}\right)$$

Appropriately matching these solutions, we get a composite solution of,

(A.15)
$$\eta_{\text{comp}} = \begin{cases} \tilde{\alpha}(1-bN)\left[\text{erf}\left(\frac{\overline{X}}{\sqrt{2}\epsilon}\right) - 1 + 2\exp\left(-\frac{k_{off}[\text{P}_\text{i}]}{k_D^0}\overline{X} + \frac{e^{-\beta\gamma}}{\beta}\left(e^{-\beta\overline{X}}-1\right)\right)\right] & : \quad \overline{X} > 0 \\ \tilde{\alpha}(1-bN)\left[\text{erf}\left(\frac{\overline{X}}{\sqrt{2}\epsilon}\right) + 1\right] & : \quad \overline{X} < 0 \end{cases}$$

where $\tilde{\alpha} = \alpha\sqrt{\pi/2}$. This result is still in terms of $N = \int_{-\infty}^{\infty}\tilde{\eta}(\overline{X})d\overline{X}$. To solve for N, we approximate the solution to $\tilde{\eta}$ by neglecting the inner solution, since it is only valid within ϵ of zero, and is consequently of order ϵ. Therefore, we approximate N as,

$$\begin{aligned} N &= \int_{-\infty}^{\infty}\tilde{\eta}(\overline{X})d\overline{X} \\ &= \int_0^{\infty} 2\tilde{\alpha}(1-bN)\exp\left(-\frac{k_{off}[\text{P}_\text{i}]}{k_D^0}\overline{X} + \frac{e^{-\beta\gamma}}{\beta}\left(e^{-\beta\overline{X}}-1\right)\right)d\overline{X} + \mathcal{O}(\epsilon) \end{aligned} \tag{A.16}$$

In the absence of P_i, we can analytically solve this integral using the exponential integral function, $E_1(x) = \int_1^{\infty}\left(\exp(-xt)/t\right)dt$, to get (neglecting $\mathcal{O}(\epsilon)$ terms)

$$N \sim \frac{\frac{2\tilde{\alpha}}{\beta}\left[e^{\frac{-e^{-\beta\gamma}}{\beta}}E_1\left(\frac{e^{-\beta\gamma}}{\beta}\right)\right]}{-1 + \frac{2\tilde{\alpha}b}{\beta}\left[e^{\frac{-e^{-\beta\gamma}}{\beta}}E_1\left(\frac{e^{-\beta\gamma}}{\beta}\right)\right]}$$

Substituting this expression into the composite solution in Eq. A.15 gives a semi-analytical expression for the solution.

A.1.4.2. *Unloaded shortening rate scales with ϕ.* With this result, we are particularly interested in the unloaded shortening velocity of the system, where the force is zero, i.e. we find v such that,

$$0 = \int_{-\infty}^{\infty}\eta_{comp}(x)\kappa(x+d)dx \tag{A.17}$$

This equation can be simplified and rewritten in dimensional form, given $\text{P}_\text{i} = 0$, and implementing the effect of pH by scaling attachment and detachment rates by ψ and ϕ, respectively, ($\kappa_a^{6.5}(x) = \psi\kappa_a^{7.4}(x)$, $k_D^{6.5}(x) = \phi k_D^{7.4}(x)$):

$$0 \sim \int_0^{\infty}\left[\exp\left(\left(\frac{\phi}{v}\right)\frac{k_BTk_D^0e^{-\frac{\kappa d\delta}{k_BT}}}{\kappa\delta}\left(e^{-\frac{\kappa\delta x}{k_BT}}-1\right)\right)\right](x+d)dx \tag{A.18}$$

Eq. A.18 gives the result that unloaded shortening speed is proportional to the unloaded ADP release rate. In particular, suppose that the solution of Eq. A.18 when $\phi = 1$ is defined as V_0^1. Then, since ϕ and v appear only as a ratio, $v = \phi V_0^1$ solves Eq. A.18.

A.1.5. Effect of Parameters on Fiber Level Measurements. We have shown that isometric force depends both on attachment rate and detachment rate. Specifically, isometric force can increase or decrease depending on whether ϕ is greater than or less than $\frac{1+K}{1+(K/\psi)}$. Conversely, unloaded shortening rate is proportional to ϕ. Thus, by tuning both ϕ and ψ, isometric force and unloaded shortening rate can be adjusted independently.

Muscle fiber experiments suggest that a drop in pH causes a drop in isometric force and unloaded shortening rate at low temperature, but a much smaller reduction in isometric force at physiological temperature [e.g. Knuth et al., 2006]. Our model, and the analysis above, suggests that this result can be explained by differential temperature sensitivity between attachment scaling (ψ) and detachment scaling (ϕ). In particular, if a drop in pH causes a 20-30% drop in unloaded shortening rate regardless of temperature, then the model predicts a 20-30% drop in ADP release rate. However, if that drop in pH decreases attachment more at low temperature (65-70%) than at high temperature (35-55%), then isometric force will drop significantly at low temperature (40-50%) but only modestly (10-20%) at high temperature, in agreement with fiber measurements (Fig. A.2).

A.2. Simulation Details

Our approach for simulating mini-ensemble experiments in the laser trap are detailed in section 2.3 of the main text. To generate the plots in Fig. 2.5 of the main text, in addition to simulating mini-ensemble experiments, we also simulated single molecule and motility experiments. Here, we describe how we modified the approach outlined in section 2.3 of the main text to describe these experiments.

A.2.1. Mini-Ensemble Simulation. The approach is identical to section 2.3 of the main text, except we use the kinetic scheme for the branched pathway model (Fig. 2.5A of the main text).

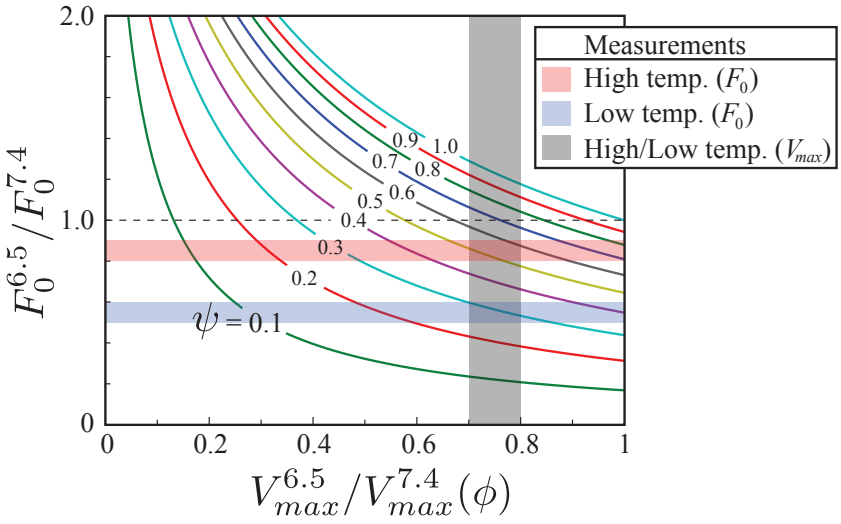

Figure A.2. pH-dependent changes in isometric force (F_0) and unloaded shortening speed (V_{max}) can be adjusted independently in the model. A drop in pH scales ADP release rate by ϕ, which then scales V_{max} (Eq. A.18). A drop in pH scales the weak to strong binding transition (k_a) by ψ, which leads to the contour lines (Eq. A.10). With different choices of ϕ and ψ, experimental measurements on skinned muscle fibers (Knuth et al. [2006], shaded regions) can be replicated. The set of ϕ, ψ values representing no change in F_0 is shown as a dashed line. Note that we use V_{max} to refer to generic unloaded shortening speed, and not simply the unloaded shortening speed estimated with a Hill fit. Also note that Knuth et al. [2006] reduced pH from 7.0 to 6.2.

A.2.2. Single Molecule Laser Trap. The approach is identical to section 2.3 of the main text, except we use the kinetic scheme for the branched pathway model (Fig. 2.5A of the main text), and only one molecule. To compare our simulations to experimental measurements, we analyzed our simulated data using mean-variance analysis outlined in Patlak [1993], Guilford et al. [1997]. Event lifetime (used in section A.4.4 of this supplement) was determined with window widths of 10, 20, 40, 80, 160, 320, 640, 1280, and 2560 ms. A representative example is shown in Fig. A.3.

A.2.3. Motility Assay. The approach is identical to section 2.3 of the main text, except we use the kinetic scheme for the branched pathway model (Fig. 2.5A of the main text), and 50 independent myosin heads. The assumption that mechanical equilibrium occurs immediately requires an equilibration of forces on myosin molecules, since no force is being applied to the actin filament. In this assay, the effective actin concentration is assumed saturating, so that all myosin bind at the same rate of k_a.

For a given ATP concentration, the result of this simulation is the position of the actin filament as a function of time. A linear curve is fit to this result, and the resulting slope is the speed of the

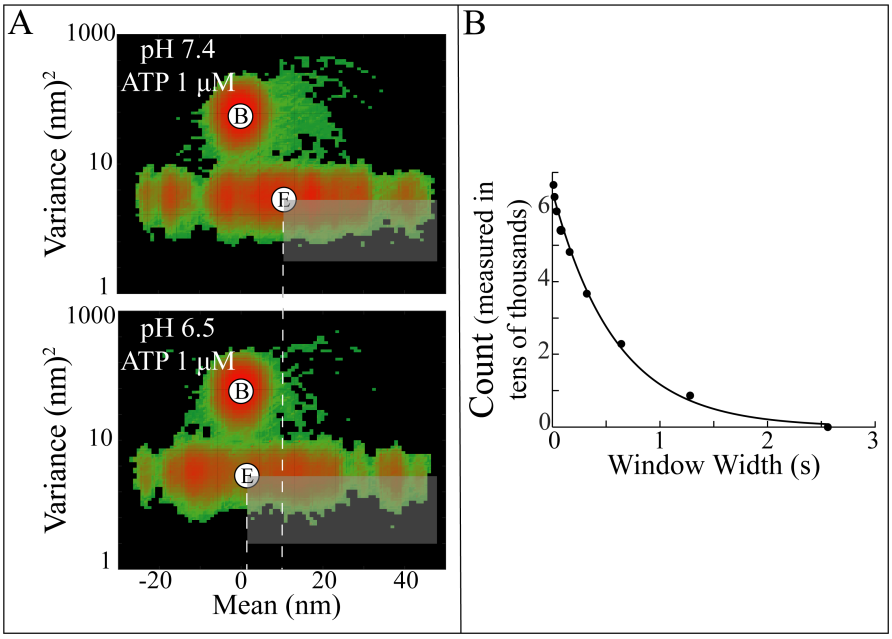

Figure A.3. Mean variance analysis, applied to simulated single molecule data. **A)** 2D histograms of mean and variance from simulated single molecule data under Control (pH 7.4) and Acidic (pH 6.5) conditions at low ATP ($T = 1\mu$M). The center of the distributions for the baseline (B) and event (E) populations are labeled, and a clear pH-dependent reduction in the mean position of the event population is observed [c.f. Debold et al., 2008]. A region of this distribution that contains only the event population is then selected for lifetime measurements (shaded region at lower right). Lifetime estimate from fits of number of data points as a function of window width.

actin filament for a given [ATP]. The simulation is repeated for various ATP concentrations, and the result is actin velocity as a function of [ATP].

A.2.4. Fiber Level. The approach is identical to section 2.3 of the main text, except we use the kinetic scheme for the branched pathway model (Fig. 2.5A of the main text), and 300 independent myosin heads [e.g. Longyear et al., 2017]. We use an ATP concentration of 3 mM. Additionally, in the process of equilibrating forces, instead of summing forces to be 0 to reach mechanical equilibrium, as we do in our motility simulations (section A.2.3), we now sum to various force values, to simulate a constant force being applied to the system. The result of the motility simulation is actin speed, so by repeating this for various force values, the result is a relationship between force and velocity.

These simulations provide relationships between force-velocity and force-power, the same results as the steady-state solution of the integro-PDE model (section A.1.2). However, it is possible (see

section A.5) that details of the experimental protocol will introduce deviations from the integro-PDE simulations. Thus, the purpose of these simulations is to more closely follow a particular experimental protocol in order to generate force-velocity curves. Following Pate et al. [1995], we only simulate force-velocity data for intermediate force values, and then fit these values with a Hill curve to generate the force-velocity and power-velocity relations (solid lines in Fig. 2.6B of the main text). To do so, we randomly pick values between a minimum force of 15 pN and maximum forces of 120, 100 and 35 pN for the cases of neutral pH + No P_i, acidic pH + No P_i, and acidic pH + high P_i respectively. Though there are differences between these curves and the curves generated from solving the integro-PDEs, they agree qualitatively.

A.3. Estimating Parameters for low pH

Here we discuss additional details of the simulation results discussed in sections 2.4.1 and 2.4.2 of the main text.

A.3.1. Estimating N and k_a^2 in the mini-ensemble measurements. These are details of the simulations underlying our estimates of $N = 12$ and $k_a^2 = 2.2\text{s}^{-1}$ in Table 2.2 of the main text. To determine N and k_a^2 we fit the mini-ensemble measurements for pH 7.4 [Woodward and Debold, 2018]. Using the methods described in section 2.3 of the main text, we simulated mini ensemble experiments for ensemble sizes between 5 and 21 myosin heads, and for second myosin attachment rates of $k_a^2 = 2.2, 5, 7, 10, 15, 20,$ and 30s^{-1}. Error was defined as the sum of the squared difference between simulated and experimental cumulative probability distributions of event duration and maximum force. Due to the stochasticity of the simulations, we averaged the results of five simulations to determine the best values (see Fig. A.4). These fits identify a range of ensemble sizes and second myosin attachment rates that give good agreement between model and data (the blue region in Fig. A.4a). Previous estimates of k_a^2 have been similar to the single molecule binding rate k_a^1 [Walcott et al., 2012, Debold et al., 2013], so we chose $k_a^2 = 2.2\text{s}^{-1}$. At this value, the ensemble size is predicted to be $N = 14 \pm 2$ (Fig. A.4b). We chose a value at the bottom of this range ($N = 12$), based on exploratory simulations that suggested we would get

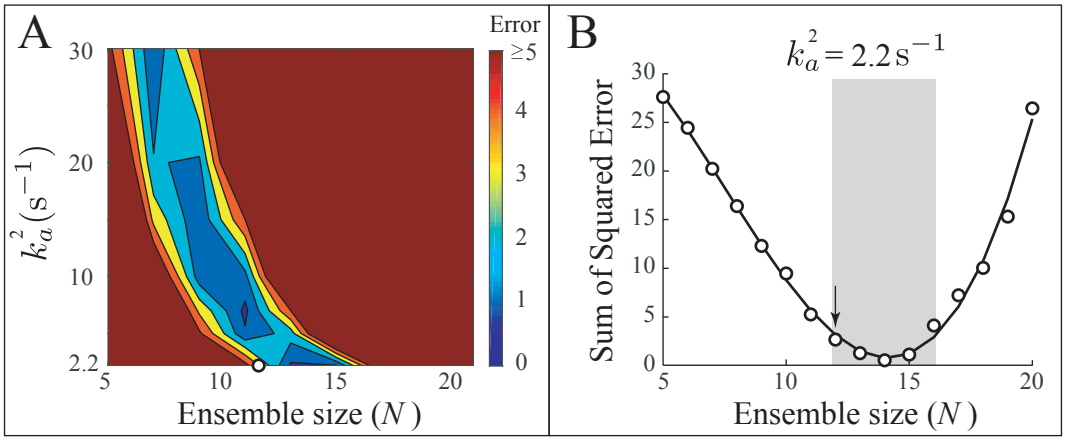

Figure A.4. Estimating ensemble size (N) and cooperative attachment (k_a^2) in the mini-ensemble assay at neutral pH. **A)** Contour of error (sum of squared difference between modeled and measured cumulative probability distribution) as a function of the two parameters. A region of low error (blue) identifies a set of N, k_a^2 combinations that are consistent with the data. We chose parameters near to, but not exactly at, the fitting minimum (hollow dot). **B)** Fixing $k_a^2 = 2.2\mathrm{s}^{-1}$ identifies a range of ensemble sizes that are consistent with the data (shaded region). We chose an ensemble size at the lower boundary of this region ($N = 12$), based on exploratory simulations suggesting that the model would fit the low pH measurements better.

better agreement with the low pH data. Note that, as we will show, our results do not depend on these choices.

A.3.2. Changing k_D^0 and k_R does not reproduce low pH data. These are details of the simulations underlying Fig. 2.3B of the main text. To determine whether a decrease in k_D and and increase in k_R could reproduce the measurements of Woodward and Debold [2018] at pH 6.5, we ran mini-ensemble simulations for various combinations of ADP release and rebinding rates (all combinations of $k_D^0 = 150$, 200, 250, 300, and 350 s^{-1}, $k_R = 0$, 50, 100, and 200 s^{-1}, a total of 20 different conditions), and compared the results to the measurements. Error was defined as the sum of the squared difference between simulated and experimental cumulative probability distributions of the force and lifetime of events. Due to the stochasticity of the simulations, we averaged the results of five simulations to determine the best values.

A.3.3. Changing k_D^0, k_R and k_a does reproduce low pH data. These are details of the simulations underlying Fig. 2.3C of the main text. We performed the same simulations as before (section A.3.2), using the same combinations of ADP release and rebinding rates, for three

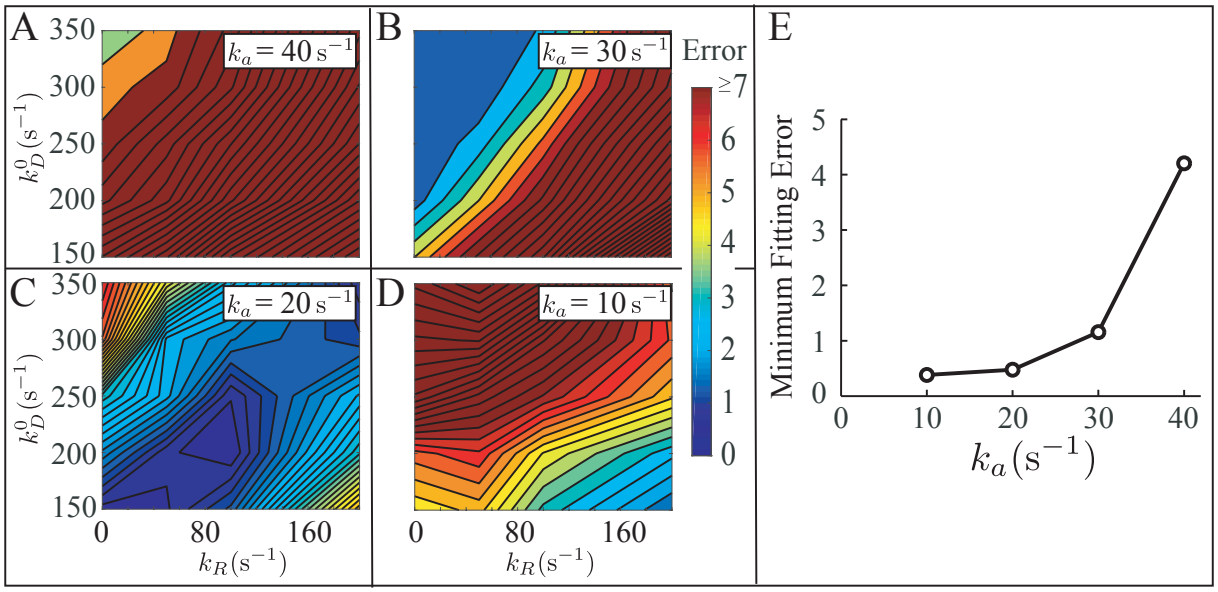

Figure A.5. First simulations: fitting mini-ensemble data at pH 6.5 requires a decrease in k_a and k_D^0 and an increase in k_R. This is a more detailed version of Figs. 2.3B and C of the main text, including contour plots for $k_a = 30$ and $10\mathrm{s}^{-1}$. **A, B, C** and **D)** all show fitting error as a function of k_R and k_D^0 for different attachment rates ($k_a = 40, 30, 20$ and $10\mathrm{s}^{-1}$, respectively). **E)** shows the minimum obtained over all values of k_R and k_D^0 for the four different k_a values. This minimum fitting error comes from running simulations on a refined grid about the minima in A-D.

different attachment rates ($k_a = 30, 20,$ and $10\mathrm{s}^{-1}$, 20 simulations at each k_a, replicated five times to minimize stochasticity, see Fig. A.5B, C and D, respectively).

A.3.4. These results are generic. We assume that (1) $N = 12$ and $k_a^2 = 2.2\mathrm{s}^{-1}$; and (2) the relative scaling of k_R^1, k_R^2 and k_R is the same as the scaling of k_a^1, k_a^2 and k_a (i.e. $k_R^1 = k_R^2 = 0.055k_R$). In order to show that our conclusions do not depend on these assumptions, we ran a series of additional simulations.

To show that our results do not depend on our estimates of N, we re-ran the simulations shown in Fig. A.5 (and Figs. 2.3B, C of the main text) with two different ensemble sizes $N = 11$ and $N = 7$, with k_a^2 picked to minimize error between the model and mini ensemble measurements at pH 7.4, $k_a^2 = 7$ and $k_a^2 = 30\mathrm{s}^{-1}$, respectively (see Fig. A.4A for fitting error between model and mini ensemble measurements at pH 7.4 as a function of N and k_a^2). These simulations are qualitatively identical to the simulations in Fig. A.5 (and Figs. 2.3B, C of the main text), with lower k_a values giving a much better fit to the experimental data, and predicting best-fit parameters with a decrease in k_D^0 and increase in k_R (Fig. A.6A and B).

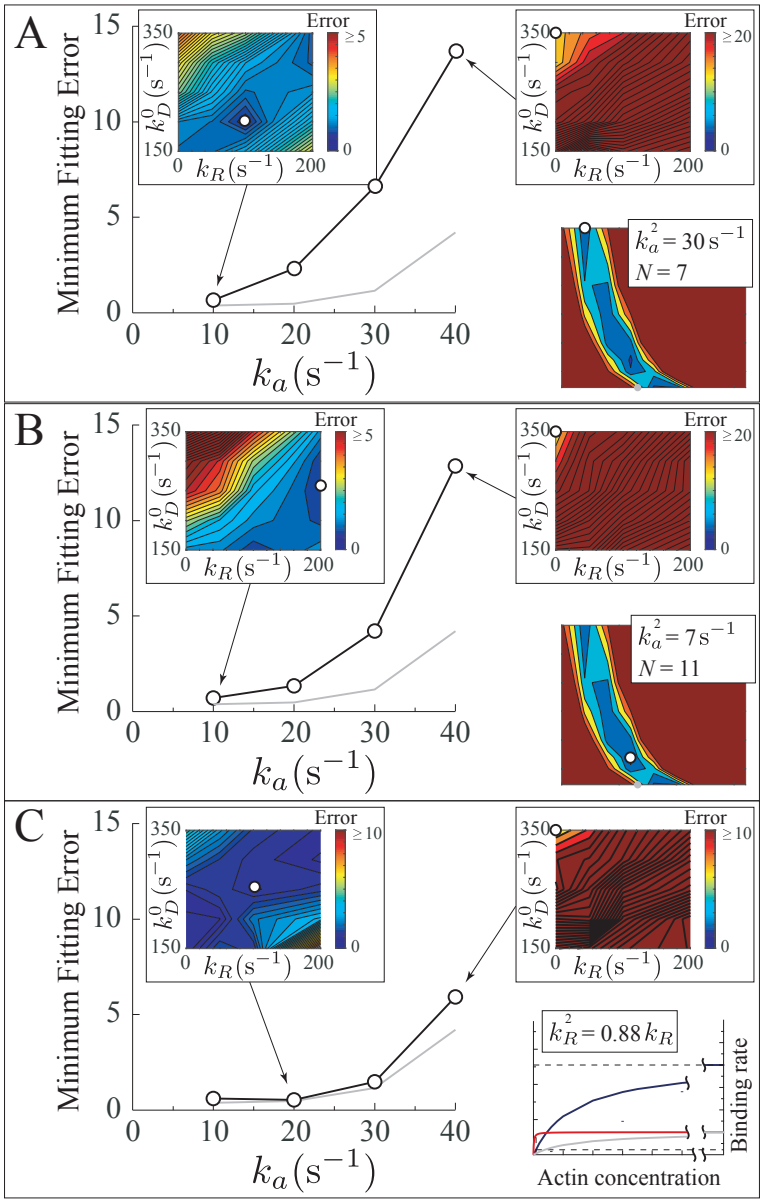

Figure A.6. A reduction in k_a is necessary to reproduce low pH measurements, independent of ensemble size estimates or rebinding cooperativity. **A** and **B)** show comparisons between the model and our mini ensemble measurements at low pH for $N = 7$, $k_a^2 = 30\mathrm{s}^{-1}$ (A) and $N = 11$, $k_a^2 = 7\mathrm{s}^{-1}$ (B). Both plots are qualitatively the same as for the parameter set, $N = 12$, $k_a^2 = 2.2\mathrm{s}^{-1}$ (shown in gray, for reference). Inset at lower right shows a reproduction of Fig. A.4 with parameters for the given simulation shown as a hollow dot, and the parameter set, $N = 12$, $k_a^2 = 2.2\mathrm{s}^{-1}$ shown as a gray dot. **C)** shows the effect of different rebinding cooperativity, i.e. different scaling of k_R^1, k_R^2 and k_R. In section A.4.3 we argue that rebinding scales differently with actin concentration than attachment. This plot shows comparisons between the model and our mini ensemble simulations for this different scaling. The qualitative results are the same whether rebinding scales the same way (gray) or differently than attachment. Inset at lower right shows a reproduction of Fig. A.9 with the two different scaling assumptions. Data from Woodward and Debold [2018].

To show that our results do not depend on our assumption of k_R^1, k_R^2, and k_R scaling (i.e. $k_R^1 = k_R^2 = 0.055k_R$), we re-ran the simulations shown in Fig. A.5 (and Figs. 2.3B, C of the main text) with a different scaling relationship. Specifically, in section A.4.3, we show that single molecule data suggests that the scaling of k_R^1, k_R^2 and k_R is different from the scaling of k_a^1, k_a^2 and k_a. Simulations with this different scaling ($k_R^1 = k_R^2 = 0.88k_R$) are qualitatively identical to the simulations in Fig. A.5 (and Figs. 2.3B, C of the main text), with lower k_a values giving a much better fit to the experimental data, and predicting best-fit parameters with a decrease in k_D^0 and increase in k_R (Fig. A.6C).

A.4. Estimating parameters in the presence of P_i

This section discussed how we determined the best-fit parameters for the branched pathway model at pH 6.5 (Tables 2.2 and 2.3 of the main text).

A.4.1. Estimating k_a and k_D^0. The fits to mini-ensemble measurements in Fig. A.5 suggest that attachment rate at low pH (k_a) should be $\sim 25\%$ of the attachment rate at neutral pH, i.e. $k_a = 10\text{s}^{-1}$. With this estimate of k_a, we can then estimate the best values of k_D^0 and k_R. To determine these values, we ran motility simulations as described in section A.2.3, varying ADP release and rebinding rates ($k_D^0 = 50, 100, 150, 200, 250, 200,$ and 250s^{-1}, and $k_R = 0, 10, 50, 100,$ and 200s^{-1}, 35 different conditions), and fixing attachment rate of $k_a = 10\text{s}^{-1}$. Error is defined as the sum of the squared difference between measured and simulated velocity, scaled by the 95% confidence interval (data and 95% confidence intervals imported from a PDF of Debold et al. [2011], using customized Matlab code). Due to the stochasticity in our simulations, we average over 3 simulations. There is a narrow range of ADP release rates that result in best fits (Fig. A.7A). To minimize error, we estimate $k_D^0 = 100\text{s}^{-1}$. The fitting error is largely insensitive to rebinding rate (k_R).

A.4.2. Estimating k_R and k_{off}. Motility speed at pH 6.5 is accelerated by the presence of 30mM P_i. A non-zero value of k_{off} is required to describe this acceleration. Additionally, the agreement between the model and the data is highly sensitive to the rebinding rate, k_R. We therefore ran a series of simulations of these motility experiments with $k_a = 10\text{s}^{-1}$, $k_D^0 = 100\text{s}^{-1}$, $k_R =$

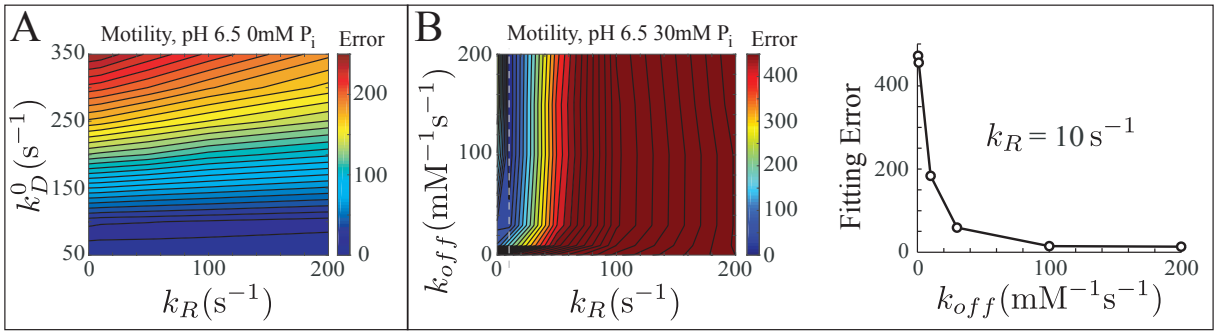

Figure A.7. Motility data at low pH [Debold et al., 2011] provide estimates of model parameters k_D^0, k_R and k_{off}. **A)** Comparison between model and data at low pH and in the absence of P_i provide an estimate of $k_D^0 = 100\text{s}^{-1}$, but are largely insensitive to k_R. **B)** Comparison between model and data at low pH and in the presence of 30mM P_i with $k_D^0 = 100\text{s}^{-1}$ provide an estimate of $k_R = 10\text{s}^{-1}$ and $k_{off} = 100\text{s}^{-1}$. Curve at right shows fitting error vs. k_{off} along dashed line in contour plot at left. In all plots, $k_a = 10\text{s}^{-1}$.

$0, 10, 50, 100,$ and 200s^{-1} and $k_{off} = 0.5, 1, 10, 30, 100, 150,$ and $200\text{mM}^{-1}\text{s}^{-1}$ (35 simulations). To minimize stochasticity, we averaged three sets of these simulations. Error for these simulations (defined as the sum of squared error between model and simulation, scaled by 95% confidence interval) allows us to estimate $k_R = 10\text{s}^{-1}$, and is relatively insensitive to k_{off}, provided that it is higher than $\sim 100\text{mM}^{-1}\text{s}^{-1}$ (Fig. A.7b). We therefore choose $k_{off} = 100\text{mM}^{-1}\text{s}^{-1}$.

A.4.3. Cooperativity in rebinding. The motility measurements in the presence of P_i are dependent on a low rebinding rate ($k_R = 10\text{s}^{-1}$); however, single molecule measurements require a higher rebinding rate in order to fit the decreased step size seen at low pH [Debold et al., 2008]. This apparent contradiction can be reconciled if myosin has a different affinity for actin when rebinding than when binding.

More specifically, cooperativity arises in the laser trap because myosin binding restricts vertical fluctuations of the actin filament. We model this cooperativity with different attachment rates when zero, one or more myosin are bound to actin (k_a^1, k_a^2, and k_a, respectively). From our measurements of ATP hydrolysis in solution, and assuming that ATP hydrolysis rate scales linearly with k_a, the measurement of $k_a^1 = 2.2\text{s}^{-1}$ [Longyear et al., 2017] corresponds to an actin concentration of $\sim 1\mu$M in the laser trap (see Fig. A.8, blue line).

The relative scaling of k_a^1, k_a^2 and k_a depends on how binding rate varies with actin concentration. If rebinding has a different relationship than binding, then k_R^1, k_R^2 and k_R would not scale in

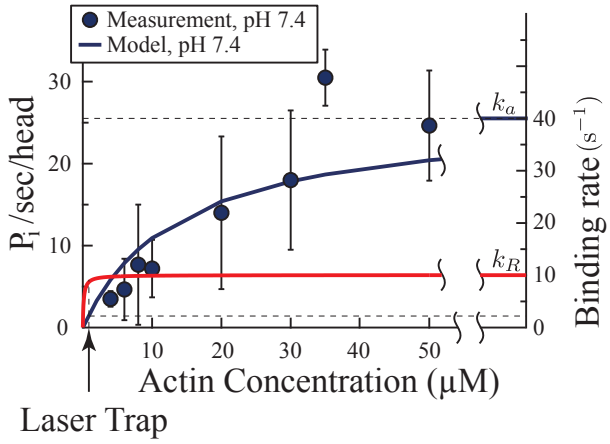

Figure A.8. The different scaling of attachment (blue) and rebinding (red) with actin concentration suggested by single molecule data. If ATP hydrolysis rate is limited by, and therefore scales linearly with, the weak to strong binding transition, then measurements of MgATP hydrolysis from Woodward and Debold [2018] (blue dots) show how k_a scales with actin concentration (axes at right). Given an attachment rate of 2.2s^{-1} [Longyear et al., 2017] the effective actin concentration in the single molecule laser trap is $\sim 1\mu$M (dashed lines). To fit the ATP-dependent reduction in myosin step size observed in the laser trap [Debold et al., 2008], we predict a different relationship between actin concentration and rebinding rate, k_R (red curve). Note, for clarity, we have removed some of the data points at low actin concentration.

the same manner. In order to reconcile the differences in rebinding needed to fit our motility and single molecule measurements, we predict that myosin has a greater affinity for actin in rebinding, so that even at the low actin concentration of the laser trap ($\sim 1\mu$M) the rebinding rate is only slightly less than saturating ($k_R^1 = 8.8\text{s}^{-1}$ vs. $k_R = 10\text{s}^{-1}$, see Fig. A.8, red line).

A.4.3.1. *Theoretical model for apparent step size variation with ATP.* We estimated this value of k_R^1 as follows: given the relatively weak stiffness of the laser trap (~ 0.02pN/nm), myosin's power-stroke generates only a small amount of force (~ 0.2pN). Therefore, any attached myosin experiences little force, other than the forces due to thermal motion. If we neglect the force dependent rate constants, assume $[\text{P}_\text{i}] = 0$ in Eq. A.1, and consider steady-state, then the probability of a myosin molecule being in one of the four available states can be found from solving the following

equations:

$$\begin{aligned} 0 &= -k_D N_1 + k_a^1 N_4 \\ 0 &= k_D N_1 - k_T[T]N_2 + k_R N_3 \\ 0 &= k_T[T]N_2 - (k_R^1 + k_h^+)N_3 + k_h^- N_4 \\ 0 &= k_h^+ N_3 - (k_a^1 + k_h^-)N_4 \end{aligned} \tag{A.19}$$

with the numbering as in Fig. A.1 and, from top to bottom, each equation representing the time rate of change of N_1 to N_4, respectively. Note that, since we are modeling the behavior of a single molecule in the laser trap, the rebinding and attachment rates are k_R^1 and k_a^1, respectively.

The attachment flux from state 4, via the weak to strong binding transition, is given by $k_a N_4$ and the attachment flux from state 3, via rebinding, is given by $k_R N_3$. Thus, the probability of binding through the weak to strong binding transition (and taking a 10nm step) is given by $P_{10} = k_a^1 N_4/(k_a^1 N_4 + k_R^1 N_3)$, while the probability of rebinding (and taking a 0nm step) is given by $P_0 = k_R^1 N_3/(k_a^1 N_4 + k_R^1 N_3)$. Solving Eq. A.19 gives the following expressions for these values in terms of the rate constants

$$\begin{aligned} P_{10} &= \frac{k_h^+ k_a^1}{k_h^+ k_a^1 + (k_a^1 + k_h^-)k_R^1} \\ P_0 &= \frac{(k_a^1 + k_h^-)k_R^1}{k_h^+ k_a^1 + (k_a^1 + k_h^-)k_R^1} \end{aligned} \tag{A.20}$$

When calculating step size via mean-variance analysis ([Patlak, 1993, Guilford et al., 1997]), the average of the binding events is taken, weighted by the total time attached. Thus, given expressions for the probability density of binding lifetime via the binding and rebinding pathways, ρ_{10} and ρ_0 respectively, the total time of 10nm and 0nm events is proportional to $P_{10}\int_0^\infty t\rho_{10}dt$ and $P_0\int_0^\infty t\rho_0 dt$, and the average step size, $\langle d\rangle$, is then

$$\langle d\rangle = \frac{10P_{10}\int_0^\infty t\rho_{10}dt}{P_{10}\int_0^\infty t\rho_{10}dt + P_0\int_0^\infty t\rho_0 dt} \tag{A.21}$$

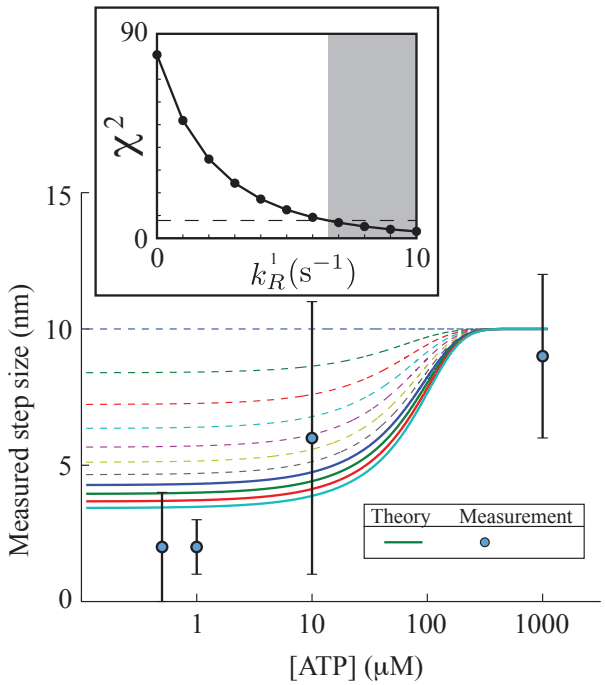

Figure A.9. Fitting single molecule measurements [Debold et al., 2008] requires a rebinding rate $k_R^1 > 6.6\mathrm{s}^{-1}$. Plots shows different theoretical step size predictions (Eq. A.24) for $k_R^1 = 0, 1, \ldots, 10\mathrm{s}^{-1}$ (top to bottom). Curves significantly different from the data are shown in dashed lines. Inset shows the χ^2 error between model and data, with significance ($p < 0.05$) shown as the dashed line. When $k_R^1 > 6.6\mathrm{s}^{-1}$, the model is not different from the data (shaded region).

Events that proceed through the binding pathway detach through two sequential steps (ADP release, ATP binding), so that

$$\rho_{10} = \frac{k_D k_T[T]}{k_D - k_T[T]} \left(e^{-k_T[T]t} - e^{-k_D t} \right) \tag{A.22}$$

while events that proceed through the rebinding pathway detach a single step (ATP binding), so that

$$\rho_0 = k_T[T] e^{-k_T[T]t} \tag{A.23}$$

There is presumably some minimal resolution of the laser trap, below which events cannot be detected t_{min}, as well as some maximal event lifetime beyond which events cannot be conveniently measured t_{max}. We can substitute these values for 0 and ∞, respectively, in Eq. A.21 and then

solve to get

$$\langle d \rangle = \frac{10 \frac{(k_h^+ k_a^1) k_D}{k_T[T] - k_D} I_{10}}{(k_a^1 + k_h^-) k_R^1 I_0 + \frac{(k_h^+ k_a^1) k_D}{k_T[T] - k_D} I_{10}} \tag{A.24}$$

where

$$\begin{aligned} I_{10} &= \left(\frac{t}{k_T[T]} + \frac{1}{(k_T[T])^2} \right) e^{-k_T[T]t} \Big|_{t_{min}}^{t_{max}} - \left(\frac{t}{k_D} + \frac{1}{(k_D)^2} \right) e^{-k_D t} \Big|_{t_{min}}^{t_{max}} \\ I_0 &= \left(\frac{t}{k_T[T]} + \frac{1}{(k_T[T])^2} \right) e^{-k_T[T]t} \Big|_{t_{min}}^{t_{max}} \end{aligned}$$

Evaluating Eq. A.24 for different choices of k_R^1 (using $t_{min} = 0.01$s, and $t_{max} = 2$s) and comparing it to the measurements of Debold et al. [2008], we find that $k_R^1 < 6.6\text{s}^{-1}$ generates curves that are significantly different from the data (Fig. A.9, significance set at $p < 0.05$, χ^2 test). Thus, we must pick $6.6\text{s}^{-1} < k_R^1 < k_R = 10\text{s}^{-1}$., which motivates our choice of $k_R^1 = 8.8\text{s}^{-1}$. As shown in Fig. 2.5A of the main text, our detailed simulations of the laser trap (described in section A.2.2) agree with the theoretical model in Eq. A.24.

A.4.4. Validation of parameters. To define all of the parameters at low pH, we used mini-ensemble data [Woodward and Debold, 2018] at pH 7.4 (to estimate N and k_a^2) and pH 6.5 (to estimate k_a), motility data [Debold et al., 2011] at pH 6.5 and with 0 mM P_i (to estimate k_D^0) and with 30 mM P_i (to estimate k_{off} and k_R) and single molecule data [Debold et al., 2008] at pH 6.5 (to estimate k_R^1). Note that the estimates of k_D^0, k_{off}, k_R and k_R^1 were all made without using the mini ensemble measurements at pH 6.5 and 15mM P_i [Woodward and Debold, 2018]. It is therefore possible that, with these values, the model is no longer consistent with the measurements.

We ran mini ensemble simulations as described in section A.2.1, varying ADP release and rebinding rates ($k_D^0 = 50, 100, 150, 200, 250, 200,$ and 250s^{-1}, and $k_R = 0, 10, 50, 100,$ and 200s^{-1}, 35 different conditions), and fixing attachment rate of $k_a = 10\text{s}^{-1}$ and the relative scaling of k_R, k_R^1 and k_R^2. Error is defined as the sum of the squared difference between measured and modeled cumulative probability distributions for both force and duration of events. Due to the stochasticity in our simulations, we average over 3 simulations. In good agreement with the comparison between

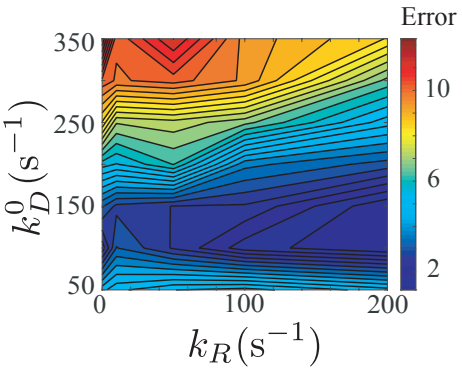

Figure A.10. Our mini ensemble measurements independently support our estimate of $k_D^0 = 100\mathrm{s}^{-1}$. A contour plot of the error between model and our measurements at pH 6.5 and in the absence of P_i shows a minimum (blue region) near $k_D^0 = 100\mathrm{s}^{-1}$ and is largely insensitive to k_R, consistent with our estimates of these parameters from the motility assay (c.f. Fig. A.7a). Parameters used in the simulation, other than k_D^0 and k_R, are given in Table 2.2 of the main text.

the model and the motility experiments (Fig. A.7a), we see a clear minimum near $k_D^0 = 100\mathrm{s}^{-1}$ (Fig. A.10). The fitting error is largely insensitive to rebinding rate (k_R).

As additional validation, when we simulate the mini ensemble measurements at pH 6.5 with 15mM P_i, we obtain histograms that are consistent with the measurements Woodward and Debold [2018]. Since these measurements were not used to specify any of the model parameters, the histograms shown in Fig. 2.5C and summarized in Table 2.4 of the main text are predictions of the model. Therefore, the mini ensemble measurements provide independent support for our parameter estimates.

Finally, Debold et al. [2008] observed a pH-dependent increase in single molecule binding lifetime at 1mM ATP. In particular, at pH 7.4, event lifetime was so short that an event population could not be identified nor a lifetime determined; while at pH 6.5, event lifetime was $t_{on} = 0.031 \pm 0.009$s. Consistent with these measurements, our model also does not generate an event population at pH 7.4; while at pH 6.5, event lifetime is $t_{on} = 0.013 \pm 0.005$. It is likely that the model would give better agreement with the data if we introduced a more realistic model for the noise in the laser trap [e.g. Longyear et al., 2017]. But even with uncorrelated noise, the model gives reasonable agreement with these single molecule event lifetimes, which depend on ADP release rate, despite the fact that this parameter was determined from comparing the model to a different experimental system: in vitro motility (and then subsequently validated, in Fig. A.10, with mini-ensemble measurements).

A.5. Unloaded velocity at low pH and high P_i

There is a discrepancy between measurements in the in vitro motility assay at low pH (pH 6.5), where the addition of 30mM P_i leads to a roughly two-fold increase in velocity [Debold et al., 2011], and measurements in muscle fibers at low pH (pH 6.2), where the addition of 30 mM P_i leads to a 20% drop in V_{max} [Knuth et al., 2006, Nelson et al., 2014]. Here we present simulation results aimed at investigating this discrepancy.

A.5.1. Extrapolation errors from Hill fits. Unloaded shortening velocity of a muscle fiber is generally estimated from measurements of shortening velocity at a series of constant force values. These data are then fit will a Hill curve, an equation of the form

$$V = V_{max}\frac{(F_0 - F)}{(F_0 + cF)}$$

Generally, measurements are not made at precisely zero force. Thus, since force velocity data are not precisely described by a Hill curve, estimates of V_{max} might differ from the actual unloaded shortening velocity. It is possible that extrapolation errors could account for the differences between the motility assay and the muscle fiber measurements.

To investigate this idea, we performed a series of simulations of the model at pH 6.5. We simulated an experimental protocol where force was measured at regular intervals between 7% and 90% of the isometric force (calculated from the PDEs, see section A.1.2). We then fit the resulting simulated data with a Hill curve (using Matlab's `fminsearch` function to minimize mean squared error).

The resulting V_{max} as a function of P_i displays biphasic behavior (Fig. A.11A). Initially, it decreases before reaching a minimum of a $\sim$ 3% decrease around 0.1mM P_i. Under these same conditions, the model predicts an increase of $\sim$ 3% (calculated from the PDEs, see section A.1.2). Thus, there are at least some conditions where the model predicts that extrapolation errors could account for a discrepancy between V_{max} estimated from Hill fits and true unloaded shortening velocity. The exact amount of this error, and its dependence on P_i, depends on the number of data points, their force values, the noise in the data, and how the Hill model is fit to the data. Note that, although 1mM P_i is well below the concentrations used in muscle experiments, it nevertheless

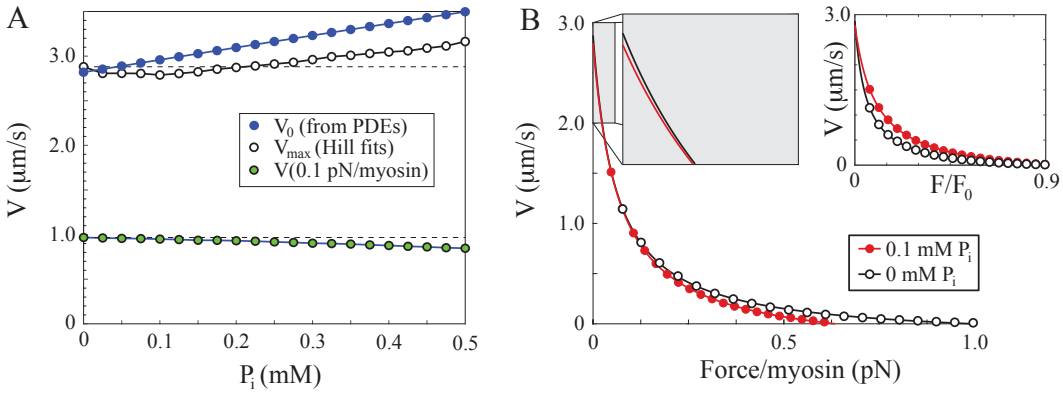

Figure A.11. Possible explanations of the discrepancy between in vitro motility and fiber measurements of unloaded shortening at low pH and in the presence of P_i. **A)** Three estimates of unloaded shortening velocity as a function of P_i. The PDE solutions (blue circles) show an increase in velocity with P_i, as observed in the in vitro motility assay. Estimates of V_{max} from Hill fits to model simulations (hollow circles) initially show a decrease in velocity with P_i, as observed in fiber experiments. Model simulations, even in the presence of a small force (green circles), show decreasing velocity with P_i. Each point represents the average of three simulations. **B)** Simulated force-velocity curves, demonstrating a P_i-induced decrease in V_{max}. The region near zero force is expanded to show the small decrease. Inset shows the same curves, rescaled to show that the same relative force values were used to generate the Hill fits.

causes a $\sim 40\%$ drop in isometric force (Fig. A.11B), similar to what is seen experimentally [Nelson et al., 2014].

A.5.2. Errors from resistive force. In *in vitro* motility experiments, actin filaments are propelled by myosin molecules through solution, and therefore experience negligible resistive drag. In a skeletal muscle fiber, there may be sources of drag, including myosin binding protein c [Previs et al., 2012]. Due to the hyperbolic nature of force-velocity relationships, even a modest resistive force could have a profound impact on velocity measurements. To demonstrate this point, we performed a series of simulations of the model at pH 6.5. We simulated an experimental protocol where a 30pN force was applied to actin (9% isometric). These simulated velocities decrease monotonically with P_i (Fig. A.11A). Indeed, since the addition of P_i causes a reduction in isometric force combined with an increase in unloaded shortening speed in the model, there is a cross-over point where the addition of P_i has no effect. This point occurs at around 4% isometric force.

APPENDIX B

Chapter 3 Appendix (Weak-Binding Paper)

Supplementary Information for

"Force-velocity and tension transient measurements from *Drosophila* jump muscle reveal the necessity of both weakly-bound cross-bridges and series elasticity in models of muscle contraction"

Published on February 18, 2021 in the *Archives of Biochemistry and Biophysics*

Joint work with:

Kaylyn M. Bell

Department of Biological Sciences, Center for Biotechnology and Interdisciplinary Studies, Rensselaer Polytechnic Institute, Troy, NY

Amy K. Loya

Department of Biomedical Engineering, Rensselaer Polytechnic Institute, Troy, NY

Douglas M. Swank

Department of Biological Sciences, Center for Biotechnology and Interdisciplinary Studies and Department of Biomedical Engineering, Rensselaer Polytechnic Institute, Troy, NY

Sam Walcott

Department of Mathematical Sciences, Worcester Polytechnic Institute, Worcester, MA

B.1. Modeling

B.1.1. Variable Definitions.

Notation	Description
d	Power-stroke size
x	Extension of myosin molecule
κ	Stiffness of myosin
k_BT	Boltzmann's constant times temperature
δ	Parameter describing myosin's force-dependent chemistry
$E = \kappa\delta d/k_BT$	Non-dimensional parameter describing myosin's force-dependent chemistry
$v_{\max}$	Unloaded shortening velocity
$k_D(x)$	ADP release rate
k_D^0	Unloaded ADP release rate
$\mathcal{S}$	Length of stretch of half-sarcomere (nm) in a force-transient protocol
F_0	Isometric force
F_p	Force produced by a cross-bridge post-stretch in force-transient protocol
F_{nc}	Non-cross-bridge force present in force-transient measurement (same as F_{nc}^0 in section B.6.2)
$\eta_i(x,t)$	Probability density that myosin is bound in state i with an extension x
$N_i(t)$	Probability that myosin is in state i
$\kappa_w^+(x)$	Rate density for transition from unbound to bound states 5 to 1
$k_{w_0}^+$	Overall attachment rate
k_a, k_T, k_h^+, k_h^-	Rate constants for transition between states in kinetic scheme
[ATP]	ATP concentration

Notation	Description
l, τ, V, $\hat{x}$, $\hat{\eta}$, L	Non-dimensional parameters for steady-state analytical solution (see section B.1.3.2)
$G(x, \mu)$	Normalized Gaussian function in terms of x with mean μ (see section B.1.4.2)
$\alpha_i(t)$, $\mu_i^j(t)$, $A(t)$, $b_i(t)$	Parameters for solving non-steady-state approximation (see section B.1.4.2)
F_{xb}^0, F_{xb}^p	Cross-bridge forces pre- and post-stretch, respectively, in force transients (see section B.6.2)
F_{nc}^0, F_{nc}^p	Non-cross-bridge forces pre- and post-stretch, respectively, in force transients (see section B.6.2)
$V(x)$	Potential energy function

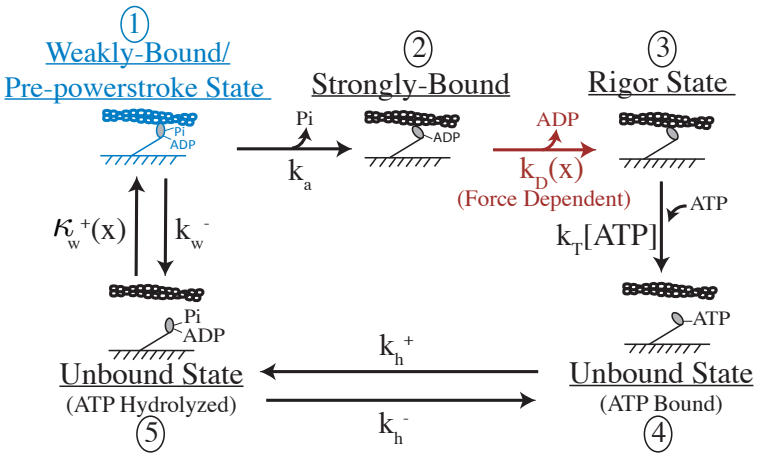

Figure B.1. Five-state kinetic scheme detailing myosin's interaction with actin, including a weakly-bound state labeled in blue.

B.1.2. Mathematical Formulation of Model. In this section, we describe the mathematical implementation of the five-state model in Fig. 3.1B in the main text, and reproduced here in Fig. B.1. The specific details of the four-state model are similar (see Walcott et al. [2012] for more

detail). Myosin and actin interact in the cyclical pattern described by the kinetic scheme. Beginning with state 1, myosin is bound to actin in a pre-power-stroke form with ADP and inorganic phosphate (P_i) in its nucleotide binding site. In some order, myosin releases P_i and undergoes a conformational change, shifting to a post-power-stroke form with ADP still in the active site (state 2). ADP is released in a force-dependent manner and actin and myosin stay bound in a post-power-stroke rigor state (state 3). ATP can then bind to the empty active site on myosin, causing dissociation of myosin from actin (state 4). Finally, ATP is hydrolyzed and myosin is unbound with ADP and P_i in the active site (state 5), and the cycle can begin again.

To transform this model into a system of equations, we must consider the force-dependence in the system. We use x to denote the molecular extension of a myosin molecule. When myosin is in an unbound state (states 4 and 5), it is not attached to actin, so there is no force on the molecule. Thus, the probability of being in one of these states is simply a function of time, denoted $N_i(t)$. However, when myosin is bound to actin, it is bound with a particular extension, x. Thus, for bound states (states 1, 2, and 3), we must define the probability density of myosin being bound in state i with an extension x as $\eta_i(x,t)$. The probability of being in one of the bound states is therefore $N_i(t) = \int_{-\infty}^{\infty} \eta_i(x,t)dx$.

We also must consider molecular extension when defining transitions between states. When myosin binds to actin, it does so with a particular extension. Thus, the transition from unbound to weakly bound (state 5 to state 1) must be defined as a rate density, $\kappa_w^+(x)$, giving an overall attachment rate of $k_{w_0}^+ = \int_{-\infty}^{\infty} \kappa_w^+(x)dx$. Additionally, ADP release rate (transition from state 2 to state 3) is dependent on force, and is therefore a function of molecular extension, $k_D(x)$.

Assuming a dense binding limit (i.e. that myosin can bind anywhere on the actin filament), a large number of cross-bridges, and the above notation, the five-state kinetic scheme can be expressed

by the following system of integro-PDEs:

$$
\begin{aligned}
\frac{\partial \eta_1}{\partial t} + v\frac{\partial \eta_1}{\partial x} &= \kappa_w^+(x)N_5 - (k_w^- + k_a)\eta_1 \\
\frac{\partial \eta_2}{\partial t} + v\frac{\partial \eta_2}{\partial x} &= k_a\eta_1 - k_D(x)\eta_2 \\
\frac{\partial \eta_3}{\partial t} + v\frac{\partial \eta_3}{\partial x} &= k_D(x)\eta_2 - k_T[ATP]\eta_3 \\
\frac{dN_4}{dt} &= k_T[ATP]\int_{-\infty}^{\infty}\eta_3 dx + k_h^- N_5 - k_h^+ N_4 \\
\frac{dN_5}{dt} &= \int_{-\infty}^{\infty} k_w^-\eta_1 dx + k_h^+ N_4 - \left(k_h^- + \int_{-\infty}^{\infty}\kappa_w^+(x)dx\right)N_5 \\
1 &= \int_{-\infty}^{\infty}\eta_1 dx + \int_{-\infty}^{\infty}\eta_2 dx + \int_{-\infty}^{\infty}\eta_3 dx + N_4 + N_5
\end{aligned}
\tag{B.1}
$$

where the final equation gives conservation of mass.

ADP release is dependent on molecular extension and, based on experimental measurements [Veigel et al., 2003, Kad et al., 2007, Bell, 1978], we use the form:

$$k_D(x) = k_D^0 \exp\left(-\frac{\kappa(x+d)\delta}{k_B T}\right)$$

where k_D^0 is ADP release rate in the absence of force, κ is myosin's stiffness (assuming myosin acts as a linear spring), d is myosin's power-stroke size, $k_B T$ is Boltzmann's constant times temperature, and δ is a parameter, with units of distance, that describes myosin's force-dependent properties. Additionally, assuming that myosin's attachment probability varies exponentially with the energy required for myosin to bind with a given extension, we define the following rate density:

$$\kappa_w^+(x) = k_{w_0}^+\sqrt{\frac{\kappa}{2\pi k_B T}}\exp\left(-\frac{\kappa x^2}{2k_B T}\right)$$

All other rate constants (denoted k_w^-, k_a, k_T, k_h^-, k_h^+) are constant values.

With this, the mathematical model is described in full. Below, we detail the techniques used to solve this system under various conditions, resulting in expressions for $\eta_i(x,t)$ and $N_i(t)$. We can then calculate an expression for force. Force per myosin molecule is defined as the probability

that myosin is in a force-producing state (states 1, 2, and 3), times the force it produces when bound. Noting that myosin has bound but has not undergone a power-stroke in state 1 (i.e. it has extension x), and has undergone a power-stroke of step size d in states 2 and 3 (i.e. it has extension $(x+d)$), we get the following calculation for force:

$$F = \int_{-\infty}^{\infty} \kappa\eta_1(x,t)x dx + \int_{-\infty}^{\infty} \kappa\eta_2(x,t)(x+d)dx + \int_{-\infty}^{\infty} \kappa\eta_3(x,t)(x+d)dx \tag{B.2}$$

In the following sections, we present both numerical solutions and analytical approximations for the system under various conditions. The numerical methods are important because they provide accurate and robust solutions to the system. However, they are often computationally expensive and inefficient. This makes optimization without a good initial guess time consuming, and sometimes impossible.

We develop analytical approximations to improve the optimization process. While less accurate, our approximations have two advantages. First, they give an efficient way to search parameter space. This allows us to quickly determine a good initial guess of best-fit parameters that can then be used with the less efficient, but more accurate, numerical solutions. Additionally, our analytical approximations provide intuition about our system, which is particularly useful when implementing the full model solutions.

B.1.3. Steady-State Solutions. To compare the model to force-velocity and energetics measurements, we must solve the system under steady-state conditions. First, we note that all of the experimental measurements we consider are done for conditions of high ATP concentration, $[ATP]$. The transition rate from state 3 to state 4 is dependent on this concentration, and thus, high concentrations of ATP results in a negligible population of cross-bridges in rigor. This allows us to simplify the system by assuming that myosin transitions directly from state 2 to state 4 at a rate of $k_D(x)$. With this simplification and the assumption of steady-state, the system in Eq. B.1 becomes:

$$v\frac{d\eta_1}{dx} = -(k_w^- + k_a)\eta_1 + \left(\frac{k_w^- + k_a}{k_{w_0}^+}\right)\kappa_w^+(x)N_1 \tag{B.3}$$
$$v\frac{d\eta_2}{dx} = k_a\eta_1 - k_D(x)\eta_2$$

B.1.3.1. *Numerical Solution for Steady-State.* To numerically solve the system of ordinary differential equations (ODEs) in Eq. B.3 for a given velocity value, v, we simultaneously implement a root find using Matlab's `fsolve` function and an ODE solver using Matlab's `ode15s`. We use the root find to determine the value of N_1 by solving $N_1 - \int_{-\infty}^{\infty}\eta_1(x)dx = 0$, and the ODE solver to find $\eta_1(x)$ and $\eta_2(x)$. We use a solver specialized for stiff ODEs because of the exponential term $(k_D(x))$, which becomes large at the boundary. We can then calculate the force using Eq. B.2, resulting in a relationship for force as a function of velocity.

B.1.3.2. *Analytical Solution for Steady-State.* To solve for an analytical solution under steady-state conditions, it is most convenient to non-dimensionalize the system in Eq. B.3. To do so, we define the following non-dimensional parameters: $\ell = \sqrt{2k_BT/\kappa}$, $\tau = 1/(k_w^- + k_a)$, $V = v\tau/\ell$, $\hat{x} = x/\ell$, $\hat{\eta} = \eta\ell$, $E = \kappa\delta d/k_BT$, $L = \ell/d$.

With this notation, the equation for η_1 becomes,

$$V\frac{\partial\hat{\eta_1}}{\partial\hat{x}} = -\hat{\eta_1} + \frac{1}{\sqrt{\pi}}e^{-\hat{x}^2}N_1 \tag{B.4}$$

This can be analytically solved using an integrating factor. Using the convention that $v < 0$ for shortening, which therefore gives the boundary condition that $\hat{\eta_1}(\infty) = 0$, we get the solution,

$$\hat{\eta_1} = \frac{N_1}{2V}e^{1/(4V^2)}e^{-\hat{x}/V}\left[-1 + \mathrm{erf}\left(\hat{x} - \frac{1}{2V}\right)\right] \tag{B.5}$$

Next, we must solve for η_2. We implement the η_1 solution with the equation for η_2 in Eq. B.3 to get,

$$v\frac{\partial\eta_2}{\partial x} = -k_D^0\exp\left(-EL\hat{x} - E\right)\eta_2 + \frac{k_aN_1}{2Vl}e^{1/(4V^2)}e^{-\hat{x}/V}\left[-1 + \mathrm{erf}\left(\hat{x} - \frac{1}{2V}\right)\right] \tag{B.6}$$

To solve, we introduce a new non-dimensional length scale and rescale with $\overline{x} = x/d$ and $\overline{\eta_2} = d\eta_2$. Note that ℓ is small compared to d, so we can also define $L = \ell/d = \varepsilon$.

Finally, we define two non-dimensional parameters, $T_a = k_a\tau/\varepsilon$ and $T_d = k_D^0\tau/\varepsilon$. Both of these parameters include τ, the time scale of weak binding, which is assumed to be fast compared to strong binding. Thus, τ is $\mathcal{O}(\varepsilon)$, and T_a and T_d are both $\mathcal{O}(1)$. We can therefore simplify Eq. B.6 to be,

$$\frac{\partial\overline{\eta_2}}{\partial\overline{x}} = \frac{-T_d}{V}\exp\big(-E\overline{x}-E\big)\overline{\eta_2} + \frac{T_aN_1}{V}\left[\frac{1}{2\varepsilon V}e^{1/(4V^2)}e^{-\overline{x}/(\varepsilon V)}\left(-1+\operatorname{erf}\left(\frac{\overline{x}}{\varepsilon}-\frac{1}{2V}\right)\right)\right] \tag{B.7}$$

We solve for η_2 using a matched asymptotic expansion. First, we construct the outer solution away from zero. In this region, we must solve,

$$\frac{\partial\overline{\eta_2}}{\partial\overline{x}} = \frac{-T_d}{V}\exp(-E\overline{x}-E)\overline{\eta_2} \tag{B.8}$$

which gives the solution,

$$\overline{\eta_2}^{\text{out}} = A\exp\left(\frac{T_de^{-E\overline{x}-E}}{EV}\right) \tag{B.9}$$

Next, for the inner solution near zero, we must solve,

$$\frac{\partial\overline{\eta_2}}{\partial\overline{x}} = \frac{T_aN_1}{V}\left[\frac{1}{2\varepsilon V}e^{1/(4V^2)}e^{-\overline{x}/(\varepsilon V)}\left(-1+\operatorname{erf}\left(\frac{\overline{x}}{\varepsilon}-\frac{1}{2V}\right)\right)\right] \tag{B.10}$$

To solve, we must first define a layer coordinate to rescale into the layer. We divide the length parameter by ε, which we can write using our original notation: $\overline{x}/\varepsilon = \hat{x}$. Rescaling Eq. B.10 allows us to solve for the inner solution with an arbitrary constant. Noting that $\overline{\eta_2}^{\text{in}}(\infty) = 0$, we can solve for this constant to get the solution

$$\overline{\eta_2}^{\text{in}} = \frac{T_aN_1}{2V}\left(\operatorname{erf}(\hat{x}) + e^{1/(4V^2)}e^{-\hat{x}/V}\left(1+\operatorname{erf}\left(\frac{1}{2V}-\hat{x}\right)\right)-1\right) \tag{B.11}$$

Matching these solutions near zero, we get the following composite solution:

$$\eta_2^{\text{comp}} = \begin{cases} \eta_2^{\text{in}} & \forall x,\hat{x},\overline{x} \\ \eta_2^{\text{in}} + \eta_2^{\text{out}} - \eta_2^{\text{match}} & \text{for } x,\hat{x},\overline{x} < 0 \end{cases}$$

where

$$\eta_2^{\text{out}} = \frac{-T_a N_1}{V} \exp\left(\frac{-T_d e^{-E}}{EV}\right) \exp\left(\frac{T_d e^{-E\overline{x}-E}}{EV}\right)$$

$$\eta_2^{\text{in}} = \frac{T_a N_1}{2V}\left(\text{erf}(\hat{x}) + e^{1/(4V^2)} e^{-\hat{x}/V}\left(1 + \text{erf}\left(\frac{1}{2V} - \hat{x}\right)\right) - 1\right) \tag{B.12}$$

$$\eta_2^{\text{match}} = \frac{-T_a N_1}{V}$$

This expression for η_2 can be integrated to solve for N_2, since $N_2 = \int_{-\infty}^{\infty} \eta_2(x,t)dx$. A value for N_2 then allows us to solve for N_1.

Combining all of the above, we have fully defined analytical expressions for η_1 and η_2. As a final step, we can use Eq. B.2 to solve for force as a function of shortening velocity.

B.1.4. Non-Steady-State Solutions. In the force transient experiments, the muscle fiber is activated and held isometrically, stretched on a very rapid time scale, and then held isometrically again. Therefore, to compare the model to these measurements, we assume isometric conditions and solve for force as a function of time.

Again, we assume conditions of high ATP, reducing our five-state model to not include the negligibly populated state 3. Additionally assuming isometric conditions (i.e. $v = 0$), the system (Eq. B.1) reduces to the following:

$$\begin{aligned} \frac{\partial \eta_1}{\partial t} &= \kappa_w^+(x) N_5 - (k_w^- + k_a)\eta_1 \\ \frac{\partial \eta_2}{\partial t} &= k_a \eta_1 - k_D(x)\eta_2 \\ \frac{dN_5}{dt} &= k_w^- N_1 + k_h^+(1 - N_1 - N_2 - N_5) - (k_h^- + k_{w_0}^+)N_5 \end{aligned} \tag{B.13}$$

B.1.4.1. *Numerical Solution for Non-Steady-State.* To numerically solve the system, we use the method of characteristics to convert these partial differential equations (PDEs) to a system of ODEs at each x. We then implement a fourth-order Runge-Kutta algorithm (RK4) in Matlab to solve

the system of ODEs. We implement our own RK4 instead of using one of Matlab's suite of ODE solvers because of the integral constraint, $N_i = \int_{-\infty}^{\infty} \eta_i(x,t)dx$. This constraint results in coupling between the characteristics, so that the ODEs are coupled and cannot be solved individually.

To implement RK4, we first solve the system analytically in steady-state ($t = 0$). Our simulation begins at the time of stretch, and so the initial condition is the steady-state distributions shifted by the stretch amplitude. For each value of x, we have a system of ODEs. We use the RK4 algorithm to take a step forward in time, using the values of η_1, η_2, N_1, N_2 and N_5 at the previous time step, to solve for the values of η_1, η_2 and N_5 at the next point in time. After the time step, we integrate the new distributions for η_1 and η_2 to get the new N_1 and N_2 values. Repeating this process, our final result is $\eta_1(x,t)$ and $\eta_2(x,t)$, and we can use Eq. B.2 to solve for $F(t)$.

B.1.4.2. *Analytical Approximation for Non-Steady-State.* Given both the x and t-dependence in the non-steady-state system (Eq. B.13), this system cannot be solved analytically. Instead, we develop the following moment approximation [Zahalak, 1981], which allows us to approximate the system of PDEs as a set of ODEs, which we can then optimize with greater efficiency.

Recall that $\eta_1(x,t)$ and $\eta_2(x,t)$ are the probability densities that myosin is weakly or strongly-bound, respectively, with a particular extension, x at time t. We assume the attachment rate varies exponentially with the energy required for myosin to bind with a particular extension, which means that the attachment rate is a normalized Gaussian function centered at 0. Thus, myosin molecules attach into a weakly-bound state based on this function, and so we approximate the η_1 distribution as a Gaussian function. For the strongly-bound cross-bridges, transition into this state occurs in the same manner, but detachment is force-dependent and favors smaller extensions, so we approximate the η_2 distribution with a Gaussian centered slightly to the right of 0. Throughout our approximation, we allow these means to vary when appropriate, but assume that their standard deviations are constant (this is equivalent to truncating our moment approximation).

Next, we implement a separation of time scales and solve the system on each interval. The force transient response suggests three time scales: 1) Pre-stretch: the muscle is activated and has reached steady-state, 2) Fast time: the stretch occurs at the start of this interval, all bound cross-bridges are stretched, and the fast weakly-bound cross-bridges re-adjust, and 3) Slow time: the

weakly-bound cross-bridges are in steady-state and the strongly-bound cross-bridges slowly adjust back from the stretched position.

We solve each time scale individually below. In the following, we use G to denote normalized Gaussian functions with mean μ so that $\int_{-\infty}^{\infty} G(x,\mu)dx = 1$.

Pre-Stretch/Isometric: Pre-stretch the muscle has been activated and allowed enough time to reach steady-state. We approximate the pre-stretch η distributions as described above,

$$\eta_1 = \alpha_1(t)G_1(x,0) \tag{B.14}$$
$$\eta_2 = \alpha_2(t)G_2(x,\mu_2^a(t))$$

Using these approximations, we can transform our system in Eq. B.13 into a system of ordinary differential equations:

$$\frac{d\alpha_1}{dt} = k_{w_0}^+ N_5 - (k_w^- + k_a)\alpha_1$$

$$\frac{d\alpha_2}{dt} = k_a\alpha_1 - \alpha_2 \int_{-\infty}^{\infty} k_D(x)G_2(x,\mu_2^a(t))dx$$

$$\frac{d\mu_2^a}{dt} = \frac{-\sigma^2\left[\mu_2^a\left(k_a\alpha_1 - \alpha_2\int_{-\infty}^{\infty} k_D(x)G_2(x,\mu_2^a)dx\right) + \alpha_2\int_{-\infty}^{\infty} xk_D(x)G_2(x,\mu_2^a)dx\right]}{\alpha_2\left(\int_{-\infty}^{\infty} x^2G_2(x,\mu_2^a)dx - (\mu_2^a)^2\right)} \tag{B.15}$$

$$\frac{dN_5}{dt} = k_w^-\alpha_1 + k_h^+(1-\alpha_1-\alpha_2-N_5) - (k_h^- + k_{w_0}^+)N_5$$

For the purposes of our calculation, we are only interested in the pre-stretch steady-state force. We solve the above system under steady-state conditions by implementing a non-linear root find and using Matlab's `fsolve` function. This gives steady-state values for α_1^{ss}, α_2^{ss}, $\mu_2^{a,ss}$ and N_5^{ss}. Finally Eq. B.2 can be used to calculate pre-stretch isometric force.

Fast Time: We assume that the stretch occurs at the start of this time scale. This means that the steady-state distributions of η_1 and η_2 are shifted by the amplitude of the stretch imposed, s. Throughout this fast time scale, the weakly-bound cross-bridges adjust back to steady-state, so the η_1 distribution adjusts from the stretched position back to be centered at 0. The strongly-bound cross-bridges act on a much slower time scale, and so we assume they are constant and are well-approximated by the Gaussian in the shifted position.

Under these conditions, our distributions become:

$$\eta_1 = A(t)G_1(x, \mu_1^b(t)) + (\alpha_1^{ss} - A(t))G_1(x, 0) \tag{B.16}$$
$$\eta_2 = \alpha_2^{ss} G_2(x, \mu_2^B)$$

with $A(0) = \alpha_1^{ss}$, $\mu_1^b(0) = s$, $\mu_2^B = \mu_2^{a,ss} + s$. Note that here, α_1^{ss}, α_2^{ss}, and $\mu_2^{a,ss}$ are the respective steady-state values from the previous solution for pre-stretch conditions.

On this fast time scale, we additionally assume that N_5 is in steady-state. This allows us to solve the system, and using the initial condition that $\eta_1(x, 0) = \alpha_1^{ss} G_1(x, s)$, we get an expression for η_1,

$$\eta_1 = \alpha_1^{ss} G_1(x, s) e^{-(k_w^- + k_a)t} + \frac{k_w^+(x) N_5^{ss}}{k_w^- + k_a}\left(1 - e^{-(k_w^- + k_a)t}\right) \tag{B.17}$$

And finally, we can again use Eq. B.2 to solve for $F(t)$ on this time scale.

Slow Time: On the final time scale, we assume that the weakly-bound cross-bridges have re-adjusted, and now the strongly-bound cross-bridges are adjusting from the stretched distribution back to steady-state. Thus, the η_1 distribution stays centered near 0, and the η_2 distribution begins in a shifted position and adjusts back to be centered near 0, as follows:

$$\eta_1 = a_1(t)G_1(x, 0) \tag{B.18}$$
$$\eta_2 = a_2(t)G_2(x, \mu_2^a(t)) + b_2(t)G_2(x, \mu_2^b(t))$$

with $a_1(0) = \alpha_1^{ss}$, $a_2(0) = 0$, $b_2(0) = \alpha_2^{ss}$, $\mu_2^a(0) = 0$, and $\mu_2^b(0) = \mu_2^{a,ss} + s$. Again, note that steady-state values refer to pre-stretch steady-state.

To solve this, we must assume that $\mu_2^a << \mu_2^b$, i.e. that the means of the two Gaussians for the stretched and un-stretched positions are far apart. This allows us to assume that there are neighborhoods around both μ_2^a and μ_2^b where they are separate, and can therefore be integrated independently.

We use these approximations in Eq. B.18 to transform the system of PDEs in B.13 into the following set of ODEs:

$$\frac{da_1}{dt} = k_{w_0}^+ N_5 - (k_w^- + k_a)a_1$$

$$\frac{da_2}{dt} = k_a a_1 - a_2 \int_{-\infty}^{\infty} k_D(x) G_2(x, \mu_2^a) dx$$

$$\frac{db_2}{dt} = -b_2 \int_{-\infty}^{\infty} k_D(x) G_2(x, \mu_2^b) dx$$

(B.19)

$$\frac{d\mu_2^a}{dt} = \frac{-\sigma^2 \left[\mu_2^a(t) \left(k_a a_1 - a_2 \int_{-\infty}^{\infty} k_D(x) G_2(x, \mu_2^a) dx \right) + a_2 \int_{-\infty}^{\infty} x k_D(x) G_2(x, \mu_2^a) dx \right]}{a_2 \left[\int_{-\infty}^{\infty} x^2 G_2(x, \mu_2^a) dx - (\mu_2^a)^2 \right]}$$

$$\frac{d\mu_2^b}{dt} = \frac{-\sigma^2 \left[-\mu_2^b \int_{-\infty}^{\infty} k_D(x) G_2(x, \mu_2^b) dx + \int_{-\infty}^{\infty} x k_D(x) G_2(x, \mu_2^b) dx \right]}{\int_{-\infty}^{\infty} x^2 G_2(x, \mu_2^b) dx - (\mu_2^b)^2}$$

$$\frac{dN_5}{dt} = k_w^- a_1 + k_h^+ (1 - a_1 - a_2 - b_2 - N_5) - (k_h^- + k_{w_0}^+) N_5$$

This system of ODEs is much faster to solve numerically than our original system of PDEs.

Thus, with the above approximation, we have separated the force transient behavior into three time scales, approximated the system of PDEs with a system of ODEs, solved numerically, and

calculated the resulting force. In total, we have an efficient method for approximating $F(t)$. Additionally, we find that this approximate solution is very close to the more accurate full numerical solution (Fig. B.2). Thus, this approximation is advantageous because it can be used to preliminarily fit force transient measurements, resulting in a very good approximation of best-fit parameters, which can then be used as an initial condition to optimizing the more accurate full RK4 numerical solution.

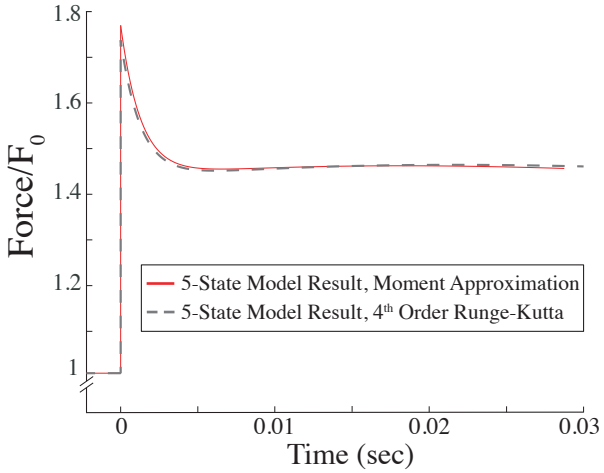

Figure B.2. Model simulation of a force transient response to a quick stretch: The model can be solved numerically using fourth-order Runge-Kutta (see section B.1.4.1) to provide an accurate result for force as a function of time (gray, dotted line). For efficiency, the model can additionally be approximated using separation of time scales and a modified moment approximation (see section B.1.4.2), resulting in a method of solving the system that is both a very good approximation to the numerical solution (red, solid line), and efficient enough to perform preliminary parameter optimizations.

B.2. Four-State Model + Viscous Drag

B.2.1. Weak binding acts as a viscous drag. In the motivation section of the main text, we begin by introducing a four-state model (Fig. 3.1A of main text) which has been previously shown to describe molecular muscle measurements and force-velocity measurements from muscle fibers [Walcott et al., 2012, Newhard et al., 2019]. Based on experimental evidence [Eisenberg and Hill, 1985, Brenner, 1987, Cooke and Holmes, 1986, Stein et al., 1979, Brenner et al., 1982, 1984], we hypothesize that this model must additionally include a weakly-bound interaction between actin and myosin, leading to the five-state model (Fig. B.1 and Fig. 3.1B of the main text). Given that weakly-bound myosin molecules rapidly bind and unbind from the actin filament without

undergoing a power-stroke [Brenner, 1987, Stein et al., 1979], and given that the rate constants for weak binding (k_w^- and k_a) do not depend on force, these cross-bridges act as a viscous drag on the system [Srinivasan and Walcott, 2009] (Fig. B.3). This provides us with another method of efficiently approximating the five-state model in force-velocity measurements: we can add a viscous drag to the four-state model.

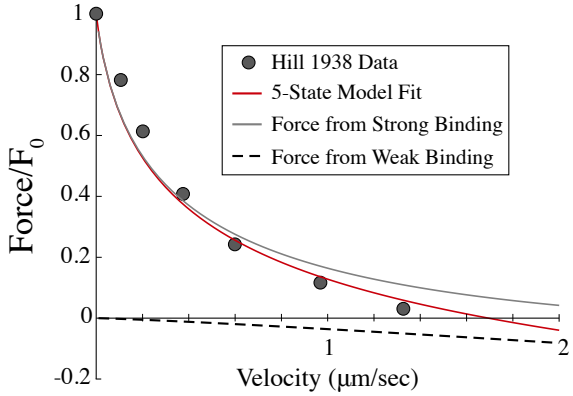

Figure B.3. Weakly-bound cross-bridges act as a viscous drag. The five-state model fits force-velocity measurements (red line, data from Hill [1938]). This total force is comprised of the force from strongly-bound cross-bridges (gray, solid line) and force from weakly-bound cross-bridges (black, dotted line). The linear relationship between force and velocity generated by the weakly-bound cross-bridges demonstrates that they act as a viscous drag on the system.

We initially use this method to fit the force-velocity data of A. V. Hill and the energetics data of W. O. Fenn, and to motivate the necessity of a weakly-bound state in the main text. To do so, we solve the four-state model to get force as a function of shortening velocity, and then subtract a linear function from this result. The slope of this line determines the amount of viscous drag, or equivalently, the amount of weakly-bound cross-bridges. With this force-velocity relationship, we can also calculate total energy as a function of force. We find that the four-state model with viscous drag is able to simultaneously fit Hill's force-velocity and Fenn's energetics data, motivating our hypothesis that weak binding is necessary to consistently model muscle measurements.

B.2.2. Parameter optimization and the four-state model. In addition to motivating our hypothesis, we used the four-state model with drag to identify parameters that can describe our own force-velocity measurements (Figs. 3.2D and 3.3B of the main text, and B.13B) because it has fewer parameters and is more computationally efficient than the five-state model. The parameter

combinations for the four-state model with drag were identified by fixing a particular amount of drag (i.e. amount of weakly-bound cross-bridges), and performing an optimization to determine the best fit ADP release rate (k_D^0) and force-dependent parameter (E). We use a matched asymptotic analytical solution to the four-state model to get close to the best-fit parameters, and then perform the final optimization using a numerical solution to the four-state model. We optimize using Matlab's `fminsearch`, and define the error as the sum of the squared difference between the model and measurements divided by the number of data points. In the four-state model at steady-state, E and k_D^0 are the only two unknown parameters. Our results are plotted as gray squares in Fig. B.4A.

This parameter optimization is much simpler than the equivalent optimization with the five-state model, which includes three additional unknown parameters (k_w^-, k_a, and $k_{w_0}^+$), which determine the time scale and amount of weak binding. In fact, the combinations of E and k_D^0 that fit the five-state model to force-velocity measurements are not unique, but are dependent on the time scale of weak-binding. Thus, to fit the five-state model, we must fix one of the weak-binding parameters (either k_w^- or k_a), which specified the time scale of weak binding, and then fit the other unknown parameters. By fixing E at different values, we get combinations of E and k_D^0 that result in good fits of the five-state model to the force-velocity measurements (colored symbols in Fig. B.4a).

These fits demonstrate two important results. First, we find that as the time scale of weak binding increases, the five-state model results approach those of the four-state plus drag (Fig. B.4). Second, when we violate the assumption that weak binding is fast compared to strong binding, the four-state model plus drag underestimates the ADP release rate necessary to fit our measurements, i.e. the k_D^0 values predicted from the the four-state model plus drag are a lower bound to those predicted by the five-state model. This latter fact is useful when we compare the five-state model fits to our force-velocity and force transient measurements. Because the best-fit k_D^0 value at a given E for the force transient measurements are always less than the equivalent k_D^0 value for our force-velocity measurements, the five-state model force-velocity fits will give parameters equivalent to, or worse than, those from the four-state plus drag. Therefore, for simplicity, we use the four-state plus drag force-velocity parameters (Figs. 3.2D and 3.3B of the main text, and B.13B) to compare to force transient results.

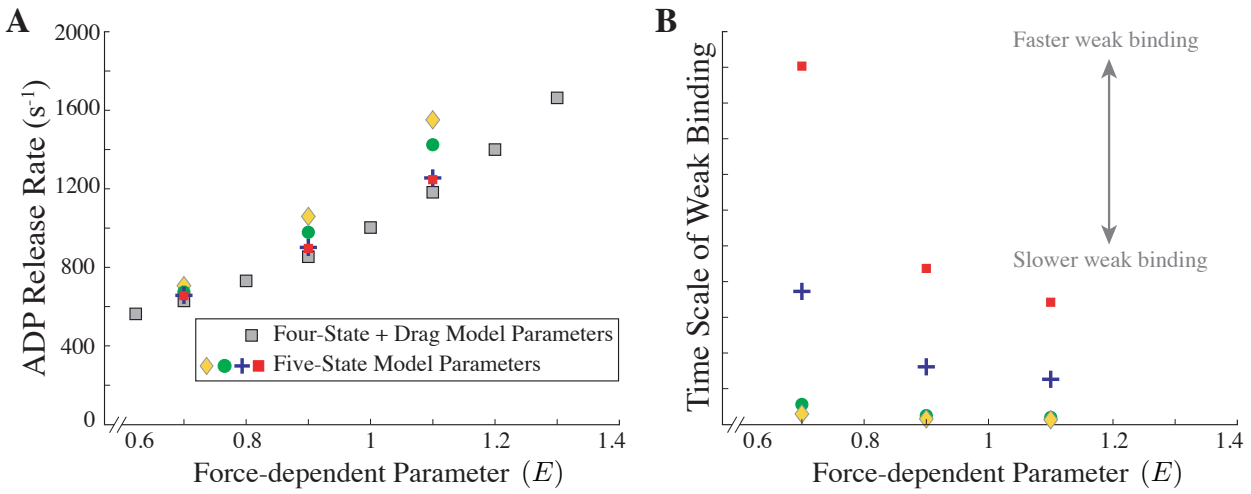

Figure B.4. As the time scale of weak-binding increases, the five-state model approaches the four-state model plus drag. **A:** Best-fit combinations of unloaded ADP release rate (k_D^0) and the force-dependent parameter (E) for the four-state model plus various amounts of drag (gray squares) and the five-state model with various weak-binding time scales (colored symbols). For each colored symbol, one of the weak binding parameters (k_w^- or k_a) was fixed along with the force-dependent parameter (E), and the other parameters were optimized. The four-state model parameters are a lower bound to the five-state results. **B:** This panel illustrates the weak-binding time scale corresponding to each colored symbol in panel A. As the time scale of weak binding increases, the five-state predictions in panel A approach those of the four-state model.

B.3. Weak Binding is Necessary for Consistent Force-Dependence: Modeling Classic Measurements of the Energetics of Muscle (Fenn 1923) and the Force-Velocity Relationship (Hill 1938)

In the main text, we motivate the necessity of a weakly-bound state in modeling the interaction between actin and myosin by fitting the four- and five-state models to classic measurements from W.O. Fenn (1923) and A.V. Hill (1938). Here, we discuss how we model these measurements, the details of the optimization, and the statistical significance of our results.

B.3.1. Modeling the energetics of muscle. In his work, W.O. Fenn measured energy liberation during muscle contraction. Experimentally, a muscle was maximally stimulated for a fixed time and allowed to shorten a fixed distance. Fenn measured the work done by the muscle and the heat produced as a function of the load imposed [Fenn, 1923].

To model this relationship, we first note that due to conservation of energy, total energy is equal to work done plus heat released. In our case, ATP hydrolysis fuels the cyclical interaction

between actin and myosin, so total energy is equivalent to the energy of ATP hydrolysis, which we call E_{ATP}. One molecule of ATP is hydrolyzed each time a myosin molecule completes the actomyosin cycle. Thus, the flux through an irreversible step of the cycle gives the rate of ATP consumption, which is proportional to the time derivative of E_{ATP} (the proportionality constant is the energy of ATP hydrolysis). We integrate this expression to get $E_{ATP}(v)$ where v is velocity. Additionally using our calculated force-velocity relationship, we have an expression for total energy as a function of force, which directly relates to Fenn's measurements.

Implementing the above with the five-state model, we find that weak binding has a minimal effect on this calculation. With the addition of weakly-bound cross-bridges, the muscle must do more work to overcome the resistive force of these cross-bridges. However, we find that the magnitude of this work is small compared to the work necessary for the muscle to raise the weight (Fig. B.5). Additionally, the magnitude of the overall work is small compared to the heat produced by the muscle. In Fenn's original measurements, the heat produced was an order of magnitude larger than the work done by the muscle [Fenn, 1923].

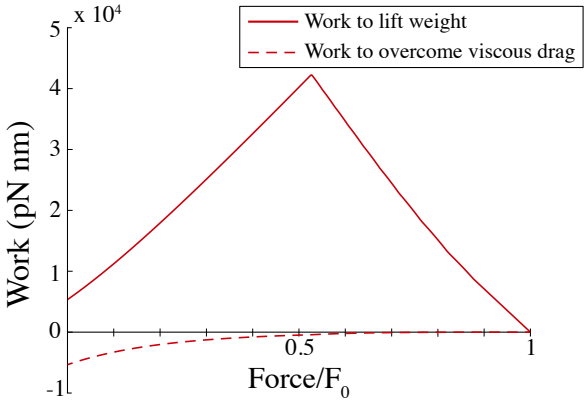

Figure B.5. Weak binding has a minimal effect on work done by a muscle. Simulating Fenn's experimental protocol using the five-state model results in work done by the muscle to lift the weight (red solid line) that is much larger than the work done to overcome resistive force from weakly-bound cross-bridges (dotted red line).

B.3.2. Fitting model to energetics and force-velocity data. To compare the model to Hill's force-velocity and Fenn's energetics data, we first solve for the model's force-velocity relationship (see section B.1). This is directly comparable to Hill's measurements. Next, based

on the above calculation, we solve for total energy as a function of force, which is comparable to Fenn's measurements.

We fit the four- and five-state models to the data [Hill, 1938, Fenn, 1923]. In the case of the energetics data, we multiply the normalized force data by 0.9. This gives a better fit between model and data, and we justify it by the fact that true isometric force of a muscle is extremely challenging to measure and is not directly reported in Fenn's paper. We perform fits to the data by simulating the model for a given parameter set, calculating the error as the sum of the squared difference between model and data divided by the number of data points, and optimizing using Matlab's `fminsearch`. When simultaneously fitting energetics and force-velocity data, we define the error as the sum of the individual errors, with the force-velocity error weighted slightly higher.

Because the four- and five-state models have two and four unknown parameters respectively, we tested whether the five-state model was a better fit with an F-test, which yields $p < 0.05$. We therefore conclude the five-state model gives a significantly better fit than the four-state. Additionally, we find that the five-state model fits are insensitive to one of the unknown parameters. Thus, if the five-state model differs from the four-state model by only one extra parameter, the difference between the two models is more significant.

B.4. Mismatch Between Force Transient Data and Model is not Unique to *Drosophila* Jump Muscle

In section 3.4.1 of the main text, we describe a discrepancy between our model predictions and our force transient measurements. In particular, our model predicts a peak force post-stretch (phase I) that is at least twice what we measure in *Drosophila* jump muscle. Importantly, the model prediction is a lower bound, since the calculation accounts only for force from strongly-bound cross-bridges that have undergone a power-stroke. Thus, if weakly-bound cross-bridges are also present, they will produce additional force once stretched, leading to an even larger discrepancy between model and measurements.

This difference is not unique to *Drosophila* jump muscle. In fact, measurements from a variety of vertebrates and a range of muscle fiber types result in peak forces that are similar to our

measurements (Fig. B.6, Galler et al. [1994, 1997], Straight et al. [2019], Ochala et al. [2006]). While some of the experimental measurements are above our predicted line, the majority are not. Additionally, since the predicted line is a lower bound, measurements must be well above this prediction to be fit by the model. If the weakly-bound state is significantly populated, we would expect peak forces to be higher than the predicted lower bound by a factor of 2 or more. Thus, of the fifteen measurements considered here, only four have the potential to be fit by the model (Vanzi et al. [1995], Piazzesi et al. [1997] and fiber types I and IIA from Galler et al. [1996]).

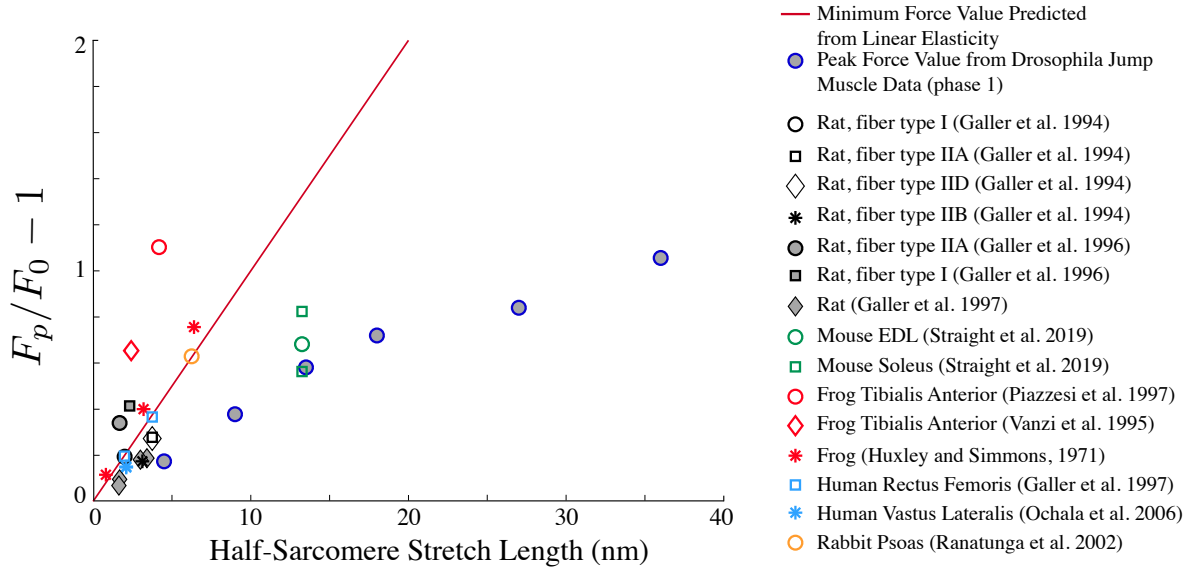

Figure B.6. Peak force above isometric force in transient response after rapid stretch (phase I) as a function of stretch size. Measurements from a variety of muscle fiber types are at or below the model's prediction.

B.5. Explanation 1: Overestimated Stretch Amplitude

In the main text, we discuss how our model, with the assumption of linear cross-bridge elasticity, is inconsistent with force transient measurements because the model predicts a peak force post-stretch that is significantly larger than that measured (Fig. 3.2B main text). In section 3.4.2, we present an argument against the possibility that this discrepancy is caused by an overestimated stretch amplitude at the sarcomere level due to series elasticity. Here, we provide further details on the computation that led to this conclusion.

B.5.1. Fitting model with decreased stretch amplitude. To fit the model to force transient measurements for the case of overestimated stretch amplitude, we allow the unknown model parameters to vary (k_w^-, k_a, k_D^0, E), and additionally include the stretch amplitude, Δs, as an unknown parameter. Note that in the force transient measurements, the force does not return to steady-state for long time, but instead remains slightly higher than the pre-stretch isometric value. Our model does not account for this residual force enhancement. Thus, in order to compare the model to the data, we must shift the force transient measurements so that the force returns to steady-state. To simulate the force transient, we solve the system numerically using RK4. To compare the results to our measurements, we define error as the sum of the squared difference between the model results and the shifted data divided by the number of data points, and optimize using Matlab's `fminsearch`.

We fit the model to a force transient measurement with a stretch amplitude of 0.5% muscle length (main text Fig. 3.2A). Assuming there is no effect of series elasticity, this corresponds to a 9 nm stretch at the half-sarcomere level. Our optimization results in a set of best-fit parameters, including a single best-fit value for the reduced stretch amplitude of $\Delta s = 0.437$ nm. The corresponding model fit is illustrated in Fig. 3.3A of the main text.

To estimate the range of Δs values that result in good fits to the data, we assume that the best-fit parameters give a perfect fit, and calculate the error in this case. We define the maximum acceptable error as $\sqrt{2} \cdot E_b$, where E_b is the error from the best-fit parameters. This gives us an estimate of the standard deviation of the best fit, and provides a benchmark for when the model is different from the data. We find that only a small range of significantly decreased stretch amplitudes ($\Delta s = 0.4 - 0.55$ nm) result in good fits to the force transient measurements (Fig. B.7).

B.5.2. Comparing parameter fits from force transient and force-velocity measurements. Next, to compare the model fits of force transient measurements to fits of force-velocity measurements, we consider combinations of two model parameters, unloaded ADP release rate (k_D^0) and the force-dependent parameter (E) (Fig. 3.3B of the main text). To determine the force transient parameters, we perform the same fits as above, but with the stretch amplitude fixed at the best fit value of $\Delta s = 0.437$ nm. For the force-velocity parameters, we perform fits to the

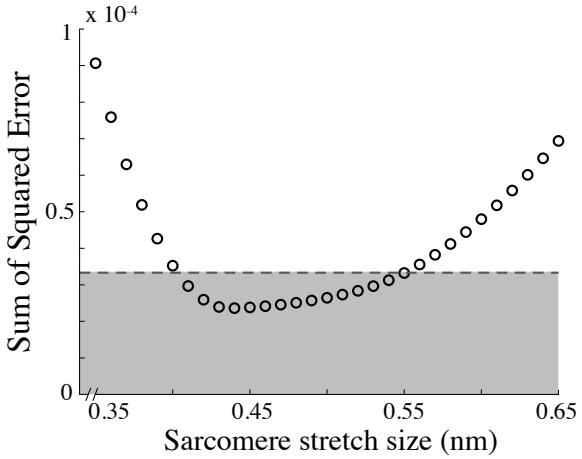

Figure B.7. Sum of the squared error as a function of the half-sarcomere stretch size. For each point, the stretch amplitude was fixed and the other parameters were optimized to fit the model to a measurement from a 0.5% muscle length stretch. Values within the shaded region are considered acceptable fits, and represent error that is within one standard deviation of the error produced by the best-fit parameters.

four-state model with various amounts of weak binding (see section B.2.2 for justification). In each case, error is defined as the sum of the squared difference between model and data divided by the number of data points, and Matlab's `fminsearch` is used for optimization.

We determine the variability in these parameters by optimizing the model to determine the best-fit parameters at a given E, and use this result to define an upper bound on the acceptable error (see section B.5.1). We sweep through k_D^0 values to determine a range that provides satisfactory fits to the data for the given E value. We perform this sensitivity analysis for both the force transient fits and the force-velocity fits (Fig. B.8).

B.5.3. Explanation 1 Extended: Strong binding cannot cause phase I and II of force transient response. In most of our analysis, we assume that phase I and II in the force transient response are attributed to weakly-bound cross-bridges that rapidly re-equilibrate post-stretch (Fig. 3.1F main text). However, it is also possible that the weakly-bound cross-bridges act on a faster time scale than the temporal resolution of the force transient measurements (i.e. the time between data points, $\Delta t = 0.125$ ms). In this case, weakly-bound cross-bridges re-equilibrate before the first measurement post-stretch, and phase I and II of the force transient response are

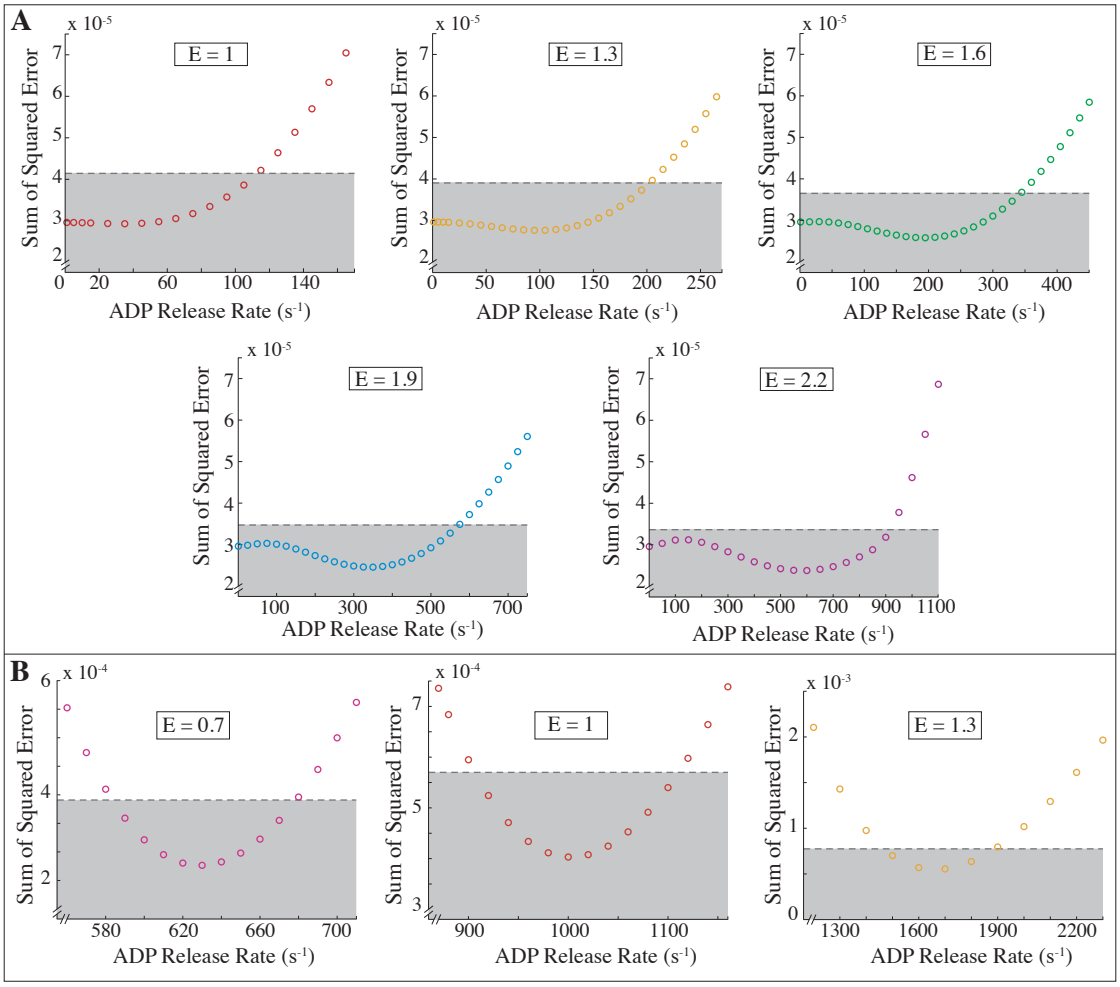

Figure B.8. Sensitivity analysis for fitting model to data. In each, the gray shaded regions denote acceptable error, and represent error that is within one standard deviation from the error produced by each best-fit. These results are used to determine the error bars in Figs. 3.2D and 3.3B of the main text, and Fig. B.13B. **A)** Sum of the squared error in fitting force transient measurements as a function of ADP release rate for a fixed force-dependence. For each panel, the five-state model (including Δs as an unknown parameter) is fit to the force transient measurement from a 0.5% muscle length stretch. **B)** Sum of the squared error in fitting force-velocity measurements as a function of ADP release rate for fixed force-dependence. For each panel, the four-state model plus drag was fit to force-velocity measurements.

solely due to strongly-bound cross-bridges. Then, phase III and IV would arise from some other mechanism that is not included in our model.

To test our assumption that phase I and II are due to weakly-bound cross-bridges, we tested the viability of the model as described above, with weakly-bound cross-bridges acting on a time scale faster that the resolution of the measurements. To do so, we implemented two fourth-order Runge-Kutta algorithms to solve for force as a function of time. The first begins at the instant of

stretch and iterates through time using a small time step ($\Delta t = 0.00625$ ms) until it reaches the first point in time post-stretch from our measurements, $t = 0.125$ ms. The second RK4 algorithm begins at this time point and iterates through time using a larger step size ($\Delta t = 0.05$ ms). In this way, we can capture the rapid response of the weak-binding cross-bridges without having to maintain a short, and computationally inefficient, time step. We fix two of the weak binding parameters (k_w^- and $k_{w_0}^+$) to be large enough so that the weakly-bound cross-bridges have re-equilibrated by the end of our first RK4 simulation. We can then compare the result of the second RK4 simulation with our force transient measurement, ensuring that the peak is solely due to strongly-bound cross-bridges.

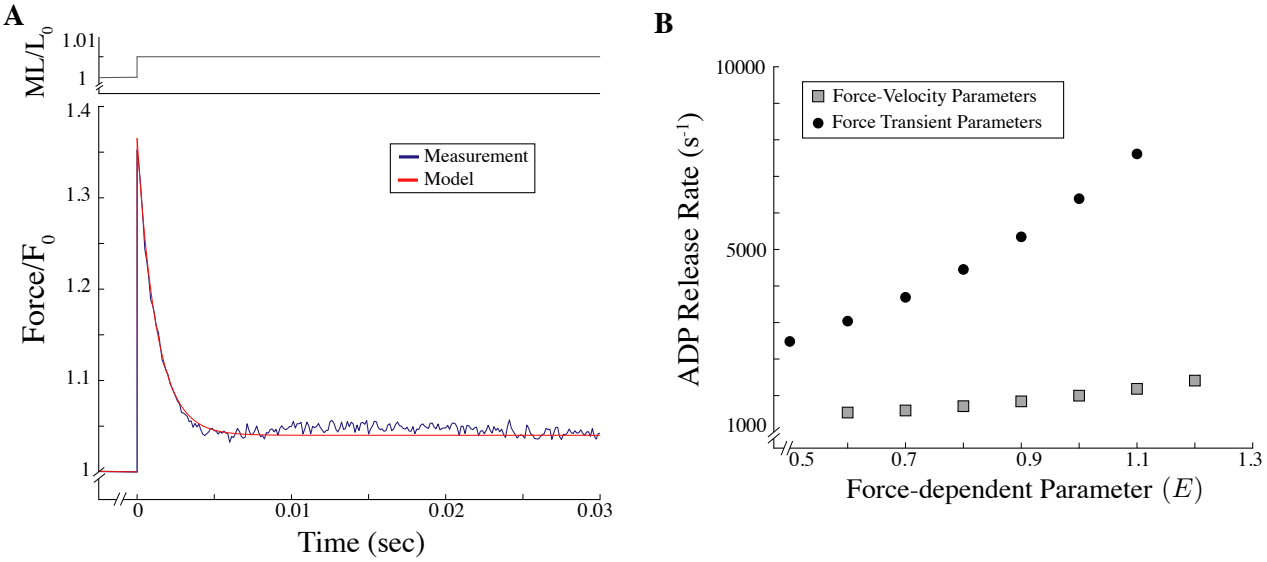

Figure B.9. The model cannot simultaneously fit the force transient and force-velocity measurements with the assumption that the peak in force post-stretch is solely attributable to strongly-bound cross-bridges. **A)** Assuming strong-binding causes the peak in force post-stretch, the five-state model can fit the derivative of the force transient trace for a 0.5% muscle length stretch. The corresponding force trace is reproduced here. The model result has been shifted to account for an offset in the result due to fitting the derivative. The best-fit parameters suggest a decreased stretch amplitude ($\Delta s = 3.61$) and a negligible force-dependence ($E = 0.01$). **B)** Combinations of unloaded ADP release rate and the force-dependent parameter that fit the force transient measurements under these conditions (black circles) are inconsistent with those required to fit force-velocity measurements (gray squares). To fit model to data, the weak binding parameters k_w^- and $k_{w_0}^+$ were fixed to be large, and the five-state model was fit to both the force-velocity and force transient measurements.

As with our other models, this model is inconsistent with the measured peak force from our force transient traces (main text Fig. 3.2B). We must therefore adjust for this discrepancy, and we do so by letting the stretch amplitude be a parameter of fit (see section 3.4.2 of the main text

for justification). Additionally, because phase III and IV of the force transient response would not be described by this model, we fit the derivative of the force transient trace. The advantage of this approach is that the derivative is invariant to the addition of a constant value being added to the force trace. Since phase III and IV act on a longer time scale that phase I and II, they are reasonably well approximated by a constant in this model.

With these assumptions and with this implementation, the model is able to fit our force transient measurements (Fig. B.9A). However, it requires a small force-dependence and large unloaded ADP release rate (best-fit gives $E = 0.01$ and $k_D^0 = 830.07$ s^{-1}) to be able to reproduce the timescale of phase I and II. As we fix E and optimize the fit to the data, we find that the predicted ADP release rate is too large to be consistent with the fits to our force-velocity measurements (Fig. B.9B). Thus, phase I and II are too fast to be due to strongly-bound cross-bridges, and we conclude that the peak force cannot be attributed to detachment of strongly bound cross-bridges in this manner.

B.6. Explanation 2: Unexplained Force

In section 3.4.3 of the main text, we briefly present an argument against the presence of an additional force, not due to actin and myosin, in the force transient measurements. Here, we discuss our methods (sections B.6.1, B.6.2, B.6.3, B.6.4) and findings (section B.6.5) in more detail.

B.6.1. Passive force in force transient measurements. When we consider that the force transient measurements may include additional non-cross-bridge forces, one possibility is that passive elements in the muscle fiber are contributing to the measured force. Our model only accounts for force from cross-bridge interactions, and therefore would not reproduce passive force.

To control for this, we perform the force transient measurements at low calcium concentrations (pCa 8.0). At this low calcium concentration, there is very little cross-bridge cycling, and thus any force produced can be attributed to passive elements. We find that the force produced for pCa 8.0 is negligible compared to that produced at a saturating calcium concentration of pCa 5.0 (Figs. B.10A, B). In particular, we find that the pre-stretch isometric stress value for pCa 5.0 is 15 - 20 times greater than the pre-stretch isometric stress value for pCa 8.0 (Fig. B.10C). Notably, this difference

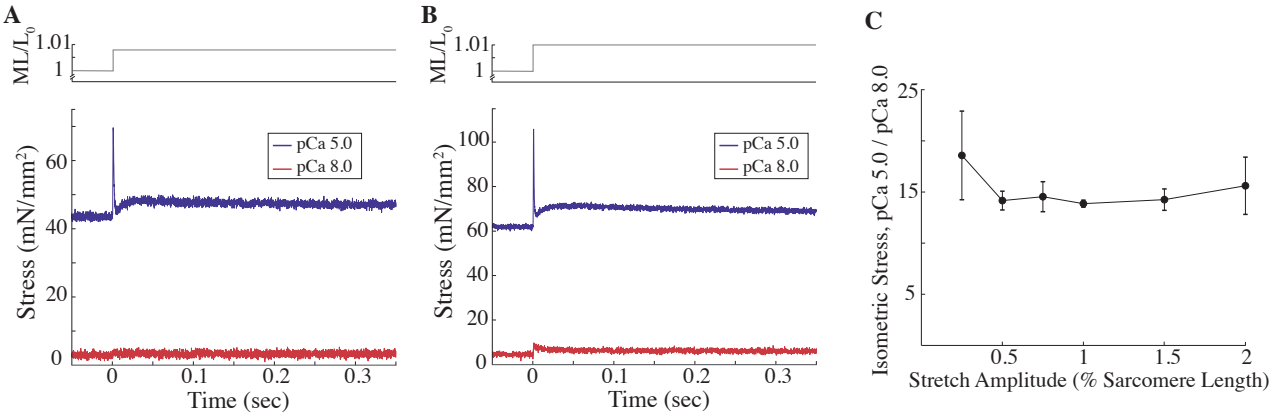

Figure B.10. Passive stress produced for pCa 8.0 is negligible compared to active stress produced at pCa 5.0. **A**, **B)** Stress (mN/mm^2) as a function of time (sec) for muscle fibers quickly stretched a small percentage of their length (A: 0.75% ML, B: 1% ML) at saturating calcium concentration of pCa 5.0 (blue) and low calcium concentration of pCa 8.0 (red). **C)** Ratio of pre-stretch isometric stress at pCa 5.0 compared to that at pCa 8.0 at various stretch amplitudes. Each data point includes values from two fibers. Together, these plots illustrate that the passive force produced at low calcium concentrations is negligible, and about 15 times less than that produced at saturating concentrations.

in magnitude is present for all of the fibers and at every stretch amplitude we considered, confirming that the force from passive elements is negligible across all of our experimental conditions.

B.6.2. Adjusting model to include non-cross-bridge force. While the above experiments show that purely passive elements are not contributing significantly to force, there is evidence that some elastic elements in muscle stiffen in the presence of calcium [Labeit et al., 2003] or that non-cross-bridge elements can contribute to force [Leonard and Herzog, 2010]. It is possible, then, that the contribution of these elements to muscle force underlie the discrepancy between our measurement of peak force, and that predicted by Eq. 3.1 of the main text, reproduced below:

$$\frac{F_p}{F_0} = \frac{(\mathcal{S}+d)\kappa}{d\kappa} = \frac{\mathcal{S}}{d} + 1 = \frac{1800 \cdot s\%}{d} + 1 \tag{B.20}$$

where κ is myosin's stiffness, d is myosin's step size, F_p is peak force post-stretch, F_0 is pre-stretch isometric force, and $\mathcal{S}$ is stretch length:

We call the force produced by these non-cross-bridge elements an "unexplained force". To account for this, we let it be a parameter in the model. Additionally, we let this value be different

pre- and post-stretch. Thus, the force calculation in Eq. B.20 becomes,

$$\frac{F_p}{F_0} = \frac{F_{xb}^p + F_{nc}^p}{F_{xb}^0 + F_{nc}^0} \tag{B.21}$$

where F_{xb}^0 and F_{xb}^p are the cross-bridge forces pre- and post-stretch, and F_{nc}^0 and F_{nc}^p are the non-cross-bridge forces pre- and post-stretch, respectively. While this initially introduces two new parameters to the model, we can use the following calculation to reduce it to just one new parameter.

The model predicts that for long time after stretch, the force from cross-bridges will be equal to the pre-stretch cross-bridge isometric force. In the force transient data, however, the post-stretch steady-state value is slightly higher than the pre-stretch value. We must account for this residual force enhancement [Koppes et al., 2015], which would not be reproduced by these models [Walcott and Herzog, 2008] and would therefore lead to inaccurate parameter estimation. We account for this, and reduce the number of parameters-of-fit, with the following calculation, where F^* denotes the post-stretch steady-state value normalized to the pre-stretch steady-state in the data:

$$\lim_{t\to\infty} \frac{F_p}{F_0} = \frac{F_{xb}^0 + F_{nc}^p}{F_{xb}^0 + F_{nc}^0} = F^* \tag{B.22}$$

The force transient measurements determine the F^* value, and thus we can solve for F_{nc}^p in terms of F_{nc}^0. Thus, to account for this non-cross-bridge force, we fit the force transient measurements to,

$$\frac{F_p}{F_0} = \frac{F_{xb}^p + F^*(F_{nc}^0 + F_{xb}^0) - F_{xb}^0}{F_{xb}^0 + F_{nc}^0} \tag{B.23}$$

where the cross-bridges forces are determined from the five-state model and F_{nc}^0 is an additional parameter of fit that determines the amount of unexplained force due to non-cross-bridge effects.

B.6.3. Fitting model with unexplained force. To fit the model to the force transient measurements for the case of unexplained force, we allow the unknown model parameters to vary (which now includes the parameter for additional unexplained force, F_{nc}^0). Note that in this case, we fix the stretch amplitude to be at the true experimental value. We use RK4 to solve the system for force as a function of time, define error as the sum of the squared difference between model and data divided by the number of data points, and use Matlab's `fminsearch` to optimize the parameters.

The optimization results in a set of best-fit parameters, including a best-fit value for F_{nc}^0. To determine the range of F_{nc}^0 values that can result in good fits to the data, we bound the error by $\sqrt{2} \cdot E_b$, where E_b is the best-fit error (see section B.5.1). We find that only a small range of values for F_{nc}^0 result in acceptable errors (Fig. B.11A).

Additionally, to consider the plausibility of these results, we compared the unexplained force values, F_{nc}^0, to the isometric force from cross-bridges, F_{xb}^0 (Fig. B.11B). Note that the isometric cross-bridge force changes for different amounts of unexplained force. Thus, normalizing F_{nc}^0 by F_{xb}^0 results in multiple error values for the same ratio of unexplained force to cross-bridge force (Fig. B.11B). However, there is a clear minimum and a single error value for each choice of unexplained force (Fig. B.11A). This best-fit unexplained force is 28.07 times that of isometric force from cross-bridges, and that parameters that result in acceptable error predict an unexplained force that is 27 - 28.3 times that of isometric. We conclude that it is unreasonable to expect that force transient measurements include an unexplained force of this magnitude.

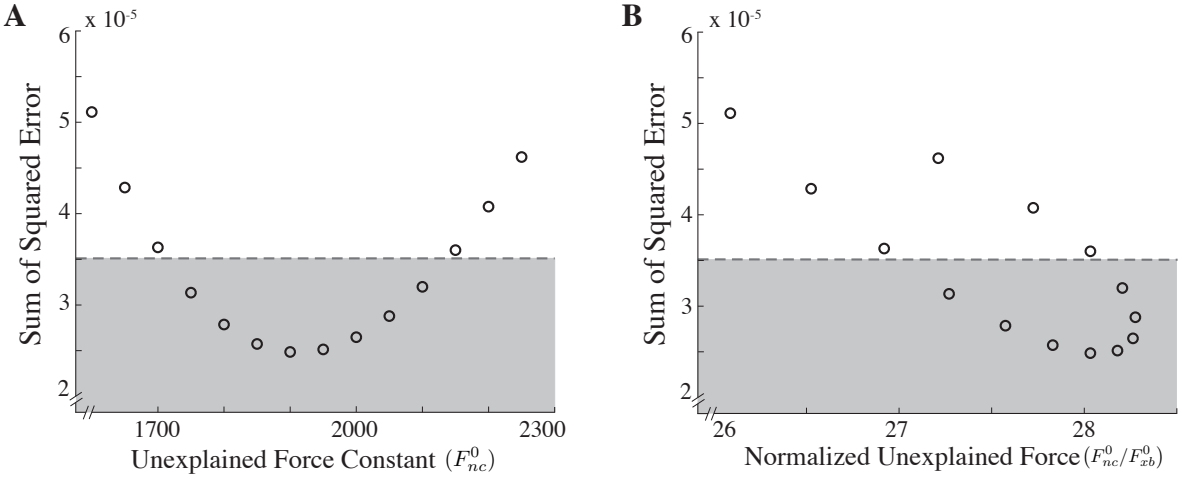

Figure B.11. Sum of the squared error as a function of: **A)** the unexplained force value, F_{nc}^0, and **B)** the unexplained force value normalized to pre-stretch isometric cross-bridge force, F_{nc}^0/F_{xb}^0. For each point, the F_{nc}^0 value was fixed, and the five-state model was fit to the force transient measurement. Values of F_{nc}^0 that result in acceptable error lie in the shaded box, which denotes error that is within one standard deviation of the best fit. The best-fit values suggest that the non-cross-bridge forces are around 28 times that of isometric cross-bridge force.

B.6.4. Comparing parameter fits from force transient and force-velocity measurements. We also compared the force transient fits to the force-velocity fits under these conditions. For the force transient measurements, we let the unknown parameters (including F_{nc}^0) vary, and determine the best-fit combinations of ADP release rate and force-dependence. The force-velocity parameters are based on the four-state plus drag fits (see section B.2.2 for justification). In both cases, error is defined as the sum of the squared difference between model and data divided by the number of data points, and Matlab's `fminsearch` is implemented for optimization. Additionally, we perform a sensitivity analysis (see section B.5.1) to consider the variability in acceptable parameters due to noise in the data (Fig. B.12).

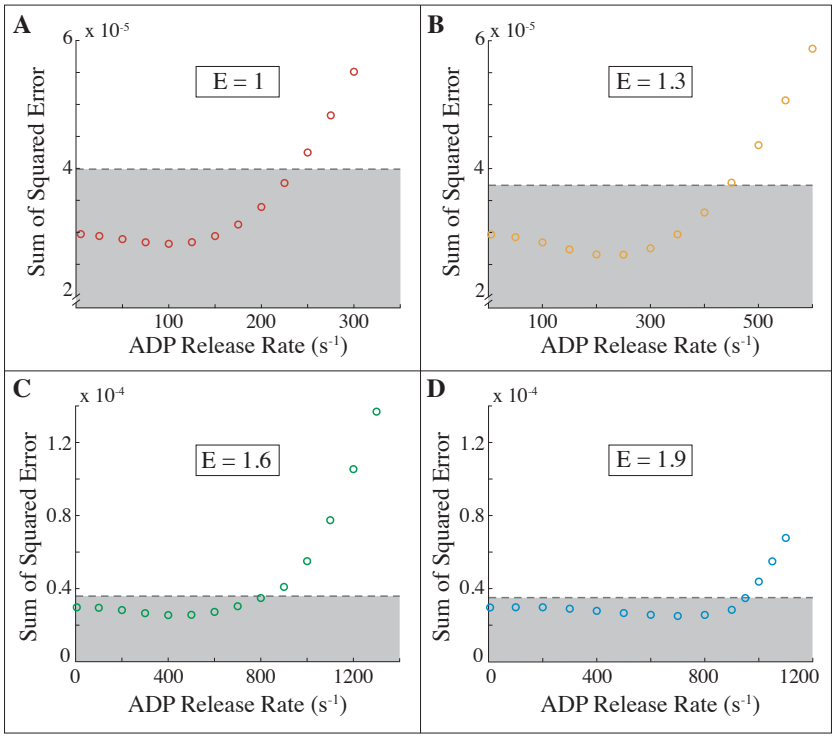

Figure B.12. Sum of the squared error in fitting force transient measurements as a function of ADP release rate for a fixed force-dependence. For each panel, the five-state model (including F_{nc}^0 as an unknown parameter) is fit to the force transient measurement from a 0.5% muscle length stretch. The gray shaded regions denote acceptable error, and represent error that is within one standard deviation from the error produced by each best-fit. This sensitivity analysis leads to the error bars on the force transient measurements in Fig. B.13B.

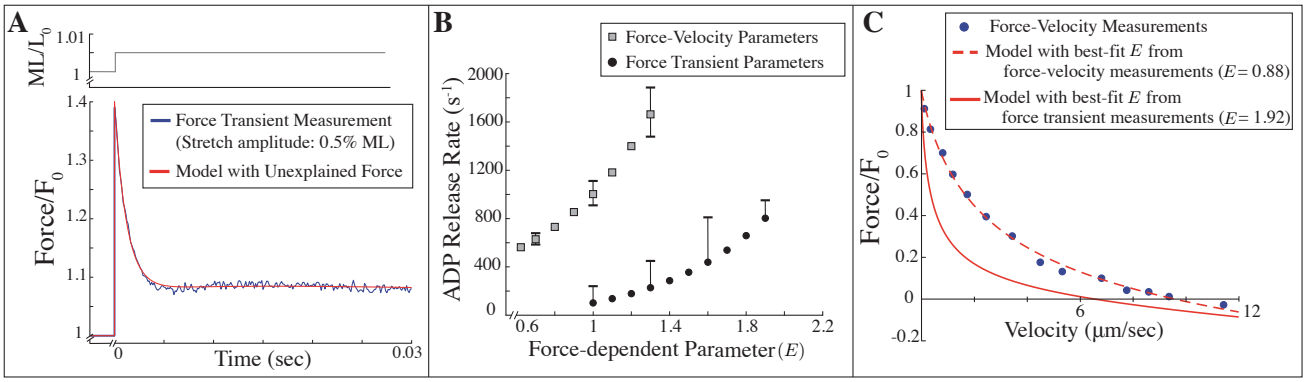

Figure B.13. The model reproduces the force transient measurements given the addition of a non-cross-bridge force, but the results are inconsistent with force-velocity measurements. **A)** Including an unexplained force in the force response that is 28.1 times that of isometric cross-bridge force allows the five-state model to fit force transient measurements. **B)** Combinations of unloaded ADP release rate and the force-dependent parameter that fit force-velocity (gray squares) and force transient (black circles) measurements when the force transient includes a non-cross-bridge force. Error bars denote parameter values that give results within one standard deviation of the best-fit error. **C)** Model fits to force-velocity measurements with k_D^0 fixed from the best-fit to the force transient measurement, and E from the best-fit to the force transient measurement (sold line) and best-fit to the force-velocity measurements (dashed line).

B.6.5. Rejection of unexplained force as explanation for model and measurement discrepancy. Comparing the five-state model with an unexplained force to our force transient measurements, we find that the optimization converges to a good fit to the entire force transient measurement, reproducing all parts of the force response (i.e., phases I-IV, Fig. B.13A). However, we reject this explanation for two reasons. The first is that the best-fit predicts an implausibly large unexplained force of about 28 times that of the isometric force from cross-bridges (Fig. B.11B).

The second reason we reject unexplained force as the source of the discrepancy between simulation and measurement is that the force-dependence required for the force transient fits is inconsistent with the force-dependence required for the force-velocity fits (Fig. B.13B). In particular, the force transients require a large force-dependence that results in a force-velocity relationship that is too curved (Fig. B.13C). This result is similar to our fits with decreased stretch amplitude due to series elasticity (main text Fig. 3.3B). In that case, the model required an increased force-dependence (i.e. larger E) to counteract the decreased stretch amplitude and to produce phase III of the force transient response (see main text, section 3.4.2). However, in the case of unexplained force, our fits have the full stretch amplitude, so we expected to see a leftward shift (toward smaller values of E) in the best-fit parameters for our force transient measurements, and therefore better agreement

with the best-fit parameters for our force-velocity measurements. Indeed, we observed such a shift (compare main text Fig. 3.3B to Fig. B.13B), but it is modest and insufficient to allow us to find a single parameter set to fit both of our measurements.

These fits still require a large force-dependence because of the large magnitude of the unexplained force. In the normalized force transient response, the amplitude of force increases (phase I and III) is measured relative to the total isometric force. Thus, if isometric cross-bridge force makes up less of the total isometric force, the amplitude of phases I and III relative to the isometric cross-bridge force increases. For example, we measured a peak force (phase I) of ~ 1.4 times isometric, which is $\sim 40\%$ above isometric force (main text Fig. 3.2A). If all force arises from cross-bridges, then this peak force results in a $\sim 40\%$ increase in cross-bridge force. However, suppose that isometric force is half due to cross-bridges and half due to an unexplained force. In this case, the increase in force due to cross-bridges will still be $\sim 40\%$ of the total isometric force but, since cross-bridges only account for half of the isometric force, this would correspond to an $\sim 80\%$ increase in cross-bridge force, and a peak force of ~ 1.8. A similar amplification occurs with phase III. This latter effect is particularly important, because for the model to fit a larger phase III, it requires a larger decrease in ADP release rate, and an increase in force-dependence (i.e. a larger E). Thus, while the full stretch amplitude in these fits results in a smaller force-dependence compared to our fits with decreased stretch amplitude (compare main text Fig. 3.3B to Fig. B.13B), this effect is mostly opposed by the large amount of unexplained force which requires larger force-dependence to fit the increased amplitude of phase III relative to isometric cross-bridge force (Fig. B.13B). Thus, we reject the explanation that including an unexplained force due to non-cross-bridge effects is the sole reason for the discrepancy we see between model and measurement.

B.7. Alternative Model Assumptions

Given the inconsistency between our measurements and our four- and five-state models, we conclude that at least one of the model assumptions is wrong. Thus, we considered the model assumptions to see if adjusting any would provide a solution to the discrepancy between model and data. We discuss these assumptions below, including the effects of non-linear elasticity of myosin,

force-dependence of weak-binding kinetics and thin-filament activation. Notably, we found that none of these effects is likely to explain the discrepancy.

B.7.1. Non-linear elasticity. One of the key model assumptions is that myosin acts as a linear spring with constant stiffness, κ, leading to a linear force-displacement relationship, $F(x) = \kappa x$. While there is some experimental evidence to support this assumption [Linari et al., 2020], there is also evidence to suggest that myosin's stiffness may be significantly lower when the molecule is compressed [Kaya and Higuchi, 2010], leading to a non-linear force-displacement curve for myosin.

We expected that such non-linear elasticity might improve the agreement between the model and our measurements. In particular, the decreased stiffness during compression would decrease resistive drag during shortening [Brizendine et al., 2015], leading to higher shortening velocities. Thus, at a given value of E, this model would need a smaller ADP release rate to counteract the increase in velocity. This would result in a downward shift in the best-fit parameters of the force-velocity fits (Fig. 3.3B main text and Fig. B.13B). Because cross-bridge stiffness during lengthening does not change, we expected drag during lengthening to remain largely unaffected, and therefore the best-fit parameters of the force transient fits to remain the same. To test this idea, we implemented non-linear myosin elasticity in our model.

To include non-linear elasticity in the model, we defined myosin's force-displacement curve to be piecewise linear, with a much smaller slope (i.e. lower myosin stiffness) for negative displacements compared to positive displacements (Fig. B.14B inset). Thus, with myosin's stiffness given by $\kappa(x)$, we get a force-displacement relationship of $F(x) = \kappa(x) \cdot x$. Additionally, in the model, myosin's probability of binding to actin with a given initial displacement depends on the negative exponential of the potential energy required to achieve that displacement (see [Walcott et al., 2012] for a discussion of this assumption). Therefore, since the force-extension function and the potential energy-extension function are related (the former is the negative derivative of the latter), when we modify the force-extension function to be non-linear, we must also modify the attachment rate as a function of extension.

We implement this as follows. Let $V(x)$ denote the potential energy. Since force is the negative derivative of the potential energy, we have

$$F(x) = -\frac{dV}{dx} \quad \Rightarrow \quad V(x) = -\int F(x)dx$$

We assume that the attachment rate is the negative exponential of the potential energy. Therefore, we get the following expression for attachment rate:

$$\begin{aligned} \kappa_w^+(x) &= k_{w_0}^+ \mathcal{C} \exp\big(-V(x)\big) \\ &= k_{w_0}^+ \mathcal{C} \exp\left(\int F(x)dx\right) \\ &= k_{w_0}^+ \mathcal{C} \exp\left(\int \kappa(x)\, x\, dx\right) \end{aligned} \tag{B.24}$$

where $\mathcal{C}$ is chosen so that $\int_{-\infty}^{\infty} \kappa_w^+(x)dx = k_{w_0}^+$.

With addition of this non-linearity, the system cannot be solved analytically. Instead, we solve the system numerically, taking care to appropriately define the non-linearity as described above. To solve for the force-velocity relationship, we implement an ODE solver in Matlab (`ode15s`) and solve the system under steady-state conditions. To solve for the force transient response with stretch, we implement fourth-order Runge-Kutta to solve the system for all x, at each point in time.

Surprisingly, we found that non-linear elasticity did not improve the agreement between our model and the measurements. This lack of agreement arises from the interaction of two competing effects, 1) the expected decrease in drag, and 2) an unexpected decrease in effective power-stroke size. This latter effect arises because, when myosin's stiffness in compression is decreased, the amplitude of the thermal excursions due to Brownian motion increase. Because myosin's stiffness is asymmetric, these thermal excursions are asymmetric, making it more likely for myosin to bind with non-zero compression. Then, when the myosin molecule undergoes its power-stroke, this initial compression decreases the effective power-stroke size.

The competition between these two effects is apparent in our simulated force-velocity curves. When the decrease in stiffness for compressed myosin is small, the decrease in drag is the dominant effect. We see this as both an increase in force for a given velocity value and an increase in unloaded shortening velocity, $v_{\max}$, as we expected (Fig. B.14A and inset, respectively). However,

when myosin's stiffness is decreased more significantly in compression, the reduction in effective power-stroke size becomes the dominant effect. We see this as a decrease in force and unloaded shortening velocity, $v_{\max}$, compared to the previous case (Fig. B.14A and inset, respectively). Thus, while non-linear myosin stiffness increases shortening rate for a given E, this effect is limited.

Additionally, although we had anticipated a minimal effect of non-linear myosin stiffness on the force transient after stretch, we observed a large effect. Non-linear myosin elasticity shifts the best-fit parameters toward a larger force-dependence at a given ADP release rate, resulting in a rightward shift in the best-fit parameters (Fig. B.14B) and thus worse agreement with the best-fit force-velocity parameters. This result is due to the decrease in effective power-stroke size, which has a similar effect as decreased stretch amplitude due to series elasticity discussed earlier (section 3.4.2 in main text). In particular, in the model the delayed increase in force in the force transient response (phase III), arises from strongly-bound cross-bridges detaching more slowly post-stretch, due to the force-dependence of ADP release. The effective reduction in power-stroke size decreases the force each myosin molecule exerts and, therefore, to maintain the phase III response for non-linear elastic cross-bridges, the force dependence of ADP release must increase. We therefore conclude that non-linear myosin elasticity is unlikely to explain the difference we observe between our model and measurements.

B.7.2. Force-dependent detachment of weakly-bound cross-bridges. In our original four- and five-state models, we assume that the only force-dependent rate constant is the ADP release rate. We make this assumption because the force-dependence in this transition has been directly observed and characterized [e.g. Veigel et al., 2003, Kad et al., 2007]. However, measurements with an ultra-fast optical trap suggest additional force-dependence in the transition from a weakly-bound state to an unbound state (i.e. state 1 to state 5 in Fig. B.1) [Capitanio et al., 2012]. To understand whether this force-dependence could explain the discrepancy between model and measurement, we explored its effect on the model.

We can gain an intuition for the effect of force-dependent detachment of weakly-bound cross-bridges by looking at a simplification of the five-state model. If weak binding is fast compared to the other state transitions, then the original five-state model (without force-dependent detachment

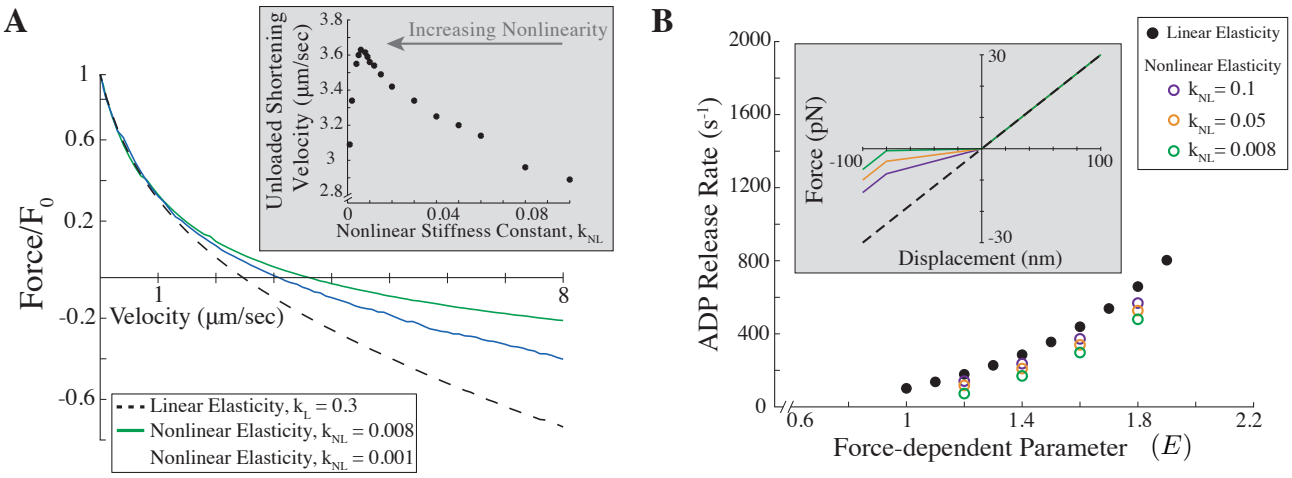

Figure B.14. Non-linear elasticity of myosin does not explain the discrepancy between model and data. **A**) Force-velocity relationship for linear (dashed line) and non-linear (solid lines) cross-bridge elasticity. Inset: unloaded shortening velocity $v_{\max}$, as a function of non-linear stiffness, illustrating that $v_{\max}$ increases and then decreases as the non-linear stiffness of myosin becomes more significant. **B)** Combinations of unloaded ADP release rate and the force-dependent parameter for linear (solid circles) and non-linear (open colored circles) cross-bridge elasticity. Inset: Force as a function of displacement for linear (dashed line) and non-linear (solid lines) cross-bridge elasticity with varying degrees of non-linearity.

of weakly bound cross-bridges) reduces to the four-state model with an additional viscous drag from the weakly-bound cross-bridges (Fig. B.15A, see section B.2). If weakly-bound cross-bridges detach more rapidly with increasing force [Capitanio et al., 2012], then the weakly-bound cross-bridges display shear-thinning behavior [Srinivasan and Walcott, 2009]. That is, the viscous drag constant decreases as shortening rate increases, leading to less drag force at higher shortening velocities (Fig. B.15B).

Rather than decreasing the disparity between the model parameters that generate good fits to our force-velocity and force transient measurements, such shear-thinning behavior has the opposite effect. Specifically, shear-thinning drag increases the slope of the best-fit parameters for the force-velocity data, shifting them further from the best-fit parameters for the force transient data (Fig. 3.3B in main text and Fig. B.13B). This is because, as discussed in our model fits to Hill's measurements (Section B.2.1), weakly-bound cross-bridges decrease the curvature of the force-velocity relationship. Thus, as we increase the amount of weak binding, we can generate good fits to force-velocity data with an increasing amount of force dependence (Fig. 3.2C in main

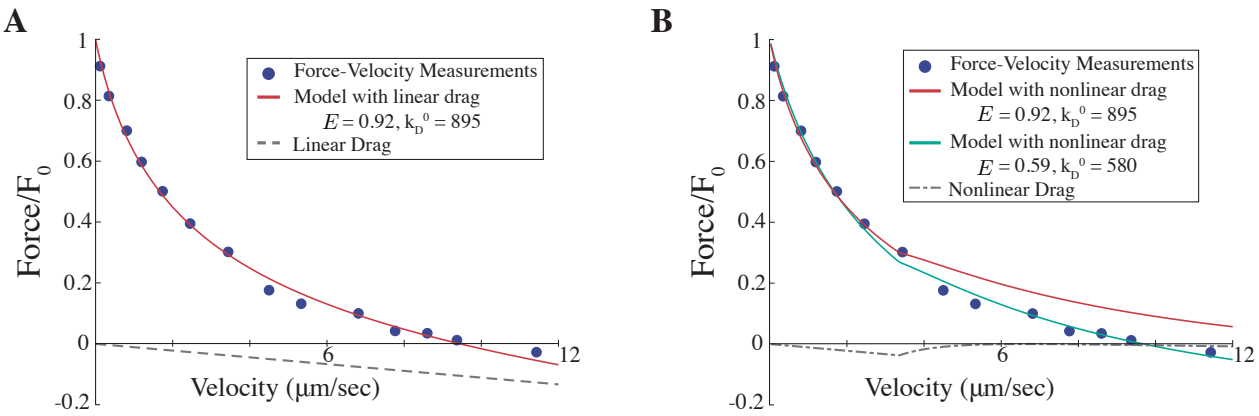

Figure B.15. Force-dependent detachment of weakly-bound cross-bridges does not explain the discrepancy between model and data. **A)** Force-velocity measurements fit with the four-state model plus viscous drag. The force from weakly-bound cross-bridges is linear with velocity (dashed line). **B)** Force-velocity measurements fit with four-state model with force-dependent detachment from the weakly-bound state. The force from weakly-bound cross-bridges is decreased at higher shortening velocities (dash-dotted gray line), providing a poor fit to the measurements (red line). The model can fit the measurements with this non-linear drag (green line), but requires a smaller force-dependence and a smaller unloaded ADP release rate.

text). Shear-thinning drag, however, is less effective in decreasing the curvature of the force-velocity curve, since the decrease in force at higher shortening velocities introduces additional curvature (Fig. B.15B). Thus, fitting our force-velocity measurements with a model that includes force-dependent detachment requires less force dependence and a smaller unloaded ADP release rate, which ultimately shifts the best-fit parameters up and left, further away from the best-fit parameters for our force-transient measurements (Fig. 3.3B in main text and Fig. B.13B). We therefore conclude that force-dependent detachment of weakly-bound cross-bridges is unlikely to explain the difference we observe between our model and measurements.

B.7.3. Thin-filament activation. Our cross-bridge models assume that one myosin's rate of strong binding (the transition from state 1 to state 2 in Fig. B.1) does not depend on whether neighboring myosin are bound. This assumption would be violated if thin-filament activation contributes to the force transient response [e.g. Greene and Eisenberg, 1980]. This mechanism is thought to occur in cardiac muscle [Campbell and Chandra, 2006, Stelzer et al., 2006]. Once a myosin molecule binds strongly to actin, it locally deforms the tropomyosin filament and facilitates the binding of nearby myosin (e.g. [Longyear et al., 2017, Craig and Lehman, 2001, McKillop and

Geeves, 1993]). The longer myosin is strongly bound to actin, the greater this effect, so that under conditions of low ATP (which extends myosin's strong binding lifetime), thin filaments can be activated at low calcium [Bremel and Weber, 1972, Kad et al., 2005]. If, as predicted by the model, phase III of the force transient response arises from strongly bound myosin whose attachment lifetime is prolonged due to the stretch imposed on the muscle fiber, this activation effect would amplify the response and increase phase III. In other words, if thin-filament activation contributed to phase III, then the model may be able to fit the data with a smaller force-dependence, which would then be more consistent with the force-dependence needed to fit our force-velocity measurements. It is therefore possible that the lack of this effect in the models is responsible for their inability to simultaneously fit our force-velocity and force transient measurements.

To test this idea, we implemented our five-state cross-bridge model with a previously developed model that includes thin-filament activation through local coupling of myosin molecules [Longyear et al., 2017]. This model includes one key parameter, ε, that describes the rate at which a single myosin molecule binds divided by the rate at which it binds in the absence of regulation. By tuning this parameter, we can effectively change the amount of local coupling between neighboring

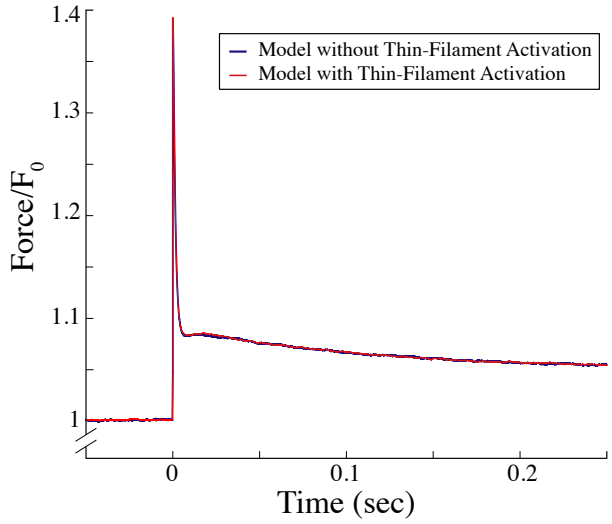

Figure B.16. Thin-filament activation does not have a significant effect on force transient results. Simulating the five-state cross-bridge model including thin-filament activation using a modified Gillespie algorithm (red line) gives nearly the same results as the five-state cross-bridge model without activation (blue line).

myosin molecules. Intuitively, we expected that increasing the amount of thin-filament activation (i.e. decreasing ε) should increase the magnitude of phase III.

Unlike the differential equation simulations presented thus far, we now use a Monte Carlo simulation to implement both the activation model and our five-state cross-bridge model. In particular, we use a modified Gillespie algorithm to iterate the system throughout time, keeping track of the force produced by the myosin molecules as a function of time. We use the parameters from our five-state model best-fit to the force transient assuming the presence of an unexplained force (as in Fig. B.13a), and adjust the force result to account for the non-cross-bridge force. We find that, even with an unreasonable amount of myosin coupling ($\varepsilon = 0.1$), the model gives nearly the same result with and without thin-filament activation (Fig. B.16). Thus, we conclude that thin-filament activation does not play a large enough role in the force transient response to solve the disparity between fitting our two measurements.

B.8. Model with Force-Dependent Detachment of Weakly-Bound Cross-Bridges and Series Elastic Element

To compare this model to our force transient measurements, we must numerically solve the full PDE system (Eq. B.1), modified to include force-dependent unbinding from the weakly bound state, of the form

$$k_w^- = k_{w0}^- e^{E_{wb}|x|/d}$$

where E_{wb} is a non-dimensional constant that determines the force-dependence of this state. The non-dimensional parameter E_{wb} is comparable to the non-dimensional parameter E, which determines the force-dependence of ADP release. However, the sign of the x dependence for this rate constant is different from the equivalent expression for k_D, since a resisting force slows, and an assisting load accelerates ADP release, while a resisting or assisting load accelerates the detachment of weakly bound cross-bridges.

The velocity, $v(t)$, in Eq. B.1 represents the velocity of actin relative to myosin. We model the series elastic element as being in series with actin. Therefore, we keep track of actin's position,

x_{actin} by solving the following equation

$$x_{actin}(t) = x_{actin}(0) + \int_0^t v(\tau)d\tau$$

Then, the series elastic element applies a force $F_{SE} = \kappa_{SE}(S + L_0 - x_{actin})$, where S is the stretch applied to the system, and L_0 is the initial length of the series elastic element (such that $\kappa_{SE}L_0 = F_{iso}$). Since the spring is in series with the cross-bridges, we require that $F_{SE} = F$, where F is the force from the cross-bridges as defined by Eq. B.2.

We numerically solve these equations as described in section B.1.4.1 (i.e., we use the method of characteristics, and our own RK4 solver), but we must do an additional root find to find the $v(t)$ at each time step that satisfies the equation $F_{SE} = F$. We start from the initial condition described in that section, though the calculation of isometric steady state is adjusted to reflect the force-dependence of k_w^-.

To make the simulations more robust, we cutoff the value of k_w^- at $100,000$ s^{-1}. That is, at x values where $k_w^-(x) > 100,000$, we set $k_w^-(x) = 100,000$. Without this, the equations become stiff and the numerical solution unreliable. With this cutoff, the simulations were faster and more reliable. We ensured that this cutoff did not affect our simulations by doubling the cutoff (to $200,000$ s^{-1}), and ensuring that our results did not change.

We used a wide grid in x, from -20 to 20 nm, with 20,000 evenly spaced points. We simulated the model for 0.01 s, with 800 evenly spaced points. Increasing the number of points or the width of the grid did not affect our results. Increasing the time of the simulations has only a minor affect on our results and increases computational expense.

To compare this model to our force-velocity measurements, we follow the procedure described in section B.1.3.1, modified to account for the force-dependence of k_w^-. The spring in series with actin does not affect these steady-state measurements.

B.8.1. The fits to the data. The unknown parameters in the model are the unloaded ADP release rate (k_D^0), the unloaded weak-binding detachment rate (k_{w0}^-), the weak-binding attachment rate (k_w^+), the stiffness of the series elastic element (κ_{ser}), the force-dependence of the detachment rate from the weakly-bound state (E_{wb}), and the force dependence of the detachment rate from the

strongly-bound state (E). We performed fits to the data by minimizing the mean squared error to our force transient (E_t) and force-velocity (E_f) measurements. The objective function that we minimized was $E_t + 10E_f$. We weighted the error from the force-velocity measurements by a factor of 10, because in preliminary simulations where we only fit the force transient or the force-velocity measurements, the mean squared error of the best-fit to the force-velocity measurements was about 10 fold less than the mean squared error of the best-fit to the force transient measurements.

We fixed the parameters E_{wb} and E, which determine the force-dependence of unbinding from the weakly- and strongly-bound states, respectively. We then used Matlab's `fminsearch` function to determine the values of the other four parameters ($k_D^0, k_{w0}^-, k_w^+, \kappa_{ser}$) that optimized the fit to the data. We fixed E_{wb} and E at a several difference values (see Fig. 3.4D of the main text). We did not include E_{wb} and E in the optimization because the reaction rates depend exponentially on these values. Therefore, if these values are not constrained, the equations can become stiff and the numerical solutions unreliable.

The optimization converged at each E, E_{wb} pair we considered. We ensured that it converged by starting each optimization from a random seed, and ensuring that each optimum discovered by the optimization was reached from at least two of these random seeds. The best-fit parameters, for $E_{wb} = 20$ and $E = 0.5$, were $k_D^0 = 1375\text{s}^{-1}$, $k_{w0}^- = 505.9\text{s}^{-1}$, $k_w^+ - 143.3\text{s}^{-1}$ and $\kappa_{SE} = 0.000732$.

Bibliography

Nuria Albet-Torres, Marieke J Bloemink, Tom Barman, Robin Candau, Kerstin Frölander, Michael A Geeves, Kerstin Golker, Christian Herrmann, Corinne Lionne, Claudia Piperio, et al. Drug effect unveils inter-head cooperativity and strain-dependent adp release in fast skeletal actomyosin. *Journal of Biological Chemistry*, 284(34):22926–22937, 2009.

R McNeill Alexander. Models and the scaling of energy costs for locomotion. *Journal of Experimental Biology*, 208(9):1645–1652, 2005.

David Allen and Håkan Westerblad. Lactic acid–the latest performance-enhancing drug. *Science*, 305(5687):1112–1113, 2004.

David G Allen, Graham Douglas Lamb, and H Westerblad. Skeletal muscle fatigue: cellular mechanisms. *Physiological reviews*, 2008.

Todd L Allinger, Marcelo Epstein, and Walter Herzog. Stability of muscle fibers on the descending limb of the force-length relation. a theoretical consideration. *Journal of biomechanics*, 29(5): 627–633, 1996.

Claudia Arbore, Laura Perego, Marios Sergides, and Marco Capitanio. Probing force in living cells with optical tweezers: from single-molecule mechanics to cell mechanotransduction. *Biophysical reviews*, 11(5):765–782, 2019.

Josh E Baker, Christine Brosseau, Peteranne B Joel, and David M Warshaw. The biochemical kinetics underlying actin movement generated by one and many skeletal muscle myosin molecules. *Biophysical journal*, 82(4):2134–2147, 2002.

Josh E Baker, Christine Brosseau, Patty Fagnant, and David M Warshaw. The unique properties of tonic smooth muscle emerge from intrinsic as well as intermolecular behaviors of myosin molecules. *Journal of Biological Chemistry*, 278(31):28533–28539, 2003.

CD Balnave and MW Thompson. Effect of training on eccentric exercise-induced muscle damage. *Journal of Applied Physiology*, 75(4):1545–1551, 1993.

George I Bell. Models for the specific adhesion of cells to cells. *Science*, 200(4342):618–627, 1978.

R Bottinelli, M Canepari, MA Pellegrino, and C Reggiani. Force-velocity properties of human skeletal muscle fibres: myosin heavy chain isoform and temperature dependence. *The Journal of physiology*, 495(2):573–586, 1996.

R Bowater and J Sleep. Demembranated muscle fibers catalyze a more rapid exchange between phosphate and adenosine triphosphate than actomyosin subfragment. *Biochemistry*, 27(14):5314–5323, 1988.

Robert D Bremel and Annemarie Weber. Cooperation within actin filament in vertebrate skeletal muscle. *Nature New Biology*, 238(82):97–101, 1972.

B Brenner, M Schoenberg, JM Chalovich, LE Greene, and E Eisenberg. Evidence for cross-bridge attachment in relaxed muscle at low ionic strength. *Proceedings of the National Academy of Sciences*, 79(23):7288–7291, 1982.

Bernhard Brenner. Mechanical and structural approaches to correlation of cross-bridge action in muscle with actomyosin atpase in solution. *Annual review of physiology*, 49(1):655–672, 1987.

Bernhard Brenner, Leepo C Yu, and Richard J Podolsky. X-ray diffraction evidence for cross-bridge formation in relaxed muscle fibers at various ionic strengths. *Biophysical journal*, 46(3):299–306, 1984.

Bernhard Brenner, Nils Hahn, Eva Hanke, Faramarz Matinmehr, Tim Scholz, Walter Steffen, and Theresia Kraft. Mechanical and kinetic properties of β-cardiac/slow skeletal muscle myosin. *Journal of muscle research and cell motility*, 33(6):403–417, 2012.

Richard K Brizendine, Diego B Alcala, Michael S Carter, Brian D Haldeman, Kevin C Facemyer, Josh E Baker, and Christine R Cremo. Velocities of unloaded muscle filaments are not limited by drag forces imposed by myosin cross-bridges. *Proceedings of the National Academy of Sciences*, 112(36):11235–11240, 2015.

Richard K Brizendine, Gabriel G Sheehy, Diego B Alcala, Sabrina I Novenschi, Josh E Baker, and Christine R Cremo. A mixed-kinetic model describes unloaded velocities of smooth, skeletal, and cardiac muscle myosin filaments in vitro. *Science advances*, 3(12):eaao2267, 2017.

Lucy M Brown and Lydia Hill. Some observations on variations in filament overlap in tetanized muscle fibres and fibres stretched during a tetanus, detected in the electron microscope after

rapid fixation. *Journal of Muscle Research & Cell Motility*, 12(2):171–182, 1991.

Stephen J Brown, Robert B Child, Stephen H Day, and Alan E Donnelly. Exercise-induced skeletal muscle damage and adaptation following repeated bouts of eccentric muscle contractions. *Journal of sports sciences*, 15(2):215–222, 1997.

EB Cady, DA Jones, J Lynn, and DJ Newham. Changes in force and intracellular metabolites during fatigue of human skeletal muscle. *The Journal of physiology*, 418(1):311–325, 1989.

Kenneth B Campbell and Murali Chandra. Functions of stretch activation in heart muscle. *The Journal of general physiology*, 127(2):89–94, 2006.

Kenneth S Campbell. Filament compliance effects can explain tension overshoots during force development. *Biophysical journal*, 91(11):4102–4109, 2006.

Kenneth S Campbell. Interactions between connected half-sarcomeres produce emergent mechanical behavior in a mathematical model of muscle. *PLoS computational biology*, 5(11), 2009.

Kenneth S Campbell. Dynamic coupling of regulated binding sites and cycling myosin heads in striated muscledynamic coupling in striated muscle. *The Journal of general physiology*, 143(3): 387–399, 2014.

Kenneth S Campbell. Compliance accelerates relaxation in muscle by allowing myosin heads to move relative to actin. *Biophysical journal*, 110(3):661–668, 2016.

Kenneth S Campbell, Paul ML Janssen, and Stuart G Campbell. Force-dependent recruitment from the myosin off state contributes to length-dependent activation. *Biophysical journal*, 115 (3):543–553, 2018.

Stuart G Campbell and Kenneth S Campbell. Mechanisms of residual force enhancement in skeletal muscle: insights from experiments and mathematical models. *Biophysical reviews*, 3(4):199–207, 2011.

Stuart G Campbell, Fred V Lionetti, Kenneth S Campbell, and Andrew D McCulloch. Coupling of adjacent tropomyosins enhances cross-bridge-mediated cooperative activation in a markov model of the cardiac thin filament. *Biophysical journal*, 98(10):2254–2264, 2010.

M Capitanio, M Canepari, P Cacciafesta, V Lombardi, R Cicchi, M Maffei, FS Pavone, and R Bottinelli. Two independent mechanical events in the interaction cycle of skeletal muscle myosin with actin. *Proceedings of the National Academy of Sciences*, 103(1):87–92, 2006.

Marco Capitanio, Monica Canepari, Manuela Maffei, Diego Beneventi, Carina Monico, Francesco Vanzi, Roberto Bottinelli, and Francesco Saverio Pavone. Ultrafast force-clamp spectroscopy of single molecules reveals load dependence of myosin working stroke. *Nature methods*, 9(10): 1013–1019, 2012.

Joseph M Chalovich and Evan Eisenberg. Inhibition of actomyosin atpase activity by troponin-tropomyosin without blocking the binding of myosin to actin. *The Journal of biological chemistry*, 257(5):2432, 1982.

Joseph M Chalovich, P Boon Chock, and Evan Eisenberg. Mechanism of action of troponin. tropomyosin. inhibition of actomyosin atpase activity without inhibition of myosin binding to actin. *Journal of Biological Chemistry*, 256(2):575–578, 1981.

P Bryant Chase and Martin J Kushmerick. Effects of ph on contraction of rabbit fast and slow skeletal muscle fibers. *Biophysical journal*, 53(6):935–946, 1988.

P Bryant Chase, J Michael Macpherson, and Thomas L Daniel. A spatially explicit nanomechanical model of the half-sarcomere: myofilament compliance affects ca 2+-activation. *Annals of biomedical engineering*, 32(11):1559–1568, 2004.

Priscilla M Clarkson and Monica J Hubal. Exercise-induced muscle damage in humans. *American journal of physical medicine & rehabilitation*, 81(11):S52–S69, 2002.

Melanie Colegrave and Michelle Peckham. Structural implications of β-cardiac myosin heavy chain mutations in human disease. *The Anatomical Record*, 297(9):1670–1680, 2014.

R Cooke, Kathleen Franks, Giovanni B Luciani, and E Pate. The inhibition of rabbit skeletal muscle contraction by hydrogen ions and phosphate. *The Journal of physiology*, 395(1):77–97, 1988.

Roger Cooke and Kenneth C Holmes. The mechanism of muscle contraction. *Critical Reviews in Biochemistry*, 21(1):53–118, 1986.

Roger Cooke and E Pate. The effects of adp and phosphate on the contraction of muscle fibers. *Biophysical journal*, 48(5):789–798, 1985.

Roger Craig and William Lehman. Crossbridge and tropomyosin positions observed in native, interacting thick and thin filaments. *Journal of molecular biology*, 311(5):1027–1036, 2001.

Christine R Cremo and Michael A Geeves. Interaction of actin and adp with the head domain of smooth muscle myosin: implications for strain-dependent adp release in smooth muscle. *Biochemistry*, 37(7):1969–1978, 1998.

Thomas L Daniel, Alan C Trimble, and P Bryant Chase. Compliant realignment of binding sites in muscle: transient behavior and mechanical tuning. *Biophysical journal*, 74(4):1611–1621, 1998.

Enrique M De La Cruz, Amber L Wells, H Lee Sweeney, and E Michael Ostap. Actin and light chain isoform dependence of myosin v kinetics. *Biochemistry*, 39(46):14196–14202, 2000.

Edward Debold. Recent insights into muscle fatigue at the cross-bridge level. *Frontiers in physiology*, 3:151, 2012.

Edward P Debold, Heman Dave, and Robert H Fitts. Fiber type and temperature dependence of inorganic phosphate: implications for fatigue. *American Journal of Physiology-Cell Physiology*, 287(3):C673–C681, 2004.

Edward P Debold, Joseph B Patlak, and David M Warshaw. Slip sliding away: load-dependence of velocity generated by skeletal muscle myosin molecules in the laser trap. *Biophysical journal*, 89(5):L34–L36, 2005.

Edward P Debold, Samantha E Beck, and David M Warshaw. Effect of low ph on single skeletal muscle myosin mechanics and kinetics. *American Journal of Physiology-Cell Physiology*, 295(1): C173–C179, 2008.

Edward P Debold, Matthew A Turner, Jordan C Stout, and Sam Walcott. Phosphate enhances myosin-powered actin filament velocity under acidic conditions in a motility assay. *American Journal of Physiology-Regulatory, Integrative and Comparative Physiology*, 300(6):R1401–R1408, 2011.

Edward P Debold, Thomas J Longyear, and Matthew A Turner. The effects of phosphate and acidosis on regulated thin-filament velocity in an in vitro motility assay. *Journal of Applied Physiology*, 113(9):1413–1422, 2012.

Edward P Debold, Sam Walcott, Mike Woodward, and Matthew A Turner. Direct observation of phosphate inhibiting the force-generating capacity of a miniensemble of myosin molecules. *Biophysical journal*, 105(10):2374–2384, 2013.

Edward Patrick Debold, Robert H Fitts, Christopher Sundberg, and Thomas M Nosek. Muscle fatigue from the perspective of a single crossbridge. *Medicine & Science in Sports & Exercise*, 2016.

Jachen Denoth, Edgar Stüssi, Gabor Csucs, and Gaudenz Danuser. Single muscle fiber contraction is dictated by inter-sarcomere dynamics. *Journal of theoretical biology*, 216(1):101–122, 2002.

TAJ Duke. Molecular model of muscle contraction. *Proceedings of the National Academy of Sciences*, 96(6):2770–2775, 1999.

KAP Edman, LA Mulieri, and B Scubon-Mulieri. Non-hyperbolic force-velocity relationship in single muscle fibres 1. *Acta Physiologica Scandinavica*, 98(2):143–156, 1976.

Evan Eisenberg and Terrell L Hill. Muscle contraction and free energy transduction in biological systems. *Science*, 227(4690):999–1006, 1985.

Evan Eisenberg, Terrell L Hill, and Yi-der Chen. Cross-bridge model of muscle contraction. quantitative analysis. *Biophysical Journal*, 29(2):195–227, 1980.

Catherine C Eldred, Dimitre R Simeonov, Ryan A Koppes, Chaoxing Yang, David T Corr, and Douglas M Swank. The mechanical properties of drosophila jump muscle expressing wild-type and embryonic myosin isoforms. *Biophysical journal*, 98(7):1218–1226, 2010.

Wallace O Fenn. A quantitative comparison between the energy liberated and the work performed by the isolated sartorius muscle of the frog. *The Journal of physiology*, 58(2-3):175–203, 1923.

Jeffrey T Finer, Robert M Simmons, and James A Spudich. Single myosin molecule mechanics: piconewton forces and nanometre steps. *Nature*, 368(6467):113, 1994.

Robert Fitts. The role of acidosis in fatigue: pro perspective. *Medicine & Science in Sports & Exercise*, 2016.

Robert H Fitts. Cellular mechanisms of muscle fatigue. *Physiological reviews*, 74(1):49–94, 1994.

LE Ford, AF Huxley, and RM Simmons. Tension responses to sudden length change in stimulated frog muscle fibres near slack length. *The Journal of physiology*, 269(2):441–515, 1977.

J Friden, M Sjöström, and B Ekblom. A morphological study of delayed muscle soreness. *Experientia*, 37(5):506–507, 1981.

S Galler, K Hilber, and D Pette. Stretch activation and myosin heavy chain isoforms of rat, rabbit and human skeletal muscle fibres. *Journal of Muscle Research & Cell Motility*, 18(4):441–448,

1997.

Stefan Galler, Thomas L Schmitt, and Dirk Pette. Stretch activation, unloaded shortening velocity, and myosin heavy chain isoforms of rat skeletal muscle fibres. *The Journal of physiology*, 478(3): 513–521, 1994.

Stefan Galler, Karlheinz Hilber, and Dirk Pette. Force responses following stepwise length changes of rat skeletal muscle fibre types. *The Journal of physiology*, 493(1):219–227, 1996.

Michael Geeves, Hugh Griffiths, Srboljub Mijailovich, and David Smith. Cooperative [ca2+]-dependent regulation of the rate of myosin binding to actin: solution data and the tropomyosin chain model. *Biophysical journal*, 100(11):2679–2687, 2011.

Anja AT Geisterfer-Lowrance, Susan Kass, Gary Tanigawa, Hans-Peter Vosberg, William McKenna, Christine E Seidman, and JG Seidman. A molecular basis for familial hypertrophic cardiomyopathy: a β cardiac myosin heavy chain gene missense mutation. *Cell*, 62(5):999–1006, 1990.

Bernadette M Glasheen, Catherine C Eldred, Leah C Sullivan, Cuiping Zhao, Michael K Reedy, Robert J Edwards, and Douglas M Swank. Stretch activation properties of drosophila and lethocerus indirect flight muscle suggest similar calcium-dependent mechanisms. *American Journal of Physiology-Cell Physiology*, 313(6):C621–C631, 2017.

AM Gordon, Andrew F Huxley, and FJ Julian. The variation in isometric tension with sarcomere length in vertebrate muscle fibres. *The Journal of physiology*, 184(1):170–192, 1966.

Michael J Greenberg, Henry Shuman, and E Michael Ostap. Inherent force-dependent properties of β-cardiac myosin contribute to the force-velocity relationship of cardiac muscle. *Biophysical journal*, 107(12):L41–L44, 2014.

Michael J Greenberg, Henry Shuman, and E Michael Ostap. Measuring the kinetic and mechanical properties of non-processive myosins using optical tweezers. In *Optical Tweezers*, pages 483–509. Springer, 2017.

Lois E Greene and Evan Eisenberg. Cooperative binding of myosin subfragment-1 to the actin-troponin-tropomyosin complex. *Proceedings of the National Academy of Sciences*, 77(5):2616–2620, 1980.

William H Guilford, Donald E Dupuis, Guy Kennedy, Junru Wu, Joseph B Patlak, and David M Warshaw. Smooth muscle and skeletal muscle myosins produce similar unitary forces and displacements in the laser trap. *Biophysical journal*, 72(3):1006, 1997.

Bin Guo and William H Guilford. Mechanics of actomyosin bonds in different nucleotide states are tuned to muscle contraction. *Proceedings of the National Academy of Sciences*, 103(26): 9844–9849, 2006.

Brian D Haldeman, Richard K Brizendine, Kevin C Facemyer, Josh E Baker, and Christine R Cremo. The kinetics underlying the velocity of smooth muscle myosin filament sliding on actin filaments in vitro. *Journal of Biological Chemistry*, 289(30):21055–21070, 2014.

David E Harris and DM Warshaw. Smooth and skeletal muscle myosin both exhibit low duty cycles at zero load in vitro. *Journal of Biological Chemistry*, 268(20):14764–14768, 1993.

Jason D Harry, Andrew W Ward, Norman C Heglund, David L Morgan, and Thomas A McMahon. Cross-bridge cycling theories cannot explain high-speed lengthening behavior in frog muscle. *Biophysical journal*, 57(2):201–208, 1990.

Walter Herzog, G Schappacher, M DuVall, Timothy R Leonard, and Jens A Herzog. Residual force enhancement following eccentric contractions: a new mechanism involving titin. *Physiology*, 31 (4):300–312, 2016.

Mark G Hibberd, Jody A Dantzig, David R Trentham, and Yale E Goldman. Phosphate release and force generation in skeletal muscle fibers. *Science*, 228(4705):1317–1319, 1985.

Lennart Hilbert, Shivaram Cumarasamy, Nedjma B Zitouni, Michael C Mackey, and Anne-Marie Lauzon. The kinetics of mechanically coupled myosins exhibit group size-dependent regimes. *Biophysical journal*, 105(6):1466–1474, 2013.

Archibald Vivian Hill. The heat of shortening and the dynamic constants of muscle. *Proc. R. Soc. Lond. B*, 126(843):136–195, 1938.

Terrell L Hill. Theoretical formalism for the sliding filament model of contraction of striated muscle part i. *Progress in biophysics and molecular biology*, 28:267–340, 1974.

Terrell L Hill. Theoretical formalism for the sliding filament model of contraction of striated muscle part ii. *Progress in biophysics and molecular biology*, 29:105–159, 1976.

Terrell L Hill, Evan Eisenberg, and Lois Greene. Theoretical model for the cooperative equilibrium binding of myosin subfragment 1 to the actin-troponin-tropomyosin complex. *Proceedings of the National Academy of Sciences*, 77(6):3186–3190, 1980.

Terrell L Hill, Evan Eisenberg, and JM Chalovich. Theoretical models for cooperative steady-state atpase activity of myosin subfragment-1 on regulated actin. *Biophysical journal*, 35(1):99–112, 1981.

Stéphanie Hody, Jean-Louis Croisier, Thierry Bury, Bernard Rogister, and Pierre Leprince. Eccentric muscle contractions: risks and benefits. *Frontiers in physiology*, 10:536, 2019.

Earl Homsher, F Wang, and James R Sellers. Factors affecting movement of f-actin filaments propelled by skeletal muscle heavy meromyosin. *American Journal of Physiology-Cell Physiology*, 262(3):C714–C723, 1992.

A.F. Huxley. Muscle structure and theories of contraction. *Progress in Biophysics and Biophysical Chemistry*, 7, 1957.

AF Huxley and Sl Tideswell. Filament compliance and tension transients in muscle. *Journal of Muscle Research & Cell Motility*, 17(4):507–511, 1996.

Andrew F Huxley and R Niedergerke. Structural changes in muscle during contraction: interference microscopy of living muscle fibres. *Nature*, 173(4412):971–973, 1954.

Andrew F Huxley and Ro M Simmons. Proposed mechanism of force generation in striated muscle. *Nature*, 233(5321):533–538, 1971.

Hugh Huxley and Jean Hanson. Changes in the cross-striations of muscle during contraction and stretch and their structural interpretation. *Nature*, 173(4412):973–976, 1954.

Akihiko Ishijima, Yoshie Harada, Hiroaki Kojima, Takashi Funatsu, Hideo Higuchi, and Toshio Yanagida. Single-molecule analysis of the actomyosin motor using nano-manipulation. *Biochemical and biophysical research communications*, 199(2):1057–1063, 1994.

Katelyn Jarvis, Mike Woodward, Edward P Debold, and Sam Walcott. Acidosis affects muscle contraction by slowing the rates myosin attaches to and detaches from actin. *Journal of muscle research and cell motility*, 39(3-4):135–147, 2018.

Katelyn J Jarvis, Kaylyn M Bell, Amy K Loya, Douglas M Swank, and Sam Walcott. Force-velocity and tension transient measurements from drosophila jump muscle reveal the necessity of both

weakly-bound cross-bridges and series elasticity in models of muscle contraction. *Archives of Biochemistry and Biophysics*, 701:108809, 2021.

Robert K Josephson, Jean G Malamud, and Darrell R Stokes. Asynchronous muscle: a primer. *Journal of Experimental Biology*, 203(18):2713–2722, 2000.

GC Joyce, PMH Rack, and DR Westbury. The mechanical properties of cat soleus muscle during controlled lengthening and shortening movements. *The Journal of physiology*, 204(2):461–474, 1969.

Neil M Kad, Scott Kim, David M Warshaw, Peter VanBuren, and Josh E Baker. Single-myosin crossbridge interactions with actin filaments regulated by troponin-tropomyosin. *Proceedings of the National Academy of Sciences*, 102(47):16990–16995, 2005.

Neil M Kad, Joseph B Patlak, Patricia M Fagnant, Kathleen M Trybus, and David M Warshaw. Mutation of a conserved glycine in the sh1-sh2 helix affects the load-dependent kinetics of myosin. *Biophysical journal*, 92(5):1623–1631, 2007.

Christina Karatzaferi, Kathleen Franks-Skiba, and Roger Cooke. Inhibition of shortening velocity of skinned skeletal muscle fibers in conditions that mimic fatigue. *American Journal of Physiology-Regulatory, Integrative and Comparative Physiology*, 294(3):R948–R955, 2008.

Christina Karatzaferi, Nancy Adamek, and Michael A Geeves. Modulators of actin-myosin dissociation: basis for muscle type functional differences during fatigue. *American Journal of Physiology-Cell Physiology*, 313(6):C644–C654, 2017.

Bernhard Katz. The relation between force and speed in muscular contraction. *The Journal of Physiology*, 96(1):45–64, 1939.

Masataka Kawai and Herbert R Halvorson. Force transients and minimum cross-bridge models in muscular contraction. *Journal of muscle research and cell motility*, 28(7-8):371, 2007.

Motoshi Kaya and Hideo Higuchi. Nonlinear elasticity and an 8-nm working stroke of single myosin molecules in myofilaments. *Science*, 329(5992):686–689, 2010.

Shannon T Knuth, H Dave, Jim R Peters, and RH Fitts. Low cell ph depresses peak power in rat skeletal muscle fibres at both 30 c and 15 c: implications for muscle fatigue. *The Journal of physiology*, 575(3):887–899, 2006.

Ryan A Koppes, Douglas M Swank, and David T Corr. A new experimental model for force enhancement: steady-state and transient observations of the drosophila jump muscle. *American Journal of Physiology-Cell Physiology*, 309(8):C551–C557, 2015.

Mihály Kovács, Judit Tóth, Csaba Hetényi, András Málnási-Csizmadia, and James R Sellers. Mechanism of blebbistatin inhibition of myosin ii. *Journal of Biological Chemistry*, 279(34): 35557–35563, 2004.

Stephen J Kron and James A Spudich. Fluorescent actin filaments move on myosin fixed to a glass surface. *Proceedings of the National Academy of Sciences*, 83(17):6272–6276, 1986.

Dietmar Labeit, Kaori Watanabe, Christian Witt, Hideaki Fujita, Yiming Wu, Sunshine Lahmers, Theodor Funck, Siegfried Labeit, and Henk Granzier. Calcium-dependent molecular spring elements in the giant protein titin. *Proceedings of the National Academy of Sciences*, 100(23): 13716–13721, 2003.

H Michael Lacker and Charles Peskin. A mathematical method for the unique determination of cross-bridge properties from steady-state mechanical and energetic experiments on macroscopic muscle. In *Lectures on mathematics in the life sciences*, pages 121–153. AMS, 1986.

Graham D Lamb, D George Stephenson, Jens Bangsbo, and Carsten Juel. Point: Counterpoint: Lactic acid accumulation is an. *J Appl Physiol*, 100:1410–1412, 2006.

Andrew P Landstrom, Michelle S Parvatiyar, Jose R Pinto, Michelle L Marquardt, J Martijn Bos, David J Tester, Steve R Ommen, James D Potter, and Michael J Ackerman. Molecular and functional characterization of novel hypertrophic cardiomyopathy susceptibility mutations in tnnc1-encoded troponin c. *Journal of molecular and cellular cardiology*, 45(2):281–288, 2008.

Tim R Leonard and Walter Herzog. Regulation of muscle force in the absence of actin-myosin-based cross-bridge interaction. *American Journal of Physiology-Cell Physiology*, 299(1):C14–C20, 2010.

Marco Linari, Michael K Reedy, Mary C Reedy, Vincenzo Lombardi, and Gabriella Piazzesi. Ca-activation and stretch-activation in insect flight muscle. *Biophysical journal*, 87(2):1101–1111, 2004.

Marco Linari, Marco Caremani, and Vincenzo Lombardi. A kinetic model that explains the effect of inorganic phosphate on the mechanics and energetics of isometric contraction of fast skeletal muscle. *Proceedings of the Royal Society B: Biological Sciences*, 277(1678):19–27, 2010.

Marco Linari, Gabriella Piazzesi, Irene Pertici, Jody A Dantzig, Yale E Goldman, and Vincenzo Lombardi. Straightening out the elasticity of myosin cross-bridges. *Biophysical Journal*, 118(5): 994–1002, 2020.

Stan L Lindstedt, PC LaStayo, and TE Reich. When active muscles lengthen: properties and consequences of eccentric contractions. *Physiology*, 16(6):256–261, 2001.

Chao Liu, Masataka Kawana, Dan Song, Kathleen M Ruppel, and James A Spudich. Controlling load-dependent kinetics of β-cardiac myosin at the single-molecule level. *Nature structural & molecular biology*, 25(6):505–514, 2018.

Paola Llinas, Tatiana Isabet, Lin Song, Virginie Ropars, Bin Zong, Hannah Benisty, Serena Sirigu, Carl Morris, Carlos Kikuti, Dan Safer, et al. How actin initiates the motor activity of myosin. *Developmental cell*, 33(4):401–412, 2015.

Vincenzo Lombardi and Gabriella Piazzesi. The contractile response during steady lengthening of stimulated frog muscle fibres. *The Journal of Physiology*, 431(1):141–171, 1990.

Thomas Longyear, Sam Walcott, and Edward P Debold. The molecular basis of thin filament activation: from single molecule to muscle. *Scientific Reports*, 7(1):1822, 2017.

Y Luo, Roger Cooke, and Edward Pate. A model of stress relaxation in cross-bridge systems: effect of a series elastic element. *American Journal of Physiology-Cell Physiology*, 265(1):C279–C288, 1993.

RW Lymn and Edwin W Taylor. Mechanism of adenosine triphosphate hydrolysis by actomyosin. *Biochemistry*, 10(25):4617–4624, 1971.

Alf Månsson. Actomyosin-adp states, interhead cooperativity, and the force-velocity relation of skeletal muscle. *Biophysical journal*, 98(7):1237–1246, 2010.

Alf Månsson, Marko Ušaj, Luisa Moretto, and Dilson E Rassier. Do actomyosin single-molecule mechanics data predict mechanics of contracting muscle? *International journal of molecular sciences*, 19(7):1863, 2018.

Sarkis S Margossian and Susan Lowey. [7] preparation of myosin and its subfragments from rabbit skeletal muscle. *Methods in enzymology*, 85:55–71, 1982.

Malachy P McHugh, Declan AJ Connolly, Roger G Eston, and Gilbert W Gleim. Exercise-induced muscle damage and potential mechanisms for the repeated bout effect. *Sports medicine*, 27(3):

157–170, 1999.

DF McKillop and Michael A Geeves. Regulation of the interaction between actin and myosin subfragment 1: evidence for three states of the thin filament. *Biophysical journal*, 65(2):693–701, 1993.

Srboljub M Mijailovich, Oliver Kayser-Herold, Boban Stojanovic, Djordje Nedic, Thomas C Irving, and Michael A Geeves. Three-dimensional stochastic model of actin–myosin binding in the sarcomere lattice. *Journal of General Physiology*, 148(6):459–488, 2016.

JE Molloy, JE Burns, J Kendrick-Jones, RT Tregear, and DCS White. Movement and force produced by a single myosin head. *Nature*, 378(6553):209, 1995.

David L Morgan and DG Allen. Early events in stretch-induced muscle damage. *Journal of applied physiology*, 87(6):2007–2015, 1999.

DL Morgan. New insights into the behavior of muscle during active lengthening. *Biophysical journal*, 57(2):209–221, 1990.

DL Morgan. An explanation for residual increased tension in striated muscle after stretch during contraction. *Experimental Physiology: Translation and Integration*, 79(5):831–838, 1994.

Joseph M Muretta, John A Rohde, Daniel O Johnsrud, Sinziana Cornea, and David D Thomas. Direct real-time detection of the structural and biochemical events in the myosin power stroke. *Proceedings of the National Academy of Sciences*, 112(46):14272–14277, 2015.

Suman Nag, Ruth F Sommese, Zoltan Ujfalusi, Ariana Combs, Stephen Langer, Shirley Sutton, Leslie A Leinwand, Michael A Geeves, Kathleen M Ruppel, and James A Spudich. Contractility parameters of human β-cardiac myosin with the hypertrophic cardiomyopathy mutation r403q show loss of motor function. *Science advances*, 1(9):e1500511, 2015.

Cassandra R Nelson, Edward P Debold, and Robert H Fitts. Phosphate and acidosis act synergistically to depress peak power in rat muscle fibers. *American Journal of Physiology-Cell Physiology*, 307(10):C939–C950, 2014.

Christopher S Newhard, Sam Walcott, and Douglas M Swank. The load dependence of muscle's force-velocity curve is modulated by alternative myosin converter domains. *American Journal of Physiology-Cell Physiology*, 316(6):C844–C861, 2019.

Kiisa C Nishikawa, Jenna A Monroy, Theodore E Uyeno, Sang Hoon Yeo, Dinesh K Pai, and Stan L Lindstedt. Is titin a 'winding filament'? a new twist on muscle contraction. *Proceedings of the Royal Society B: Biological Sciences*, 279(1730):981–990, 2012.

Takayuki Nishizaka, Hidetake Miyata, Hiroshi Yoshikawa, Shin'ichi Ishiwata, and Kazuhiko Kinosita Jr. Unbinding force of a single motor molecule of muscle measured using optical tweezers. *Nature*, 377(6546):251, 1995.

Thomas M Nosek, Kimberly Y Fender, and Robert E Godt. It is diprotonated inorganic phosphate that depresses force in skinned skeletal muscle fibers. *Science*, 236(4798):191–193, 1987.

Julien Ochala, David J Dorer, Walter R Frontera, and Lisa S Krivickas. Single skeletal muscle fiber behavior after a quick stretch in young and older men: a possible explanation of the relative preservation of eccentric force in old age. *Pflügers Archiv*, 452(4):464–470, 2006.

Styliani C Pastra-Landis, Ted Huiatt, and Susan Lowey. Assembly and kinetic properties of myosin light chain isozymes from fast skeletal muscle. *Journal of molecular biology*, 170(2):403–422, 1983.

Edward Pate and Roger Cooke. A model of crossbridge action: the effects of atp, adp and p i. *Journal of Muscle Research & Cell Motility*, 10(3):181–196, 1989.

Edward Pate, Meenesh Bhimani, Kathy Franks-Skiba, and Roger Cooke. Reduced effect of ph on skinned rabbit psoas muscle mechanics at high temperatures: implications for fatigue. *The Journal of Physiology*, 486(3):689–694, 1995.

Joseph B Patlak. Measuring kinetics of complex single ion channel data using mean-variance histograms. *Biophysical journal*, 65(1):29–42, 1993.

Thomas H Pedersen, Ole B Nielsen, Graham D Lamb, and D George Stephenson. Intracellular acidosis enhances the excitability of working muscle. *Science*, 305(5687):1144–1147, 2004.

G Piazzesi, M Linari, M Reconditi, F Vanzi, and V Lombardi. Cross-bridge detachment and attachment following a step stretch imposed on active single frog muscle fibres. *The Journal of physiology*, 498(1):3–15, 1997.

Gabriella Piazzesi and Vincenzo Lombardi. A cross-bridge model that is able to explain mechanical and energetic properties of shortening muscle. *Biophysical journal*, 68(5):1966, 1995.

EJ Potma, IA Van Graas, and GJ Stienen. Influence of inorganic phosphate and ph on atp utilization in fast and slow skeletal muscle fibers. *Biophysical Journal*, 69(6):2580–2589, 1995.

Joseph D Powers, C David Williams, Michael Regnier, and Thomas L Daniel. A spatially explicit model shows how titin stiffness modulates muscle mechanics and energetics. *Integrative and comparative biology*, 58(2):186–193, 2018.

Michael J Previs, S Beck Previs, J Gulick, J Robbins, and DM Warshaw. Molecular mechanics of cardiac myosin-binding protein c in native thick filaments. *Science*, 337(6099):1215–1218, 2012.

Uwe Proske and David L Morgan. Muscle damage from eccentric exercise: mechanism, mechanical signs, adaptation and clinical applications. *The Journal of physiology*, 537(2):333–345, 2001.

Dilson E Rassier and Walter Herzog. Considerations on the history dependence of muscle contraction. *Journal of applied physiology*, 96(2):419–427, 2004.

Ivan Rayment, Hazel M Holden, Michael Whittaker, Christopher B Yohn, Michael Lorenz, Kenneth C Holmes, and Ronald A Milligan. Structure of the actin-myosin complex and its implications for muscle contraction. *Science*, 261(5117):58–65, 1993.

Massimo Reconditi, Marco Linari, Leonardo Lucii, Alex Stewart, Yin-Biao Sun, Peter Boesecke, Theyencheri Narayanan, Robert F Fischetti, Tom Irving, Gabriella Piazzesi, et al. The myosin motor in muscle generates a smaller and slower working stroke at higher load. *Nature*, 428(6982): 578–581, 2004.

Michael Regnier. Mechanistic complexity of contractile dysfunction in hypertrophic cardiomyopathy. *Journal of General Physiology*, 150(8):1051–1053, 2018.

Robert A Robergs, Farzenah Ghiasvand, and Daryl Parker. Biochemistry of exercise-induced metabolic acidosis. *American Journal of Physiology-Regulatory, Integrative and Comparative Physiology*, 2004.

Marv Ruona. Medical images. URL `http://www.artandsciencegraphics.com/medical-images/`.

K Saito, Takaaki Aoki, and T Yanagida. Movement of single myosin filaments and myosin step size on an actin filament suspended in solution by a laser trap. *Biophysical journal*, 66(3):769–777, 1994.

Gudrun Schappacher-Tilp, Timothy Leonard, Gertrud Desch, and Walter Herzog. A novel three-filament model of force generation in eccentric contraction of skeletal muscles. *PloS one*, 10(3), 2015.

JA Schwane and RB Armstrong. Effect of training on skeletal muscle injury from downhill running in rats. *Journal of Applied Physiology*, 55(3):969–975, 1983.

JG Seidman and Christine Seidman. The genetic basis for cardiomyopathy: from mutation identification to mechanistic paradigms. *Cell*, 104(4):557–567, 2001.

Nicholas M Sich, Timothy J O'Donnell, Sarah A Coulter, Olivia A John, Michael S Carter, Christine R Cremo, and Josh E Baker. Effects of actin-myosin kinetics on the calcium sensitivity of regulated thin filaments. *Journal of Biological Chemistry*, 285(50):39150–39159, 2010.

Raymond F Siemankowski, Meganne O Wiseman, and Howard D White. Adp dissociation from actomyosin subfragment 1 is sufficiently slow to limit the unloaded shortening velocity in vertebrate muscle. *Proceedings of the National Academy of Sciences*, 82(3):658–662, 1985.

Sivaraj Sivaramakrishnan, Euan Ashley, Leslie Leinwand, and James A Spudich. Insights into human β-cardiac myosin function from single molecule and single cell studies. *Journal of cardiovascular translational research*, 2(4):426–440, 2009.

DA Smith and MA Geeves. Strain-dependent cross-bridge cycle for muscle. *Biophysical Journal*, 69(2):524–537, 1995.

David A Smith. A new mechanokinetic model for muscle contraction, where force and movement are triggered by phosphate release. *Journal of muscle research and cell motility*, 35(5):295–306, 2014.

James A Spudich, Sarah E Rice, Ronald S Rock, Thomas J Purcell, and Hans M Warrick. Optical traps to study properties of molecular motors. *Cold Spring Harbor Protocols*, 2011(11):pdb–top066662, 2011.

Manoj Srinivasan and Sam Walcott. Binding site models of friction due to the formation and rupture of bonds: state-function formalism, force-velocity relations, response to slip velocity transients, and slip stability. *Physical Review E*, 80(4):046124, 2009.

Walter Steffen, David Smith, Robert Simmons, and John Sleep. Mapping the actin filament with myosin. *Proceedings of the National Academy of Sciences*, 98(26):14949–14954, 2001.

Leonard A Stein, Richard P Schwarz Jr, P Boon Chock, and Evan Eisenberg. Mechanism of the actomyosin adenosine triphosphatase. evidence that adenosine 5'-triphosphate hydrolysis can occur without dissociation of the actomyosin complex. *Biochemistry*, 18(18):3895–3909, 1979.

Julian E Stelzer, Lars Larsson, Daniel P Fitzsimons, and Richard L Moss. Activation dependence of stretch activation in mouse skinned myocardium: implications for ventricular function. *The Journal of general physiology*, 127(2):95–107, 2006.

Julian E Stelzer, Stacey L Brickson, Matthew R Locher, and Richard L Moss. Role of myosin heavy chain composition in the stretch activation response of rat myocardium. *The Journal of physiology*, 579(1):161–173, 2007.

Urs Stoecker, Ivo A Telley, Edgar Stüssi, and Jachen Denoth. A multisegmental cross-bridge kinetics model of the myofibril. *Journal of theoretical biology*, 259(4):714–726, 2009.

Chad R Straight, Kaylyn M Bell, Jared N Slosberg, Mark S Miller, and Douglas M Swank. A myosin-based mechanism for stretch activation and its possible role revealed by varying phosphate concentration in fast and slow mouse skeletal muscle fibers. *American Journal of Physiology-Cell Physiology*, 317(6):C1143–C1152, 2019.

Jongmin Sung, Suman Nag, Kim I Mortensen, Christian L Vestergaard, Shirley Sutton, Kathleen Ruppel, Henrik Flyvbjerg, and James A Spudich. Harmonic force spectroscopy measures load-dependent kinetics of individual human β-cardiac myosin molecules. *Nature communications*, 6 (1):1–9, 2015.

Douglas M Swank. Mechanical analysis of drosophila indirect flight and jump muscles. *Methods*, 56(1):69–77, 2012.

Douglas M Swank, Linda Wells, William A Kronert, George E Morrill, and Sanford I Bernstein. Determining structure/function relationships for sarcomeric myosin heavy chain by genetic and transgenic manipulation of drosophila. *Microscopy research and technique*, 50(6):430–442, 2000.

Yasuharu Takagi, Earl E Homsher, Yale E Goldman, and Henry Shuman. Force generation in single conventional actomyosin complexes under high dynamic load. *Biophysical journal*, 90(4): 1295–1307, 2006.

JA Talbot and DL Morgan. Quantitative analysis of sarcomere non-uniformities in active muscle following a stretch. *Journal of Muscle Research & Cell Motility*, 17(2):261–268, 1996.

Bertrand CW Tanner, Thomas L Daniel, and Michael Regnier. Sarcomere lattice geometry influences cooperative myosin binding in muscle. *PLoS computational biology*, 3(7), 2007.

Bertrand CW Tanner, Thomas L Daniel, and Michael Regnier. Filament compliance influences cooperative activation of thin filaments and the dynamics of force production in skeletal muscle. *PLoS Comput Biol*, 8(5):e1002506, 2012.

Jil C Tardiff. Sarcomeric proteins and familial hypertrophic cardiomyopathy: linking mutations in structural proteins to complex cardiovascular phenotypes. *Heart failure reviews*, 10(3):237–248, 2005.

Ivo A Telley and Jachen Denoth. Sarcomere dynamics during muscular contraction and their implications to muscle function. *Journal of muscle research and cell motility*, 28(1):89–104, 2007.

Taro QP Uyeda, Stephen J Kron, and James A Spudich. Myosin step size: estimation from slow sliding movement of actin over low densities of heavy meromyosin. *Journal of molecular biology*, 214(3):699–710, 1990.

F Vanzi, G Piazzesi, M Linari, M Reconditi, and V Lombardi. An analysis of the tension transient after a step stretch imposed during an isometric tetanus. *Biophysical journal*, 68(4 Suppl):370s, 1995.

Claudia Veigel, Justin E Molloy, Stephan Schmitz, and John Kendrick-Jones. Load-dependent kinetics of force production by smooth muscle myosin measured with optical tweezers. *Nature cell biology*, 5(11):980, 2003.

Sam Walcott. A differential equation model for tropomyosin-induced myosin cooperativity describes myosin–myosin interactions at low calcium. *Cellular and Molecular Bioengineering*, 6(1):13–25, 2013.

Sam Walcott. Muscle activation described with a differential equation model for large ensembles of locally coupled molecular motors. *Physical Review E*, 90(4):042717, 2014.

Sam Walcott and Walter Herzog. Modeling residual force enhancement with generic cross-bridge models. *Mathematical biosciences*, 216(2):172–186, 2008.

Sam Walcott and Sean X Sun. Hysteresis in cross-bridge models of muscle. *Physical Chemistry Chemical Physics*, 11(24):4871–4881, 2009.

Sam Walcott, Patricia M Fagnant, Kathleen M Trybus, and David M Warshaw. Smooth muscle heavy meromyosin phosphorylated on one of its two heads supports force and motion. *Journal of Biological Chemistry*, 284(27):18244–18251, 2009.

Sam Walcott, David M Warshaw, and Edward P Debold. Mechanical coupling between myosin molecules causes differences between ensemble and single-molecule measurements. *Biophysical journal*, 103(3):501–510, 2012.

Martin R Webb, MG Hibberd, Yale E Goldman, and DR Trentham. Oxygen exchange between pi in the medium and water during atp hydrolysis mediated by skinned fibers from rabbit skeletal muscle. evidence for pi binding to a force-generating state. *Journal of Biological Chemistry*, 261 (33):15557–15564, 1986.

H Westerblad, JD Bruton, and J Lännergren. The effect of intracellular ph on contractile function of intact, single fibres of mouse muscle declines with increasing temperature. *The Journal of physiology*, 500(1):193–204, 1997.

Håkan Westerblad. Acidosis is not a significant cause of skeletal muscle fatigue. *Medicine and science in sports and exercise*, 48(11):2339–2342, 2016.

Jeffrey J Widrick, Scott W Trappe, David L Costill, and Robert H Fitts. Force-velocity and force-power properties of single muscle fibers from elite master runners and sedentary men. *American Journal of Physiology-Cell Physiology*, 271(2):C676–C683, 1996.

C David Williams, Michael Regnier, and Thomas L Daniel. Axial and radial forces of cross-bridges depend on lattice spacing. *PLoS computational biology*, 6(12), 2010.

John R Wilson, KK McCully, Donna M Mancini, B Boden, and Britton Chance. Relationship of muscular fatigue to ph and diprotonated pi in humans: a 31p-nmr study. *Journal of Applied Physiology*, 64(6):2333–2339, 1988.

Roger C Woledge, Nancy A Curtin, and Earl Homsher. Energetic aspects of muscle contraction. *Monographs of the physiological society*, 41:1–357, 1985.

SA Wood, DL Morgan, and U Proske. Effects of repeated eccentric contractions on structure and mechanical properties of toad sartorius muscle. *American Journal of Physiology-Cell Physiology*, 265(3):C792–C800, 1993.

Mike Woodward and Edward P Debold. Acidosis and phosphate directly reduce myosin's force-generating capacity through distinct molecular mechanisms. *Frontiers in physiology*, 9, 2018.

Michael S Woody, Michael J Greenberg, Bipasha Barua, Donald A Winkelmann, Yale E Goldman, and E Michael Ostap. Positive cardiac inotrope omecamtiv mecarbil activates muscle despite

suppressing the myosin working stroke. *Nature communications*, 9(1):1–11, 2018.

Michael S Woody, Donald A Winkelmann, Marco Capitanio, E Michael Ostap, and Yale E Goldman. Single molecule mechanics resolves the earliest events in force generation by cardiac myosin. *eLife*, 8, 2019.

LC Yu and B Brenner. Structures of actomyosin crossbridges in relaxed and rigor muscle fibers. *Biophysical Journal*, 55(3):441–453, 1989.

George Ireneus Zahalak. A distribution-moment approximation for kinetic theories of muscular contraction. *Mathematical biosciences*, 55(1-2):89–114, 1981.

Cuiping Zhao and Douglas M Swank. The drosophila indirect flight muscle myosin heavy chain isoform is insufficient to transform the jump muscle into a highly stretch-activated muscle type. *American Journal of Physiology-Cell Physiology*, 312(2):C111–C118, 2016.